Commercial Development of a Multi-Use Personal Ventilation/Filtration Device

Propulsive Wing, LLC
Final Technical Report
EPA Agreement Number: x-83232501
Sub-recipient Agreement Number: TAD 2007-05
January 14, 2009

Investigators:
Joseph Kummer – President, Propulsive Wing, LLC
JB Allred – President, Allred & Associates, Inc.
Jensen Zhang – Professor, Syracuse University
Jingjing Pei – Graduate Student, Syracuse University

Abstract

Allergens and other contaminants in public places adversely affect many people. Poor air quality results in reduced productivity at work, and airplane travelers are often exposed to diseases from other passengers. One potential solution is through the use of personal air ventilation systems, or PAVs; however, the current technology lags the need tremendously.

Through funding from the Syracuse Center of Excellence, Propulsive Wing, LLC, in collaboration with Allred & Associates, Inc. and Syracuse University, has developed a unique personal air purifier system to reduce contaminant and allergen exposure, delivering clean, fresh air to an individual. This methodology utilizes an individual's thermal plume to enhance cleaning effectiveness, is compact, quiet, and consumes only 2 Watts of power. In addition to air quality improvement, the unit interfaces with a computer for power, control, and performance monitoring.

Analytical, computational, and experimental tools were used to achieve the design objectives. Computational fluid dynamics simulations of the personal environment and the PAV device were used to optimize the design. The Building Energy and Environmental Systems Laboratory tested particle and VOC filter media, as well as complete PAV prototypes. Results show dramatic air quality improvement and targeted delivery of this filtered air to the user.

Acknowledgement

Propulsive Wing would like to thank the Syracuse Center of Excellence and the U.S. EPA for the opportunity to pursue this project. The support of Ed Bogucz, Suresh Santanam, Lisa Cleckner, and the rest of the staff at the Center of Excellence facilitated the development of a technology we believe could have a significant impact.

This publication was made possible by Grant No. x-83232501 from the U.S. Environmental Protection Agency. Its contents are solely the responsibility of the authors and do not necessarily represent the official views of the U.S. EPA.

Table of Contents

Grant Summary

Project Period: January 1, 2008 to December 31, 2008

Objective of Project: To develop a personal filtration device for use by individuals in an office, airplane, or similar setting. This device is low power, quiet, and unobtrusive, yet efficiently filters contaminants from the air, delivering clean, filtered air to the user. By the end of the year our goal was to bring the development through the R&D phase (basic research on personal ventilation and filter design, prototyping, and laboratory testing) and start to transition into initial production. This has been successfully completed, and we anticipate production of the PAV product to begin in 2009.

Progress Summary: A comprehensive summary of the results from this project are given in the technical sections.

Budget Status: The project goals were accomplished on time and within the stated budget.

Potential for Job Creation: The grant money provided funds to support technicians and designers to work on the project. Over the course of 2008 this represented approximately 1-2 full time positions. We expect several positions related to this project will be filled in 2009 and 2010 as the units begin to have sales. Assembly of the units will occur in our Elbridge, NY facility. In addition, both Propulsive Wing and Allred & Associates expect to hire engineering staff over the next couple of years.

Publications/Presentations: Dr. Kummer gave a presentation on September 29, 2008 at the Syracuse Symposium on Environmental & Energy Systems. Also presented at the conference were two posters on the project, as well as demonstrations of the latest PAV prototype and filter testing device. Dr. Kummer also gave a presentation on December 4, 2008 for the Center of Excellence Scientific Advisory Committee at the Renaissance Hotel in Syracuse.

Patent Applications: A utility patent application was submitted to the U.S. Patent Office on September 26, 2008, on the PAV design developed here.

Supplemental Keywords: None

Relevant Web Sites: No websites have been used yet to market this product. The custom filter testing device designed and built during the 1st quarter of 2008 is now shown on the Propulsive Wing website [www.propulsivewing.com]. A website for the PAV product is planned for February 2009.

SECTION 1

CFD Simulations of the Personal Environment

1.1 Benchmark case

The benchmark case corresponds to an experiment conducted by Kato at the University of Tokyo (Nielsen et al., 2003). In this experiment a heated manikin stood in a small room with a simulated displacement ventilation setup. Data was taken at various locations in the space for the purposes of both understanding the flow around a person, as well as providing a database for computational fluid dynamics (CFD) validation.

In the work presented here, the geometry was created using the Solidworks CAD software. The geometry was then imported into the CFD software Star-CCM+ for grid creation, solving, and post-processing. Several grids were created to investigate grid convergence. The domain geometry and simulation input parameters are given in Fig. 1-1. The refined mesh is shown in Fig. 1-2.

Velocity magnitude contours in Fig. 1-3 show the rising thermal plume above the head of the person. The velocity in the core of the thermal plume is in the 0.2 to 0.25 m/s range. In Fig. 1-4, temperature contours show the stratification of the air, as well as the warm rising air in the thermal plume surrounding the person. Streamlines starting at the room inlet are plotted in Fig. 1-5, and demonstrate the path the air takes as it enters the room. Due to the relatively high velocity and short distance, most of the air initially passes by the person, setting up large recirculating regions in the room.

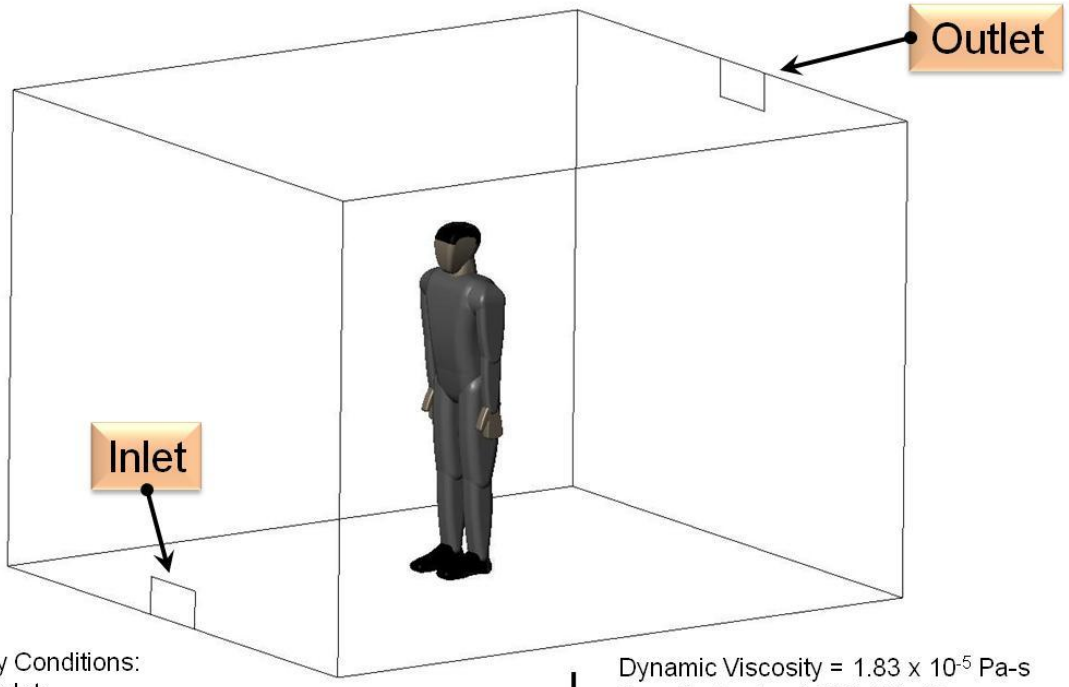

Boundary Conditions:
Velocity Inlet:
Velocity = 0.2 m/s (directed horizontally)
Temperature = 22 C
Turbulence Intensity = 30%
Turbulent Length Scale = 0.1 m
Pressure Outlet
Constant Heat Flux on Simulated Person = 16.05 W/m^2
OR Constant Temperature on Simulated Person = 31 ^oC
Density = 1.197 kg/m^3

Dynamic Viscosity = 1.83 x 10^{-5} Pa-s
Specific Heat = 1.005 J/Kg-K
Thermal Conductivity = 0.02584 W/m-K
Thermal Expansion Coefficient = 3.4 x 10^{-3}
Turbulent Prandtl Number = 0.9

Dimensions:
Overall = 3.5 m x 3 m x 2.5 m
Inlet and Outlet = 0.2 m x 0.4 m
Height of Simulated Person = 1.8 m

Fig. 1-1 Domain geometry and input parameters (CAD model of human from www.zxys.com).

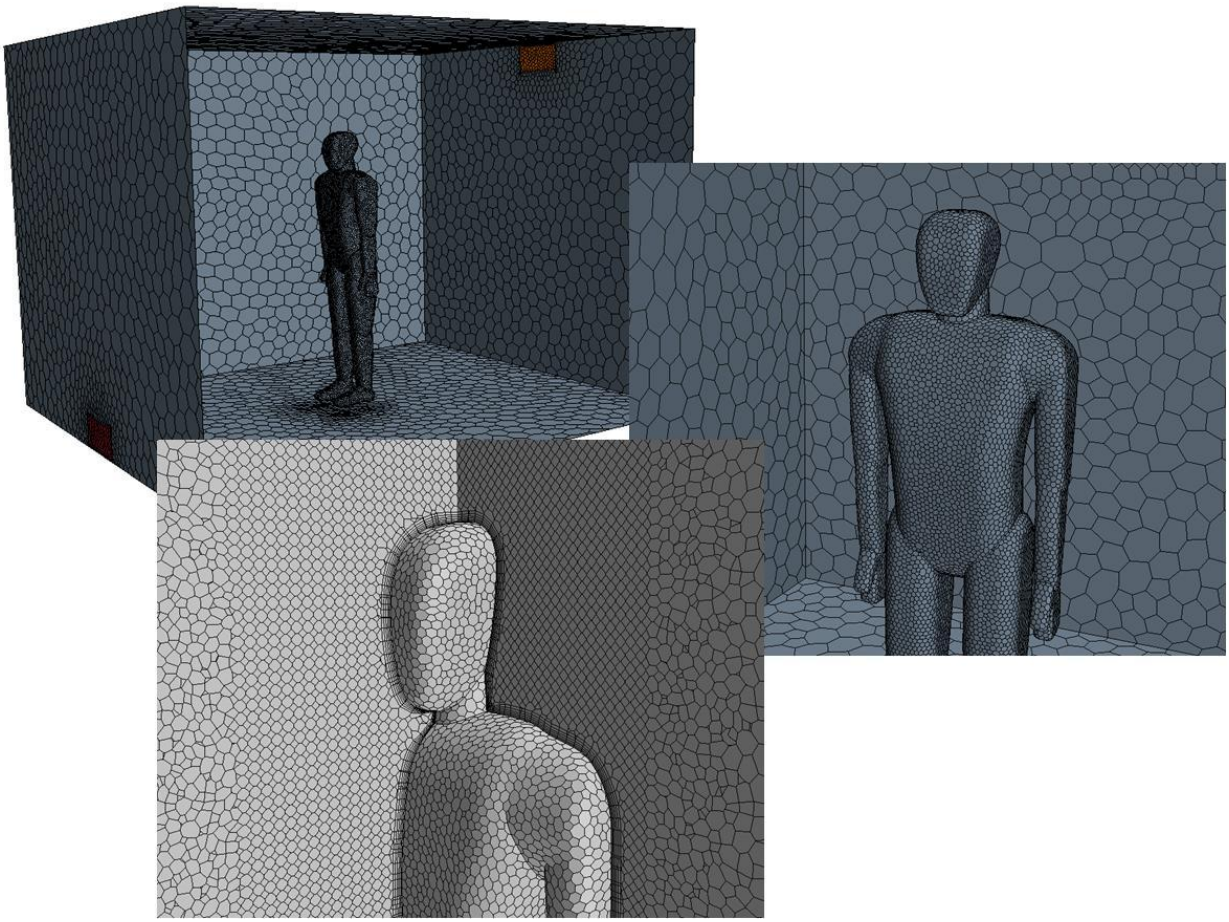

Fig. 1-2 Refined computational grid.

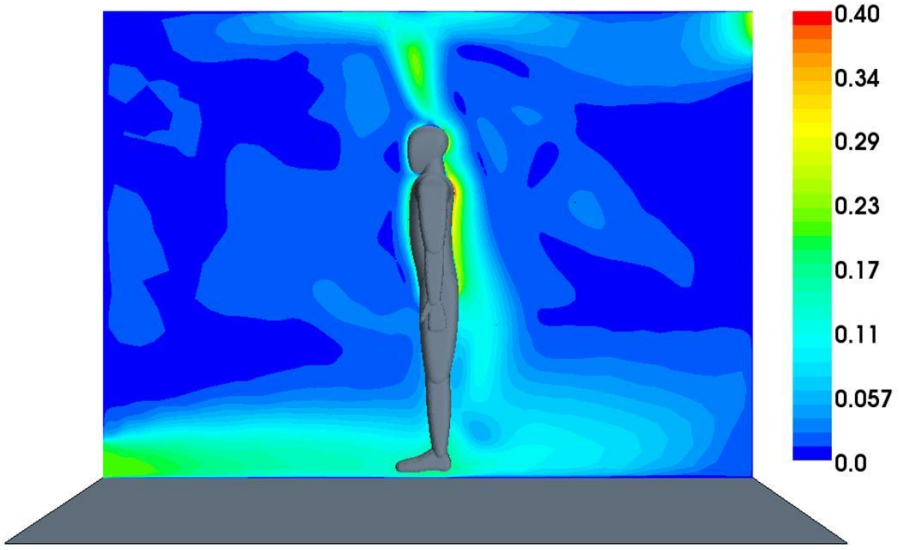

Fig. 1-3 Velocity magnitude contours (m/s).

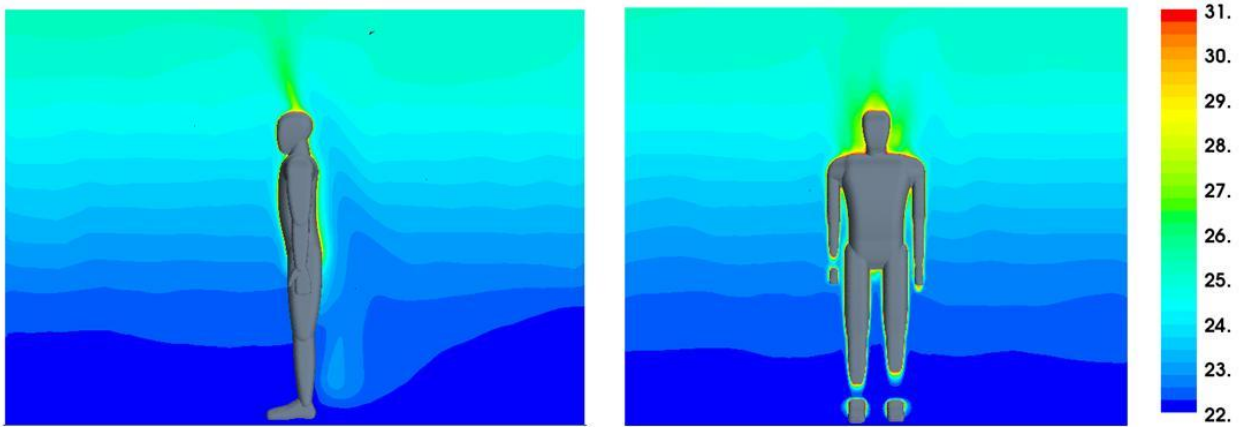

Fig. 1-4 Temperature contours (^{o}C).

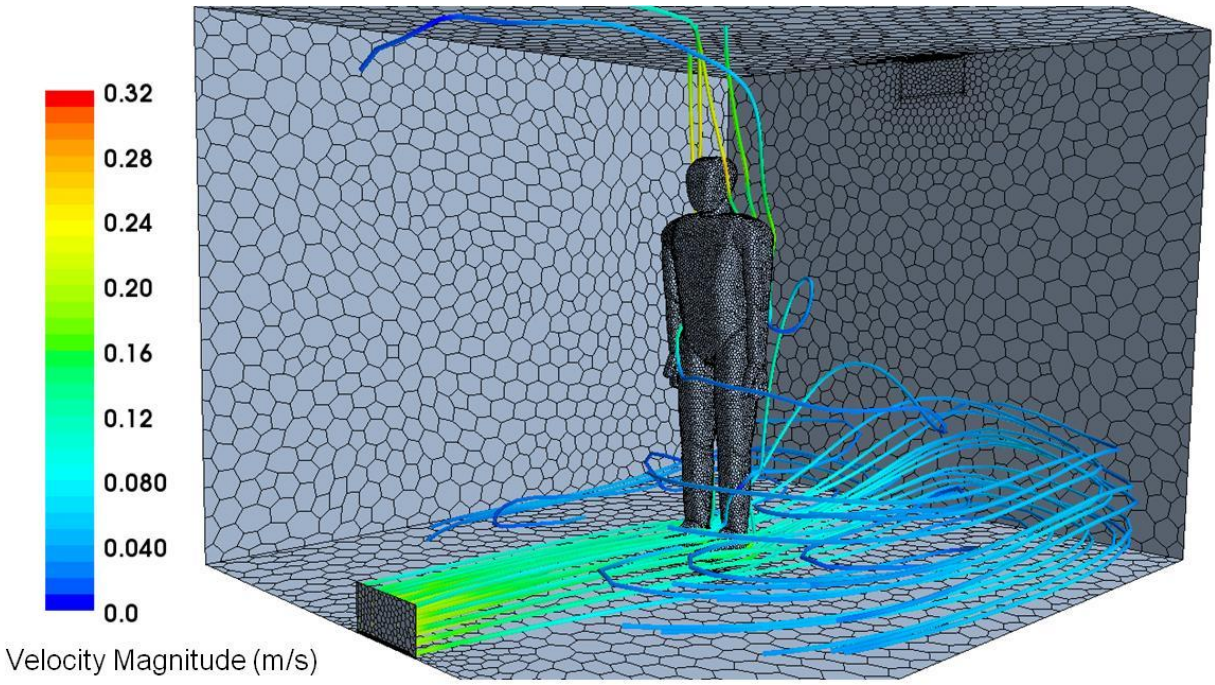

Fig. 1-5 Streamlines starting from domain inlet.

Simulation data was collected along two plot lines (shown in Fig. 1-6), one vertically rising above the head, and the other coming outward from the face. These locations correlate with similar published studies (Sideroff, 2007 and Deevy, 2008), and hence will give an indication of the accuracy of the present simulations.

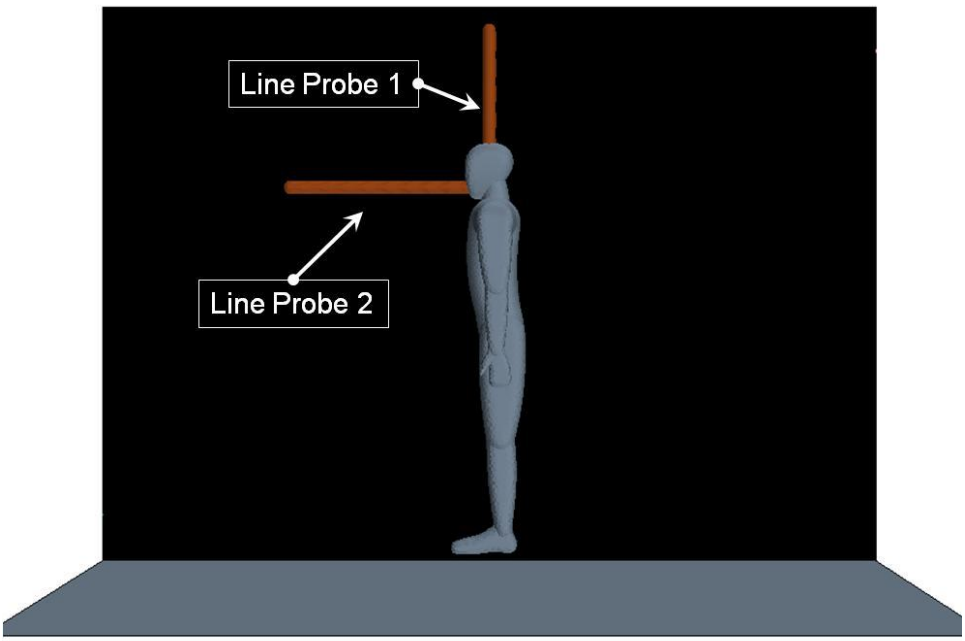

Fig. 1-6 Plot lines for simulation data collection.

Velocity magnitude and temperature above the head are plotted in Fig. 1-7 as a function of grid resolution. The velocity here was almost unchanged for the fine meshes regardless of the boundary condition used on the person; however, there was a clear difference in the calculated temperature. With the constant temperature boundary condition, the temperature above the head was predicted to be slightly higher than with the constant heat flux boundary condition. A similar trend was found along the line coming out from the face (Fig. 1-8). The temperature was not sensitive to the grid, but depended on the choice of surface boundary condition of the simulated person. For the velocity magnitude, the values near the person are very close to one another, whereas further away the coarsest grid noticeably deviates from the other three.

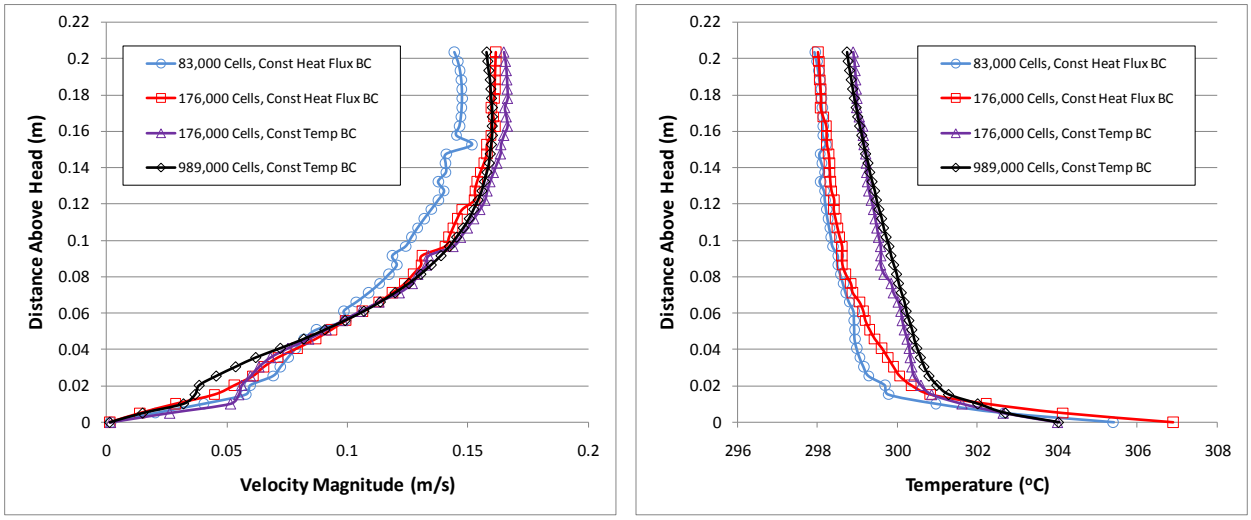

Fig. 1-7 Velocity magnitude and temperature above head as a function of grid resolution.

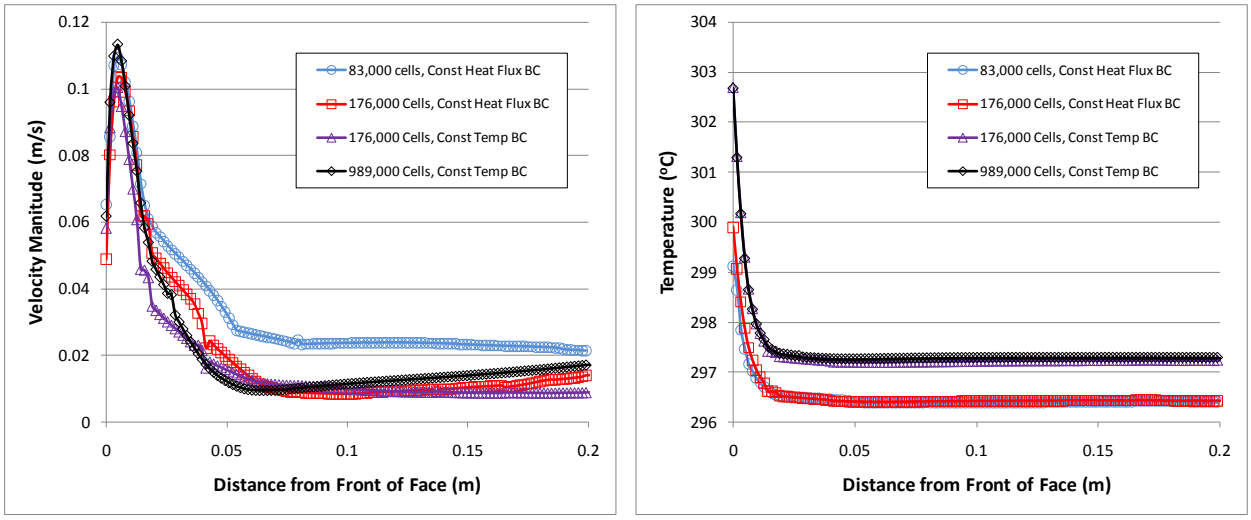

Fig. 1-8 Velocity magnitude and temperature in front of face as a function of grid resolution.

Calculations were made on the finest grid (989,000 cells) to investigate sensitivity to turbulence model choice. Runs were made using the k-e Standard, k-e Realizable, and Spalart models (shown on Figs. 1-9 and 1-10). Along line probe 1 above the head, velocity magnitude was

virtually unchanged when going from the Standard to Realizable k-e model, but the Spalart model showed a marked difference away from the person. All three models were slightly different when looking at temperature distribution.

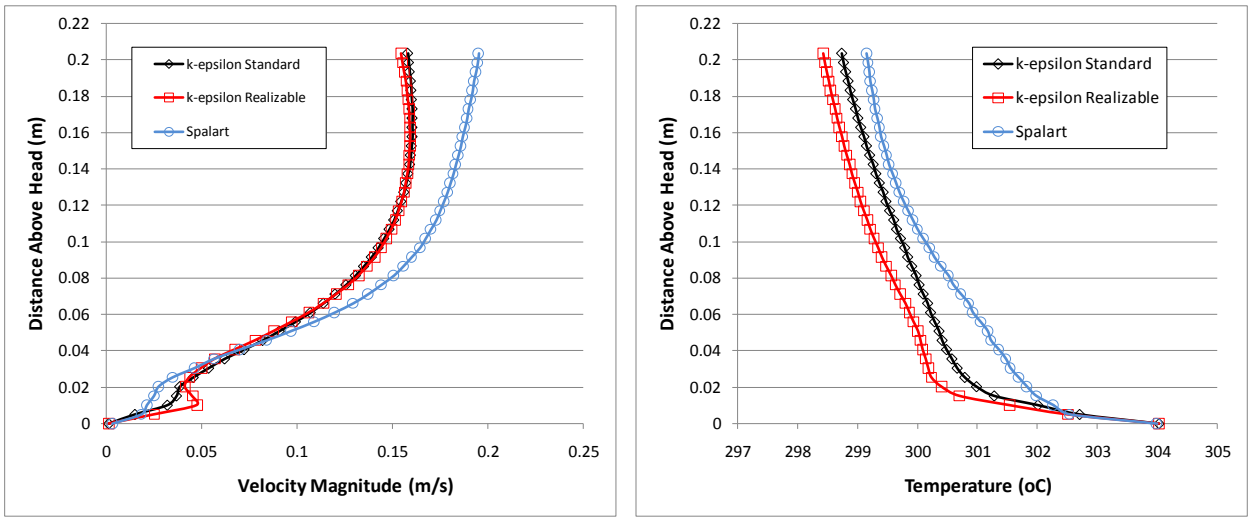

Fig. 1-9 Velocity magnitude and temperature above head as a function of turbulence model.

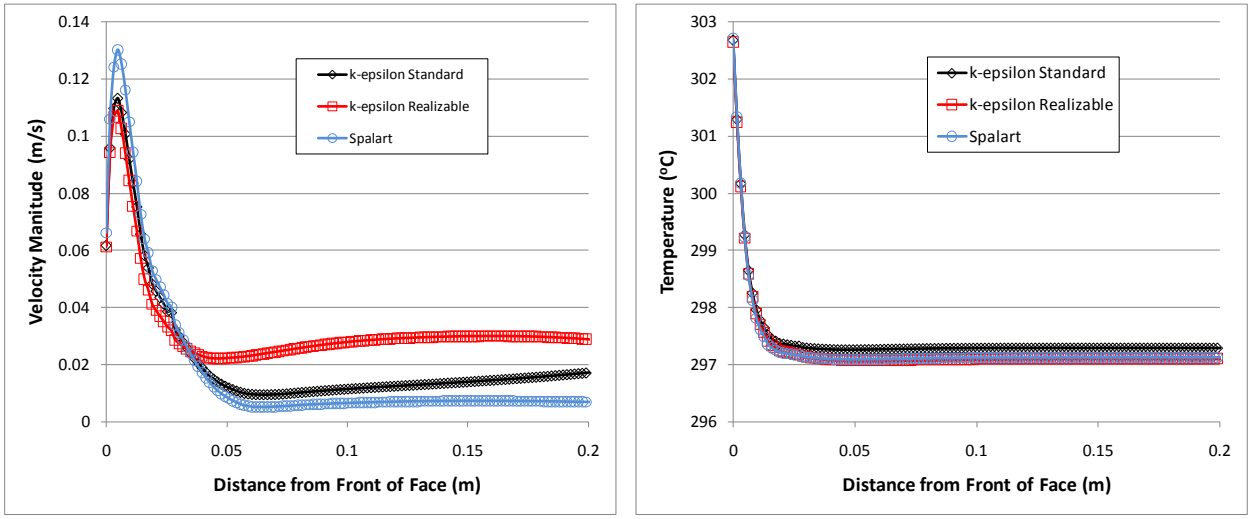

Fig. 1-10 Velocity magnitude and temperature in front of face as a function of turbulence model.

Based on a study of the literature in this area, for accuracy over a broad range of problems it is recommended to use, if possible, a constant temperature boundary condition. If the heat flux boundary condition is used, the literature suggests that it is necessary to also use a radiation model. The simulations performed here suggest that it may not be a critical decision, depending on the problem being studied and region of interest, since the results were not drastically different. In general, however, using a constant temperature on the surface of the person resulted in better convergence and numerical stability, and so this technique will be used for the proceeding simulations involving the interaction of a person and the personal air ventilation (PAV) device.

The data from this study also suggests that a grid of the type shown here with a total cell count in the 200,000 range will most likely result in sufficient grid convergence. Future grids will follow this example in terms of setup and grid resolution.

From the data in this study it is difficult to conclude which of the three tested turbulence models performs the best. Although the simulated geometry was similar to published experimental data (and the trends follow closely with those of the other investigators), the exact geometry used in the experiments was not available for direct comparisons. Based on past performance with other analyses, the k-e Standard model will be used for future studies.

1.2 Simulated Person Sitting in an Office Utilizing the "Black-Box" PAV Device

This study looked at the flow around a simulated person working in an office. The geometry was built up by starting with the person alone, and then adding furniture one piece at a time, running a simulation each time to assure that the piece was included properly. In figures 1-11 through 1-13, the final geometry is shown. The PAV device is included in the simulations. It is attached to the front of the laptop computer in order to draw in flow from the thermal plume, filter it, and exhaust the filtered air back toward the person in an effort to constitute as large of a portion of the breathed air as possible. The full PAV device, including internal flow path and fan, is replaced here with a simple inlet and outlet (i.e. only inlet and outlet boundary conditions are specified). By doing this the grid count is reduced considerably. In addition, whereas an unsteady simulation is necessary when a rotating fan is present, for the case with a "black-box" PAV device, the simulation becomes steady, thus reducing time to convergence.

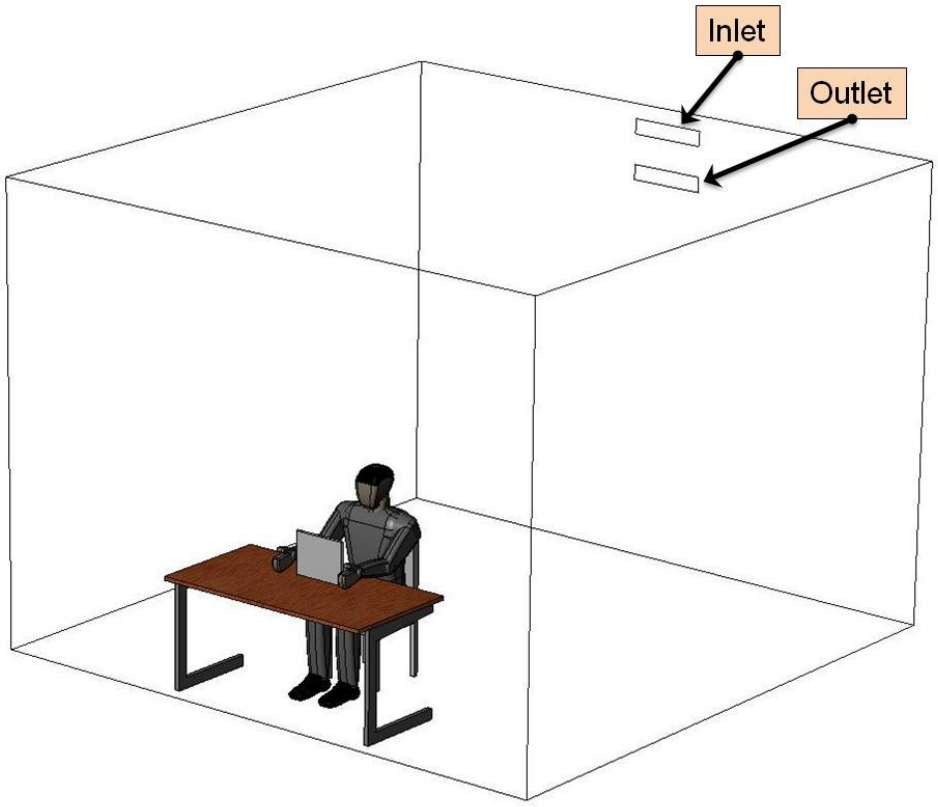

Fig. 1-11 Domain geometry for simulation of person with PAV working at a desk.

Fig. 1-12 Closeup of geometry of simulated person at desk with PAV.

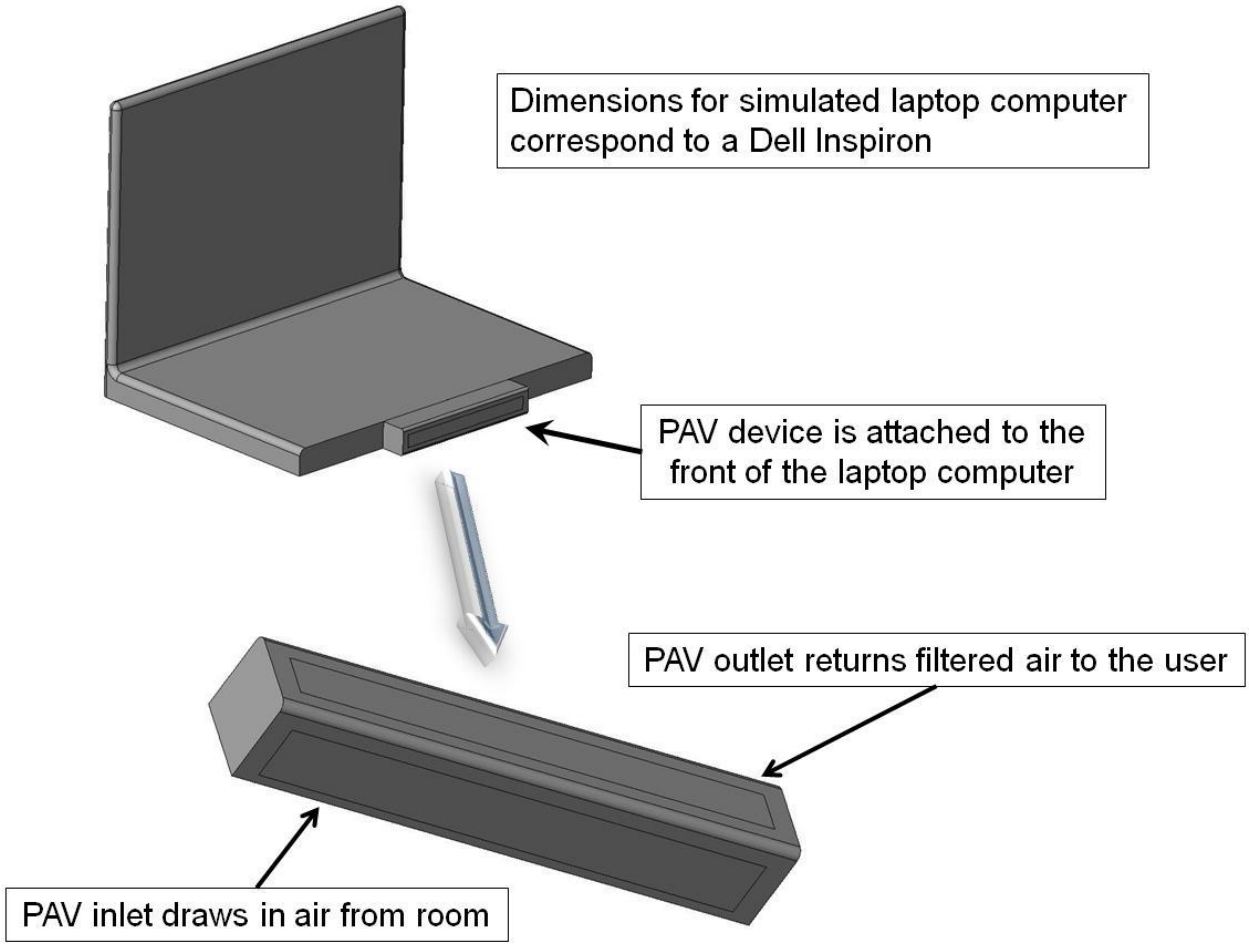

Fig. 1-13 Integration of black-box PAV into simulation.

Multiple cases were simulated, including having the PAV device both off and on. With the PAV on, 6 cases are presented: a horizontal exit jet (0 degree case), 30^{o} exit jet (measured from horizontal), and 45^{o} exit jet. For each outlet angle setting, the exit flow was simulated at a velocity of 0.5 m/s and 1.0 m/s. Figure 1-14 shows the computational mesh used for these simulations, which consisted of 673,000 cells. Grid clustering was made near the person, laptop computer, and in the proximity of the PAV device in order to adequately capture the exhaust jet.

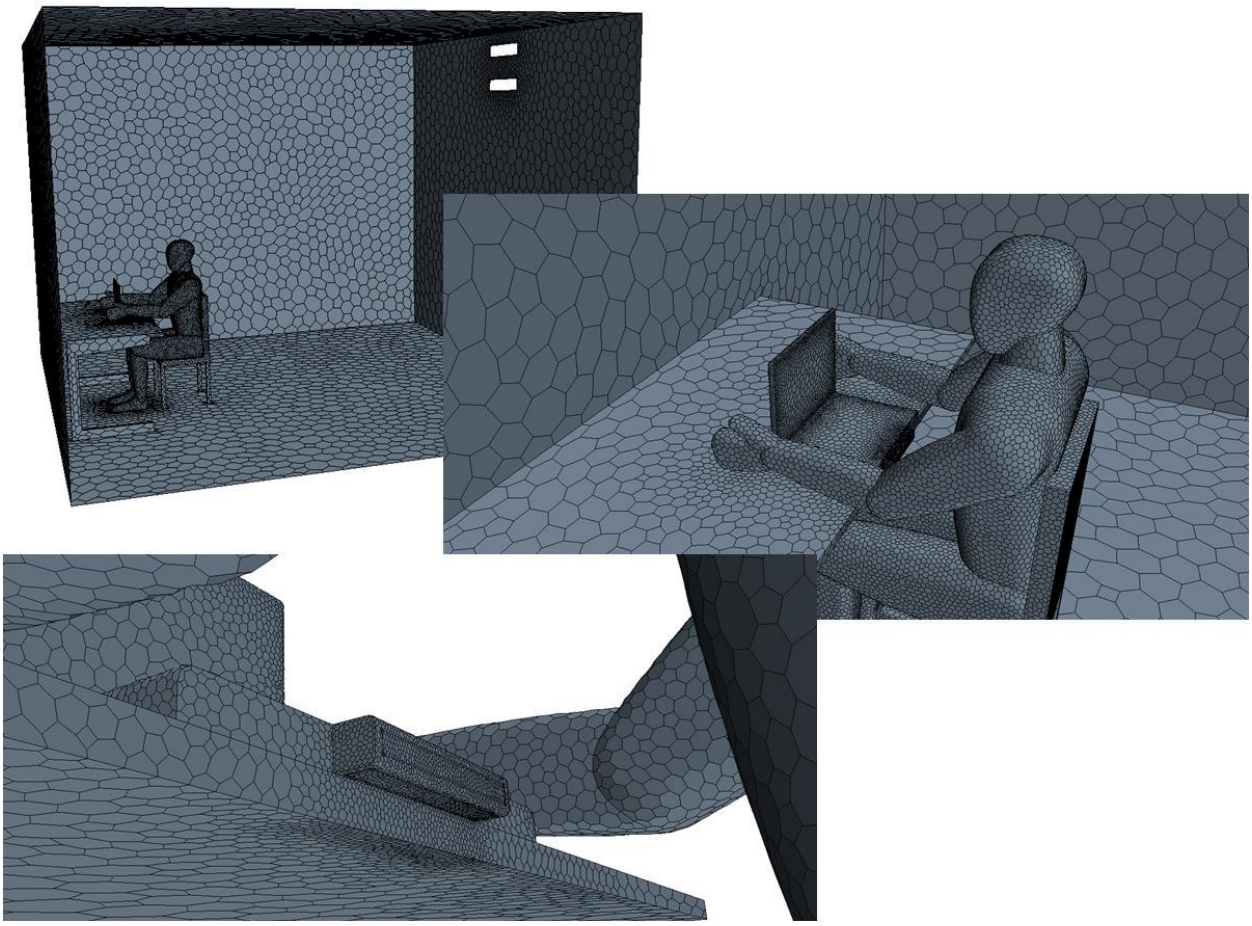

Fig. 1-14 Computational mesh for simulation of PAV device with person.

Simulation setup consisted of setting the surface temperature for both the person (31 ^{o}C) and computer (33 ^{o}C), as well as the inlet (velocity inlet) and outlet boundary conditions (velocity inlet with temperature = 26 ^{o}C) for the PAV device. With the PAV device off, velocity magnitude contours at the center-plane (shown in Fig. 1-15) clearly show the rising thermal plumes of the simulated person and laptop computer. Of particular note is the region just below the table and between the table and person. It is this air that travels up to the breathing zone. In order to effectively mitigate contaminants from the air that the person is breathing, this air must be filtered. In Fig. 1-16, the streamlines for this case plot the path the air takes to reach the breathing zone. This data confirms that the majority of the air originates from the floor. It travels up the person's lap, torso, and eventually passes their face. A large portion of the flow actually passes directly over the PAV device located at the front of the desk. This is of particular relevance to the current project, since it means that in order to provide filtered air to the user, the natural flow path of the air will not need to be altered, hence reducing the necessary energy input considerably when compared to a system that aims to drastically change the flow patterns near the person.

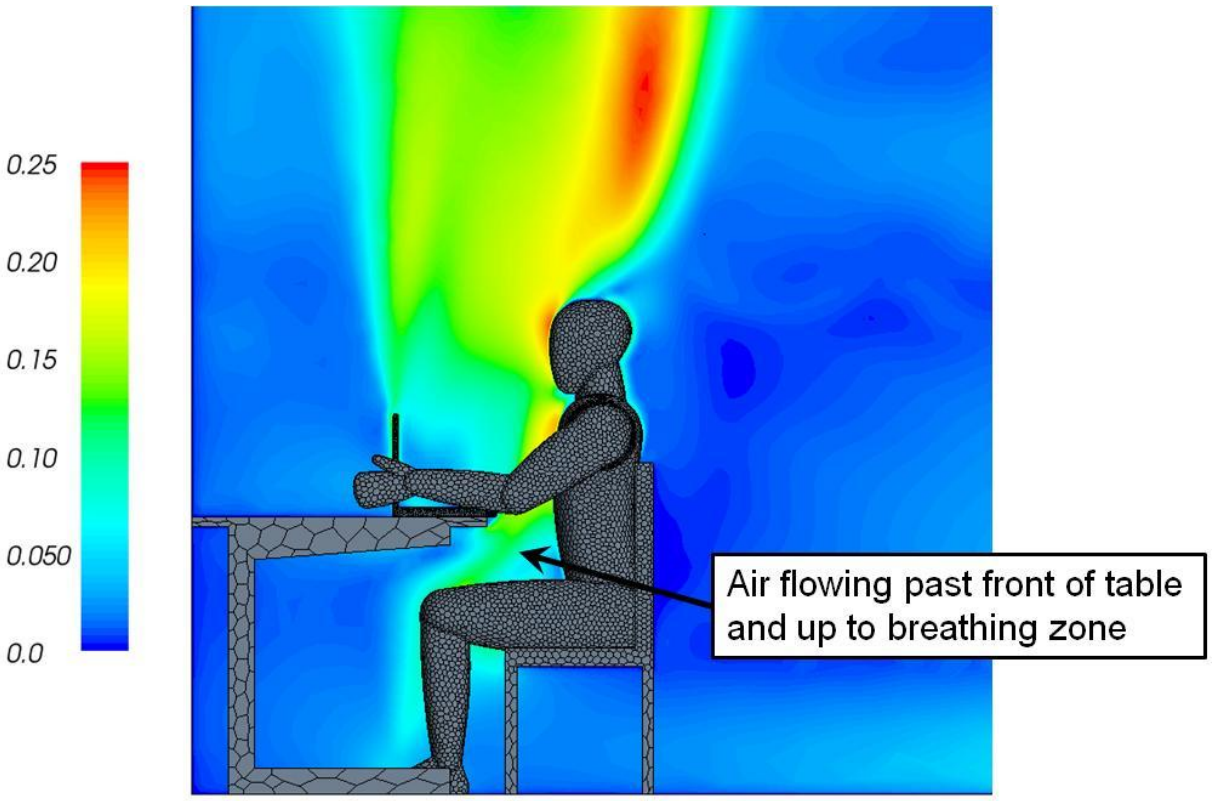

Fig. 1-15 Velocity magnitude contours at the center-plane (m/s).

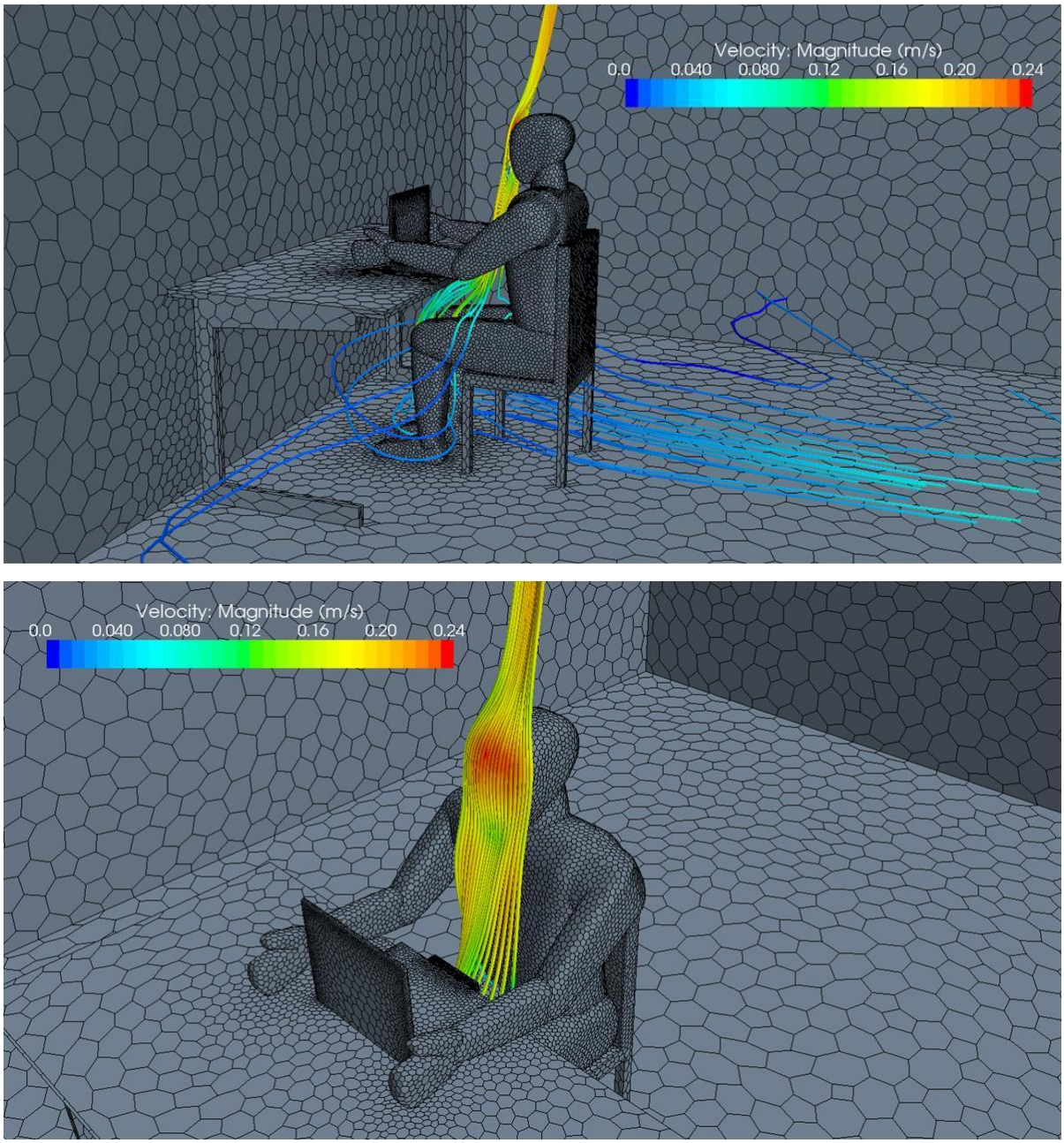

Fig. 1-16 Computational mesh for simulation of PAV device with person.

Figures 1-17 through 1-22 show the results of the simulations with the PAV device operational. For case 1, the outlet jet is directed horizontally toward the person at 1 m/s. For this case the air fully penetrates the person's thermal plume. In fact, the jet has too much momentum, by-passing the breathing zone altogether (Fig. 1-23). Figure 1-24 shows both air from the PAV device, as well as that from below the table. The blue streamlines here are from the PAV outlet. The red streamlines represent air traveling from the floor up to the breathing zone. In the case where the PAV device was off, this air simply passed straight up over the person's lap and by the PAV. In this case, with the PAV device on, essentially the same air reaches the breathing zone, only now it must flow around the PAV exhaust.

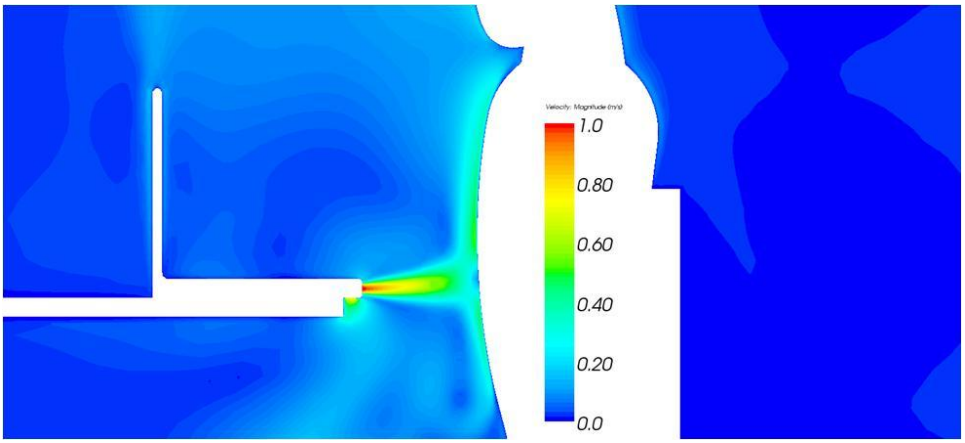

Fig. 1-17 Case 1: exhaust angle = 0^{o}, exhaust velocity = 1 m/s.

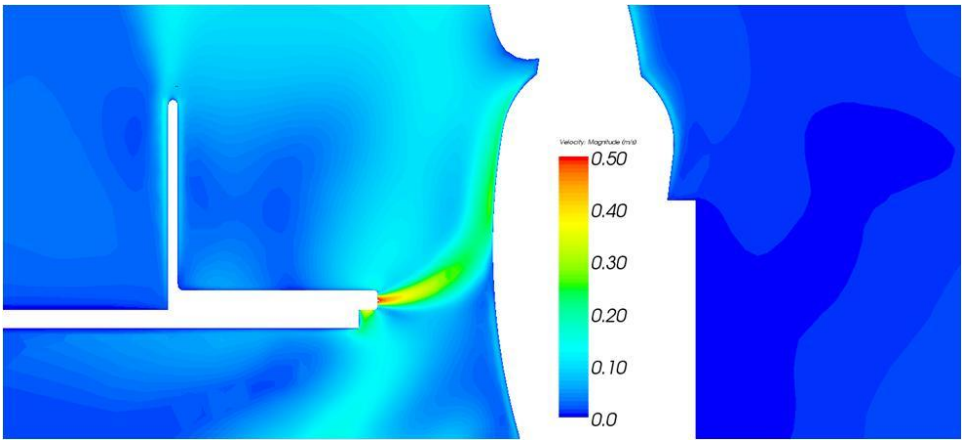

Fig. 1-18 Case 2: exhaust angle = 0^{o}, exhaust velocity = 0.5 m/s.

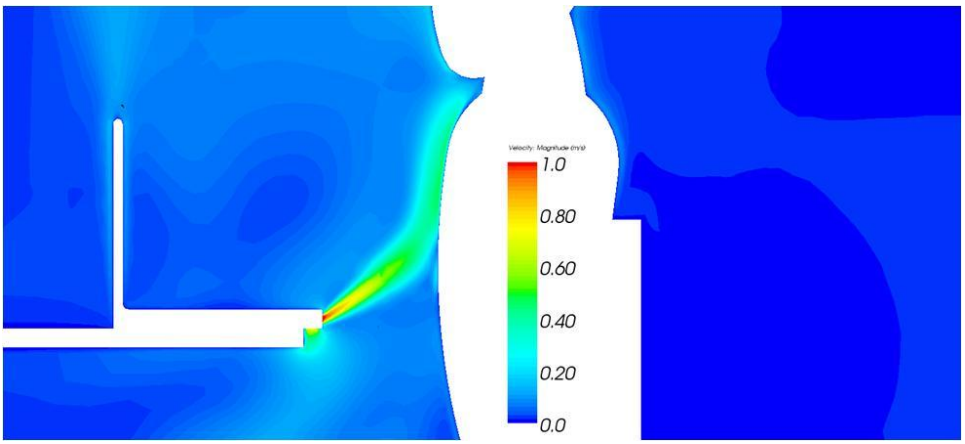

Fig. 1-19 Case 3: exhaust angle = 30^{o}, exhaust velocity = 1 m/s.

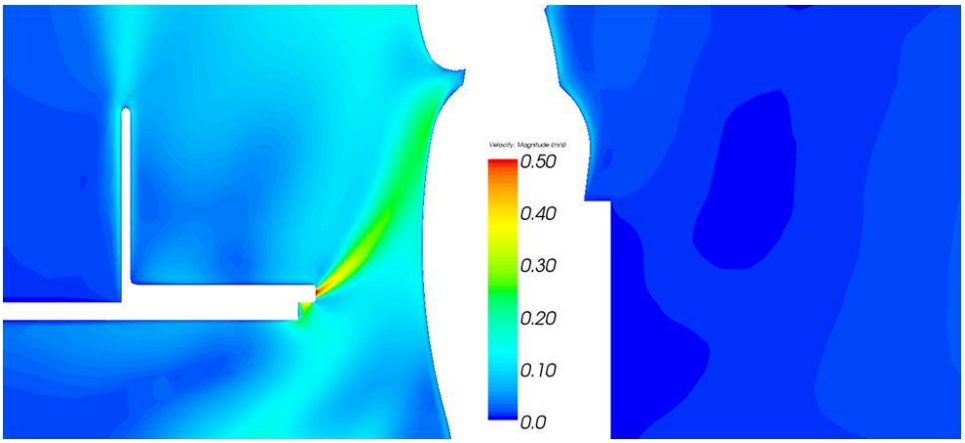

Fig. 1-20 Case 4: exhaust angle = 30^{o}, exhaust velocity = 0.5 m/s.

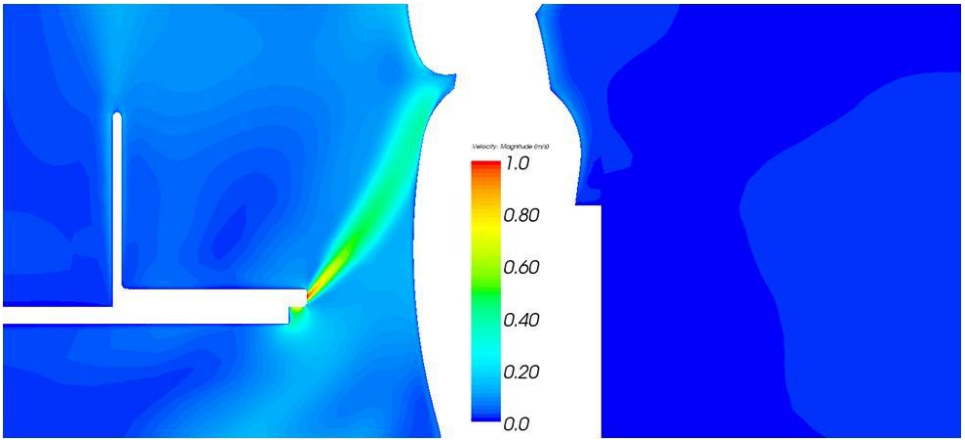

Fig. 1-21 Case 5: exhaust angle = 45^{o}, exhaust velocity = 1 m/s.

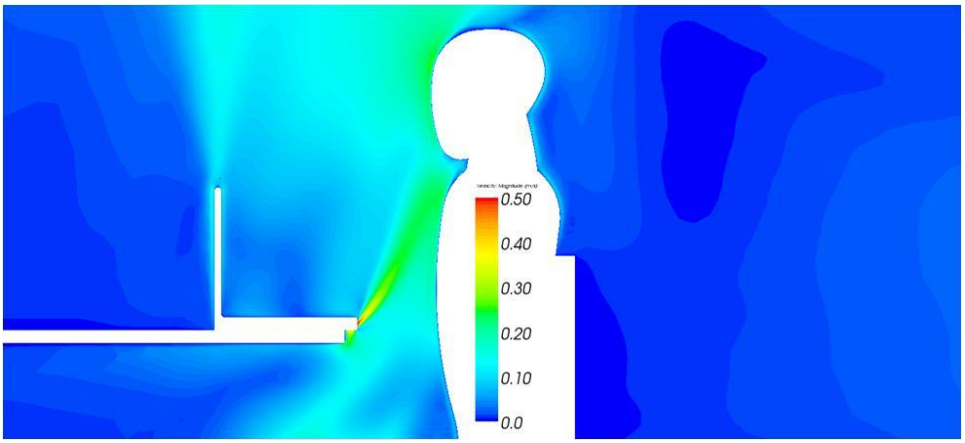

Fig. 1-22 Case 6: exhaust angle = 45^{o}, exhaust velocity = 0.5 m/s.

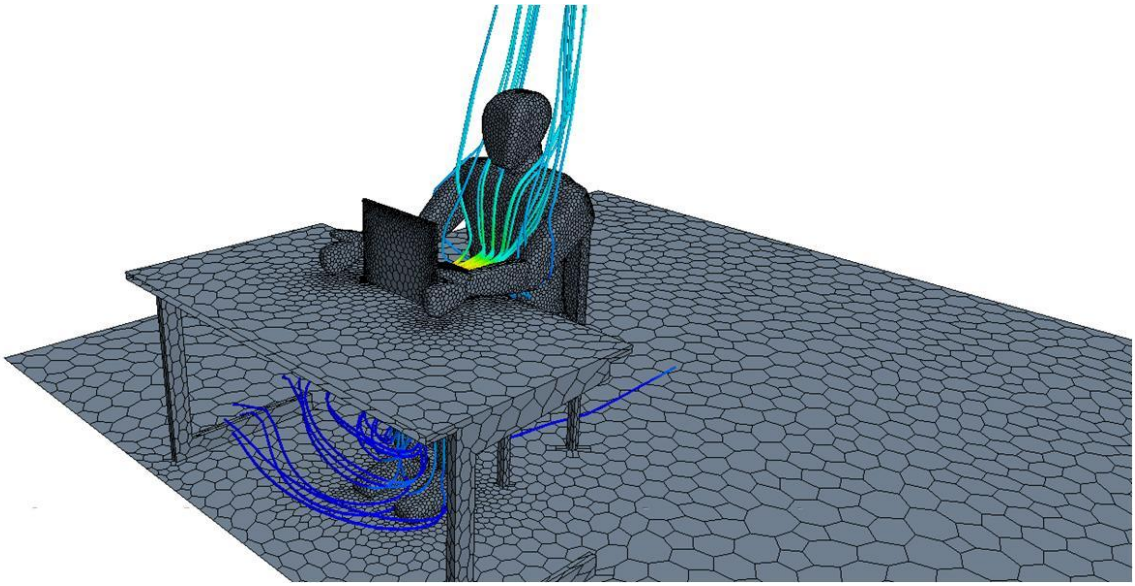

Fig. 1-23 Streamlines entering and exiting PAV device for Case 1.

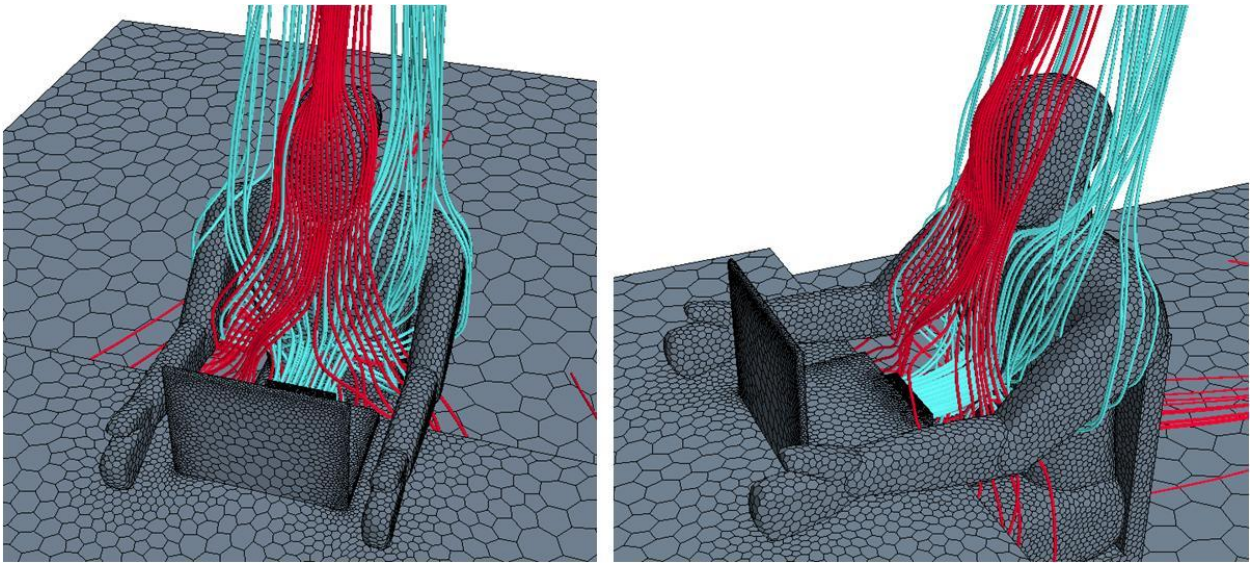

Fig. 1-24 Streamlines exiting PAV (blue) and coming from floor bypassing PAV (red).

By increasing the PAV outlet angle to 30^{o}, the filtered air flows much closer to the breathing zone (Fig. 1-25). However, the high momentum still carries it passed the face. Reducing the outlet velocity by half to 0.5 m/s caused the filtered air to remain within the breathing zone. The air leaves the PAV and convects upward by the thermal plume. This combination of outlet angle and velocity results in excellent delivery of filtered air to the person.

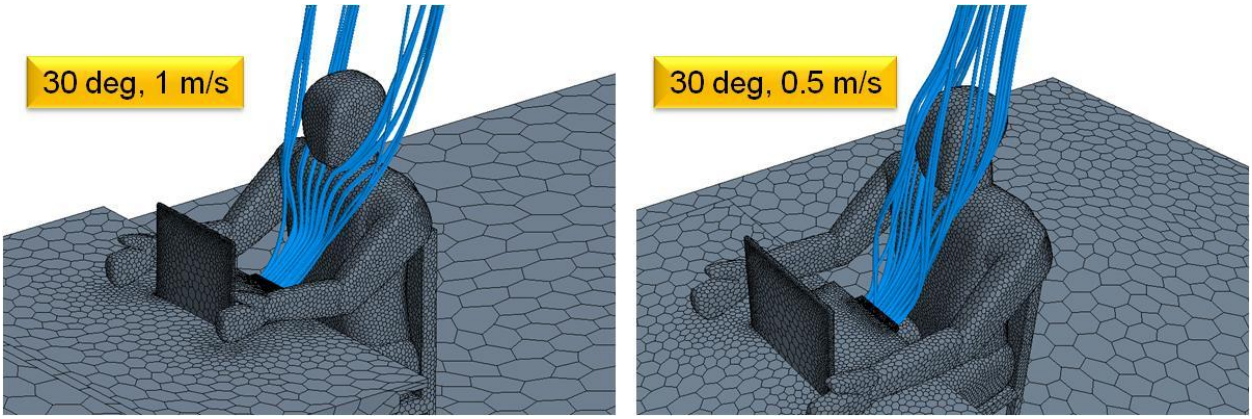

Fig. 1-25 Streamlines exiting PAV for 30^{o} exhaust angle.

At an outlet angle of 45 degrees, shown in Fig. 1-26, at 1 m/s the PAV filtered air covered the breathing zone very well. Reducing the velocity to 0.5 m/s, however, resulted in a portion of the filtered air failing to adequately reach the face. The combination of lower momentum and higher outlet angle caused the flow to become entrained in the thermal plume too soon before reaching the person.

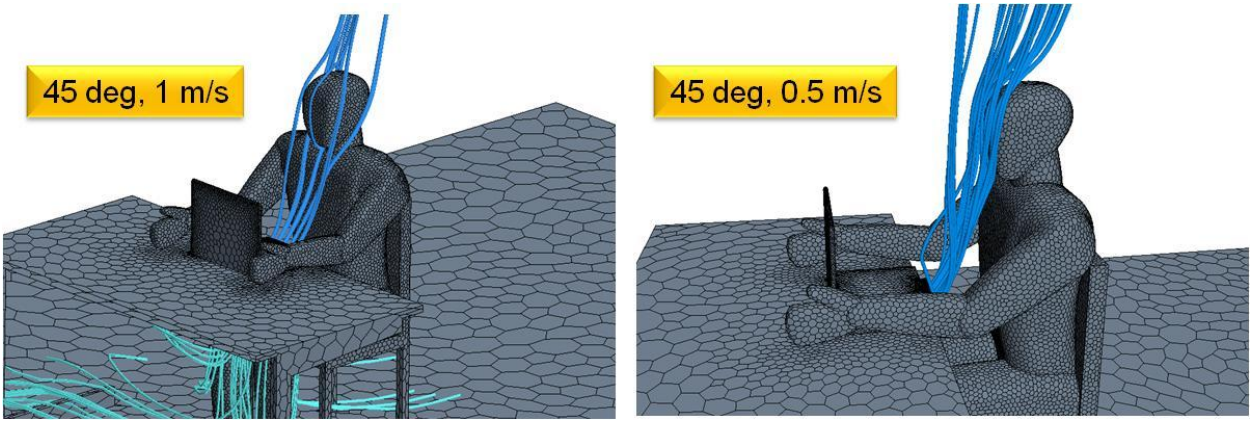

Fig. 1-26 Streamlines exiting PAV for 45^{o} exhaust angle.

For this study, the Solidworks CAD and Star-CCM+ CFD software packages were used to create complex geometries and the computational meshes. Using a “black-box” approach to simulate the PAV device significantly reduced the meshing requirements and time to converge compared with a full unsteady simulation including the rotating fan. This permitted parametric studies on the flow external to the PAV without knowing the exact internal PAV geometry a priori.

These results demonstrate that the flow entering the breathing zone originates near the floor and is significantly influenced by the individual’s thermal plume. Placing the PAV device in the natural flow path of this buoyant air, ingesting and filtering it, and then exhausting the air back toward the individual results in an efficient means to deliver clean air without any external air source (for example, a central air supply).

Results with the PAV device turned on show that there is an optimum combination of outlet flow angle and outlet velocity for delivery of the filtered air to the breathing zone. If the angle is set too low and velocity too high, the momentum in the flow carries it through the thermal plume and passed the person. By comparison, at a high angle and low velocity the air is unable to penetrate the thermal plume and instead is convected upward before reaching the face. These CFD results agree well with the observations from an experimental study performed by Melikov (Melikov et al., 2002).

SECTION 2

Selection and Testing of Candidate Filters

2.1 Testing Commercially Available Filters and Development of Custom Filters for PAV Use

The Syracuse University team in the BEESL laboratory performed a literature review of commercially available filters related to VOC and gas phase pollutants in residential houses, office buildings, and in aircraft environments. Based on this review, a media performance test was performed to determine VOC breakthrough and pressure drop across 2-layer ACF (activated carbon), 3-layer ACF, and a sandwich-type media comprised of 2 layers of ACF packed with granular activated carbon. Filtration media selected for these tests are shown in Fig. 2-1.

From these tests, the following conclusions were drawn:

1. The activated carbon coated non-woven filter medium has a short life time (under 350ppb challenge concentration, both 2-layer and 3-layer media saturated after only 1 day of testing) (Fig. 2-2).
2. The sandwich type packed AC cloth with GAC has a much longer service life and higher efficiency: the initial efficiency is about 35%, and then stays within the range of 10%-20% (Fig. 2-2).
3. With pellet shaped activated carbon (sandwich-type filter design), the pressure drop does not show significant increase over the filter media alone (Fig. 2-3).

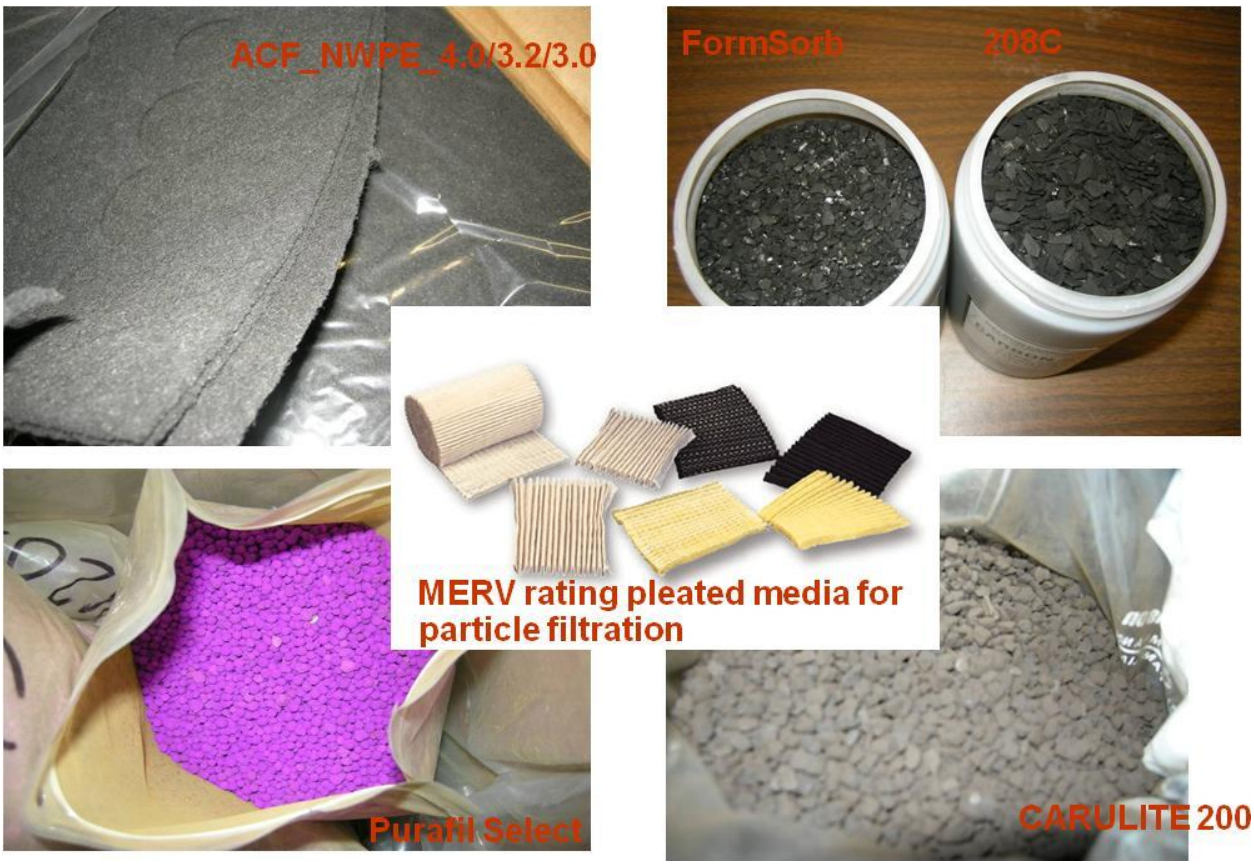

Fig. 2-1 Filtration media selected for testing.

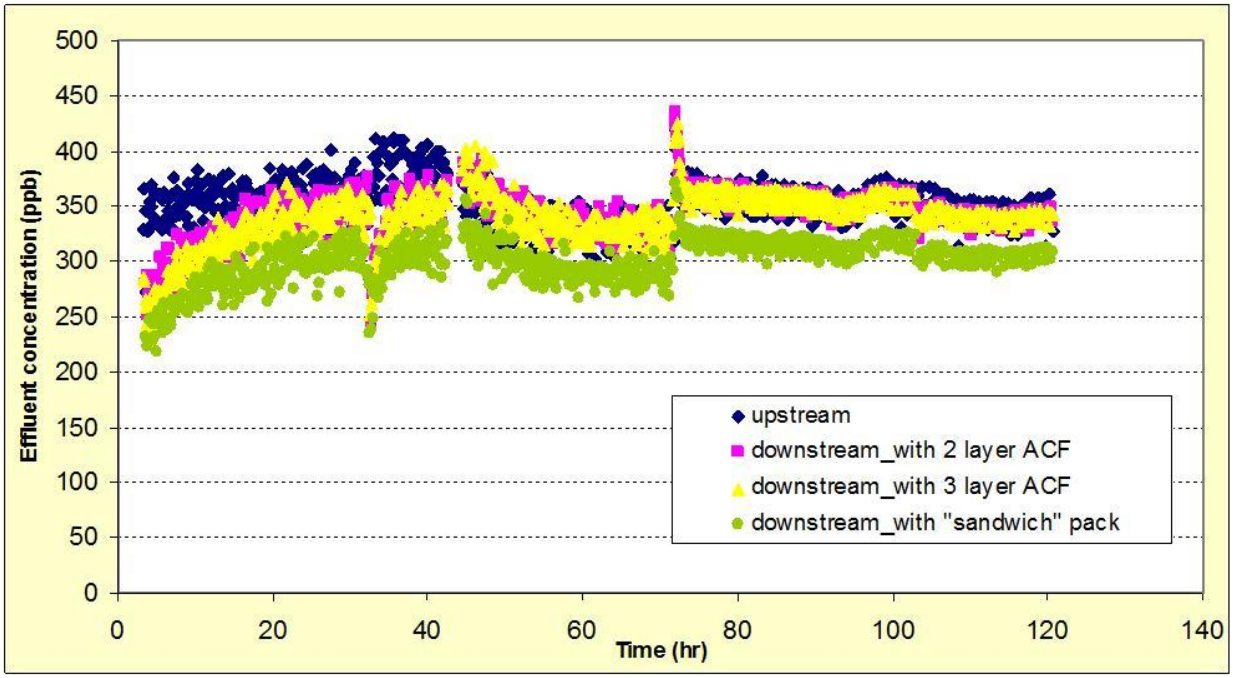

Fig. 2-2 Media performance test for activated carbon non-woven (ACF) versus sandwich filter.

Flow Rate	7 LPM	14.15 LPM	28.3 LPM
2 layer ACF	3.12	6.09	14.28
3 layer ACF	4.11	8.21	18.69
2 layer ACF with GAC (sandwich type)	2.91	5.81	13.70

Fig. 2-3 Pressure drop versus flow rate for each candidate filter type.

Implications from these data include a new activated carbon/catalyst embedded media (e.g. on particle filtration media or activated carbon cloth), which will be a good choice for this filter component arrangement. Advantages include:

1. Longer service life with pellet AC
2. Reasonable pressure drop increase
3. Simultaneous removal of different pollutants with corresponding media embedded (i.e. media for VOC, ozone, and formaldehyde)
4. Compact arrangement with simultaneous particle and gas phase pollutant removal with a single filter using a sandwich-type MERV-sorbent-MERV filter design.

Since a cross-flow fan is used in the PAV design, depending on the streamline the air takes through the fan (i.e. the path an individual air segment takes as it passes through the blades and fan center), air will both pass-through, as well as pass-by filter media. Typically only a pass-through airflow results in removal of contaminants; however, in this case the fan has a recirculating eccentric vortex region within its center that causes a significant amount of air to remain trapped within the fan for a period of time, passing the fan housing walls multiple times. We hypothesize that it may be possible to exploit this region of the fan, with airflow moving past walls, by removing additional VOCs.

To test the effect of contaminated air passing-through versus passing-by the sorbent material, a test was conducted with activated carbon pellets packed in the sample tube in a “ring” shape (pass-by), as opposed to the conventional “bed” of media (pass-through). This configuration is shown in Fig. 2-4.

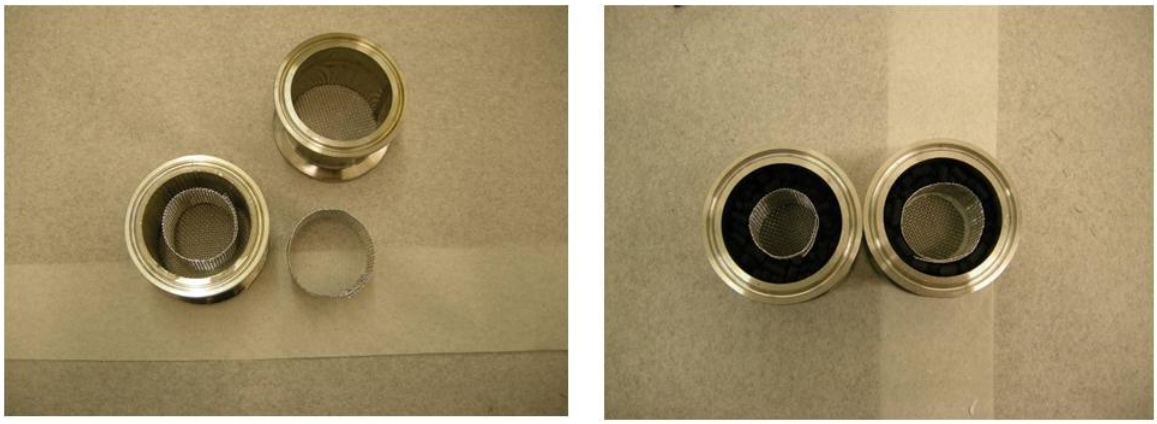

Fig. 2-4 Empty cylinders (on left) and cylinders with “rings” of activated carbon along side walls.

Results from these tests are given in Fig. 2-5, and show that with the same amount of media, the efficiency of contaminant removal via passing-by the packed sorbent (AC Ring) is much smaller than air passing-through the packed sorbent (AC Bed): 10-20% for AC Ring versus 60% for AC bed. However, when the same activated carbon distribution density was used, the removal efficiency is comparable (17% for pass-through versus 21% for pass-by).

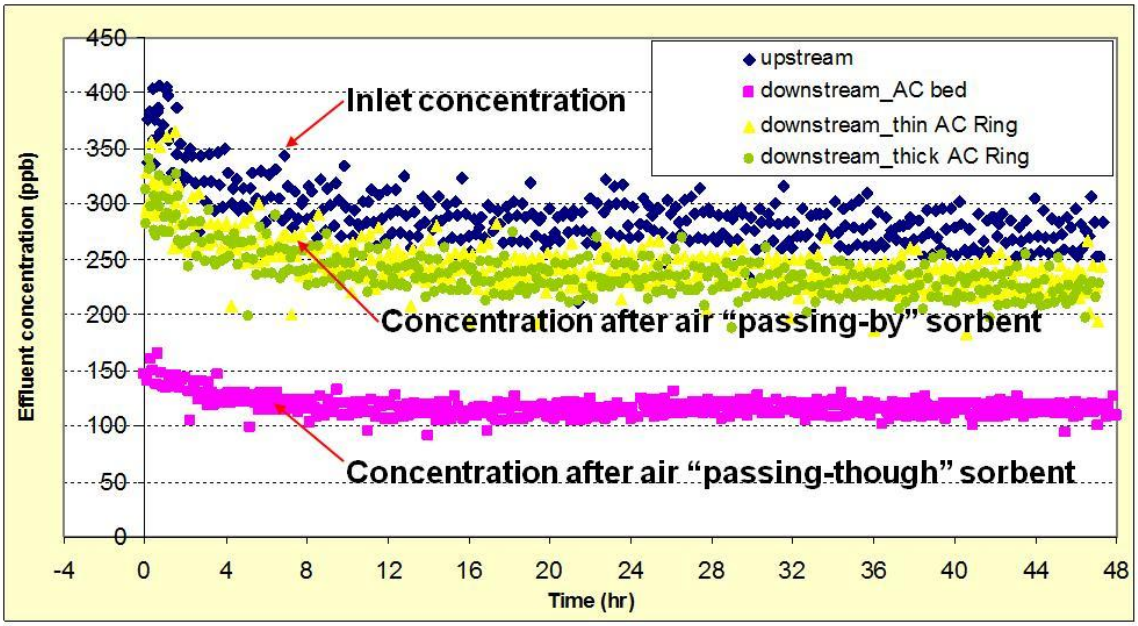

Fig. 2-5 Removal efficiency comparison for air pass-by versus pass-through.

These data imply that as long as there is the same velocity surrounding the pellets (same AC pellet distribution density), the filter efficiency does not depend on whether the air is passing-through or passing-by the media. To confirm the above implication, another test was conducted whereby small cylindrically shaped activated carbon was distributed onto a metal mesh screen to form a carbon pellet uniformly distributed AC ring (for air passing-by) and AC sheet (for air passing-through). These two cases are shown in Fig. 2-6. By doing this, the velocity will have the same order of magnitude surrounding the pellets in each case. The results in Fig. 2-7 show

that the scattered ring distribution of pellets provides excellent removal of VOCs, and that the removal increases when the length of the filter increases. In addition, the pressure drop from the scattered AC case is very low (below 1 Pa here). This finding is significant, since it means that in the case of the PAV device, by having the air pass-by the fan housing walls, and hence pass-by the filter media, it may be possible to gain additional contaminant removal performance with minimal pressure losses.

Channel No.	Shape	AC amount (g)	Packing density (g/m^2)	Efficiency
Ch#1	Cylindrical ring (3" high) formed by 3"x5.5" sheet	14.296	1343.0	35.9%
Ch#2	Cylindrical ring (0.8" high) formed by 0.8"x5.5" sheet	4.167	1467.9	11.6%
Ch#3	Round sheet with 1.875" diameter	3.498	1934.0	10.6%

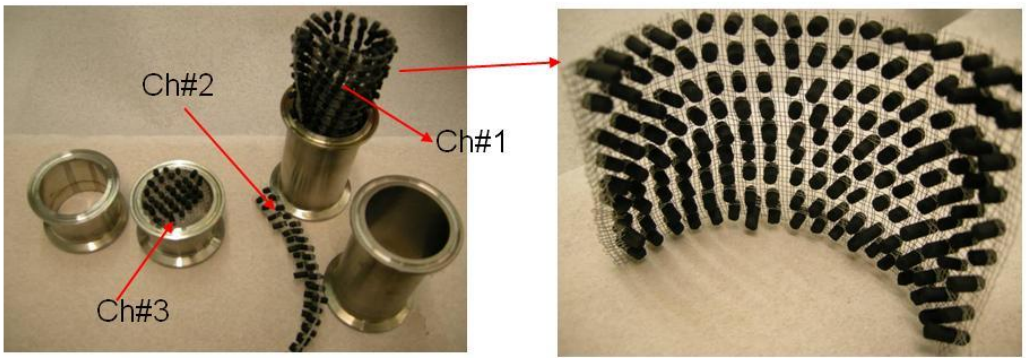

Fig. 2-6 Setup of scattered pass-through and pass-by tests.

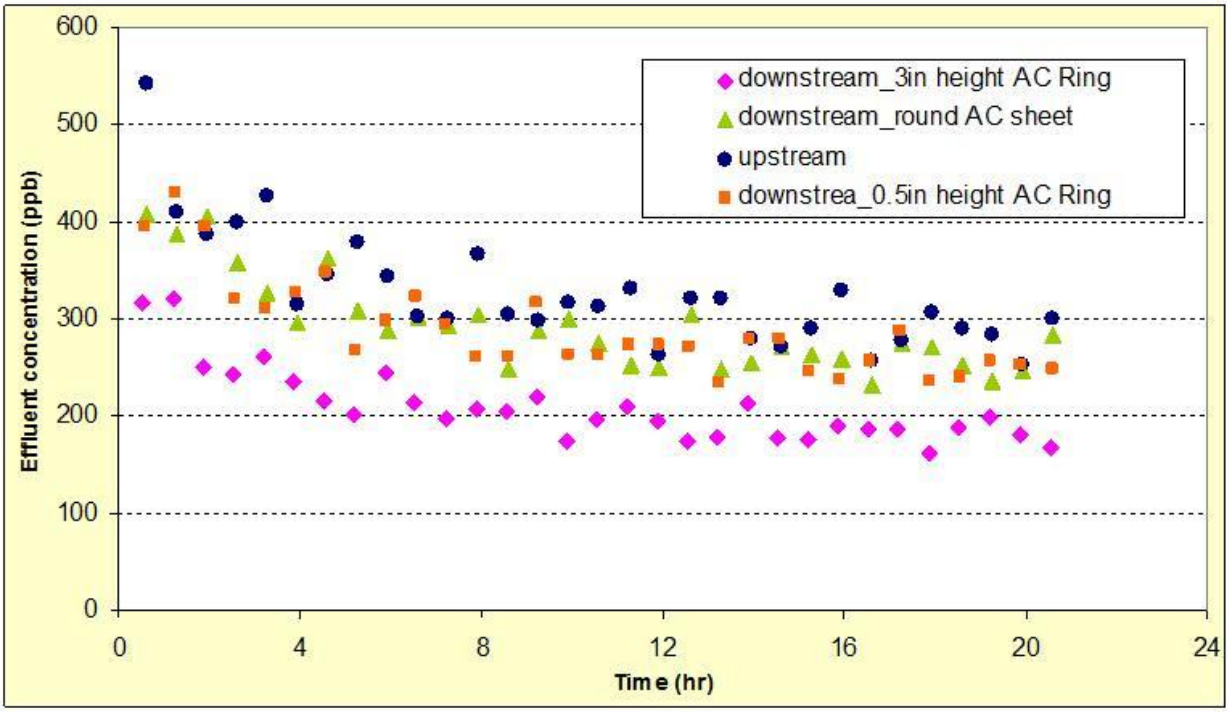

Fig. 2-7 Results from scattered pass-through and pass-by tests.

2.2 Design and Fabrication of a Particle Filter Media Test Device

Through the course of conducting filter research, it was determined by the Syracuse University team that a device was needed to test particle filters. The entire Propulsive Wing (PW), Allred & Associates (AAI), and SU group worked together to design a test fixture, which was then fabricated by PW and AAI. By custom designing and building the device, we ensured that it would meet our exact needs.

This filter testing device has the unique ability to evaluate up to 5 different particle filter media samples simultaneously. It Includes an inlet pre-filter, ports for particle generation and seeding into the mixing box, pressure drop measurement across each filter, upstream and downstream particle sampling (for filtration efficiency), and flow rate measurement and control through each sample. The entire custom unit comprising over 300 parts was designed by PW and AAI using Solidworks CAD modeling and CFD for airflow, tooling was made, components fabricated, trimmed, and finished, and the unit assembled and delivered for use in the BEESL lab at Syracuse University in only 8 weeks.

Figures 2-8 and 2-9 give CAD diagrams of the entire unit and the filter media sample cartridge, respectively. CFD simulations (Figs. 2-10 through 2-12 show a sampling of the results) were performed to calculate the pressure drop from inlet to outlet. This data was used to properly size the fan for adequate flow rate, as well as investigate any potential areas of high losses. High importance was placed on ensuring even distribution of flow between the five sampling tubes

and adequate mixing within the main box. Pictures of the completed assembly are shown in Fig. 2-13. The overall dimensions of the test unit are 30” x 24” x approximately 7.5’ tall.

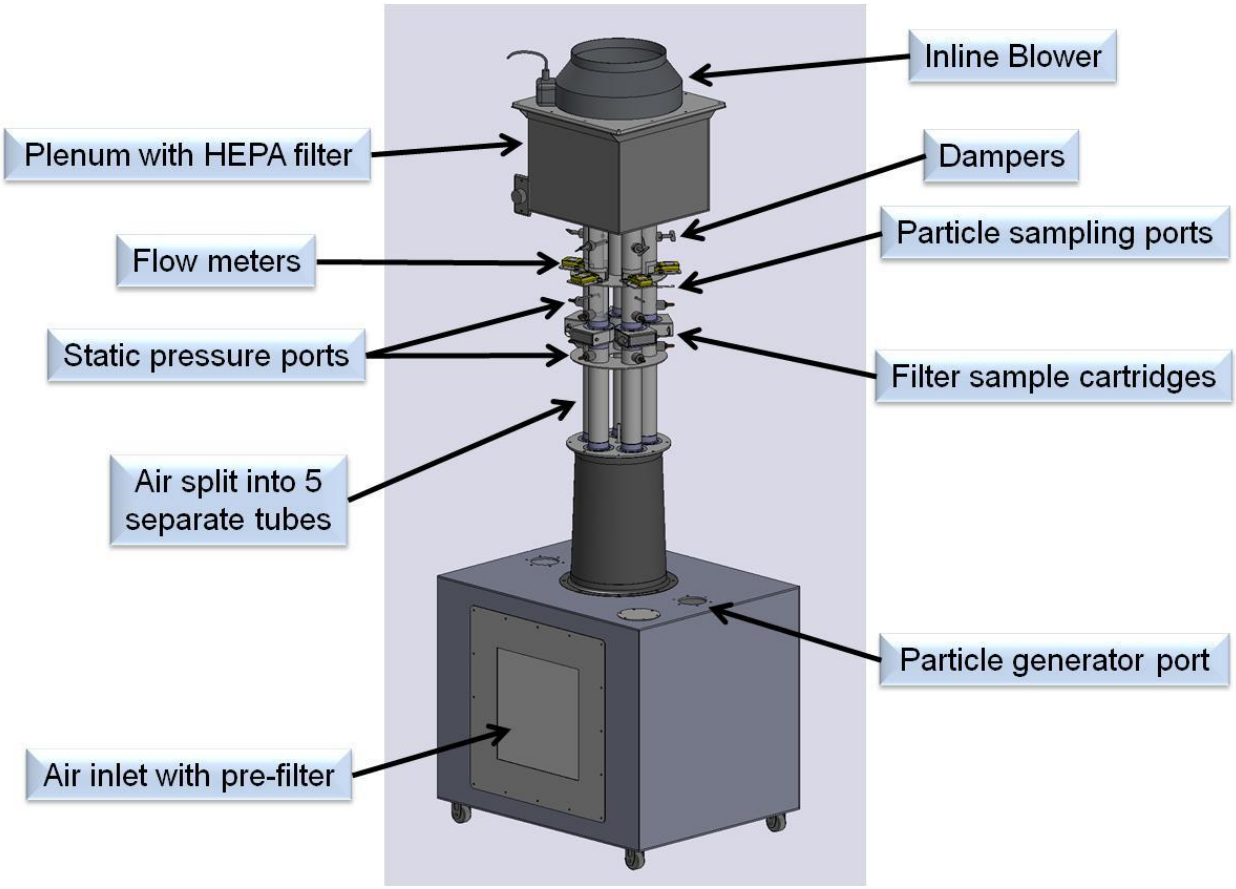

Fig. 2-8 CAD diagram of filter testing device.

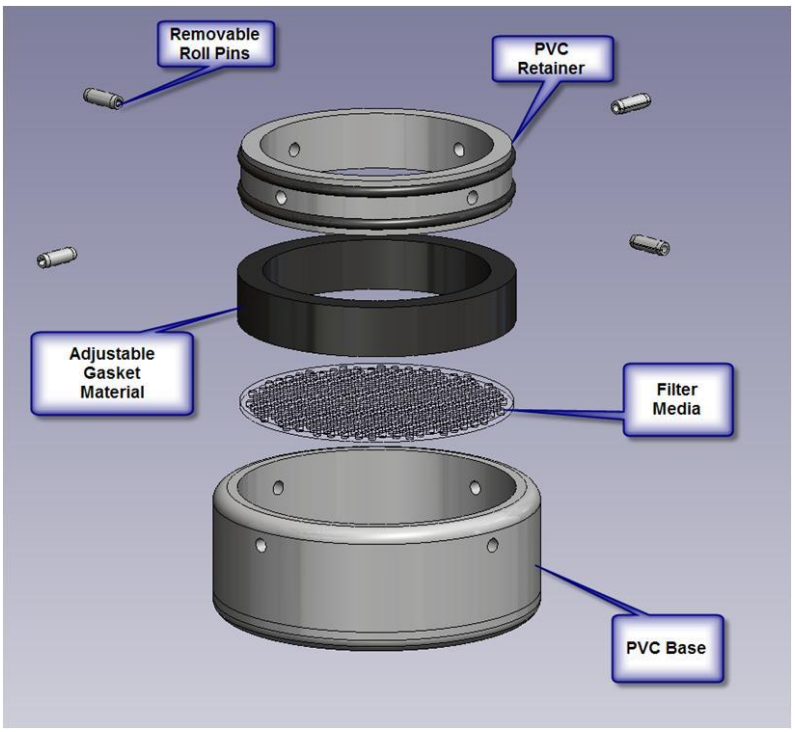

Fig. 2-9 CAD diagram of filter media sample cartridge.

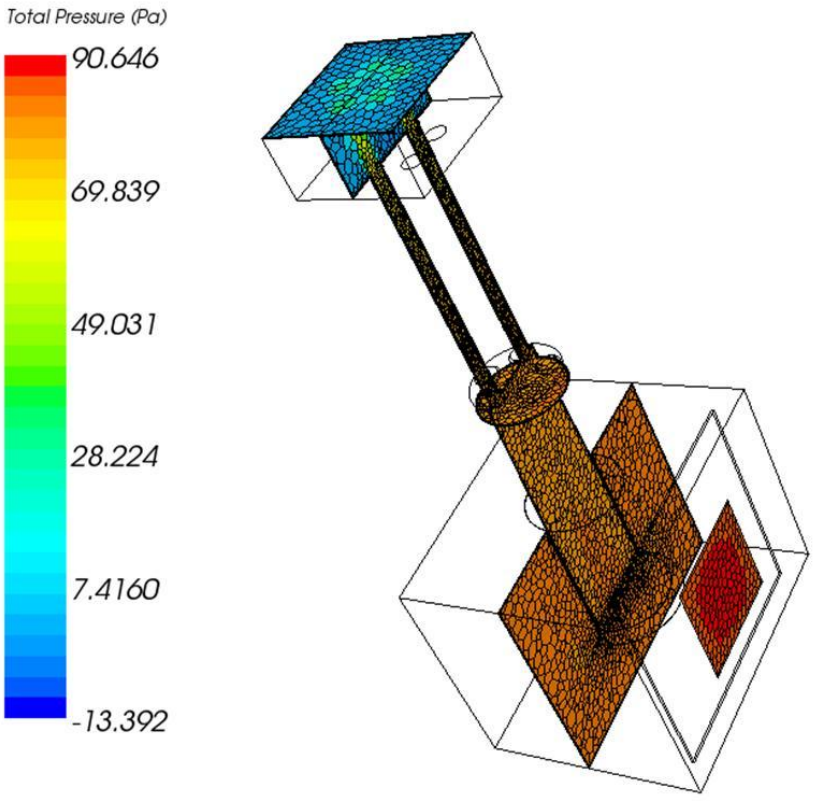

Fig. 2-10 CFD investigation of pressure losses in filter testing device.

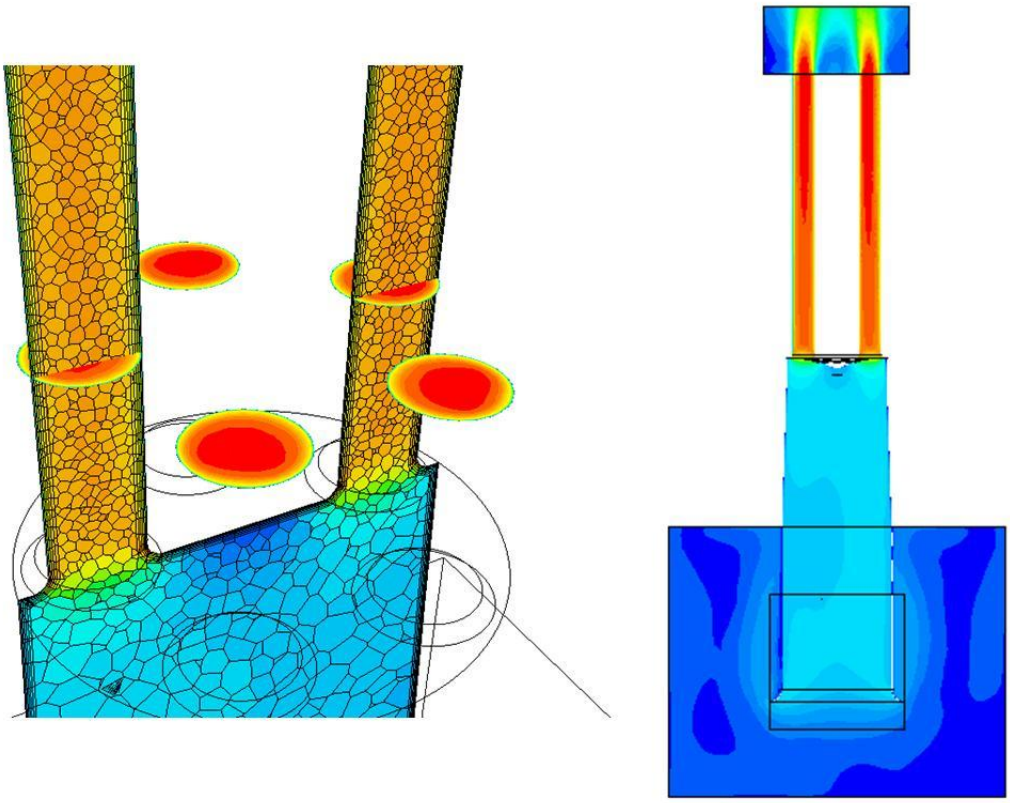

Fig. 2-11 CFD investigation of flow uniformity in sampling tubes.

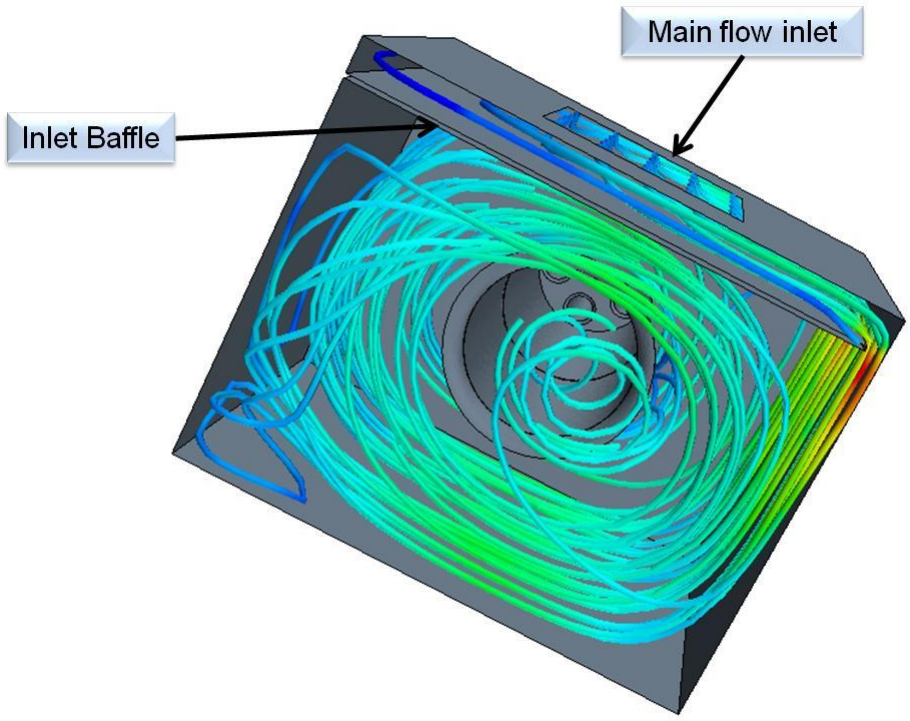

Fig. 2-12 CFD results showing substantial mixing within main box.

Fig. 2-13 Completed filter testing device.

2.3 Sandwich Filter Performance Evaluation Testing

Four groups of prototype filters were made for both VOC and particle removal efficiency tests. These filters were fabricated with different combinations of MERV rating particle filtration media and activated carbon packing densities. The filters are shown in Fig. 2-14. Here, “D” will refer to double layer MERV rating media with activated carbon sorbent in the middle. To reduce the pressure drop of the filter, some filters with single layer MERV rating media were also made with the other layer as metal mesh, and such filters are indicated with “S”. The middle part of the filter name refers to the activated carbon used, and the last number in the name indicates the sorbent media packing density with units of g/m^2.

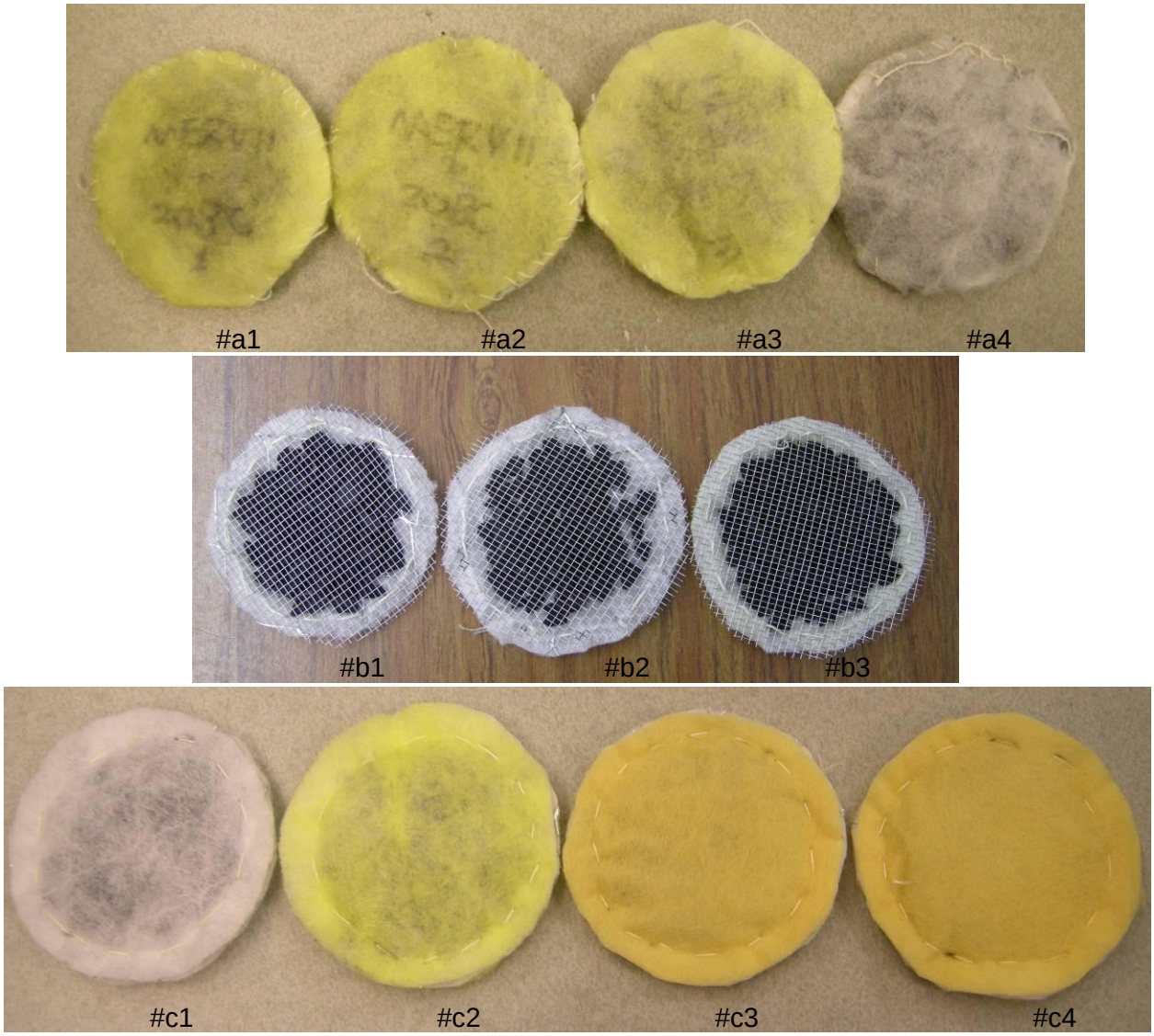

Fig. 2-14 Prototype filters for VOC and particle efficiency test.

Four groups of tests were conducted for the a, b, c, and d series of prototype filters described in Fig. 2-15. The challenge pollutant was toluene for all the tests. The concentration of upstream toluene was 300~500ppb. The VOC removal performance tests were conducted with the Air Cleaning Technology Testing System (ACTTS) shown in Fig. 2-16, which can simultaneously measure three filters. An online VOC monitor ppbRAE was used to measure the downstream VOC concentration for filters in each tested channel, as well as the concentration in the empty channel and at the inlet on a continuous basis. The flow rate through each test channel was 28.3LPM, which resulted in a face velocity of 0.26m/s.

No	#a1	#a2	#a3	#a4
Name	MERV8_D + 208C4x8 + 1034	MERV8_D + 208C4x8 + 1034	MERV8_D + 208C4x8 + 581	MERV7_D + 208C4x8 + 1183
Particle filtration media	MERV 8 double	MERV 8 double	MERV 8 double	MERV 7 double
VOC filtration media	AC 208C 4 x 8	AC 208C 4 x 8	AC 208C 4 x 8	AC 208C 4 x 8
Packing density (g/m2)	1034	1034	581	1183
No	#b1	#b2	#b3	
Name	MERV7_S + 208C4x8 + 1135	MERV7_S + 208C4x8 + 792	MERV8_S + 208C4x8 + 1393	
Particle filtration media	MERV 7 single	MERV 7 single	MERV 8 single	
VOC filtration media	AC 208C 4 x 8	AC 208C 4 x 8	AC 208C 4 x 8	
Packing density (g/m2)	1135	792	1393	
No	#c1	#c2	#c3	#c4
Name	MERV7_D + 208C4x8 + 1408	MERV8_D + 208C4x8 + 1718	MERV11_D + 208C4x8 + 1086	MERV11_D + 208C4x8 + 1758
Particle filtration media	MERV 7 double	MERV 8 double	MERV 11 double	MERV 11 double
VOC filtration media	AC 208C 4 x 8	AC 208C 4 x 8	AC 208C 4 x 8	AC 208C 4 x 8
Packing density (g/m2)	1408	1718	1086	1758
No	#d1	#d2	#d3	#d4
Name	MERV7_S + BPL4x6 + 1755	MERV7_S + BPL4x10 + 1713	MERV7_S + BPL6x16 + 1863	MERV7_S + BPL6x16 + 1381
Particle filtration media	MERV 7 single	MERV 7 single	MERV 7 single	MERV 7 single
VOC filtration media	AC BPL4x6	AC BPL4x10	AC BPL6x16	AC BPL6x16
Packing density (g/m2)	1755	1713	1863	1381

Fig. 2-15 Descriptions of filters for VOC and particle removal performance test.

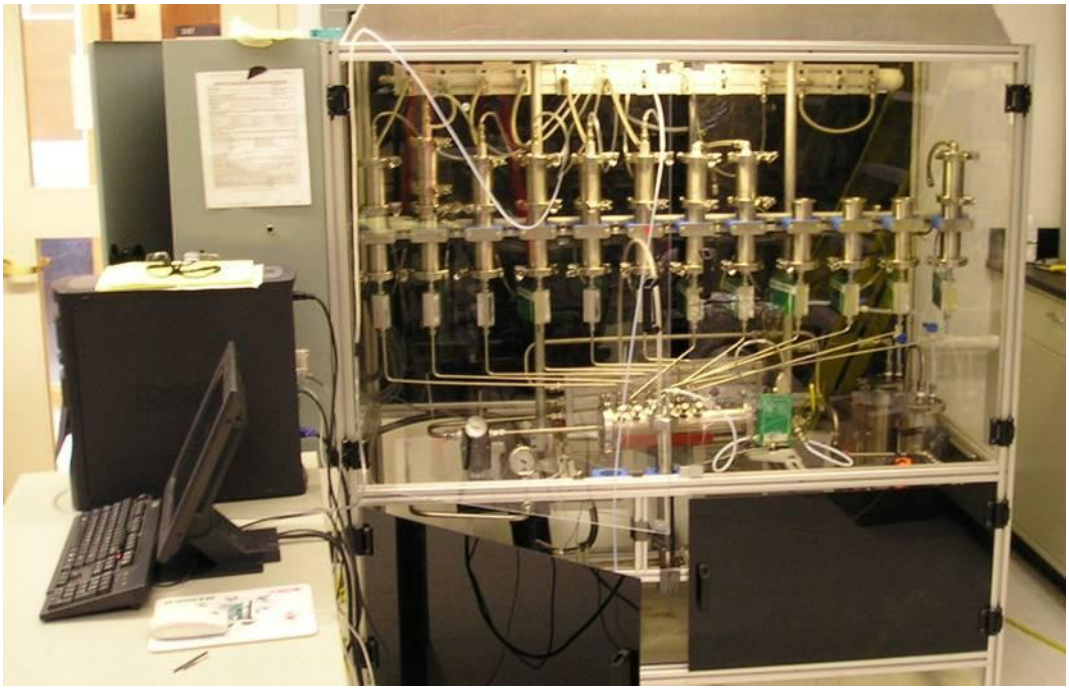

Fig. 2-16 Air Cleaning Technology Testing System (ACTTS) for VOC performance test.

The measured concentration at the inlet and downstream of each filter are given in Fig. 2-17.

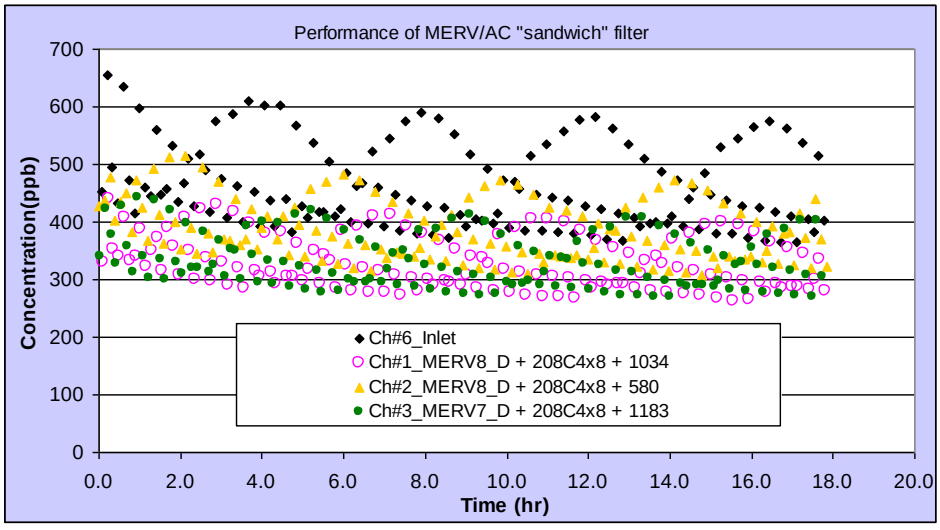

Series a filters

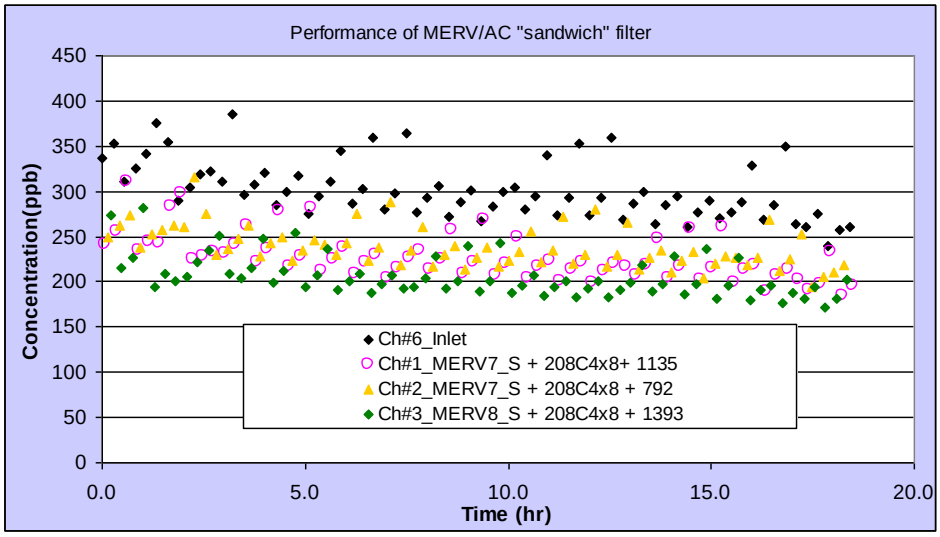

Series b filters

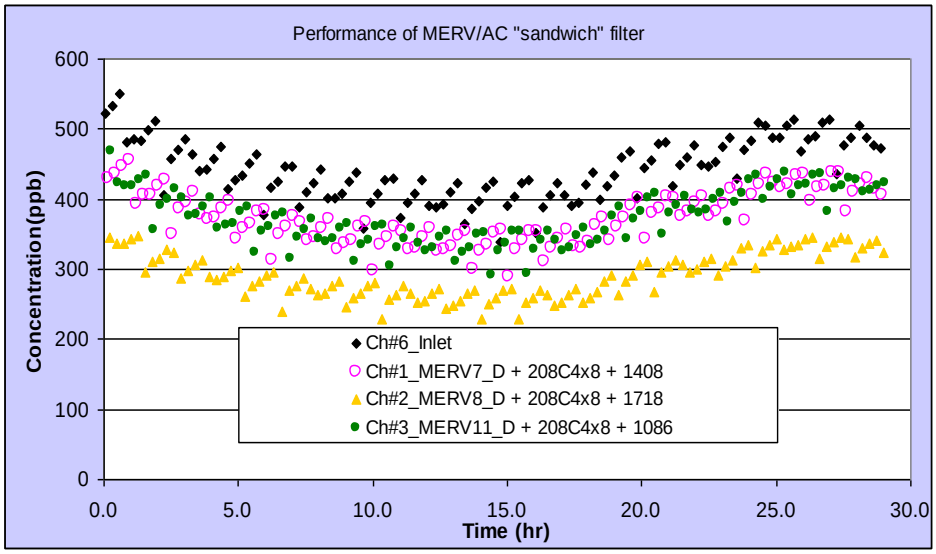

Series c filters

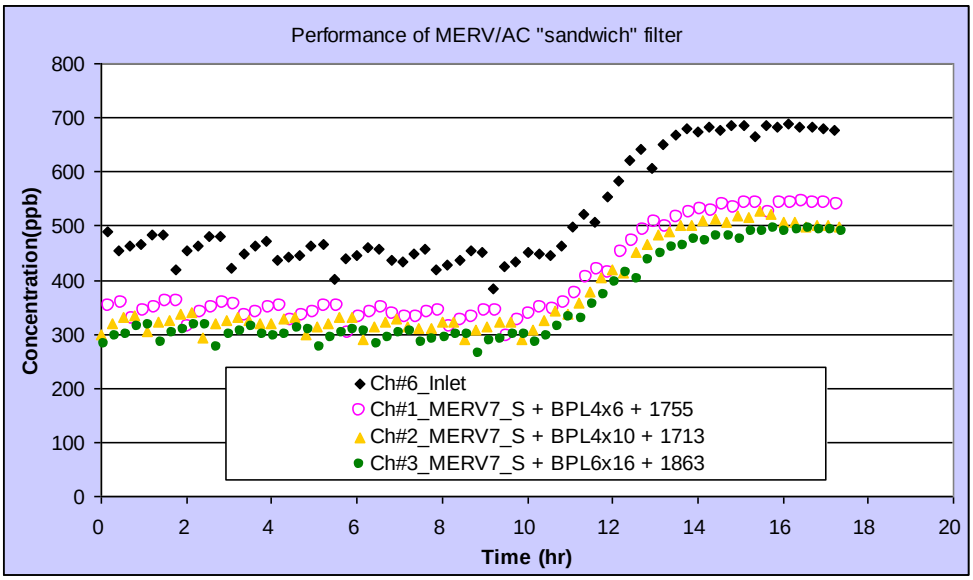

Series d filters

Fig. 2-17 Channel concentrations of the VOC removal performance tests.

2.4 Test of MERV Rating Particulate Filtration Media

The particle removal efficiency tests for single layer raw MERV rating media were conducted first before the tests for “sandwich” filters.

The single pass efficiency of MERV rating particle filtration media was already defined by ASHRAE Std. 52.2. The efficiency of four different MERV rating media (MERV7, 8, 11 and 12) was tested here with the 5-tube tester only as a check, but not to classify the media rating. The 5-tube tester can simultaneously test 5 media samples with the same upstream concentration. An automatic-switch valve system was designed and setup for the tester so that the particle concentration measurement device (APS 3321) can sample continuously and in turn downstream of the 5 tubes as well as upstream. The particles were generated by a large aerosol particle generator (TSI 8108) using KCL solution. Figure 2-18 shows the test setup. Four types of MERV rated filtration media were tested simultaneously, with each installed in one channel. One channel (channel #5) was left empty without any media to observe effects other than filtration (e.g. natural deposition on the surface of the system). The velocity/flow rate for each channel was adjusted to be almost the same value for all five tubes. Two rounds of tests were conducted with different velocities. Figure 2-19 shows the setting for each channel. The reading velocity is the one direct from the anemometer on each channel. The actual velocity of each channel is calculated based on the correction factor from the anemometer calibration.

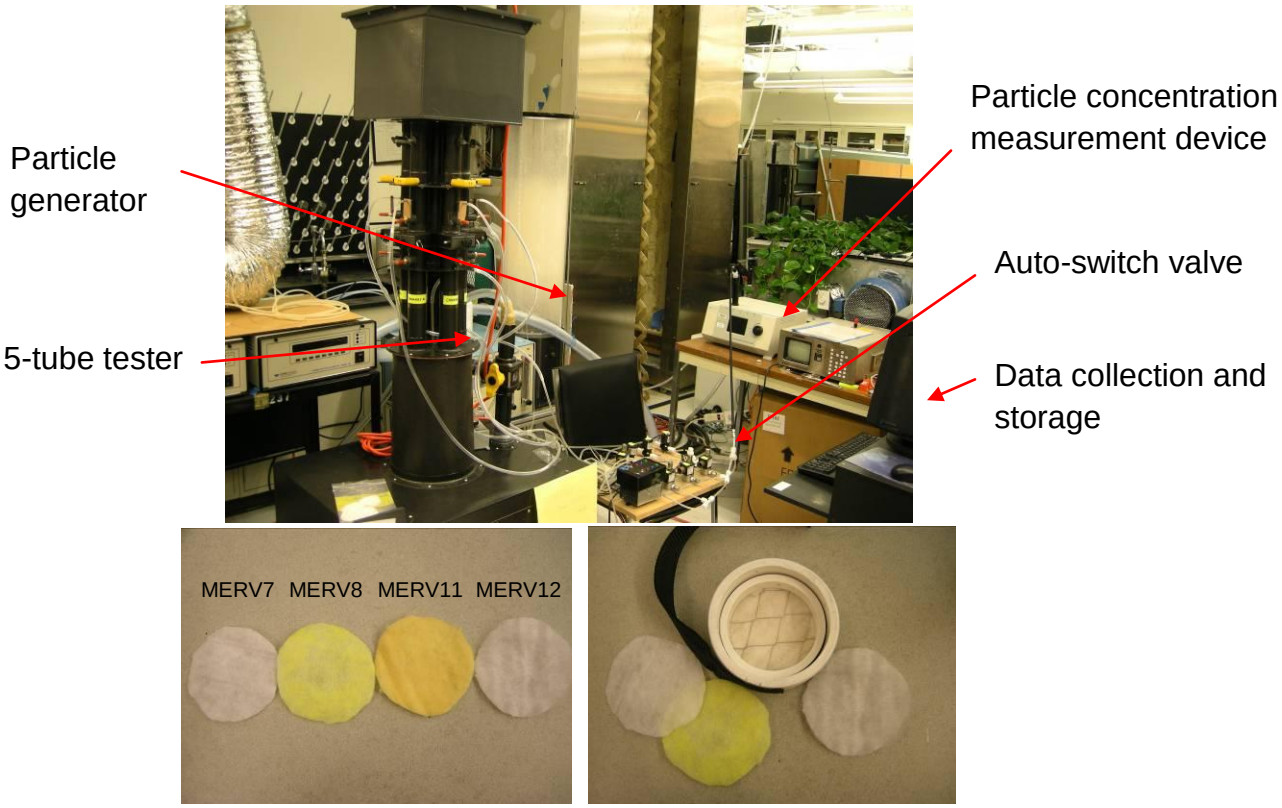

Fig. 2-18 Test system setup and tested MERV media.

Media		MERV 7	MERV8	MERV11	MERV12	blank
Test 1	Reading velocity (m/s)	5.3	5.4	5.1	5.2	5.2
	Actual velocity (m/s)	1.12	1.14	1.08	1.10	1.10
Test 2	Reading velocity (m/s)	2.6	2.4	2.6	2.5	2.4
	Actual velocity (m/s)	0.55	0.51	0.55	0.53	0.51
Test 3	Reading velocity (m/s)	2.6	2.5	2.5	2.5	2.4
	Actual velocity (m/s)	0.55	0.53	0.53	0.53	0.51

Fig. 2-19 Test media and face velocity.

The tests lasted about 1.0 hr with constant particle generation rate. To compare with ASHARE Std. 52.2 (simplified as ASHRAE later), the particles are combined into four groups: 0.523-1.075μm, 1.075-3.162μm, 3.162-5.233μm, and 5.233-11.548μm. However, due to the generated particle size distribution and the sampling system, no concentration for 5.233-11.548μm range particles was observed. Therefore, the efficiency of that range cannot be measured here. Figure 2-20 shows the 0.523-1.075μm, 1.075-3.162μm, and 3.162-5.233μm particle number concentration (#/cc) upstream and downstream of each channel for the three

tests. From test 1, as expected, it was found that the filtration efficiency increased as loading increased. The initial efficiency was calculated based on the average concentration from 0.3hr to 1.0hr for test 1, 0.5hr to 1.3hr for test 2, and 0.2hr to 0.5hr for test 3. Figure 2-21 lists the efficiency of each MERV rated media from the current test results. The ASHRAE specification for the corresponding media is also listed for comparison. However, it should be noticed that the ASHRAE Std. method is to test full scale pleated filters (typically 24" x 24") corresponding to HVAC duct installations with flow rates of 1970cfm (2.5m/s face velocity, with lower filtration velocity depending on the pleating number), whereas the results present here tested the flat raw media.

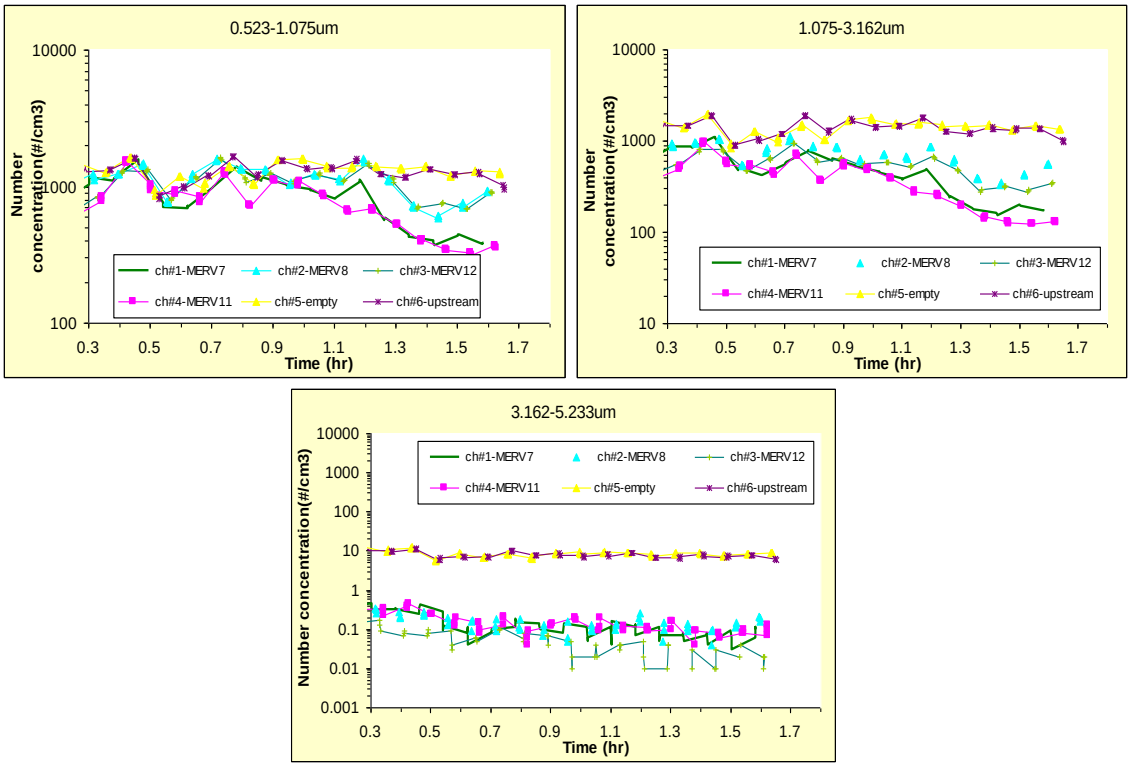

Test 1

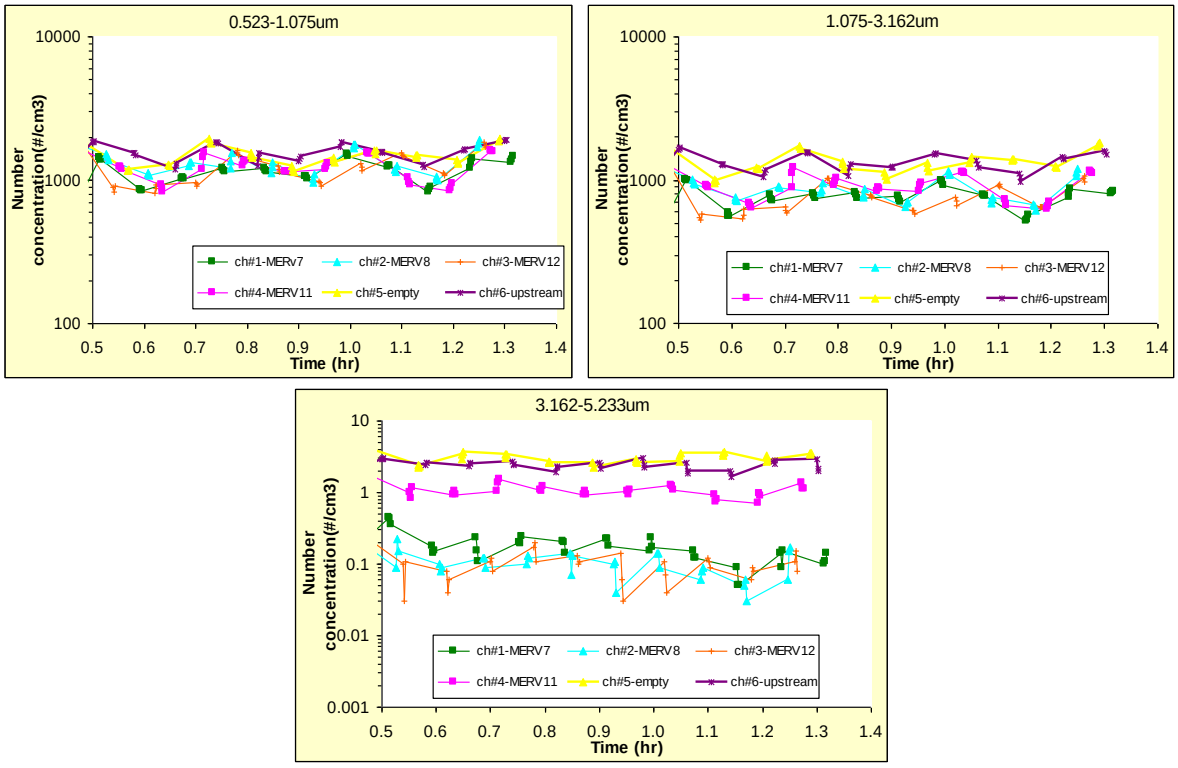
0.523-1.075um
Number concentration(#/cm3)
Time (hr)
ch#1-MERV7
ch#2-MERV8
ch#3-MERV12
ch#4-MERV11
ch#5-empty
ch#6-upstream
1.075-3.162um
3.162-5.233um

Test 2

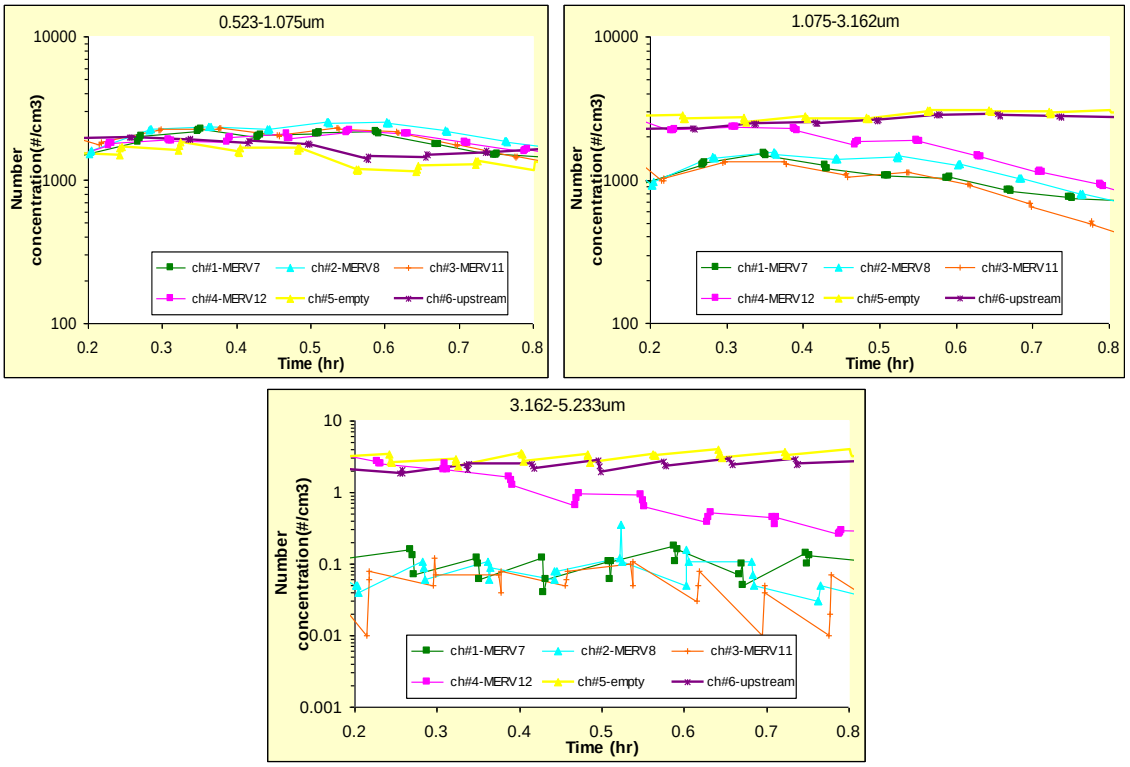

Test 3

Fig. 2-20 Particle concentrations upstream and downstream of each channel.

			Upstream	Downstream				
				ch#1-MERV7	ch#2-MERV8	ch#3-MERV11	ch#4-MERV12	ch#5-n/a
Current Test1-1m/s	0.523-1.075μm	Concentration(#/cc)	1298	1077	1240	1002	1144	1299
		Efficiency		**17.04%**	**4.46%**	**22.81%**	**11.84%**	
	1.075-3.162μm	Concentration(#/cc)	1422	674	841	562	654	1402
		Efficiency		**52.58%**	**40.83%**	**60.49%**	**53.98%**	
	3.162-5.233μm	Concentration(#/cc)	8.56	0.18	0.16	0.20	0.08	8.71
		Efficiency		**97.95%**	**98.15%**	**97.68%**	**99.12%**	
Current Test2-0.5m/s	0.523-1.075μm	Concentration(#/cc)	1586	1179	1327	1220	1199	1465
		Efficiency		**25.65%**	**16.33%**	**23.09%**	**24.41%**	
	1.075-3.162μm	Concentration(#/cc)	1355	774	857	898	744	1327
		Efficiency		**42.91%**	**36.78%**	**33.75%**	**45.12%**	
	3.162-5.233μm	Concentration(#/cc)	2.43	0.18	0.10	1.04	0.10	2.99
		Efficiency		**92.71%**	**95.72%**	**57.22%**	**96.03%**	
Current Test3-0.5m/s	0.523-1.075μm	Concentration(#/cc)	1897	2073	2342	2137	1954	1612
		Efficiency		**-9.27%**	**-23.44%**	**-12.63%**	**-2.99%**	
	1.075-3.162μm	Concentration(#/cc)	2426	1273	1459	1173	2102	2724
		Efficiency		**47.54%**	**39.85%**	**51.65%**	**13.37%**	
	3.162-5.233μm	Concentration(#/cc)	2.24	0.10	0.11	0.07	1.58	2.99
		Efficiency		**95.76%**	**95.05%**	**96.93%**	**29.63%**	
ASHRAE Std.52.2	0.3-1.0μm	Efficiency		**n/a**	**n/a**	**n/a**	**n/a**	
	1.0-3.0μm	Efficiency		**n/a**	**n/a**	**65~80%**	**>=80%**	
	3.0-10.0μm	Efficiency		**50~70%**	**>=70%**	**>=85%**	**>=90%**	

Fig. 2-21 Test results for initial single pass efficiency of MERV rating media.

Discussion of Results:

- By comparing the upstream concentration with the empty channel (ch#5), the concentration difference is about 1% in test 1 (0.12% for 0.523-1.075μm, 1.37% for 1.075-3.162μm and 1.79% for 3.162-5.233μm particles), so other particle removal effects other than filtration were negligible.
- With decreased flow rate (1m/s to 0.5m/s), the single pass efficiency decreased for particles > 1.0μm. A similar trend was not observed for particles < 1.0μm.
- For particles in the size range 0.3~1.0μm, the ASHRAE standard does not specify the efficiency for all four MERV rating media (MERV7, MERV8, MERV11, and MERV12); results from the current tests also show that the efficiency of particle removal in the range of 0.523~1.075μm is only around 20%, and sometimes even negative due to experiment uncertainty (in test 3). Therefore, it can be concluded that these media do not have significant removal efficiency for small particles less than 1.0μm.
- For particles in the size range of 1.0~3.0μm, ASHRAE does not specify efficiency for MERV 7 and MERV 8 media, but states 65~80% for MERV11 and >=80% for MERV12. In the current tests, for MERV7, the efficiency for 1.075-3.162μm particles was about 50% at 1m/s face velocity and 40%~50% at 0.5m/s; for MERV 8, the efficiency for 1.075-3.162μm particles was about 40% at 1m/s face velocity and 30%~40% at 0.5m/s. It is noticed that the efficiency of the currently tested MERV7 media is higher than MERV8 media. For MERV11, the efficiency for 1.075-3.162μm particles was about 60% at 1m/s face velocity and 30%~50% at 0.5m/s face velocity, which are lower than the ASHRAE specification 65~80%. The efficiency of MERV 12 media here for 1.075-3.162μm particles varies, but without a clearly higher efficiency than MERV11, and much lower than the ASHRAE specification (>=80%). It seems that the MERV rating for this material may be overstated for smaller particles (1.0~3.0μm)
- For particles in the size range 3.162-5.233μm, all four MERV media tested here had higher than 90% efficiency, except the two irregular points (MERV11 in test 2 and MERV 12 in test 3). The efficiencies in these tests were mostly higher than the ASHRAE specification, with no obvious difference between the four media noticed. It seems the MERV rating understates the efficiency here for large particles (3.0~10.0μm).
- Figure 2-22 shows the pressure resistance of tested MERV rating media. MERV7 has the lowest pressure resistance. For this case the pressure resistance of MERV 11 media was actually higher than MERV 12 media.

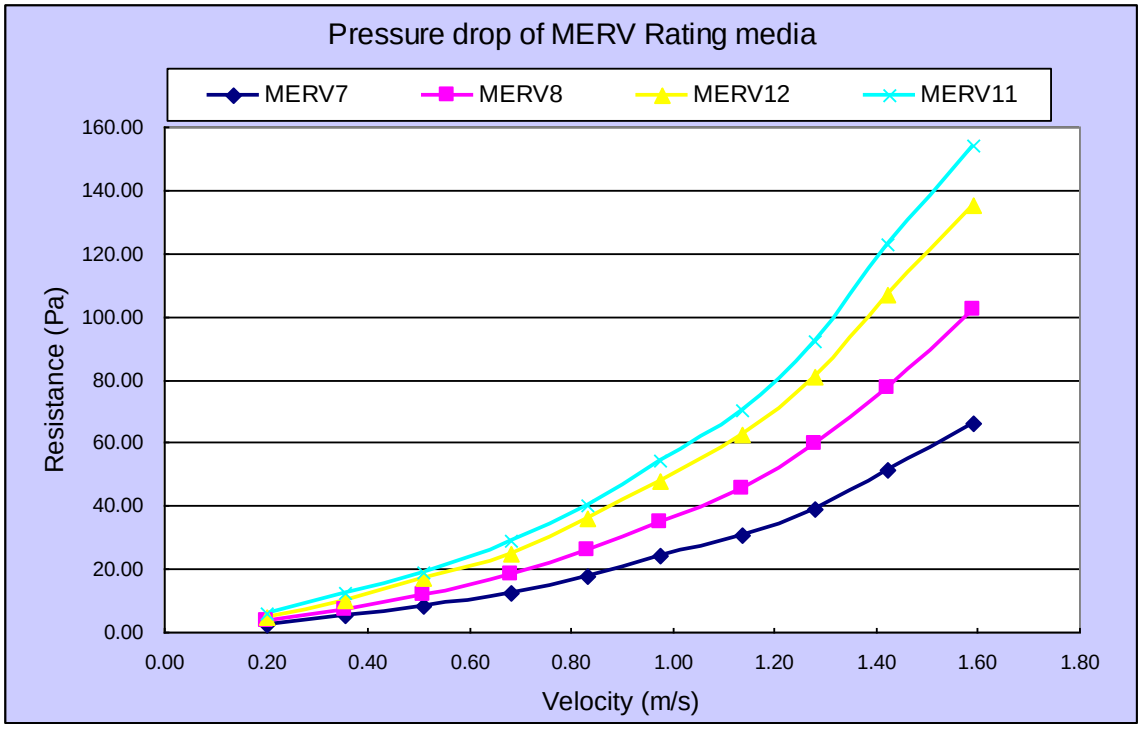

Fig. 2-22 Pressure resistance of tested MERV rating media.

2.5 Particle Removal Test of Sandwich Filters

The same test method and procedure used for the single layer MERV rating media test was used for the “sandwich” filter tests. The installation of the filters in the media holders is shown in Fig. 2-23.

Fig. 2-23 Installation of filters for particle removal performance test.

3 groups of particle tests were conducted for b, c, and d series filters, respectively. All the tests were conducted for about 1 hour. The particle removal efficiency increased as the filters loaded with particles, so the initial efficiency was calculated using the data from only the initial period of each test, where the efficiency did not show an obvious increase. Figure 2-24 shows the particle concentrations for each channel over all tests conducted.

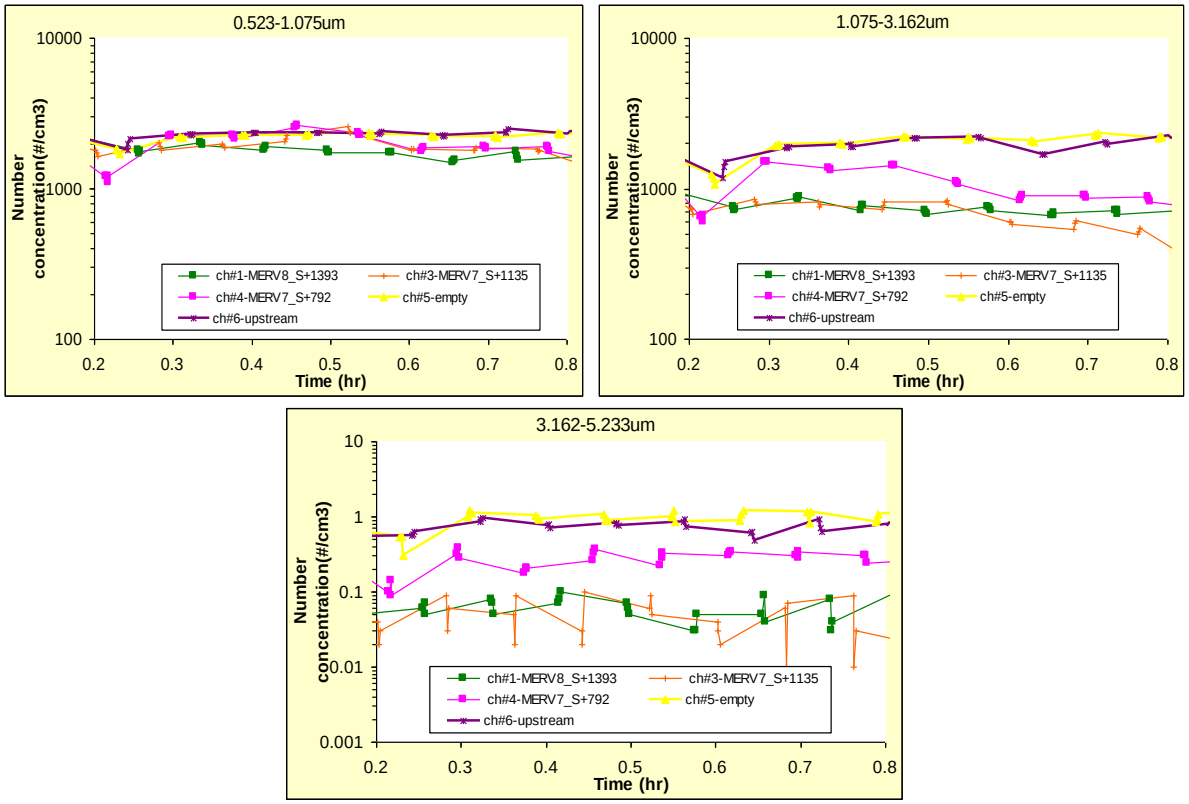

Series b filters

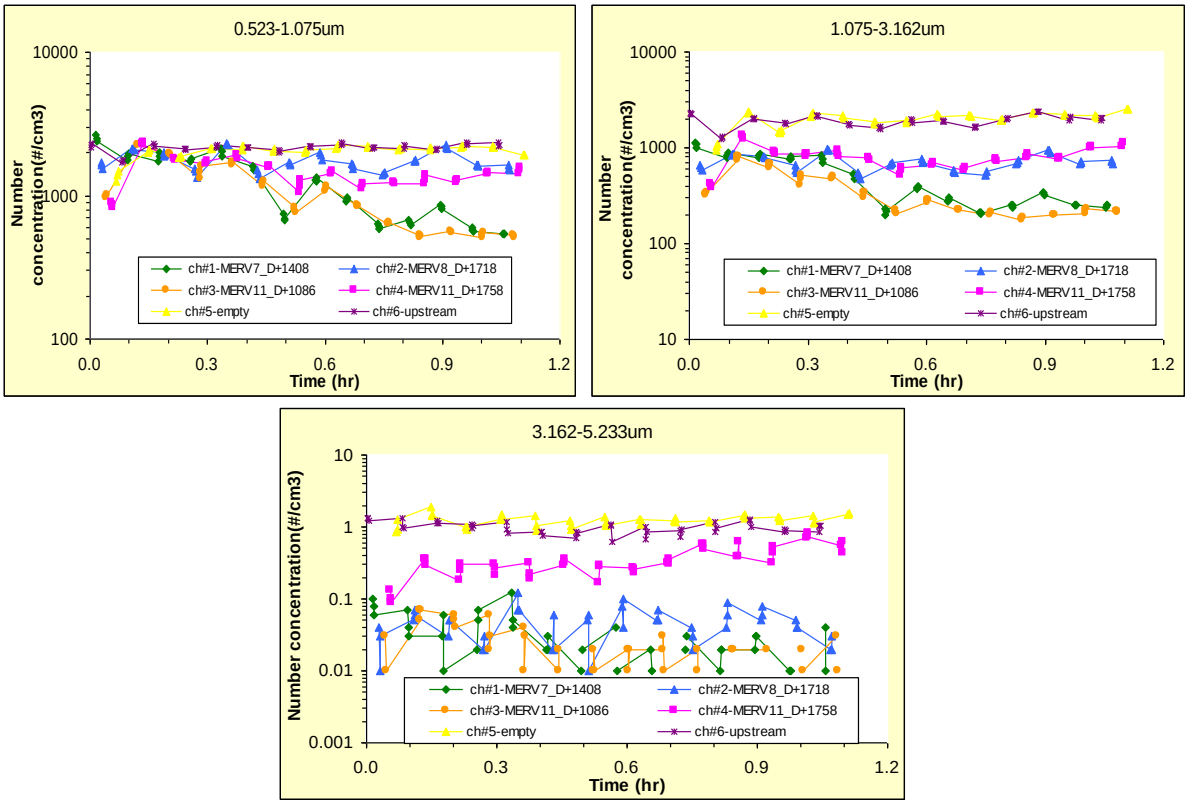

Series c filters

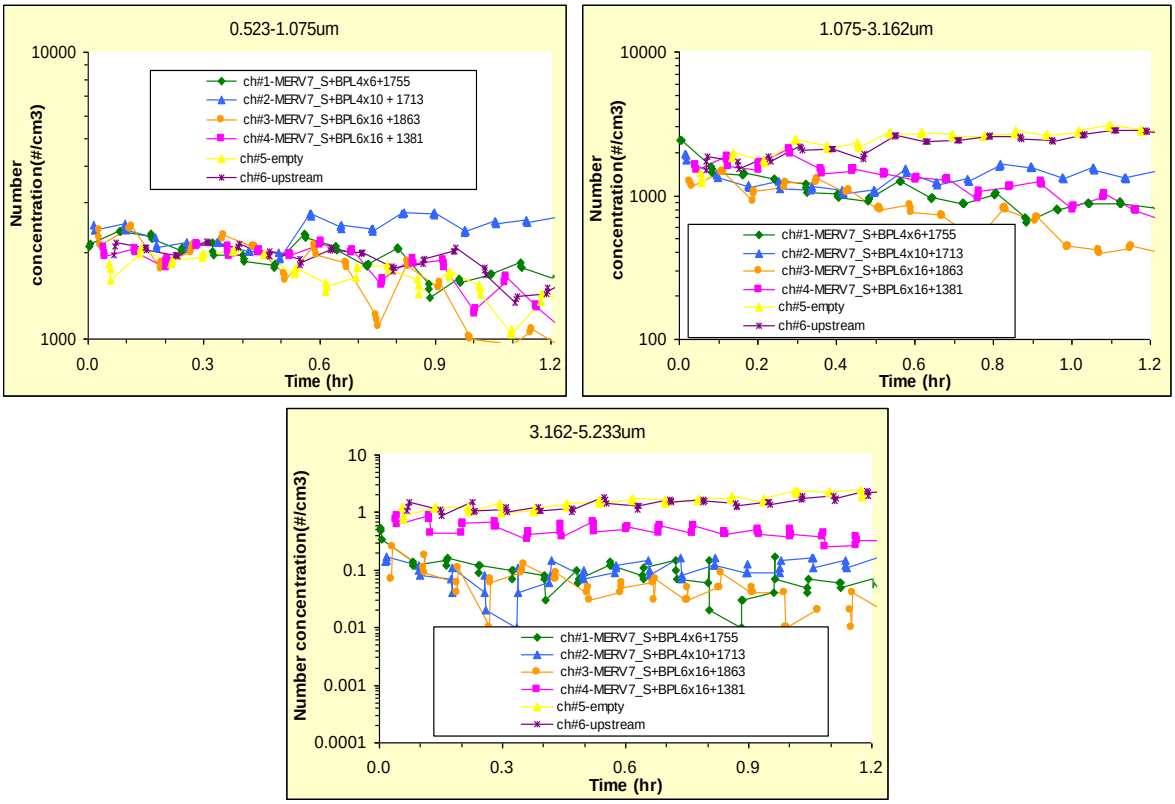

Series d filters

Fig. 2-24 Particle concentrations upstream and downstream of each channel.

The pressure drop of these “sandwich” filters was measured using an extra channel from the ACTTS, as shown in Fig. 2-25. The pressure was measured at three different flow rates: 28.3LPM, 14LPM, and 7LPM, with corresponding face velocity of 0.26m/s, 0.13m/s, and 0.06m/s.

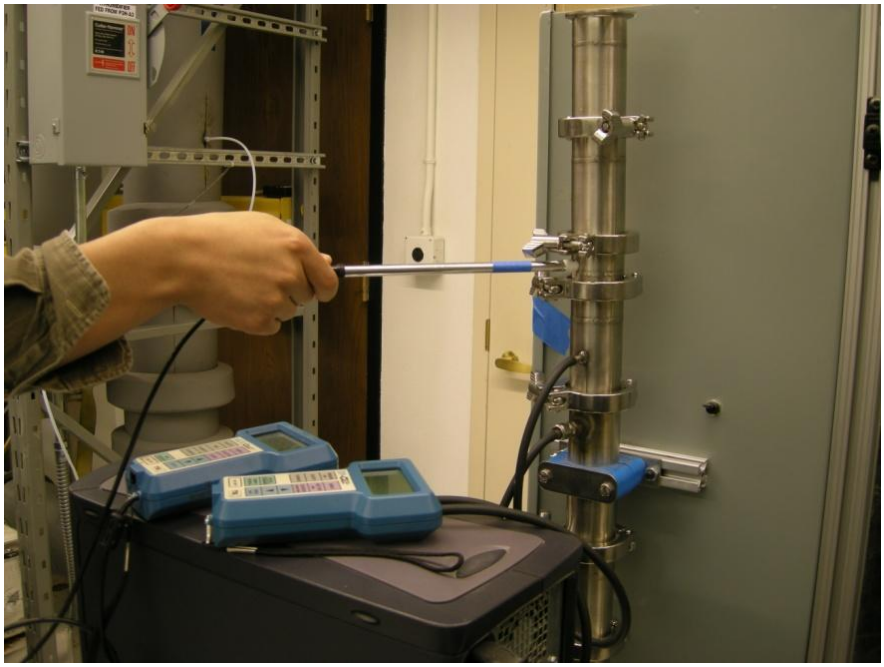

Fig. 2-25 Pressure resistance measurement channel.

The pressure resistance, initial VOC removal efficiency, and initial particle removal efficiency of the prototype sandwich filters are summarized in Fig. 2-26.

		Pressure drop (Pa)			VOC efficiency		Particle efficiency			
No.	Name	0.26 m/s	0.13 m/s	0.06 m/s	conc.	toluene	velocity	0.523-1.075 μm	1.075-3.162 μm	3.162-5.233 μm
#a1	MERV8_D + 208C4x8 + 1034	24.3	11.8	6.0		28.6%		-	-	-
#a2	MERV8_D + 208C4x8 + 1034	27.8	13.3	6.5		-		-	-	-
#a3	MERV8_D + 208C4x8 + 581	21.9	11.1	5.6		16.4%		-	-	-
#a4	MERV7_D + 208C4x8 + 1183	21.0	9.9	4.9	460ppb	27.9%		-	-	-
#b1	MERV7_S + 208C4x8 + 1135	13.4	5.9	2.9		24.6%		15.58%	64.14%	93.79%
#b2	MERV7_S + 208C4x8 + 792	10.6	4.9	2.4		21.1%		12.34%	43.60%	64.07%
#b3	MERV8_S + 208C4x8 + 1393	20.0	9.1	4.4	300ppb	31.7%	1.1m/s	23.56%	61.42%	91.78%
#c1	MERV7_D + 208C4x8 + 1408	27.8	12.0	5.5		15.3%		12.91%	59.33%	95.57%
#c2	MERV8_D + 208C4x8 + 1718	46.3	20.6	9.8		34.2%		11.00%	59.24%	95.05%
#c3	MERV11_D + 208C4x8 + 1086	60.0	27.8	13.6		15.5%		14.71%	68.44%	95.69%
#c4	MERV11_D + 208C4x8 + 1758	73.3	33.5	16.3	440ppb	-	1.2m/s	11.10%	48.96%	73.51%
#d1	MERV7_S + BPL4x6 + 1755	13.7	6.0	2.8		24.6%		0.23%	39.75%	91.572%
#d2	MERV7_S + BPL4x10 + 1713	16.4	7.0	3.3		29.2%		-2.91%	41.91%	93.841%
#d3	MERV7_S + BPL6x16 + 1863	15.3	6.5	3.0		33.7%		-2.93%	40.18%	92.869%
#d4	MERV7_S + BPL6x16 + 1381	13.6	5.8	2.6	450ppb	-	1.2m/s	1.97%	15.27%	59.571%

Fig. 2-26 Summary of prototype sandwich filter tests.

Discussion of Results:

- In terms of VOC removal efficiency, if the same activated carbon sorbent is used, it is expected from the tests of a, b, and c series filters that more media leads to higher efficiency. From the current tests, with packing density of activated carbon 208C 4x8 in the range of 1000~1500g/m^2 and challenge toluene concentration in the range of 300~500 ppb, the initial VOC removal efficiency was about 20~30%. Tests on series c filters tended to have lower efficiency compared with series a and b filters, which may be due to experimental error between each test setting. It should be noted that the results shown here are only the initial performance efficiency. The efficiency could decrease over prolonged use.
- From the tests on series d filters, which use the same type of sorbent media and the same packing density level, but different mesh size, it seems the VOC removal efficiency increases as the sorbent particle size decreases. The reason may be that larger particle sizes cause larger voids between pellets, which act as bypasses for the incoming flow. In this case a portion of the contaminated flow circumvents the primary filtering mechanism

(i.e. it does not come into contact with the sorbent pellets). However, the total capacity of the media for VOC storage may not vary much. This needs further well designed experiments to verify.

- In terms of particle removal performance, the currently used MERV rated media (MERV7, 8 and 11) do not show significant efficiency for small particles (0.523-1.075μm). The efficiency of filters with single layer MERV7 media for particles with sizes between 1.075 and 3.162μm was about 40% with face velocity of 1.2m/s, and more than 90% for 3.162-5.233μm particles (from the series d test). Filters with double layer MERV media show higher efficiency than those with single layer media (especially for large particles), but not significantly higher. The data presented in gray is considered invalid due to abnormal values. All of these data came from channel #4 of the 5-tube tester, so the problem may be in the experimental system.
- The pressure resistance of series a and series b filters was plotted versus passing velocity (Fig. 2-27a). The relationship between velocity and pressure resistance can be considered linear only in a limited low velocity range. The pressure resistance of these filters was also plotted with the flow rate based on a 5"x 0.5" inlet filter and 5"x3" filter. (Fig. 2-27b).

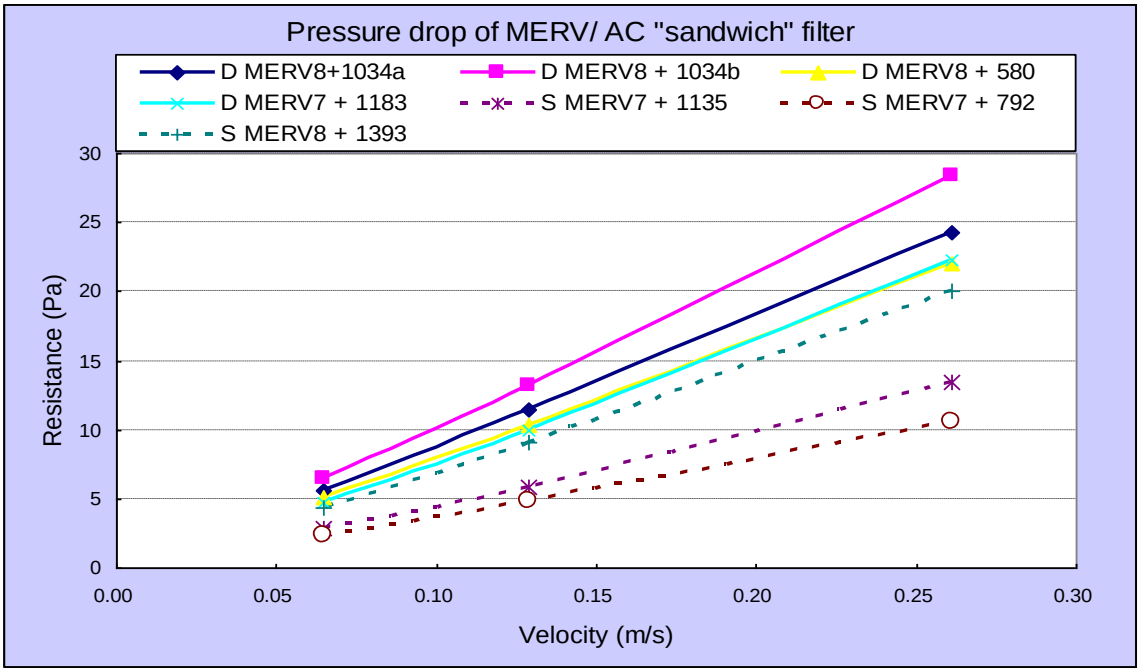

(a)

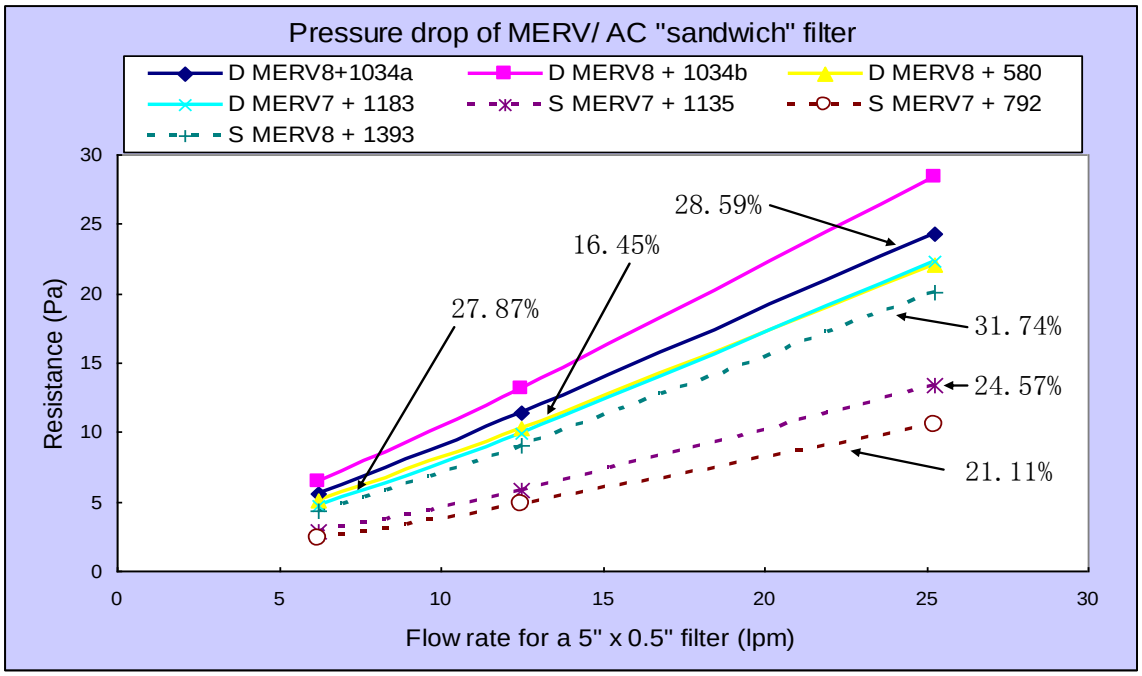

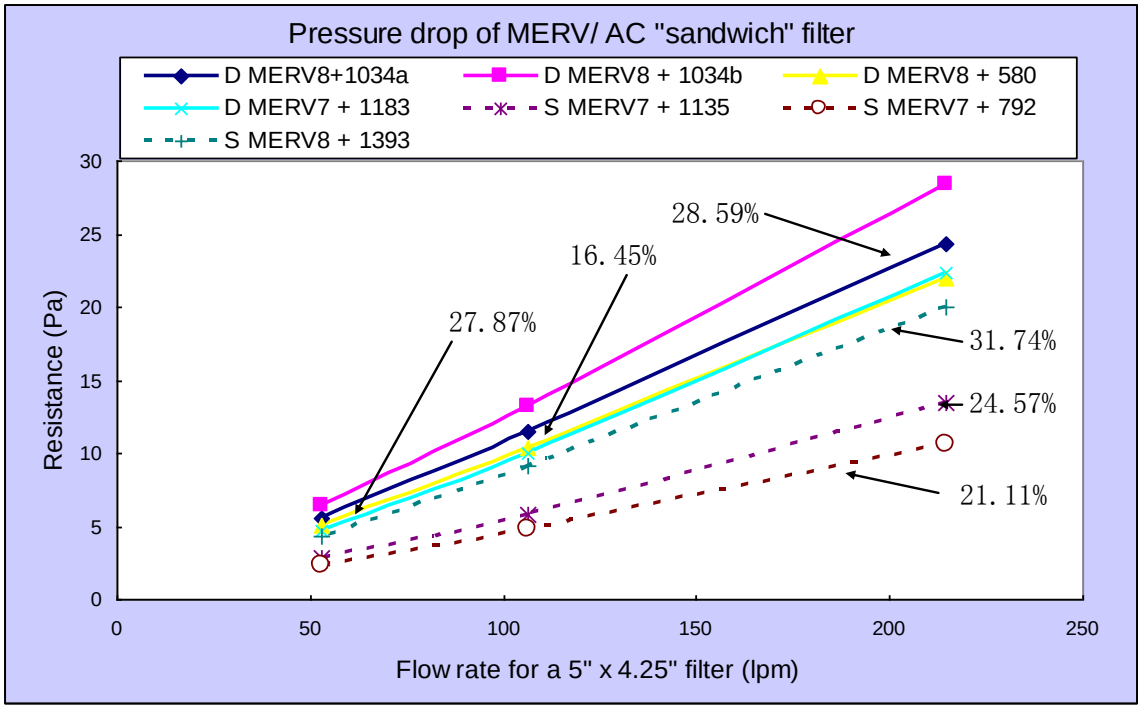

(b)

Fig. 2-27 Pressure resistance of series a and b sandwich filters.

SECTION 3

Prototype Design and Fabrication

As a prerequisite to the combined fan/filter CFD simulations, it was first necessary to calibrate the porous media model to appropriately simulate the pressure drop across the filter. The porous media model used in Star-CCM+ is given in Eq. 3.1.

$$\frac{\Delta p}{L} = -(P_i|\mathbf{v}| + P_v)\mathbf{v} \tag{3.1}$$

where $\mathbf{v}$ is the superficial velocity through the medium, Δp is the pressure drop across the filter, L is the filter thickness, and P_i and P_v are the inertial resistance and viscous resistance coefficients, respectively.

Since the velocity through the PAV filter is low, from the experimental data we concluded that a linear approximation for velocity versus pressure (i.e. $P_i = 0$) is acceptable. Figure 3-1 shows a simulation of the flow path through PAV-1 with the filter located at the inlet to the fan. The fan diameter here is 0.67 in, and the rpm was set to 6,000 rpm. P_v was set to 4,000 kg/m^{3}s. Using these inputs, it was found that the exit velocity was on the order of 1.5 to 2 m/s, or sufficiently high to meet our requirements for the PAV device. The computational mesh for this simulation is shown in Fig. 3-2. The grid consisted of 2D polyhedral cells with quadrilateral prism layer cells clustered near the blades and casing walls for adequate resolution of the boundary layer. The calculation was unsteady and included a sliding mesh region encapsulating the fan blades. The k-ε Standard turbulence model with “all y+” wall treatment was used (i.e. the law of the wall is not used exclusively close to the wall, but instead is substituted by a two-layer model with blending functions to bridge the gap between the viscous sublayer and the logarithmic regions). Calculations were run on the Propulsive Wing parallel computer cluster.

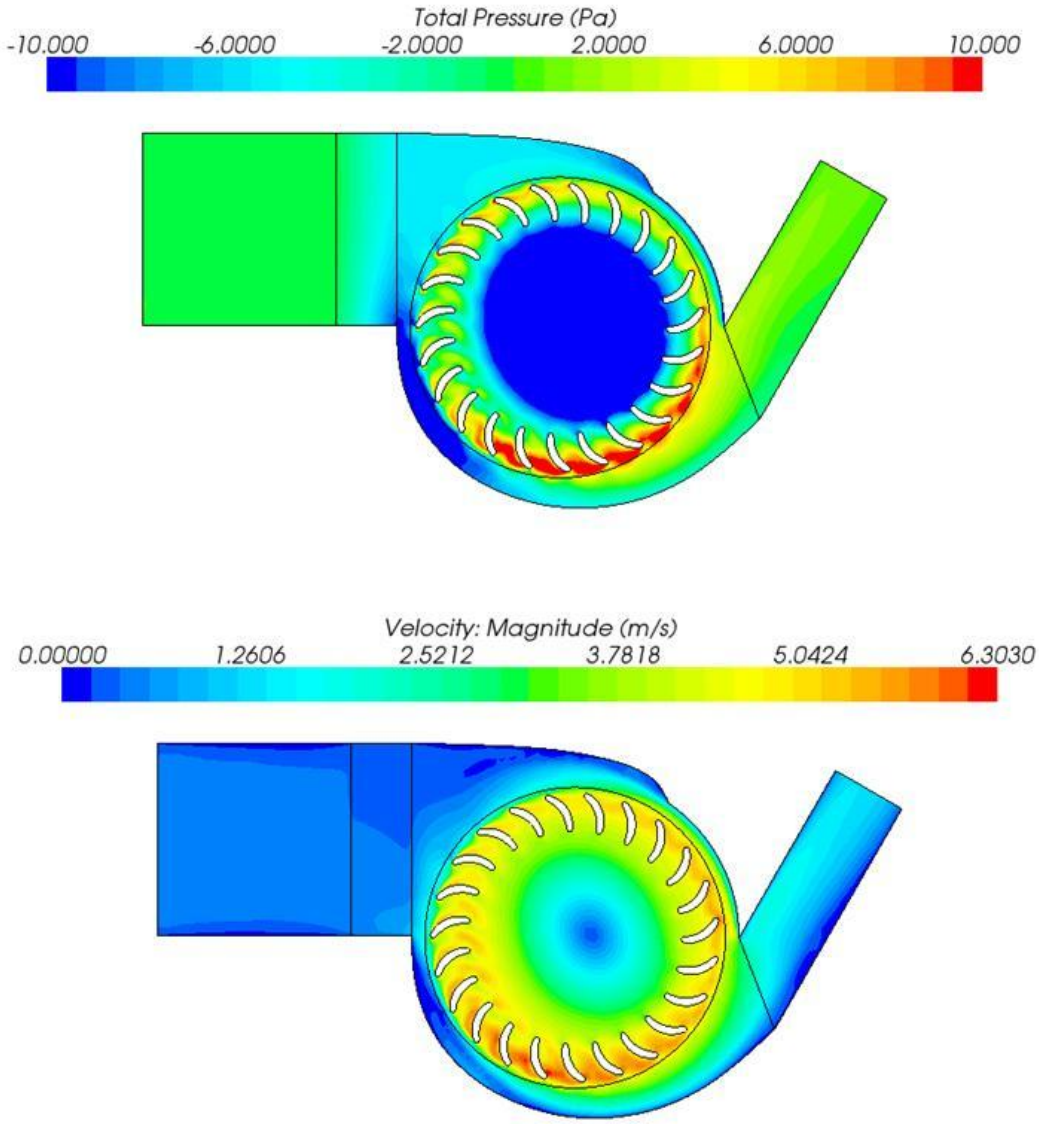

Fig. 3-1 Flow path through PAV-1.

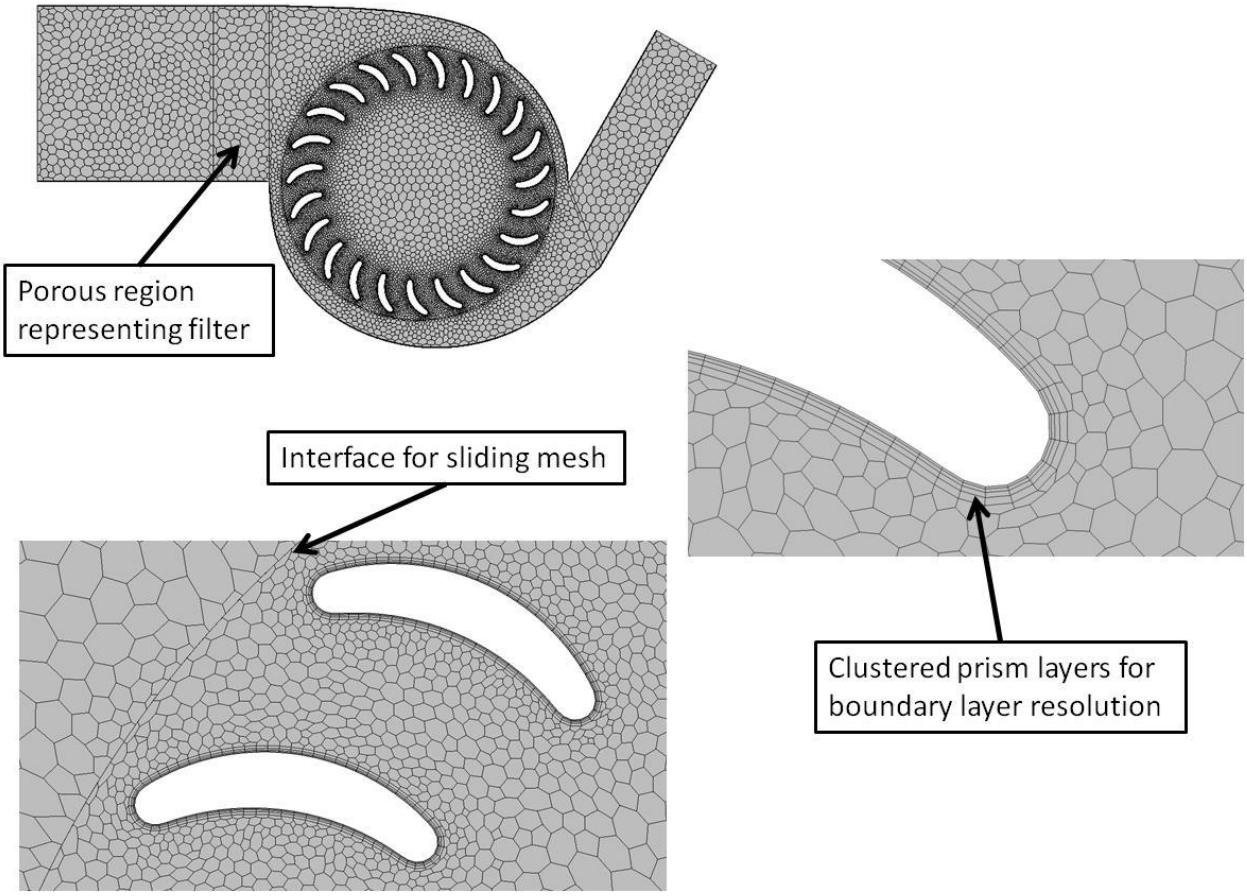

Fig. 3-2 Computational mesh for PAV-1 simulations.

Upon completion of the CFD analysis, a CAD model was development for the entire unit, including fan, motor, housing, end plates, filter holder, and room for batteries. A few 3D images of PAV-1 from Solidworks are shown in Fig. 3-3. For this prototype, the fan and motor were purchased from OLC-INC, a California-based company, as a single unit. The housing components were rapid prototyped by Design Prototyping Technologies of Syracuse, New York. Once all the components were received, the unit was assembled by an Allred & Associates technician. The completed unit is shown in Fig. 3-4.

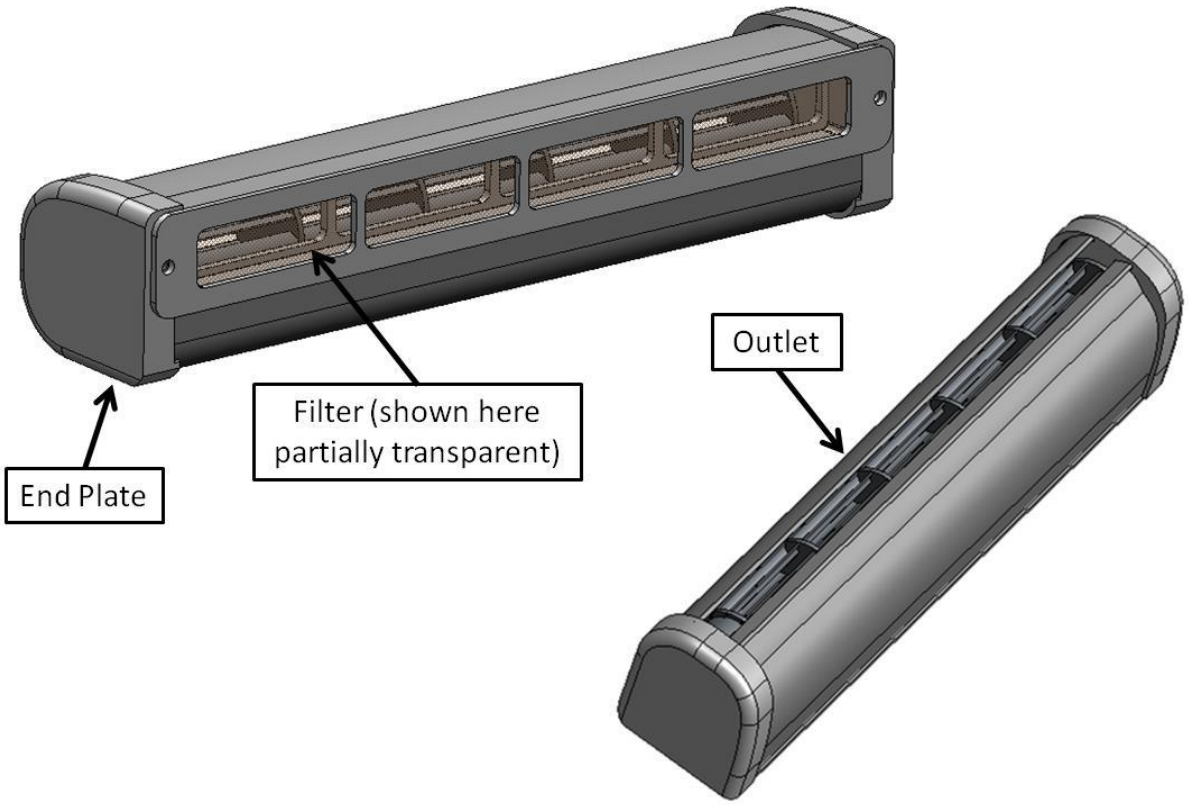

Fig. 3-3 CAD models of PAV-1.

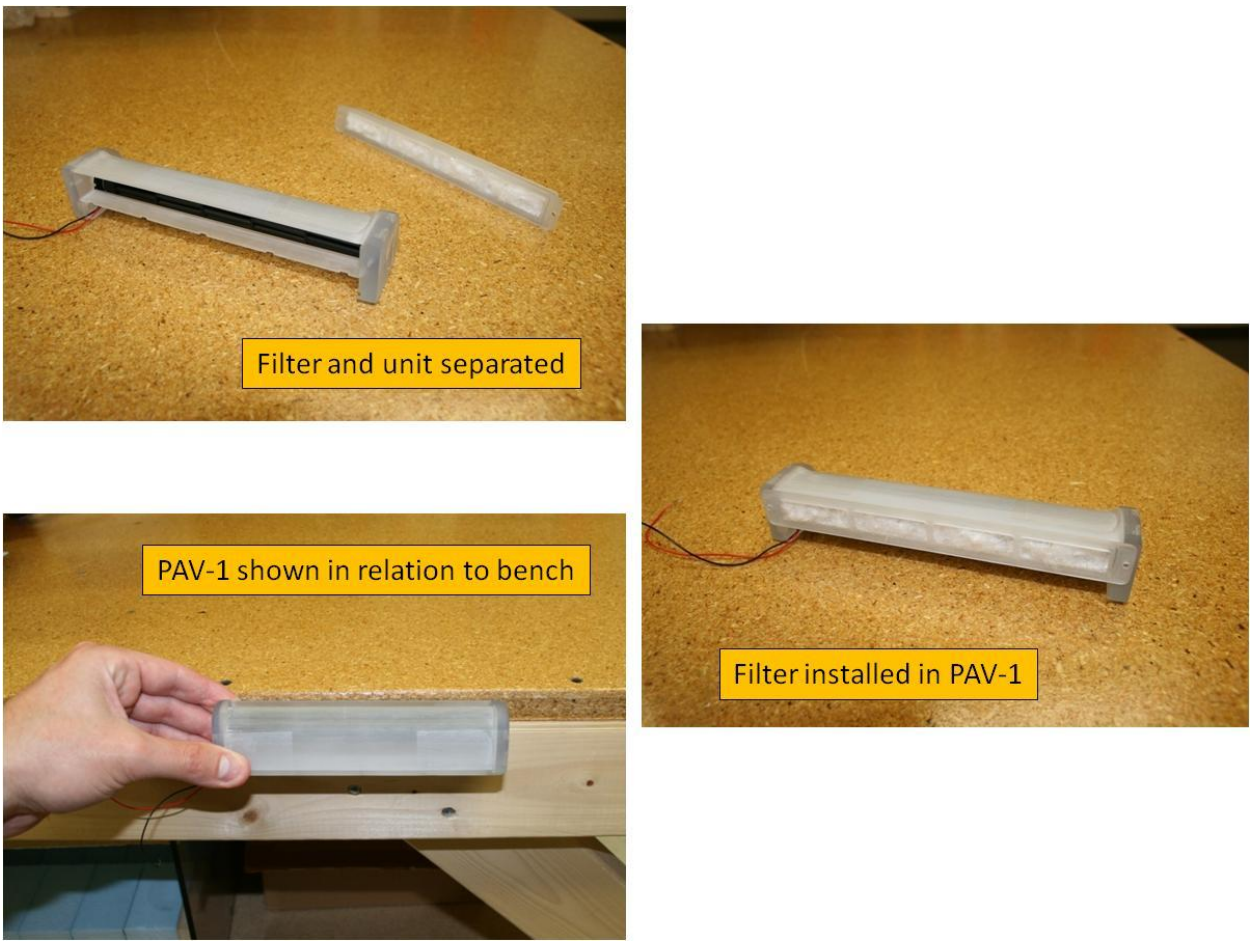

Fig. 3-4 Completed PAV-1 prototype.

Once PAV-1 was assembled, we planned to qualify the design using the Sage Action helium bubble generator, which would provide flow visualization near a person. Unfortunately, at the time PAV-1 was designed, the experimental data relating to the filters was preliminary, and the value for the linear proportionality constant in the porous model was set too low, which led (upon testing the unit) to insufficient pressure rise through the fan (and hence very low flow rate). It was found that the value for P_v should be set to 25,000 to appropriately represent the pressure drop through the filter. Regardless, even though PAV-1 was unsuccessful in terms of providing adequate flow rate, the lessons learned were valuable during redesign.

Upon further investigation of the flow field of PAV-1 it was determined that one of two things must happen: either the pressure rise through the fan must increase, or the pressure drop through the filter must decrease. Greater suction pressure is possible up to a certain point simply by increasing fan rpm; however, this results in higher noise and reduced efficiency (due to operation at extremely low flow coefficient). On the other hand, given that filtration is the primary goal of this project, reducing the thickness (or density) of the filter media in an effort to reduce pressure losses would be unacceptable, since this would defeat our goal.

A solution was found to remedy this by increasing the inlet area of the filter to the greatest possible. In this way, for a given flow rate (i.e. exit velocity), the velocity at the inlet would be minimized, thus minimizing the pressure drop. The diameter of the fan was also increased to 1.25" in order to further increase the exposed face of the inlet filter. Doing this alone, however, would still only bring the filter around approximately 120^{o} of the fan circumference (i.e. around the inlet of most "standard" cross-flow fan installations). In order to further increase the exposed area, the filter was wrapped around the backside of the housing lower wall, with a small gap left between the wall and filter inner surface. Since air takes the "path of least resistance", it was hypothesized that if the head losses incurred within the small channel leading from the backside of the lower housing around to the fan inlet were significantly less than the pressure drop through the filter, it would, in effect, double the frontal area of the filter. This would in turn reduce the filter pressure drop by half.

The geometry of the fan, housing, and filter for PAV-2 are shown in Figs. 3-5 and 3-6. Figure 3-7 shows close-ups of the CFD mesh around the fan and near the PAV exit.

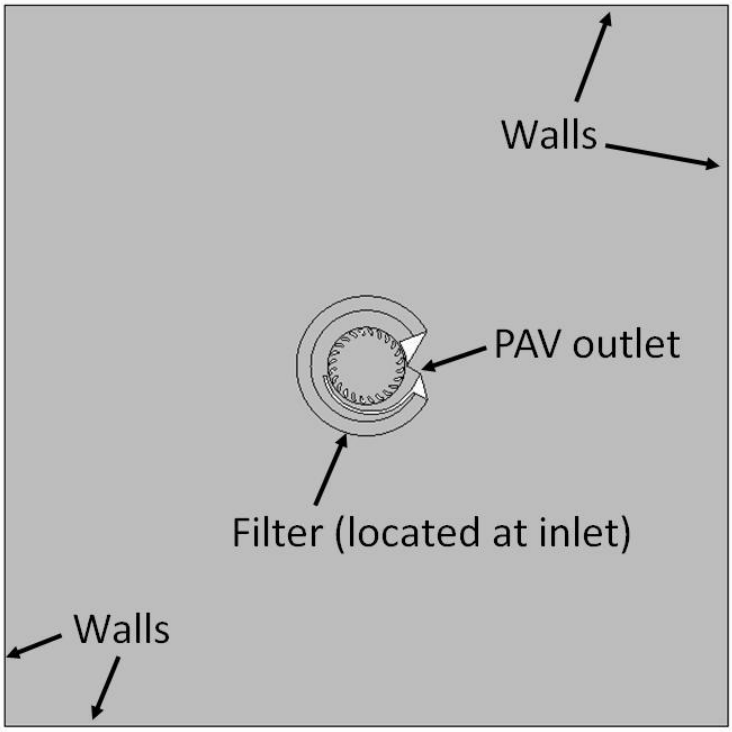

Fig. 3-5 PAV-2 computational domain.

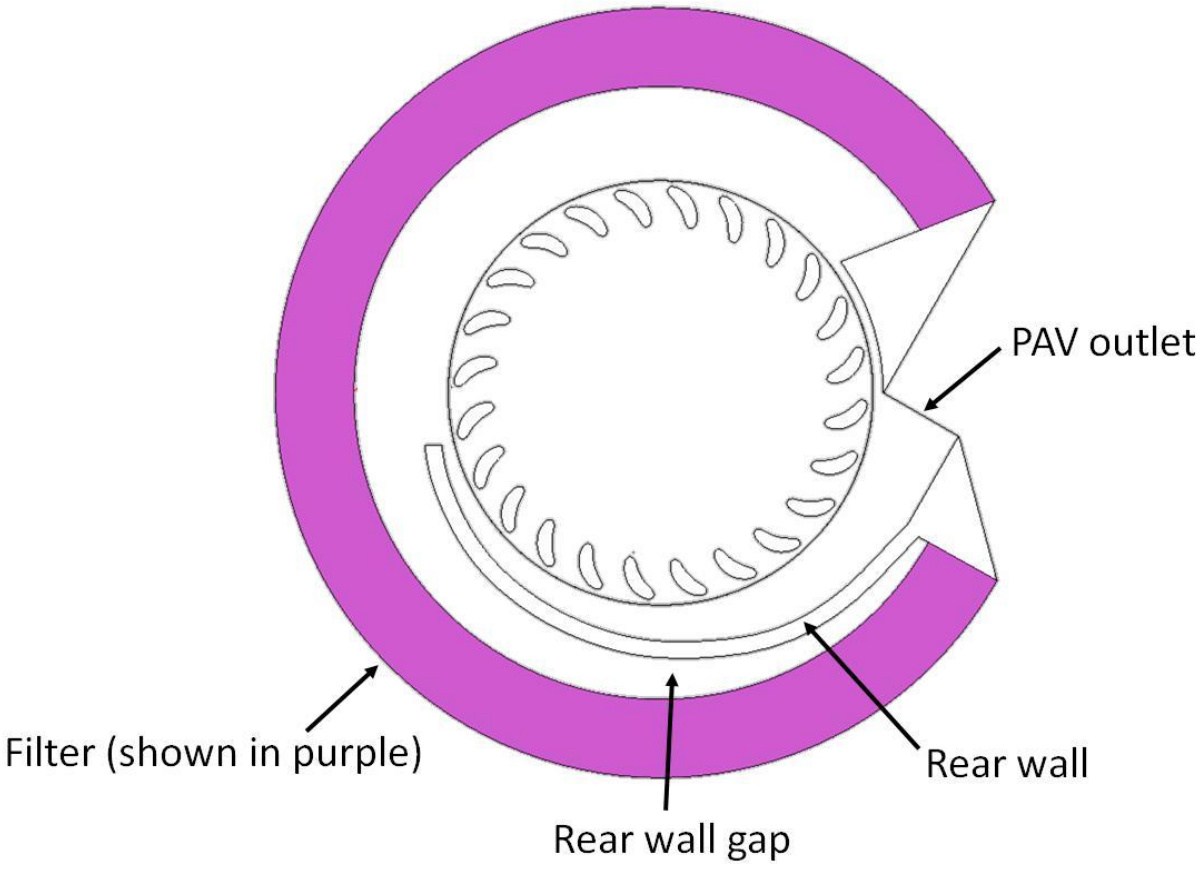

Fig. 3-6 Closeup of PAV-2 computational setup near fan.

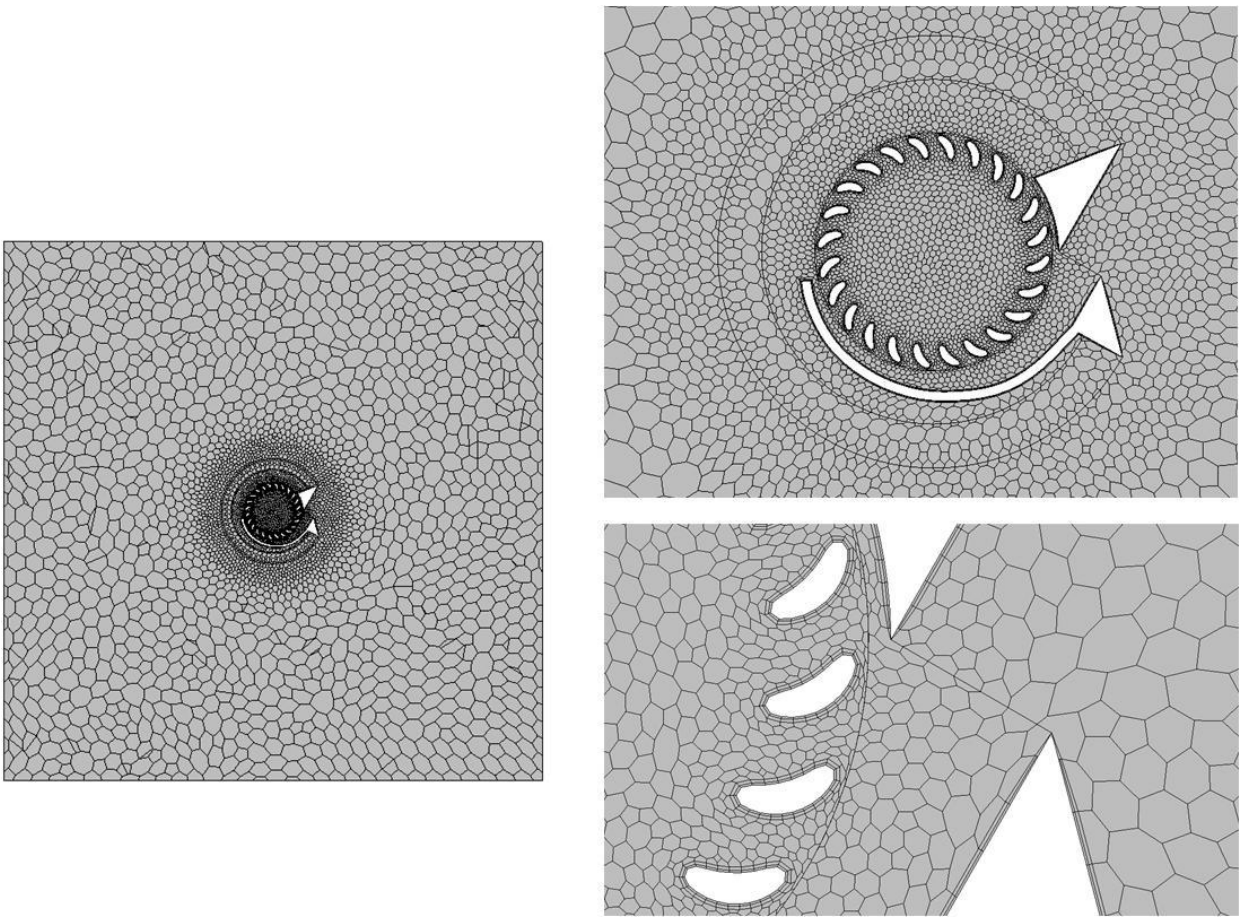

Fig. 3-7 CFD mesh for PAV-2 simulation.

Simulation results are shown in Figs. 3-8 through 3-10 at constant rpm of 3,000 while varying P_v. Without the filter present (P_v = 0), the streamlines pass right through the porous media region without losses. For a given fan speed, this would correspond to the highest flow rate condition. As the porous media resistance is increased, the streamlines align in a radial pattern, since this represents the shortest distance through the filter. At the full value of P_v = 25,000 kg/m^{3}s, even at only 3,000 rpm, the mass-averaged velocity at the exit is greater than 1 m/s. Based on the earlier CFD work of a person sitting at a desk utilizing the PAV device, an exit velocity between 0.5 and 1 m/s will suffice. CFD simulations with P_v = 25,000 kg/m^{3}s while varying rpm up to 6,000 rpm are shown in Figs. 3-11 through 3-13. For this configuration, at 6,000 rpm, the exit velocity was 4.4 m/s. For personal ventilation this may be too high; however, it may lend itself to the opportunity to either increase the MERV rating of the particle filter (or the density of the VOC adsorbent pellets), or potentially reduce the diameter of the fan.

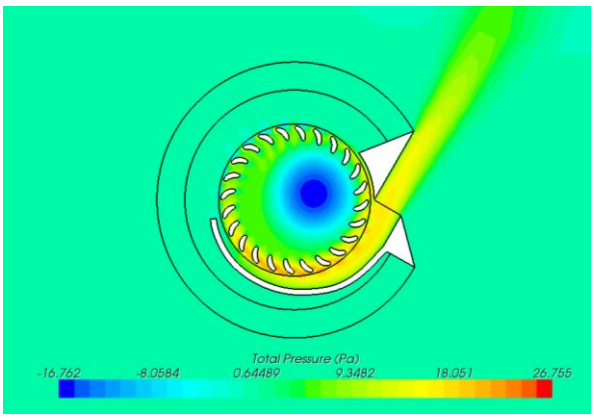

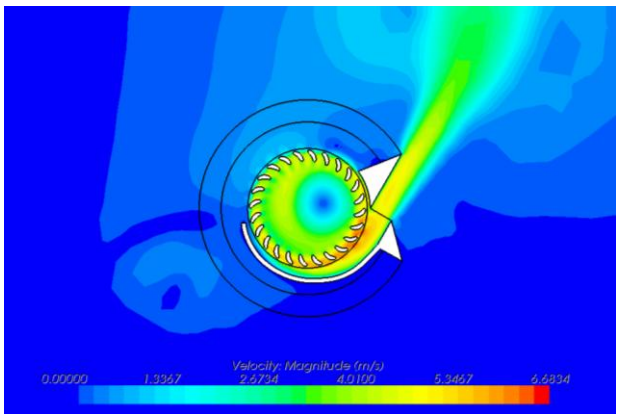

PAV 2: 3,000 rpm, $P_\nu = 0$ (No Filter)
$V_{exit} = 4.55$ m/s
Mass flow rate = 0.035 kg/s

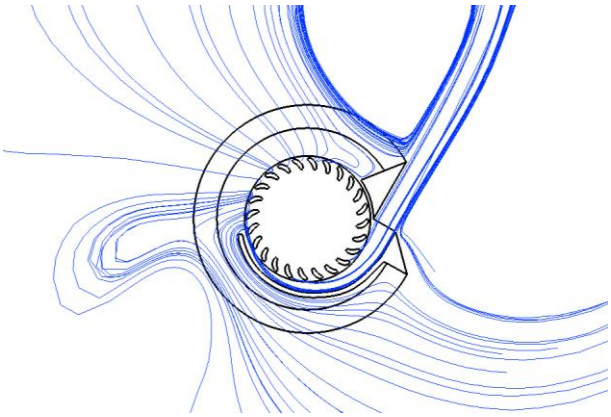

Fig. 3-8 PAV-2 simulation at 3,000 rpm and $P\nu = 0$.

PAV 2: 3,000 rpm, $P_\nu = 5{,}000$ kg/m^{3}s
$V_{exit} = 3.15$ m/s
Mass flow rate = 0.023 kg/s

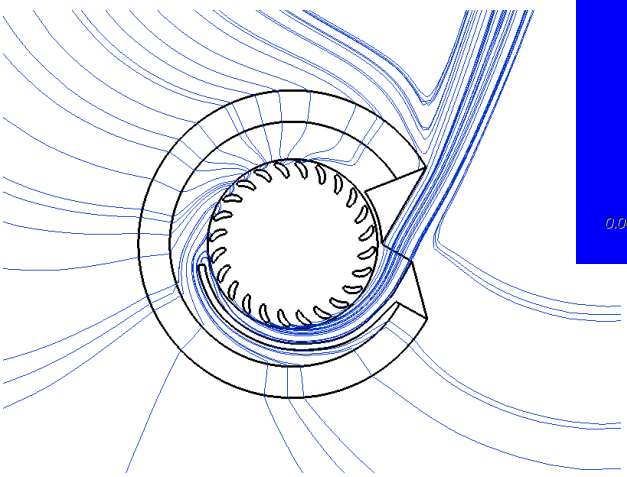

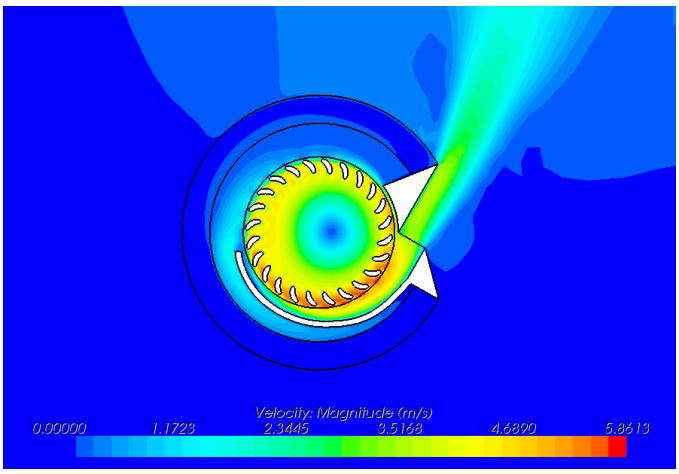

Fig. 3-9 PAV-2 simulation at 3,000 rpm and $P\nu = 5{,}000$ kg/m^{3}s.

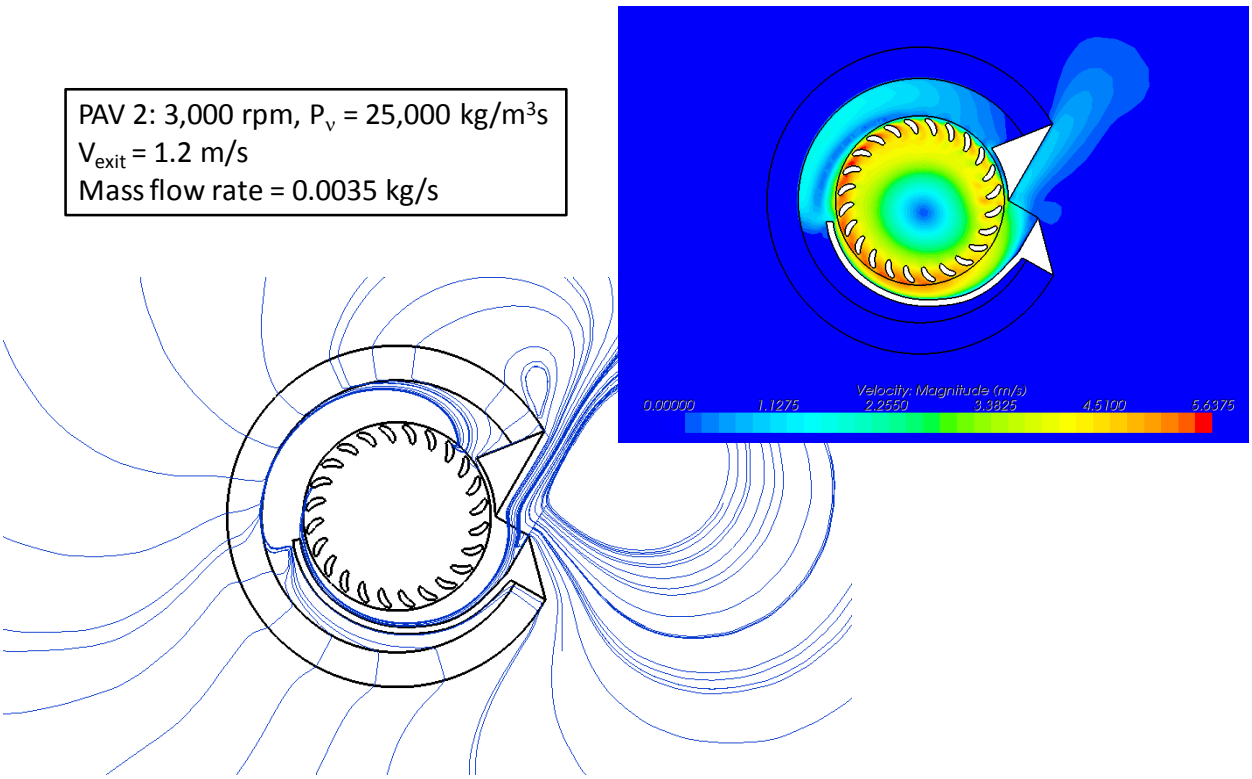

Fig. 3-10 PAV-2 simulation at 3,000 rpm and Pν = 25,000 kg/m^{3}s.

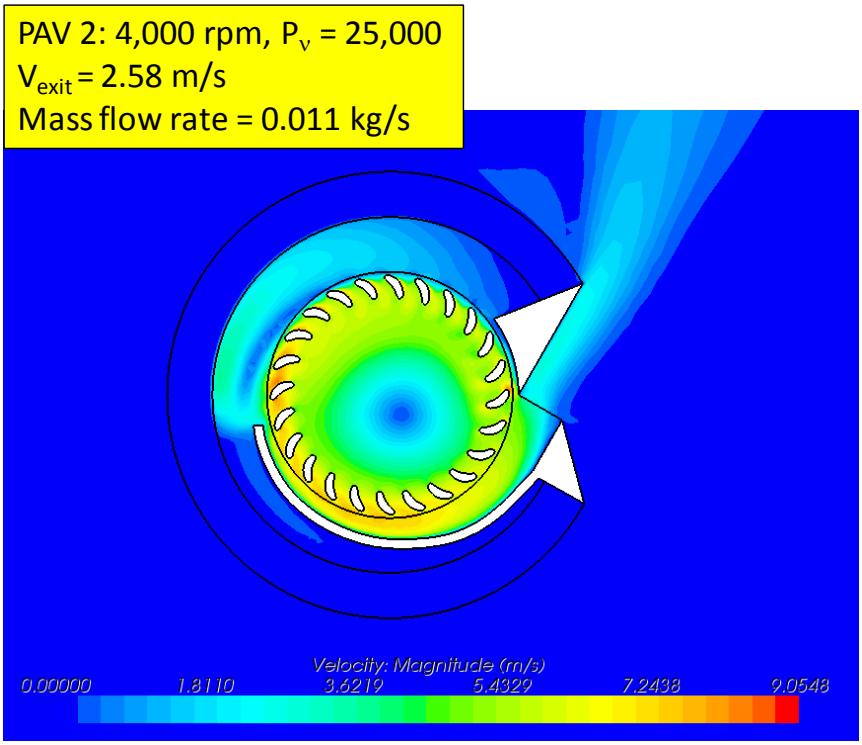

Fig. 3-11 PAV-2 simulation at 4,000 rpm and Pν = 25,000 kg/m^{3}s.

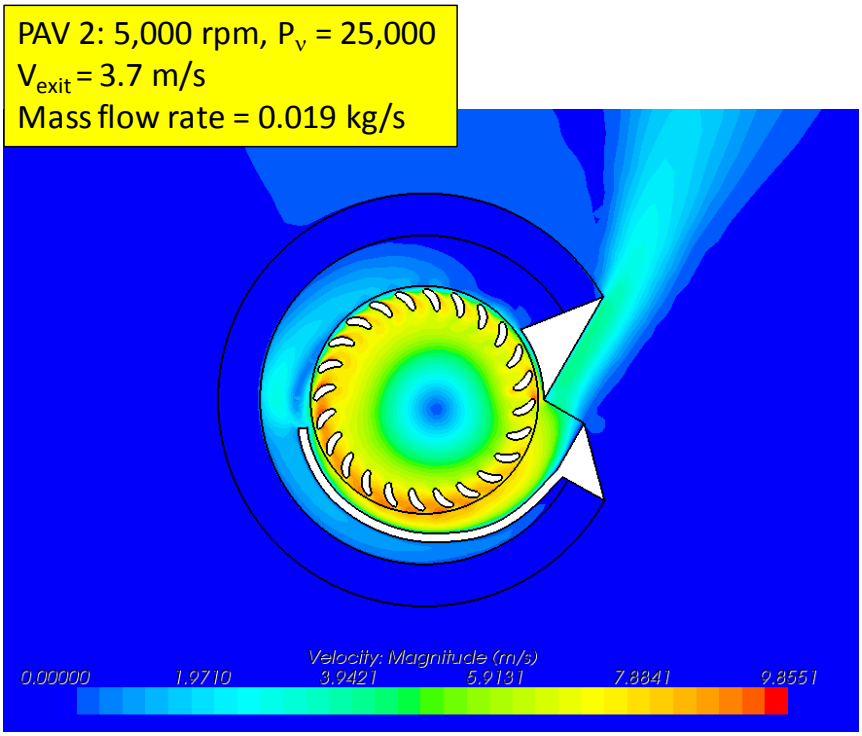

Fig. 3-12 PAV-2 simulation at 5,000 rpm and $P\nu$ = 25,000 kg/m^{3}s.

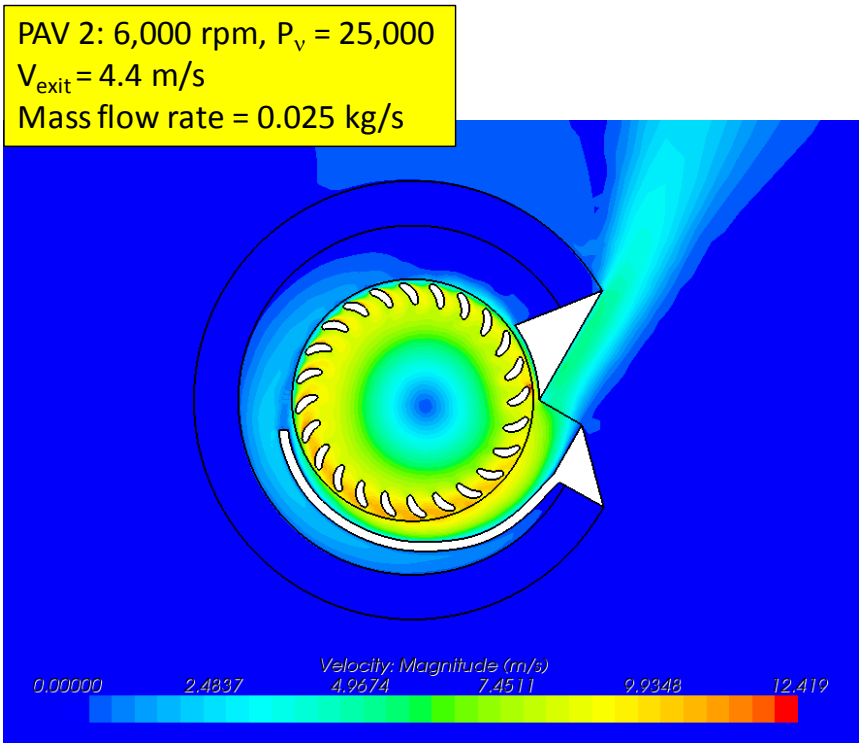

Fig. 3-13 PAV-2 simulation at 6,000 rpm and $P\nu$ = 25,000 kg/m^{3}s.

Upon completion of the CFD simulations for PAV-2, a CAD model was constructed. The final Solidworks model is shown in Fig. 3-14.

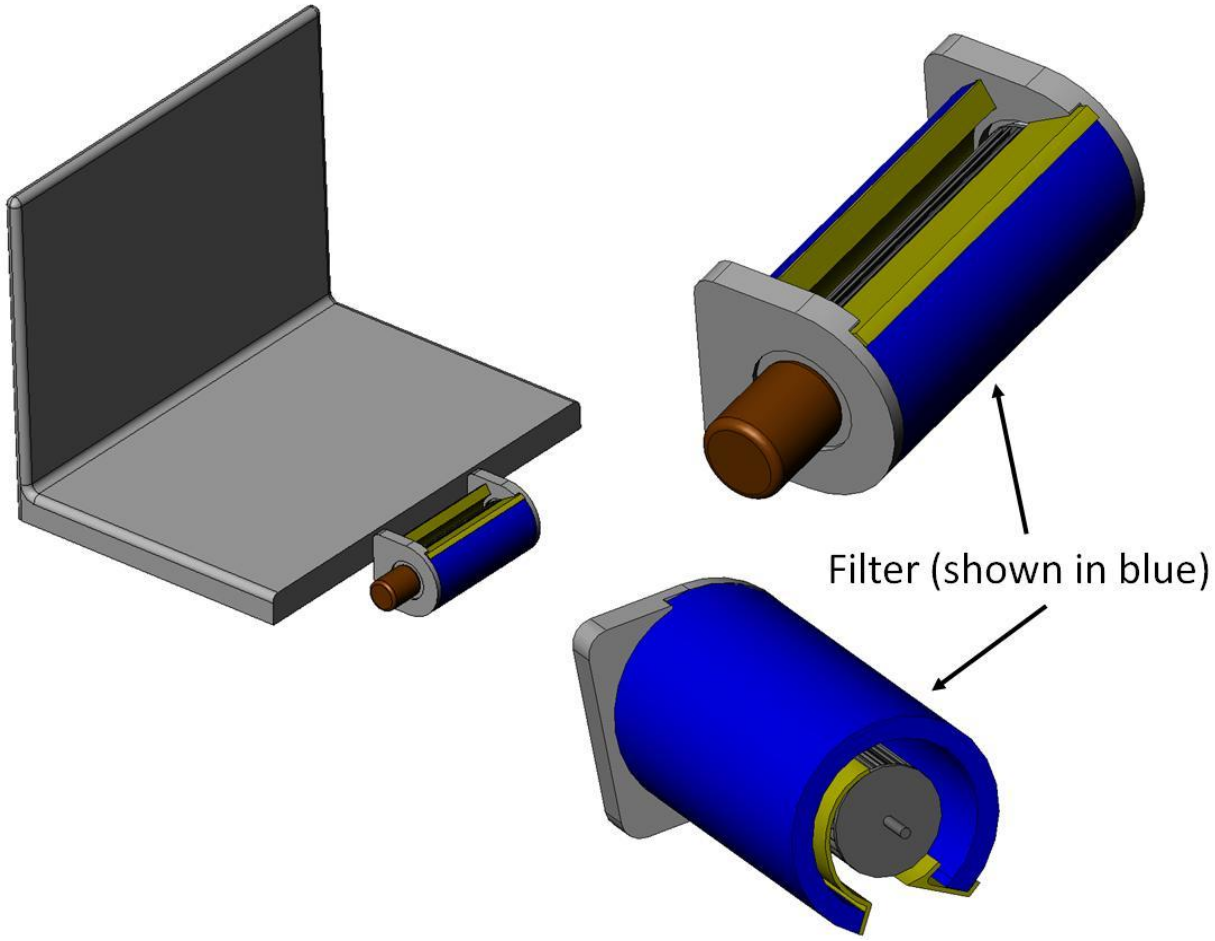

Fig. 3-14 CAD model of PAV-2 prototype.

In tandem with fabrication of the prototype, a CFD model was constructed comparable to the personal environment simulations. The same geometry was used here as before, except the previous model of the PAV device attached to the front of the computer was replaced with a similar model, but now in the shape of PAV-2. The computational mesh and geometry near the person and computer are shown in Fig. 3-15.

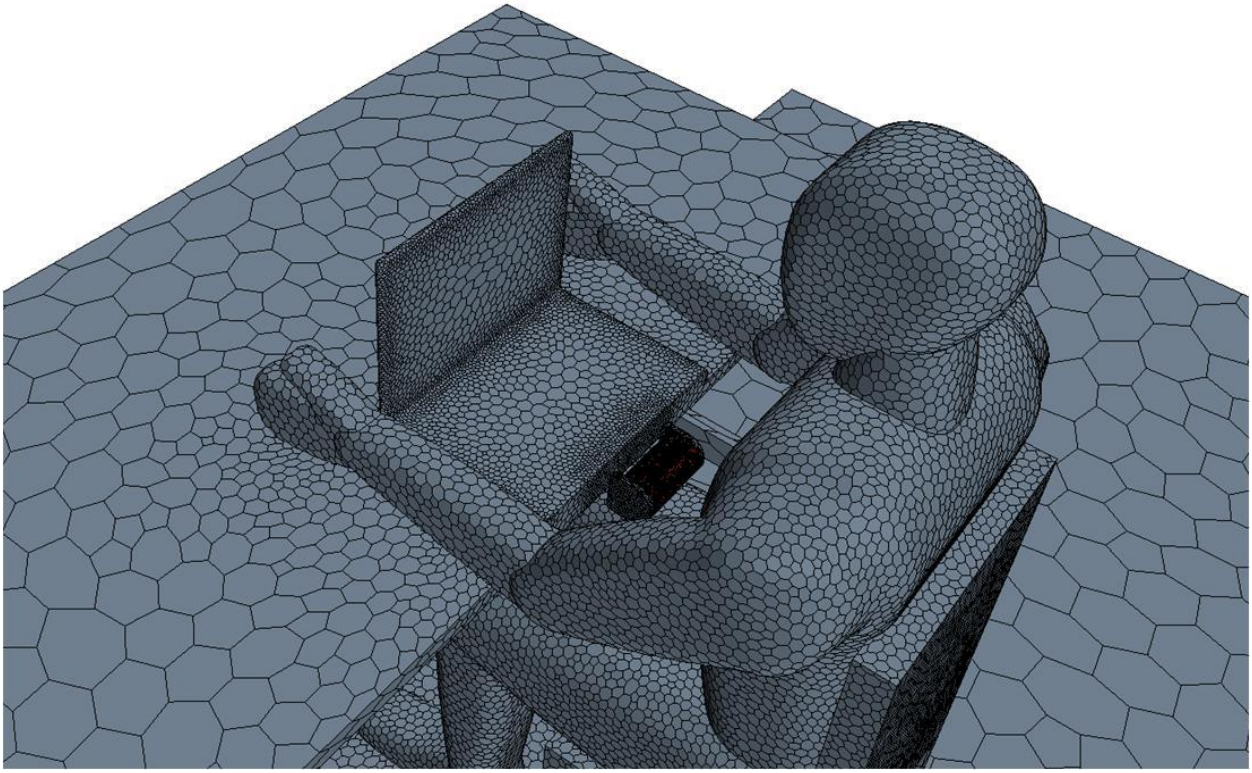

Fig. 3-15 PAV-2 simulation computational mesh.

The calculation was run with the PAV outlet velocity set to 0.5 m/s at a 30^{o} inclination from the horizontal. This was found previously to be the optimum angle for this exit velocity. Figure 3-16 shows the velocity magnitude contours for this case along a mid-plane through the domain; streamlines into and out from the PAV device are given in Figs. 3-17 through 3-19.

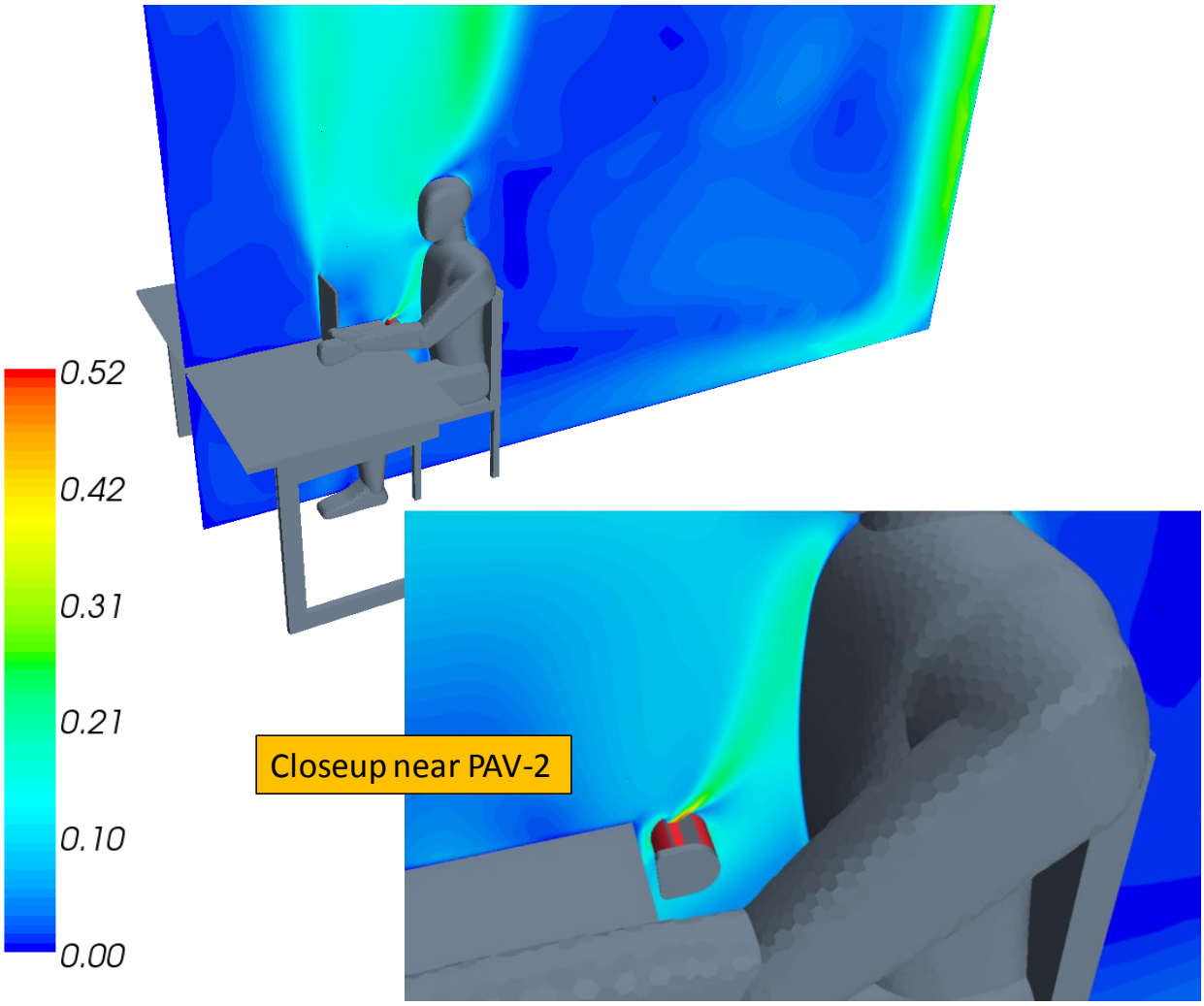

Fig. 3-16 Velocity magnitude contours along mid-plane (m/s).

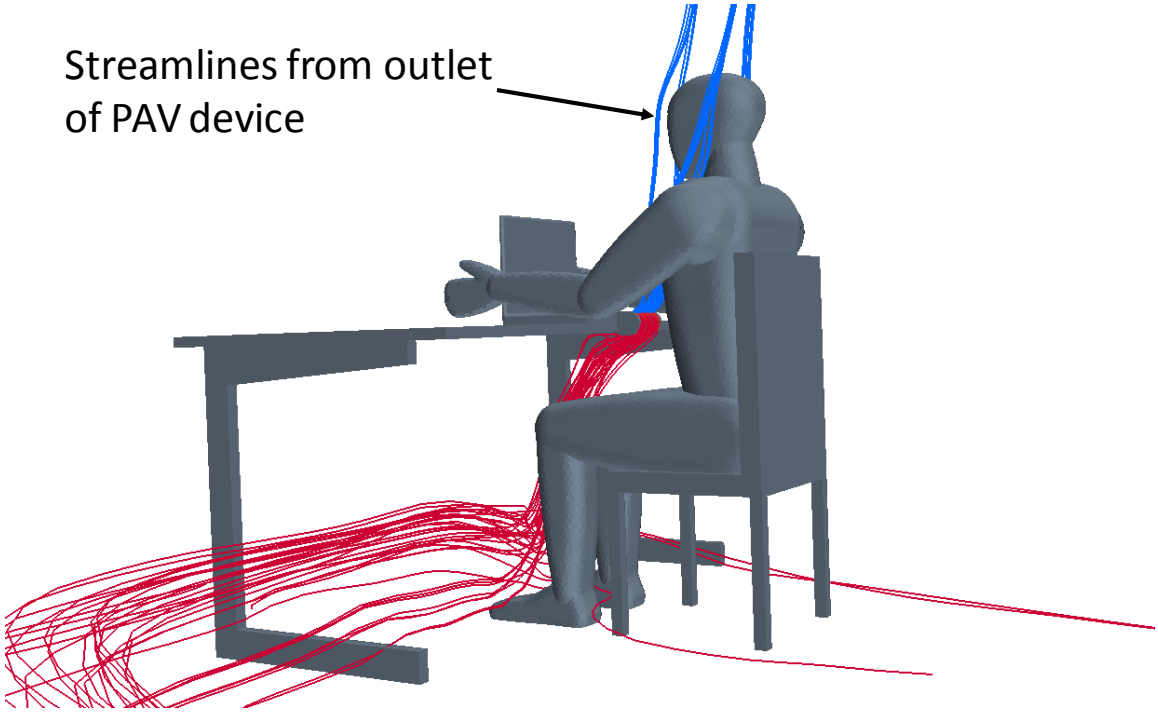

Fig. 3-17 Streamlines into and out from PAV-2 (ingested air = red, exhausted air = blue).

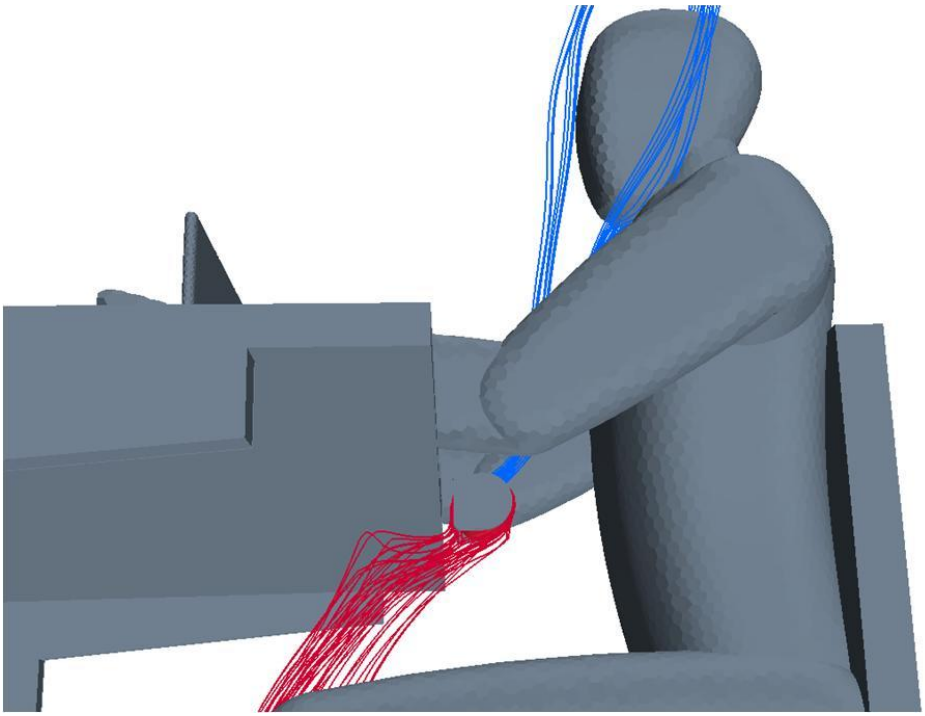

Fig. 3-18 Closeup of streamlines into and out from PAV-2.

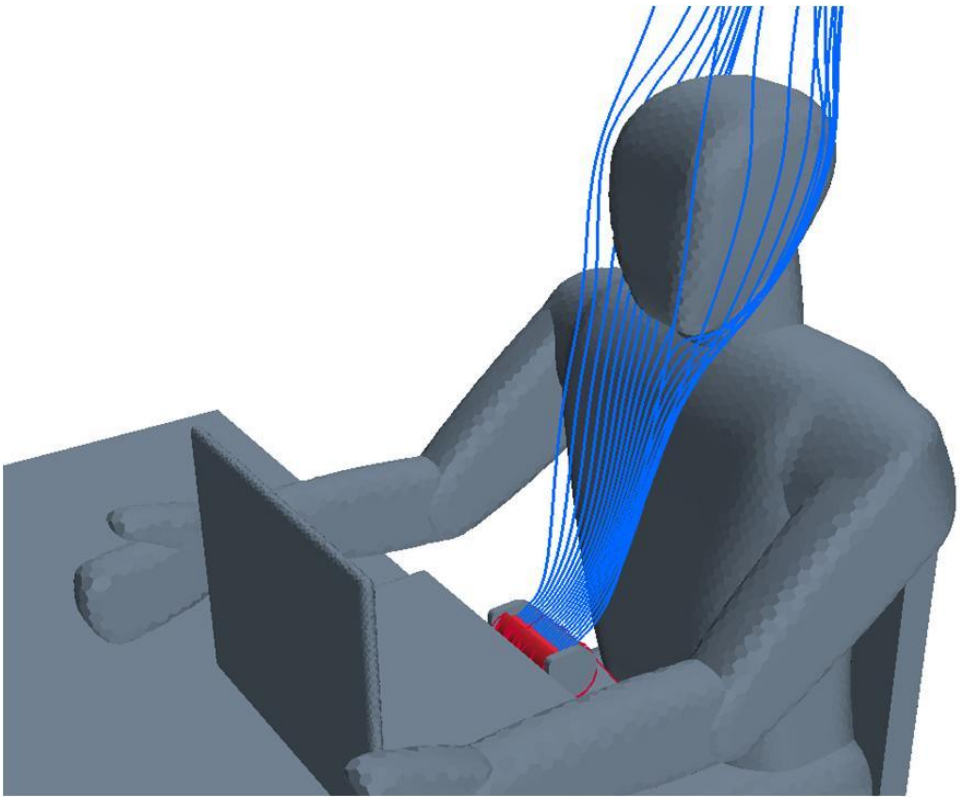

Fig. 3-19 Closeup of exhaust streamlines from PAV-2.

The results clearly show that the jet exits the PAV device toward the middle of the chest, but is then entrained by the thermal plume upward toward the face. By comparison, if the outlet velocity is increased to 1 m/s (Fig. 3-20), although the same entrainment occurs, the jet is too strong and slightly misses the face. This does not necessary mean that the person in this case will breath unfiltered air, only that the percentage of filtered to non-filtered air may be slightly worse than in the optimum case. As one final thought, based on the results presented thus far there is an ideal PAV outlet angle corresponding to a given exhaust velocity. In a practical sense, different people will enjoy differing amounts of “breeze”, and this may vary with environmental conditions (e.g. cleanliness of air, temperature, humidity, etc). Thus for the product to be successful in the marketplace, we believe that it must, at the very least, incorporate an adjustment for fan speed. In this way, depending on the individual’s preferences, as well as seating height, distance from the table, and other environmental variables, the device should accommodate most people.

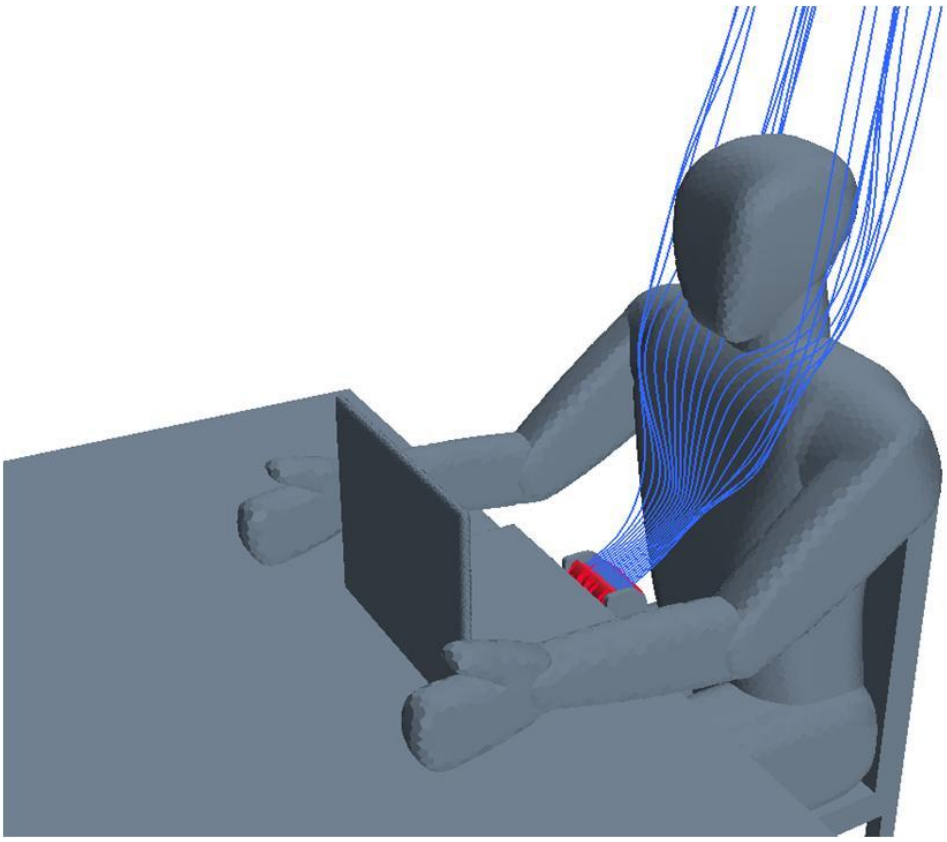

Fig. 3-20 Streamlines for exhaust velocity = 1 m/s.

Fabrication of PAV-2 (shown in Fig. 3-21) was similar to the first prototype, with the housing components rapid prototyped by DPT in Syracuse and the fan purchased from a current mass-producer of small cross-flow fans. Unlike the first prototype, PAV-2 produced a significant flow rate, so qualitative testing using the bubble generator was performed to assess the utility of the design. Video of the experiments was taken; pictures were extracted and are shown in Fig. 3-22. With the PAV device not present, the helium soap bubbles quickly rose into the breathing zone (and were often inhaled). In contrast, when the PAV device was placed on the front of the desk and turned on, the bubbles were immediately ingested into the unit. The filtered air (now bubble-free) was exhausting in a steady jet and gently flowed up to the face.

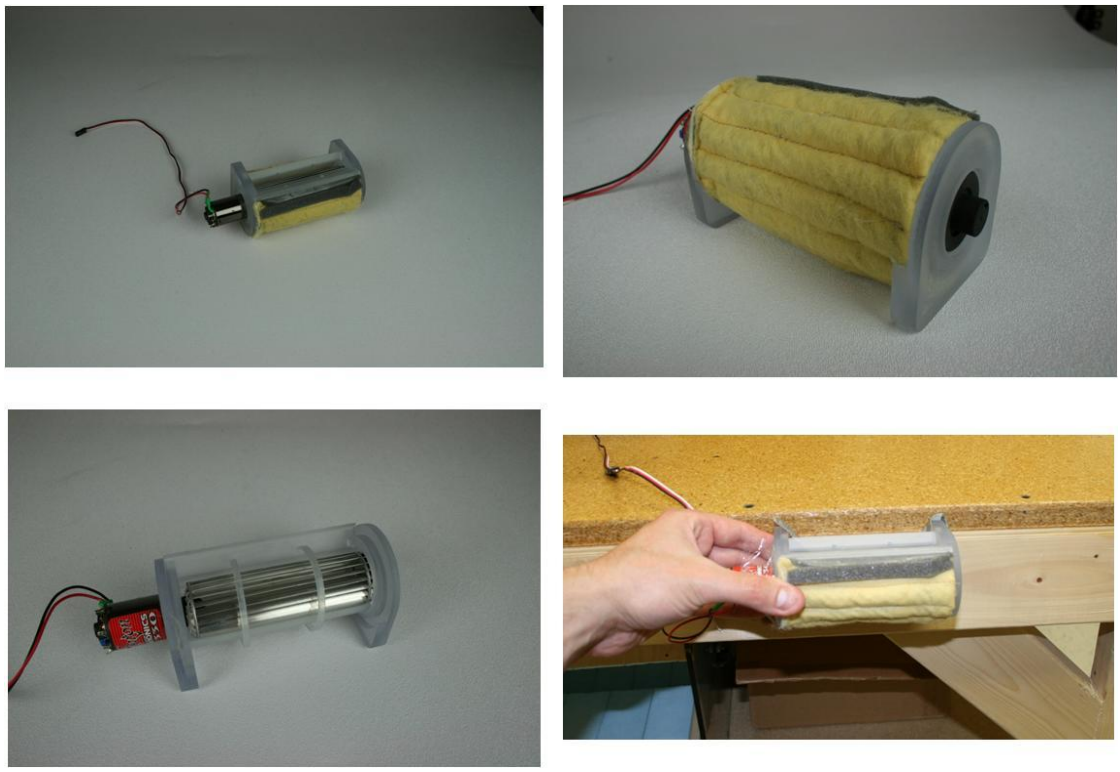

Fig. 3-21 PAV-2 prototype.

Fig. 3-22 PAV-2 testing with helium bubble generator at Propulsive Wing.

Although PAV-2 was successful technically, it was slightly too bulky and round to be practical. General opinion amongst the office staff at Allred & Associates agreed that it needed to be more compact, particularly in the direction outward toward the individual (i.e. normal to the desk face). PAV-3, shown in CAD form in Fig. 3-23 and fabricated Fig. 3-24, was essentially a redesigned version of the second prototype, but with several key changes. First, the fan diameter was reduced from 1.25” to 1.0”. At the same time the clearances and housing shapes were altered to minimize the overall thickness of the unit. We wished, however, to maintain the larger frontal area of the filter. Our solution was to elongate the shape of the housing downward. In this way, the filter area was kept large, while maintaining the compact look and feel.

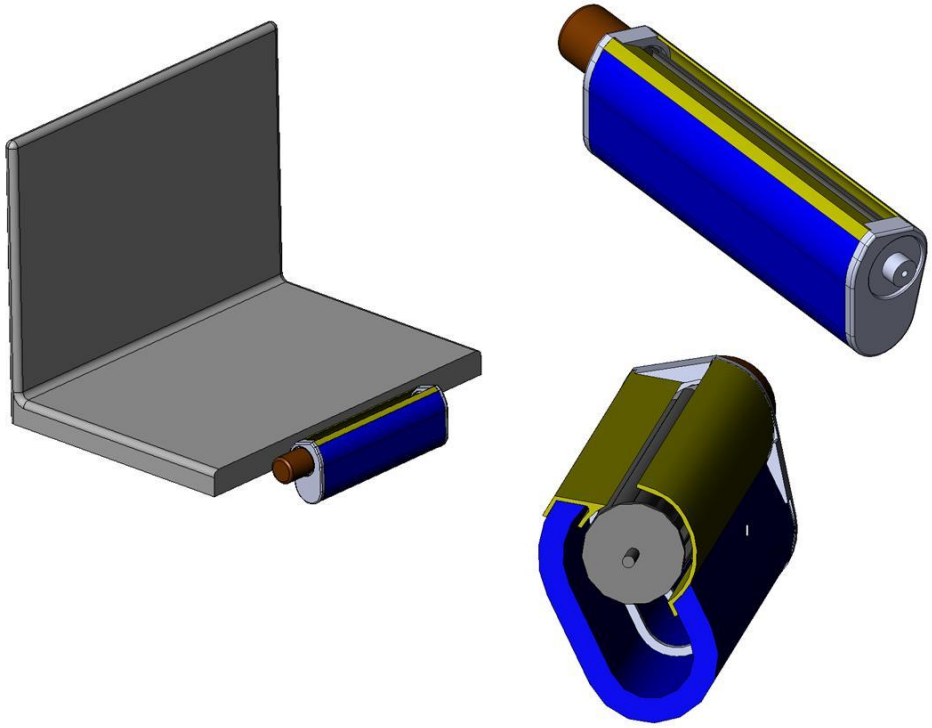

Fig. 3-23 CAD model of PAV-3 prototype.

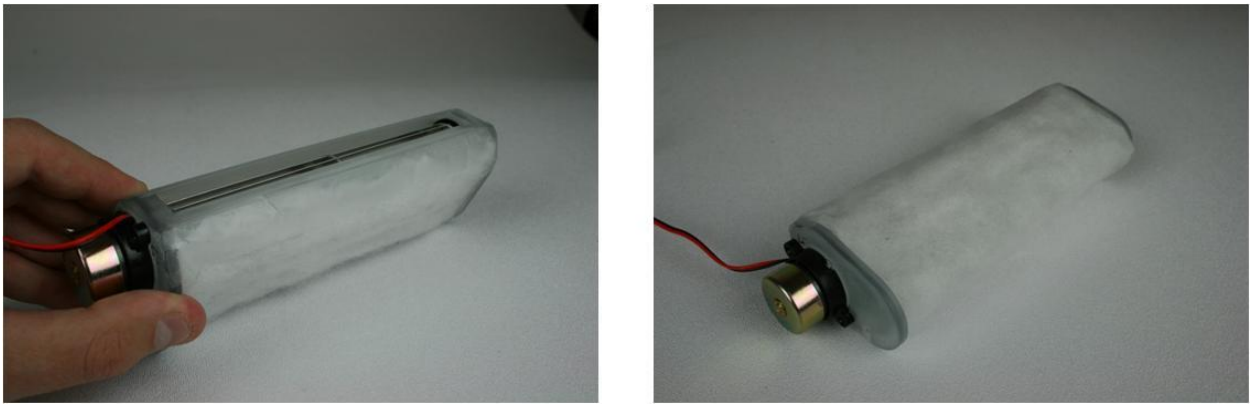

Fig. 3-24 Fabricated PAV-3 prototype.

Once fabrication was completed, PAV-3 was tested in the lab in the same manner as the previous prototype, and with similar results (Fig. 2-25). In Fig. 2-26, pictures are shown corresponding to positioning the bubble wand in various places relative to the device. These include just to the left and right of the PAV device (where the bubbles pass by the device, as well as the central breathing zone), and finally directly under the unit close to the filter (with similar results as when the wand is maintained closer to the floor).

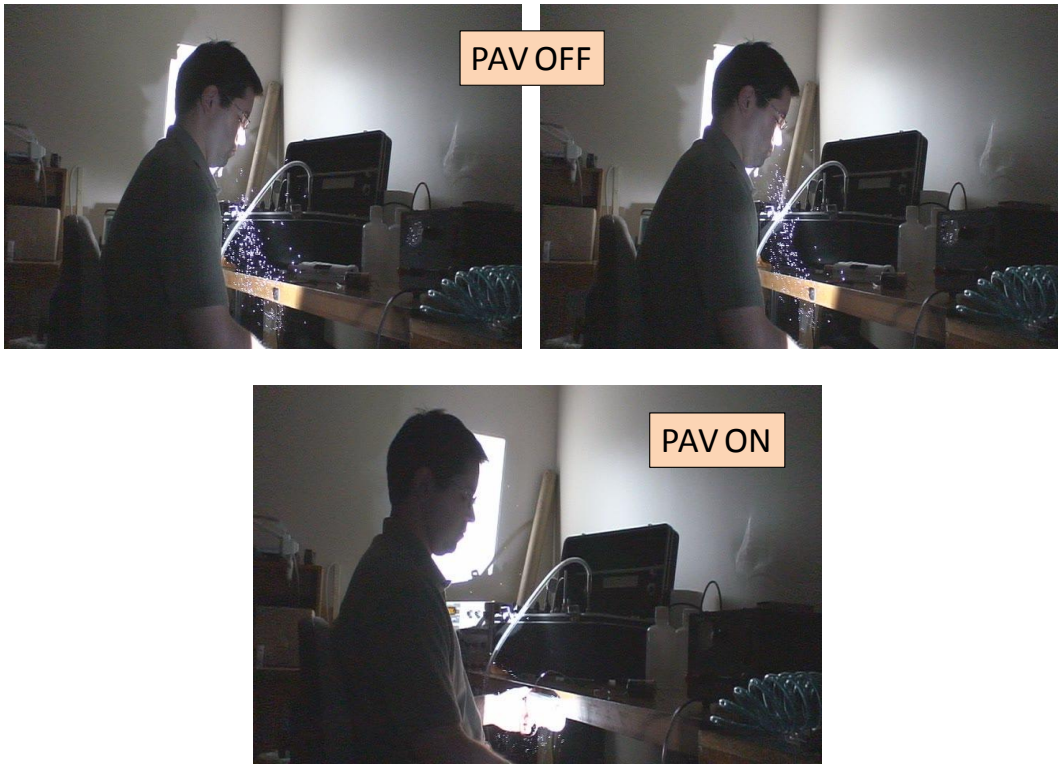

Fig. 3-25 PAV-3 testing at Propulsive Wing with helium bubble generator.

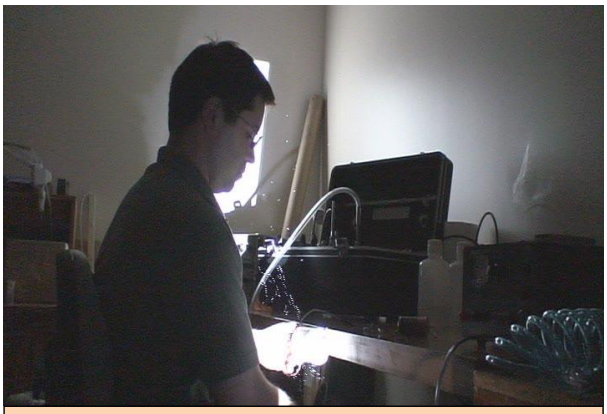

Bubbles released to the left of PAV

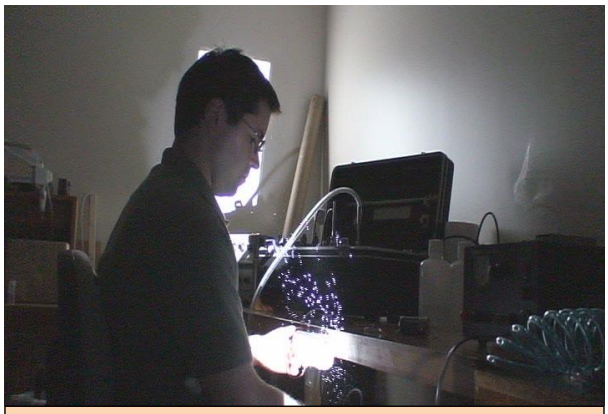

Bubbles released to the right of PAV

Bubbles released directly under PAV

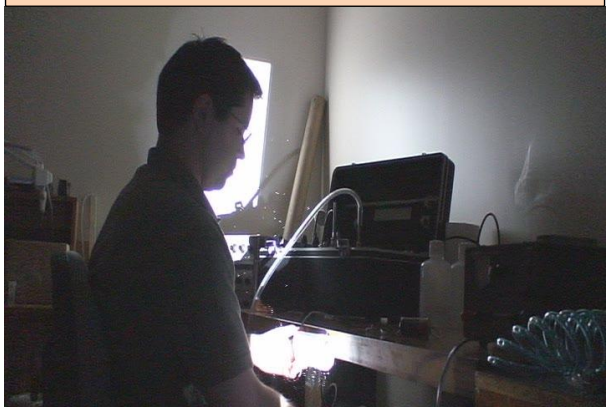

Fig. 3-26 Additional PAV-3 testing with bubble generator.

SECTION 4

Performance Evaluation of PAV Device in Syracuse University Laboratory

4.1 Introduction

To test the particle and gaseous pollutant removal performance of the PAV device, a pull-down test was conducted. The principle is: given a certain initial pollutant concentration in a well sealed chamber, when the air cleaning device is turned on, a pollutant concentration decay curve will be observed. With the assumption that the chamber is well-mixed, clean air delivery rate (CADR), which is normally used as an index for indoor portable air cleaners, can be determined. The detailed test procedure and calculation method for pull-down testing is described by Chen (W. Chen et al., 2006). The tests were conducted in the environmental chamber (IEQ chamber) located in the Syracuse University BEES Laboratory. The volume of the test chamber was 1920 ft^3. SF6 was used as a tracer gas to monitor the air leakage rate of the chamber system. Toluene and formaldehyde with target concentrations of 5 mg/m^3 and 2 or 3 mg/m^3, respectively, were used as challenge gaseous pollutants. Gaseous pollutants were generated by an evaporation method. Particles were generated using a large aerosol generator (TSI 8818) with KCL solution.

Reference tests without the PAV device, but only other test facilities in the chamber, were conducted to check the chamber status and calculate the natural decay rate of pollutants due to removal effects other than the air cleaner. This reference test was conducted at a mixing flow rate of 800 cfm.

Figure 4-1 shows the concentration decay of toluene and formaldehyde in the reference test, as well as SF6. Table 4-1 lists the air leakage rate calculated from the SF6 decay and natural decay rate of toluene. The air leakage rate was about 0.03ACH, which was within the specification of AHAM (2005), and was considered acceptable. It was observed that the natural decay rate of toluene was lower than the air leakage rate, and therefore the other removal effects of toluene in the chamber were negligible. However, the formaldehyde concentration decayed much quicker than the air leakage rate. Based on experience, this is due to condensed

water from the HVAC system coil. Actions are being taken to eliminate this effect. The natural decay rate is not calculated here.

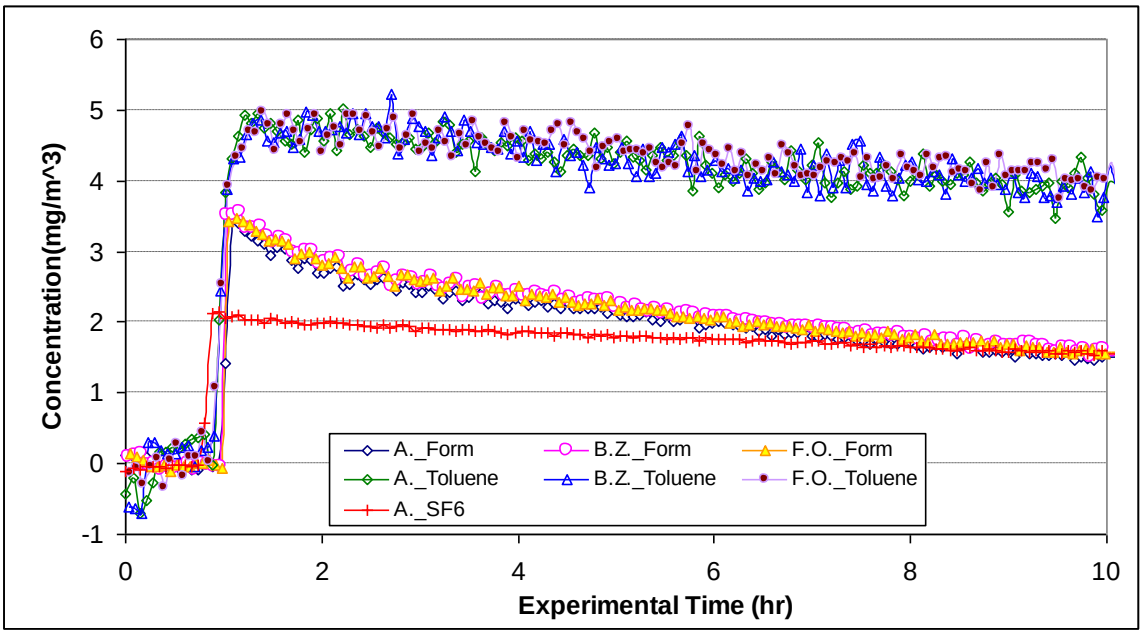

Fig. 4-1 Gaseous pollutant concentration in reference test.

Table 4-1 Air leakage rate and natural decay of toluene and formaldehyde

	Toluene			Formaldehyde		
	Filter Out	Breathing Zone	Ambient	Filter Out	Breathing Zone	Ambient
Air leakage rate calculated by SF6 (ACH)	**0.0295**	**0.0295**	**0.0301**	**0.0295**	**0.0295**	**0.0301**
Regression R^2	0.993	0.9914	0.9909	0.993	0.9914	0.9909
Natural Decay rate kn (ACH)	**0.0206**	**0.0268**	**0.0248**	**-**	**-**	**-**
Regression R^2	0.6365	0.6574	0.6632	-	-	-

Figure 4-2 shows the particle concentration decay in the reference test. The natural decay rate of particles is normally larger than the air leakage rate due to the deposition of particles onto the surface of the test system. Data from three different sampling points were averaged to get the average natural decay rate for particles in three different size ranges. The results are shown in Table 4-2.

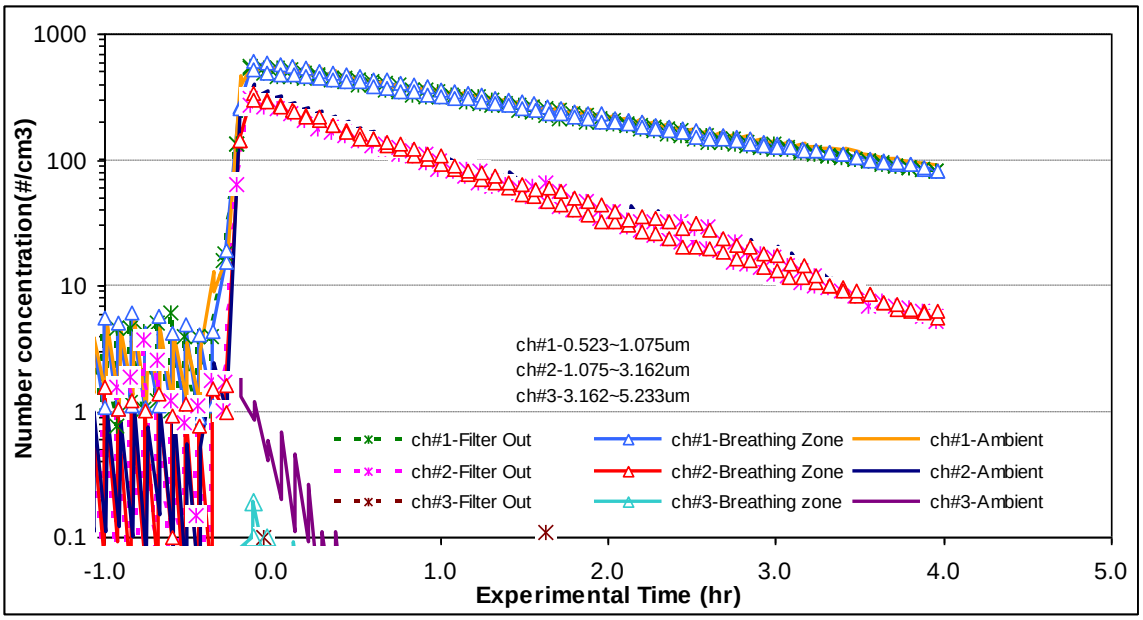

Fig. 4-2 Particle concentration decay in reference test.

Table 4-2 Natural decay of particles in reference test with 800cfm

	0.523-1.075um			1.075-3.162um			3.162-5.233um		
	Filter Out	Breathing Zone	Ambient	Filter Out	Breathing Zone	Ambient	Filter Out	Breathing Zone	Ambient
Air leakage rate calculated by SF6 (ACH)	**0.0267**	**0.0265**	**0.0266**	**0.0267**	**0.0265**	**0.0266**	**0.0267**	**0.0265**	**0.0266**
Regression R^2	0.9912	0.9888	0.9921	0.9912	0.9888	0.9921	0.9912	0.9888	0.9921
Natural Decay rate kn (ACH)	**0.4743**	**0.4762**	**0.4572**	**0.9651**	**0.9691**	**0.9773**			**6.7773**
Regression R^2	0.9937	0.9918	0.9856	0.9917	0.9922	0.9915			0.7778
Average natural decay rate (ACH)	**0.4692**			**0.9705**			**6.7773**		

4 prototype filters were made for the PAV device with different combinations of particle filtration media and gaseous pollutant adsorption media (Fig. 4-3). The detailed description of these filters is listed in Table 4-3.

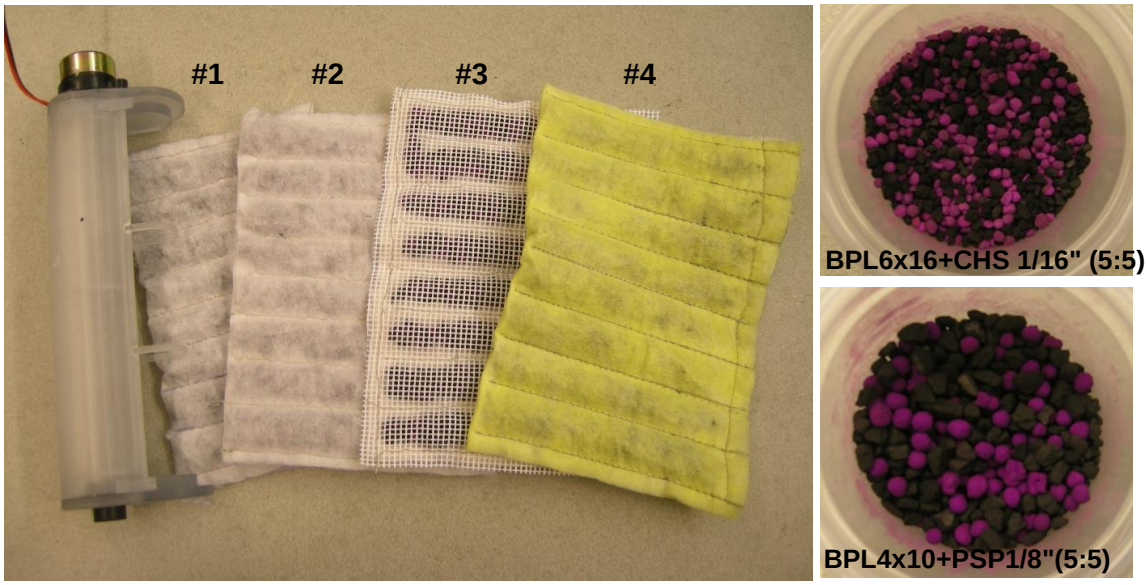

Fig. 4-3 Prototype filters for the PAV device and adsorption media used.
(Black is activated carbon media for general VOCs, purple media is for formaldehyde removal)

Table 4-3 Description of the prototype filters for the PAV device

No.	Particle filtration media	Layer number	VOC filtration media	Filter size	Weight of AC (g)	Density (g/m2)
#1	MERV7	Double	BPL4x6	6.125" x 3.75"	18.9	1278
#2	MERV7	Double	BPL6x16+CHS 1/16" (5:5)	6" x 4.25"	16.7	1017
#3	MERV11+cloth mesh	Single	BPL 4x10 +PSP 1/8" (5:5)	6.5" x 4.5"	22.6	1372
#4	MERV8	Double	BPL 6x16	6.5" x 4.5"	19.5	1033
#5	MERV7	Double	BPL 6x16	7.25" x 5"	43.8	1873

Prototype filter #4 was installed onto the PAV device. After the filter was installed, the airflow rate through the device was calculated by measuring the velocity at the outlet of the filter and the dimensions of the outlet vent. Four sampling points were measured to take an average. Figure 4-4 depicts measuring the outlet velocity.

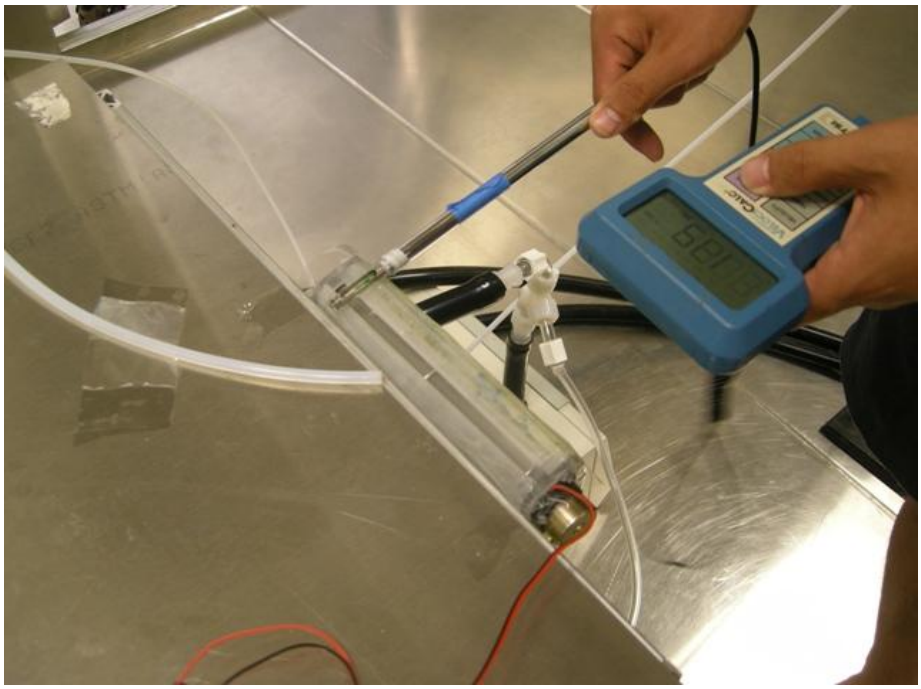

Fig. 4-4 Measurement of airflow rate through the PAV device.

Table 4-4 shows the airflow rate with prototype filter #4 (double layer MERV 8 and BPL 6x16) and the power supply set to 12V. The airflow rate was about 1.88cfm with the current settings, and varied with the power supply voltage and different filters.

Table 4-4 Airflow rate through the PAV device with Filter #4

Voltage:	12V
Velocity along the filter outlet vent (ft/min)	144.375
Dimensions of the filter outlet vent (ft^2)	0.013
Air flow rate through the PAV device (cfm)	**1.88**

4.2 Performance Test 1

This test was conducted with prototype filter #4, the DC power supply at 12V, and with toluene, formaldehyde, and particles as the challenge pollutants. The test setup is shown in Fig. 4-5. Three different sampling points were selected to measure the concentration: immediately out of the unit (Filter Out), the breathing zone of a sitting person in front of the desk (Breathing Zone), and the other position located away from the air cleaner (Ambient). The “Breathing Zone” point was 6” horizontally away and 9” higher than the “Filter Out” point. The gaseous concentration

was measured by an INNOVA 1312 multi-gas monitor and 1303 multi-point sampler and doser. The instrument monitored the concentration of the 3 sampling points continuously. The particle concentration was measured by an APS 3321 particle analyzer, and an auto-switch valve system was used for the multi-point sampling. This test was conducted with a mixing air flow rate of 800cfm.

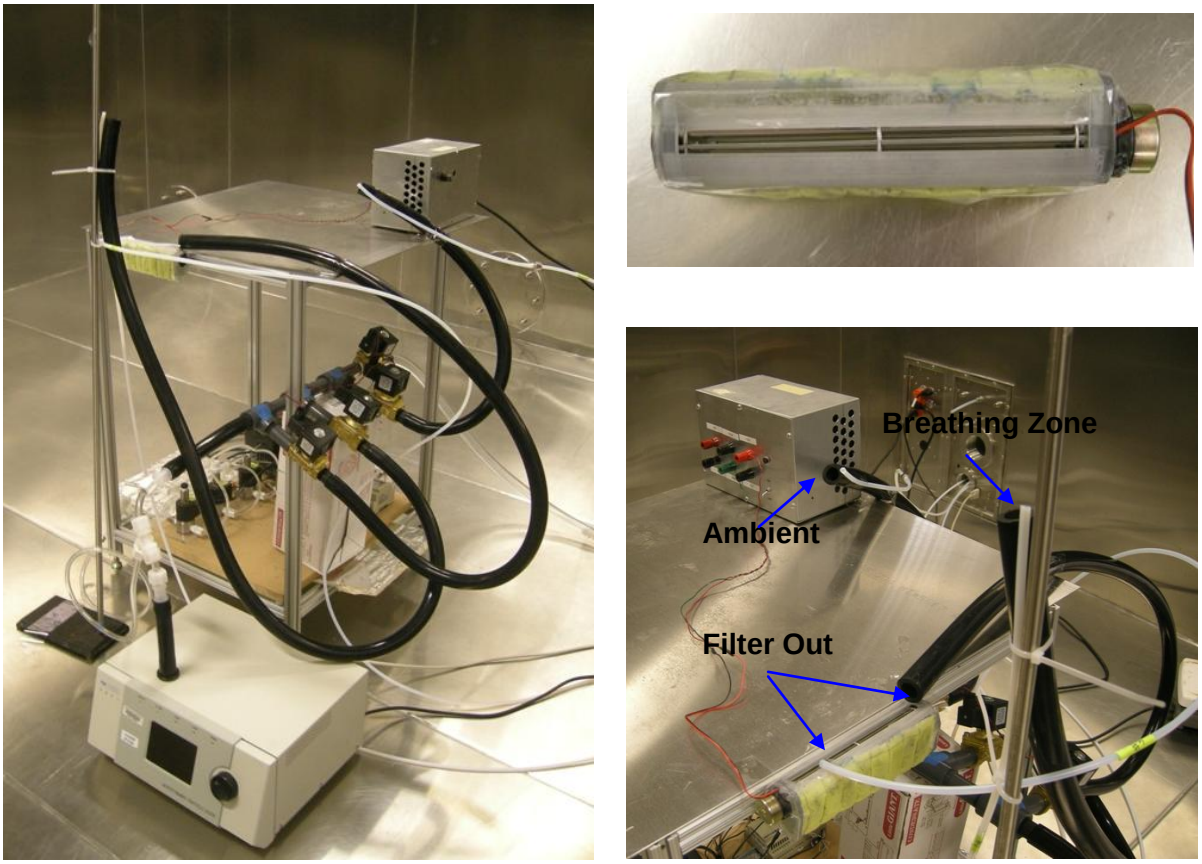

Fig. 4-5 PAV setup and sampling point for VOC and particle concentration measurements.

Figure 4-6 shows the concentration of toluene and formaldehyde at the 3 sampling points in the chamber. Time zero was the time when the PAV device was turned on. It was noticed that the background toluene concentration of “Filter Out” was higher than the other two points, which was possibly due to the tape used for attachment of the prototype filter onto the device and for fixing the device to the desk. After the PAV was turned on, the filter out concentration was lower than the breathing zone and ambient readings. The PAV device was then turned off after about 5 hours running, and it was observed that the outlet concentration increased to be higher than the other two points. Also, it was found that the concentrations at the breathing zone and ambient locations did not show significant difference.

Formaldehyde concentration decayed very quickly after injection, even before the PAV device was turned on. This was again due to the HVAC system of the chamber.

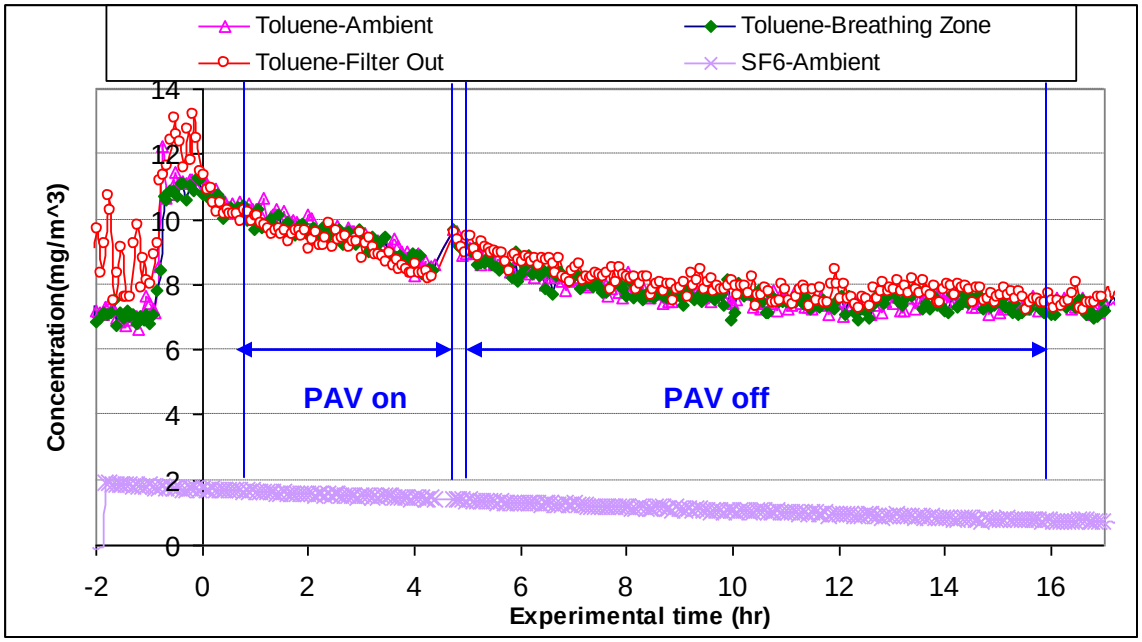

(a) toluene

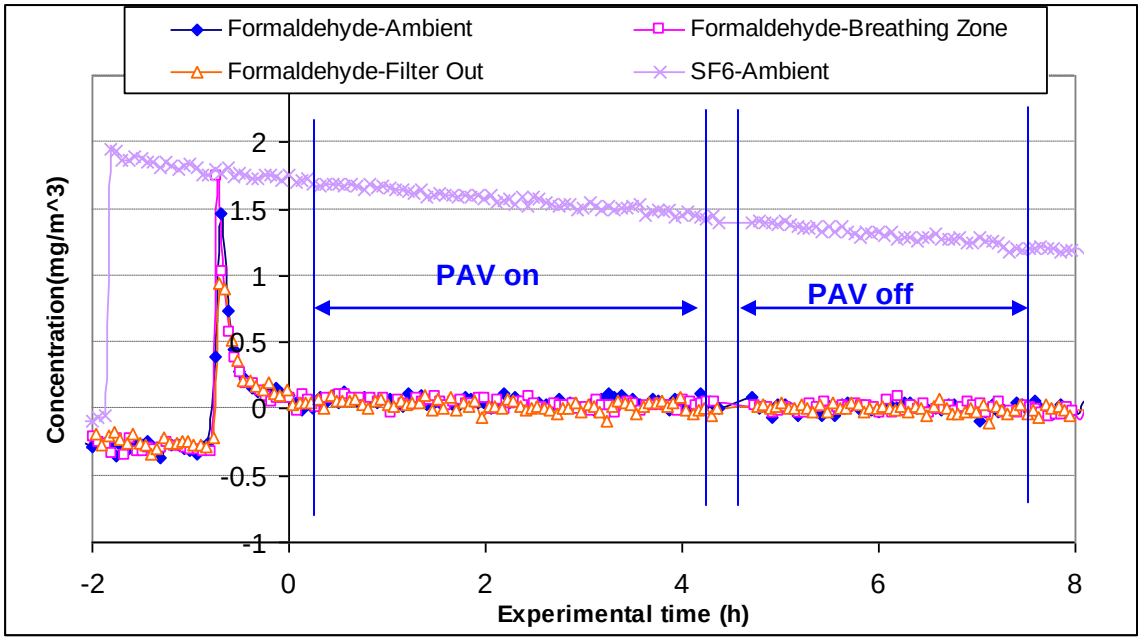

(b) formaldehyde

Fig. 4-6 Pollutant concentration decay.

Table 4-5 lists the calculated CADR of the tested air cleaner for toluene. CADR for formaldehyde was not calculated. The decay rate of toluene after turning on the air cleaner was higher than the air leakage rate, but not substantially. This was due to the large chamber volume compared with the relatively small airflow rate of the cleaner.

Table 4-5 CADR of PAV for toluene with prototype filter #4

	Toluene			Formaldehyde		
	Filter Out	Breathing Zone	Ambient	Filter Out	Breathing Zone	Ambient
Air leakage rate calculated by SF6(ACH)	**0.0397**	**0.0402**	**0.0392**	**0.0397**	**0.0402**	**0.0392**
Regression R^2	0.9384	0.9269	0.9575	0.9384	0.9269	0.9575
Decay rate calculated after turning on AC k_e (ACH)	**0.0512**	**0.0446**	**0.0533**	**-**	**-**	**-**
Regression R^2	0.8892	0.8613	0.8626			
CADR=V(k_e -k_n)/60 (CFM)	**0.37**	**0.14**	**0.45**	-	-	-

Figure 4-7 and Table 4-6 show the particle results. The CADR was also calculated for particles in different size ranges.

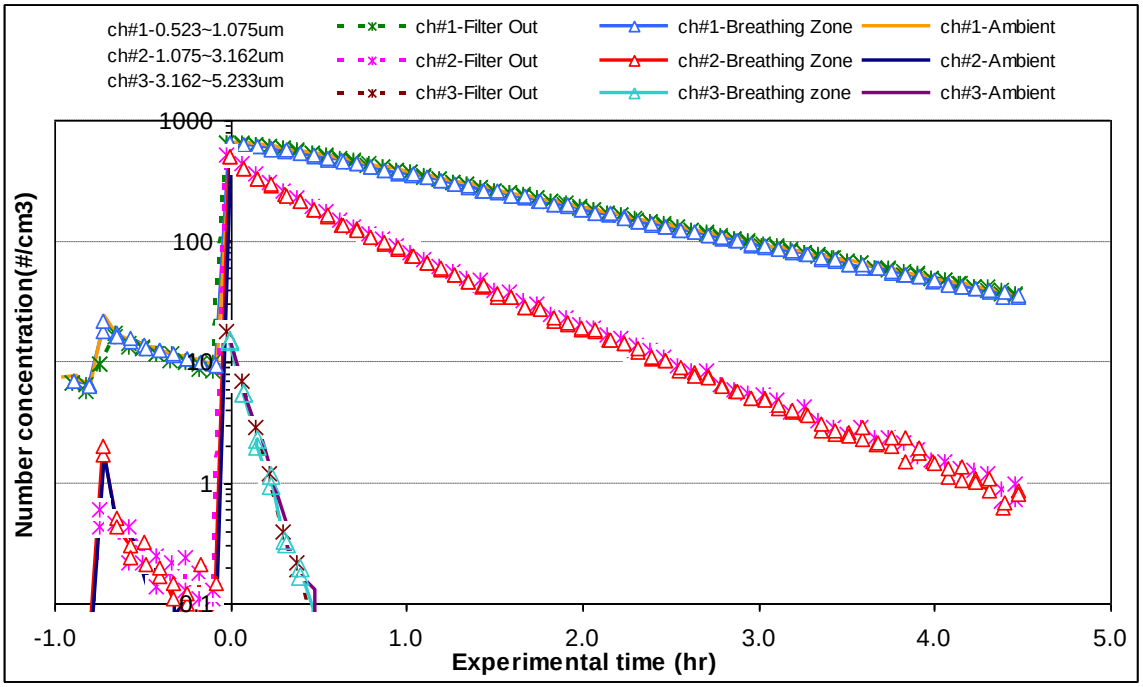

Fig.4-7 Particle concentration decay.

Table 4-6 CADR of PAV for particles with prototype filter #4

	0.523-1.075um			1.075-3.162um			3.162-5.233um		
	Filter Out	Breathing Zone	Ambient	Filter Out	Breathing Zone	Ambient	Filter Out	Breathing Zone	Ambient
Natural Decay rate kn (ACH)	**0.4692**			**0.9705**			**6.7773**		
Decay rate after turning on AC ke (ACH)	**0.6714**	**0.6731**	**0.6705**	**1.3745**	**1.3792**	**1.3824**	**11.285**	**10.786**	**11.29**
Regression R^2	0.9996	0.9995	0.9995	0.996	0.9956	0.9957	0.996	0.99	0.9948
CADR=V(ke - kn)/60 (CFM)	**6.47**	**6.52**	**6.44**	**12.93**	**13.08**	**13.18**	**144.25**	**128.28**	**144.41**

4.3 Performance Test 2

Prototype filter #2 was used for this test. The media packed in the filter was activated carbon BPL 6x16 and 8% KMnO4 impregnated activated alumina with 50:50 by weight. The mixing flow rate of the chamber was changed to 160cfm (5ACH) in this test. The airflow rate from the PAV device was measured with the same method as before (see Table 4-7).

Table 4-7 Airflow rate through the PAV device with Filter #2

Voltage:	12V
Velocity along the filter outlet vent (ft/min)	90
Dimensions of the filter outlet vent (ft^2)	0.013
Air flow rate through the PAV device (cfm)	**1.17**

The toluene and formaldehyde concentration in the chamber during the test is shown in Fig. 4-8. The measurement method was the same as in Test 1. It was noticed that during the pollutant generation period (-1hr to -0.5hr), the concentration at the outlet of the filter (Filter Out) was already lower than ambient, even without operation of the PAV. After the device was turned on, the filter out formaldehyde concentration dropped significantly below the ambient and remained at an almost constant efficiency level during the test period. However, the formaldehyde concentration decay did not strictly follow an exponential trend as expected, although it decayed in general. This was possibly due to the relative humidity change in the chamber (shown in Fig. 4-9). The signal response of the measurement instrument (INNOVA 1312) for formaldehyde is affected by water vapor concentration. For toluene, a sudden drop in concentration at filter out was noticed after the device was turned on, but increased back to the same as the ambient, and then dropped again. Such a “wave” like curve was repeated, and the reason is not clearly understood; possibly it was again the effect of relative humidity. Nevertheless, the concentration in the chamber decayed overall.

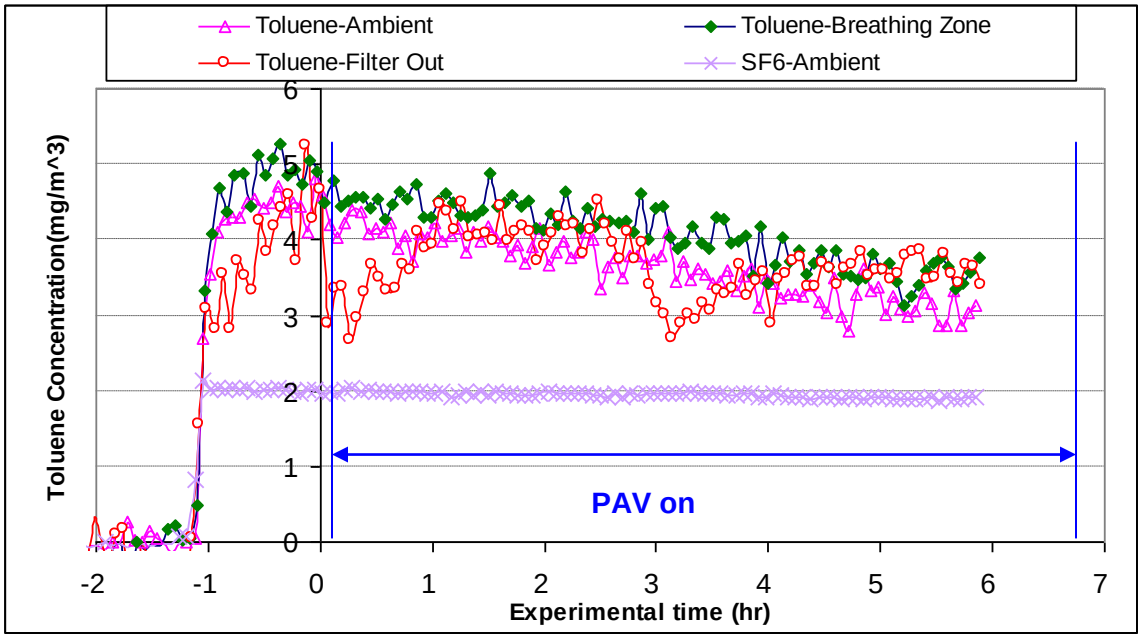

(a) Toluene

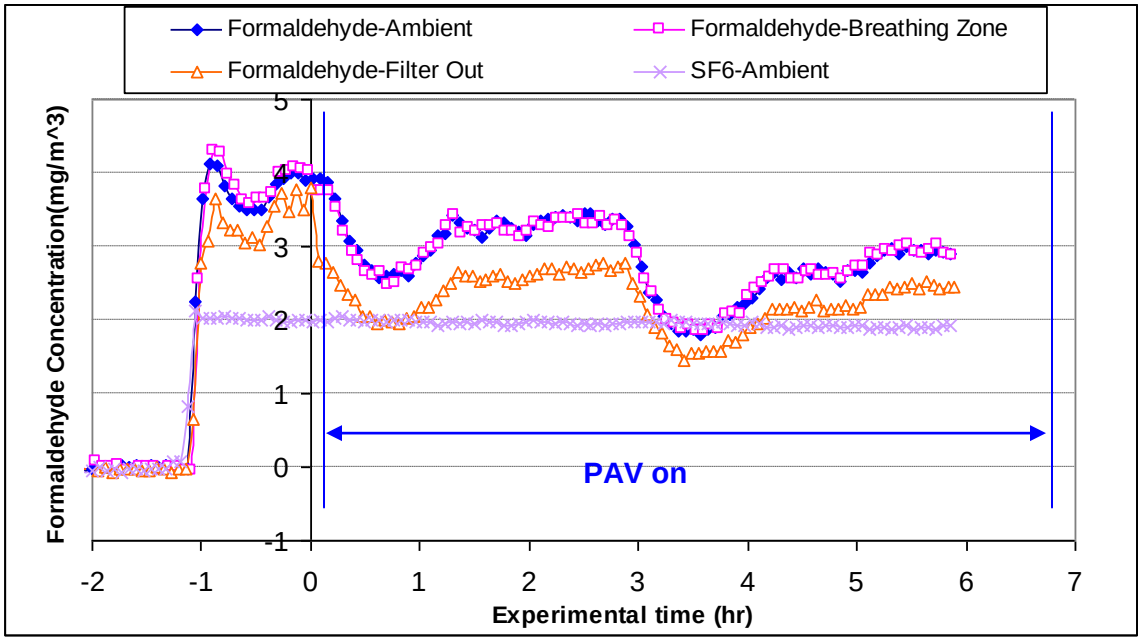

(b) Formaldehyde

Fig. 4-8 Pollutant concentration in performance test 2.

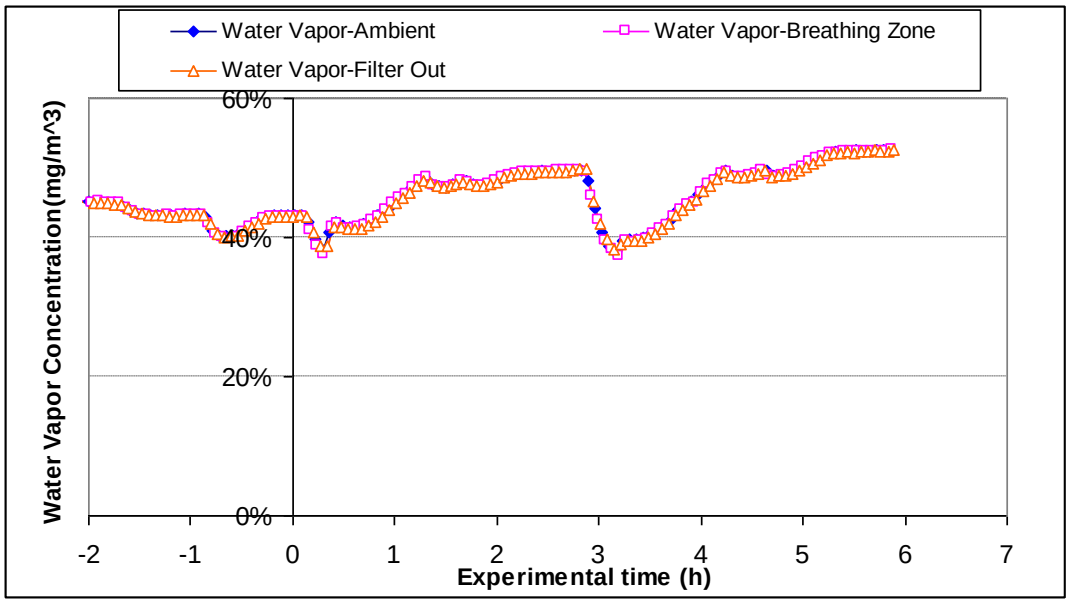

Fig. 4-9 Relative humidity in chamber during performance test 2

The air leakage rate of the chamber is less than 0.01ACH by SF6 monitor, and the natural decay rate of toluene and formaldehyde due to other effects is neglected. The clean air delivery rate (CADR) is calculated based on the concentration decay after the PAV is turned on if possible. The results are summarized in Table 4-8.

Table 4-8 CADR of PAV for gaseous pollutants with prototype filter #2 in performance test 2

	Toluene			Formaldehyde		
	Filter Out	Breathing Zone	Ambient	Filter Out	Breathing Zone	Ambient
Air leakage rate calculated by SF6(ACH)	**0.0096**	**0.0093**	**0.0088**	**0.0096**	**0.0093**	**0.0088**
Regression R^2	0.6745	0.7256	0.652	0.6745	0.7256	0.652
Decay rate calculated after turning on AC k_e (ACH)	**-**	**0.053**	**0.0621**	**-**	**0.0366**	**0.0425**
Regression R^2	-	0.7631	0.8141	-	0.1222	0.1528
CADR=V(k_e -k_n)/60 (CFM)	**-**	**1.40**	**1.71**	-	**0.87**	**1.08**
Single pass efficiency	**-**			**30% ~10%**		

The single pass efficiency of toluene and formaldehyde by the air cleaner is directly calculated by the concentration difference between “Filter Out” and “Ambient”. The single pass efficiency is plotted with time in Fig. 4-10. Due to the poor data for toluene, its efficiency could not properly be obtained for the entire test period, although an initial efficiency of 25-35% was observed. For formaldehyde, it was found that the efficiency was initially about 30% and decreased gradually to about 10-15% after 6 hours under the current challenge concentration level.

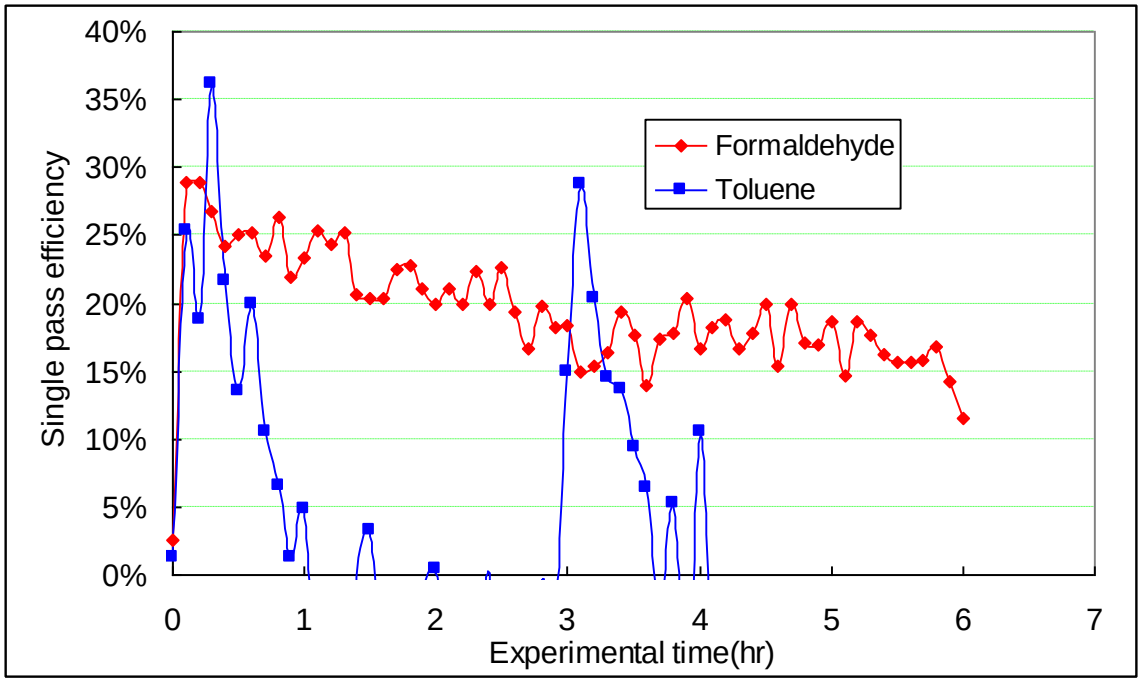

Fig. 4-10 Single pass efficiency for formaldehyde and toluene with Filter #2.

Particle concentration for the three sampling points during the test is shown in Fig. 4-11.

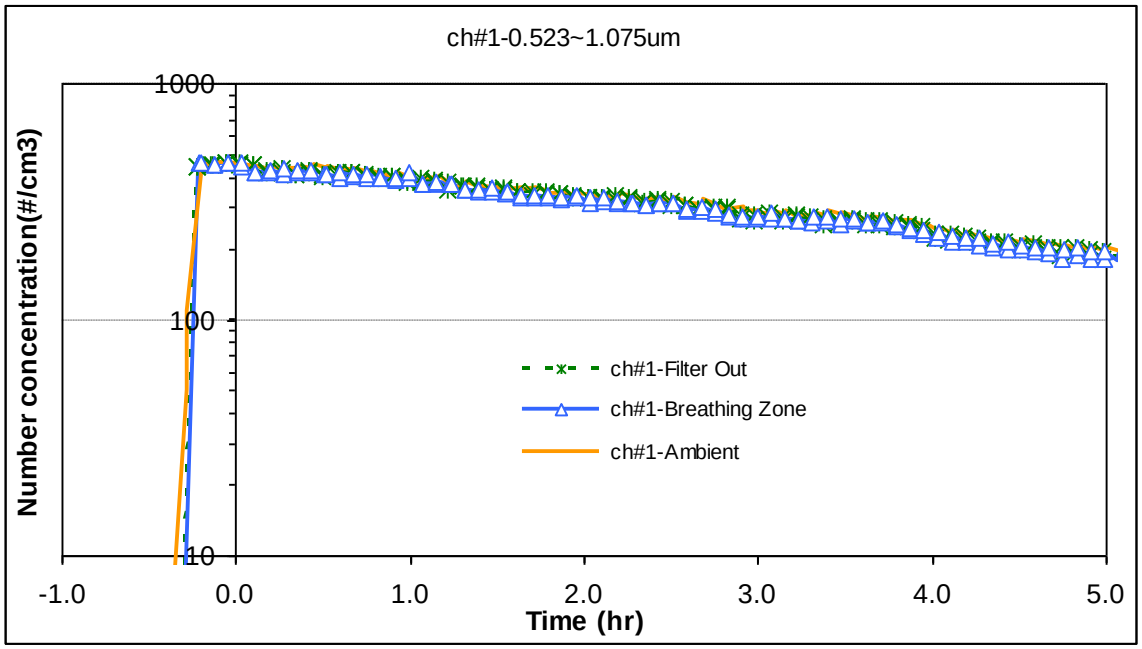

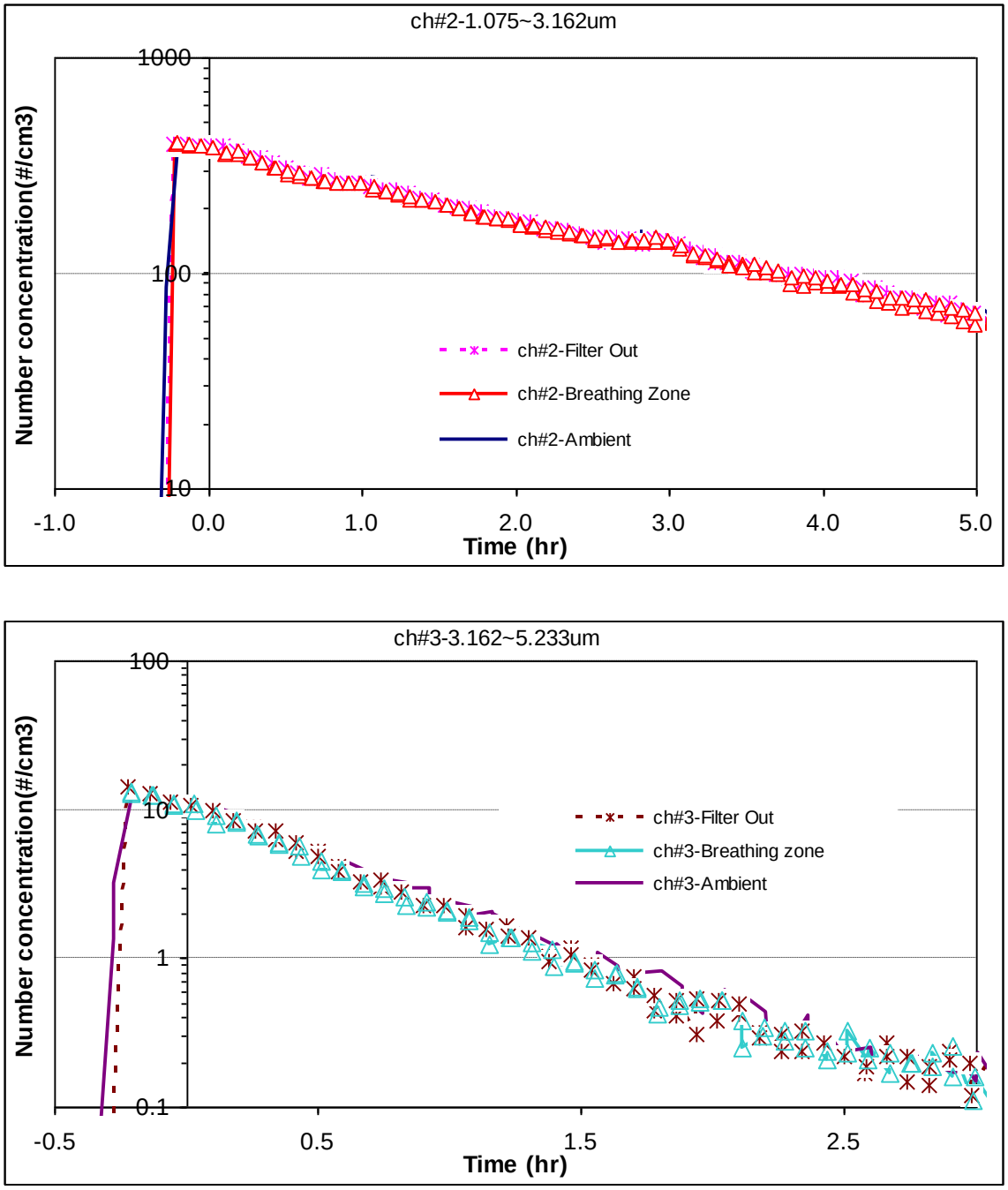

Fig. 4-11 Particle concentration decay in performance test 2.

The particle concentration difference between “Filter Out” and “Ambient” still cannot be observed in this test. This may be due to the sampling tube and location, which cannot collect the air immediately out from the cleaner. However, increased decay rate after the cleaner was turned on could be noticed for particles in all three size channels, which confirmed that the air cleaner was taking effect. The calculated CADR is listed in Table 4-9.

Table 4-9 CADR of PAV for particles with prototype filter #2 in performance test 2

	0.523-1.075um			1.075-3.162um			3.162-5.233um		
	Filter Out	Breathing Zone	Ambient	Filter Out	Breathing Zone	Ambient	Filter Out	Breathing Zone	Ambient
Natural Decay rate kn (ACH)	**0**			**0.1995**			**1.1233**		
Decay rate calculated after turning on AC ke (ACH)	**0.17**	**0.18**	**0.17**	**0.35**	**0.35**	**0.34**	**1.47**	**1.45**	**1.49**
Regression R^2	0.9843	0.9835	0.9872	0.9922	0.9916	0.9965	0.9731	0.9793	0.9885
CADR=V(ke -kn)/60 (CFM)	**5.60**	**5.63**	**5.36**	**4.89**	**4.96**	**4.64**	**10.98**	**10.53**	**11.58**

4.4 Performance Test 3

Another test with a filter packed with pure activated carbon (Filter #5 with BPL 6x16) was conducted. The airflow rate was about 1.1 cfm with filter #5.

Table 4-10 Airflow rate through the PAV device with Filter #5

Voltage:	12V
Velocity along the filter outlet vent (ft/min)	85.6
Dimensions of the filter outlet vent (ft^2)	0.013
Air flow rate through the PAV device (cfm)	**1.1**

The toluene and formaldehyde concentration is shown in Fig. 4-12. Again, the concentration of both toluene and formaldehyde at “Filter Out” is lower than “Ambient” during the pollutant generation period with PAV operation. The single-pass efficiency is shown for both toluene and formaldehyde after the device is turned on. The formaldehyde concentrations decayed in general but still in a wave-like shape. The chamber relative humidity is shown in Fig. 4-13, and the PAV CADR calculations are given in Table 4-11.

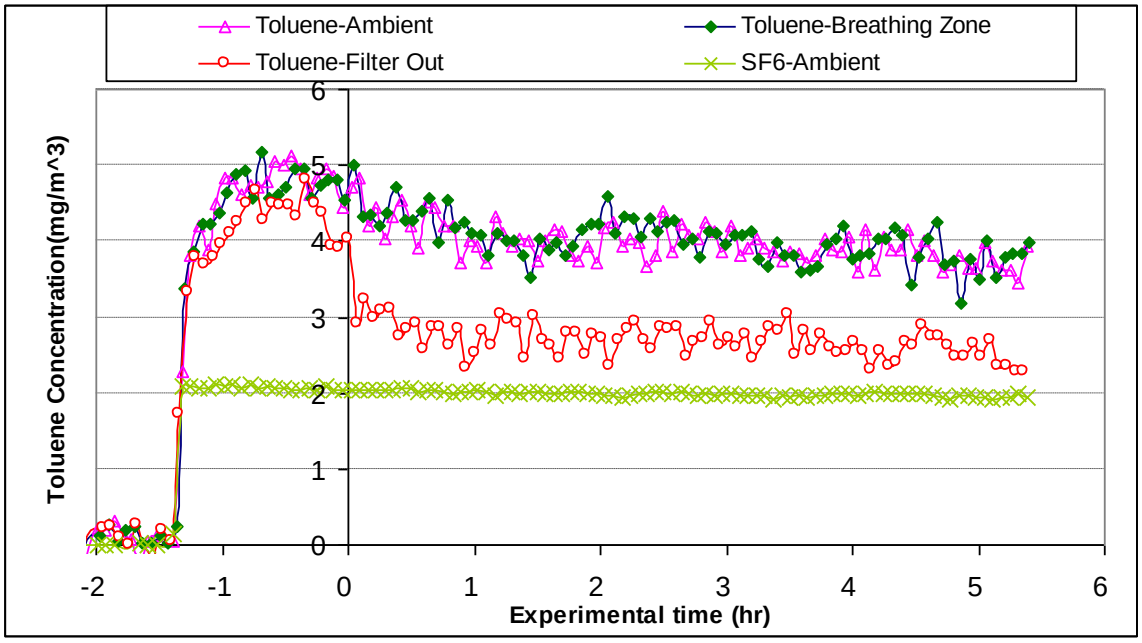

(a) toluene

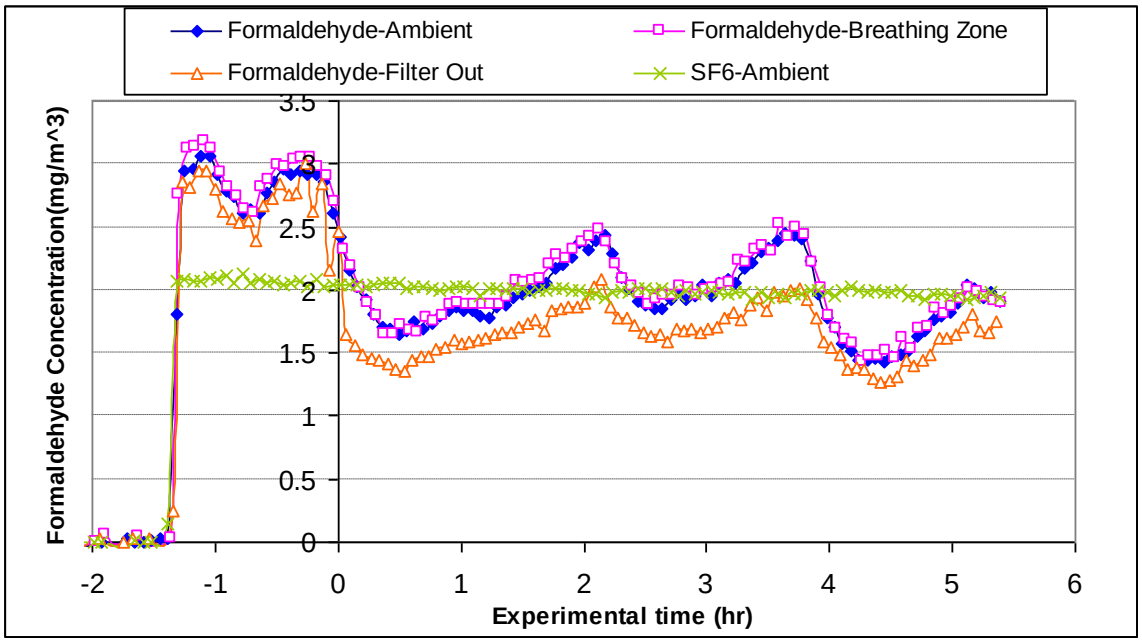

(b) formaldehyde

Fig. 4-12 Pollutant concentrations in performance test 3.

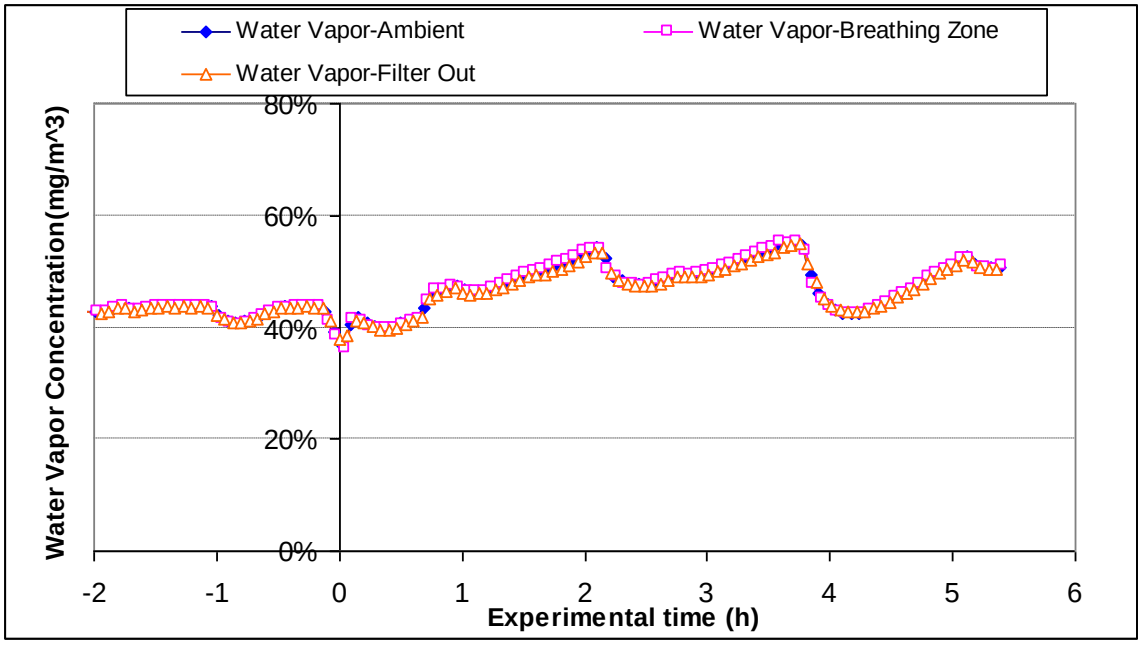

Fig. 4-13 Relative humidity in the chamber during test 3.

Table 4-11 CADR of PAV for gaseous pollutants with prototype filter #5 in performance test 3

	Toluene			Formaldehyde		
	Filter Out	Breathing Zone	Ambient	Filter Out	Breathing Zone	Ambient
Air leakage rate calculated by SF6(ACH)	**0.008**	**0.0076**	**0.0074**	**0.008**	**0.0076**	**0.0074**
Regression R^2	0.5362	0.5077	0.5343	0.5362	0.5077	0.5343
Decay rate calculated after turning on AC k_e (ACH)	**0.0266**	**0.0282**	**0.025**	**-**	**-**	**-**
Regression R^2	0.2779	0.3597	0.3679	**-**	**-**	**-**
CADR=V(k_e -k_n)/60 (CFM)	**0.60**	**0.66**	**0.56**	-	**-**	**-**
Single pass efficiency	**32.2%**			**14.3%**		

The single pass efficiency for toluene and formaldehyde during this test was directly calculated based on the concentration difference between ”Filter Out” and “Ambient”, and is plotted in Fig. 4-14. The filtration efficiency for toluene remained almost constant during the test period at about 30%. The filtration efficiency for formaldehyde was initially at 25%, and decreased to about 10% at the end of the test, with an average of 14.3%.

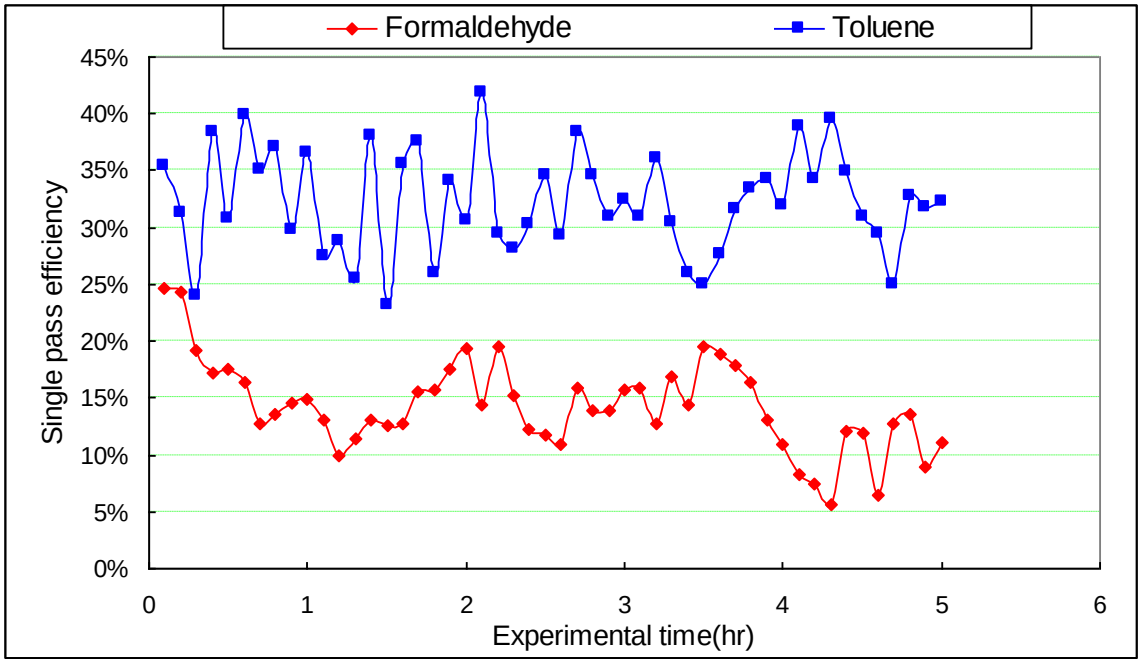

Fig. 4-14 Single pass efficiency for formaldehyde and toluene with Filter #5.

The particle concentration in this test is shown in Fig. 4-15. After modification of the sampling port, the concentration difference between Filter Out and Ambient could be noticed. The CADR calculation is listed in Table 4-12.

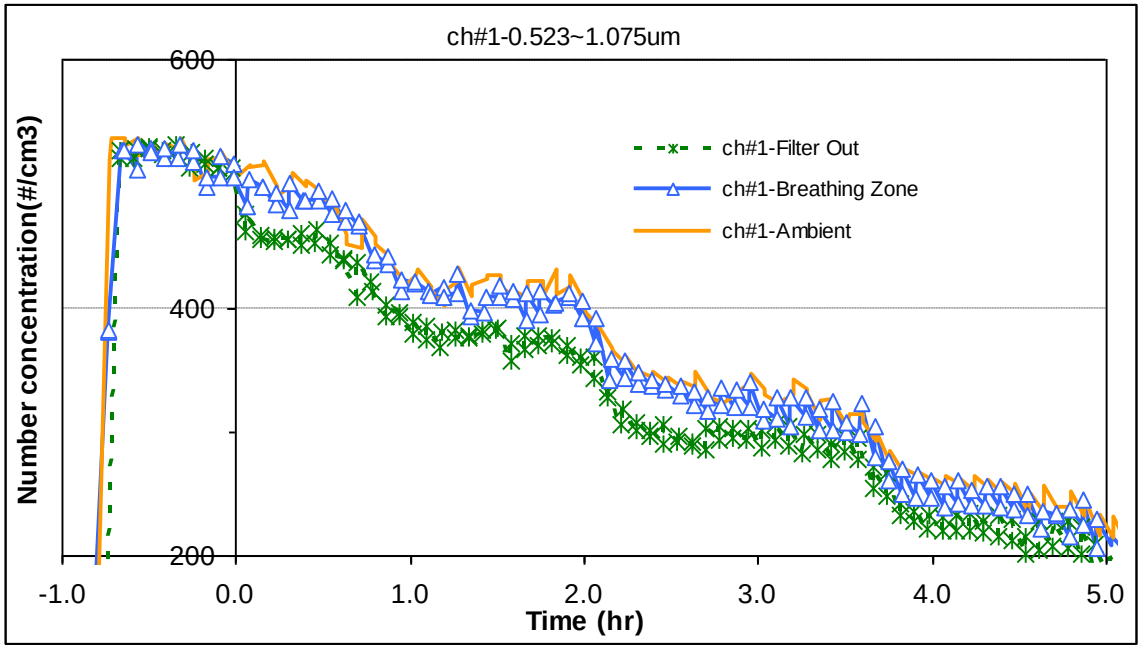

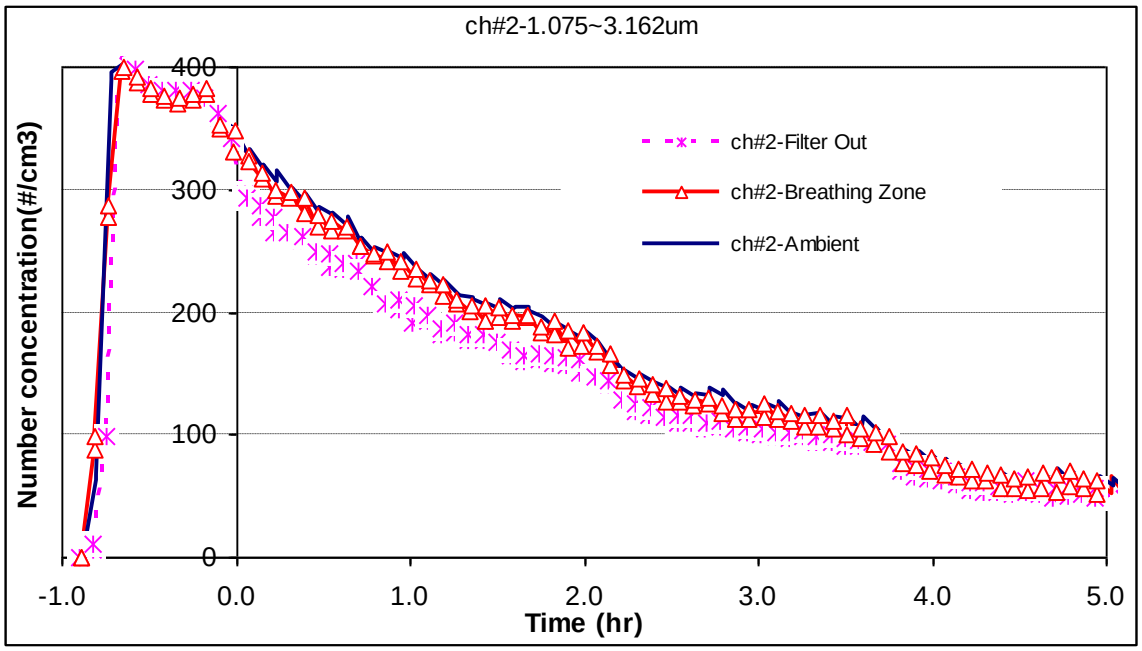

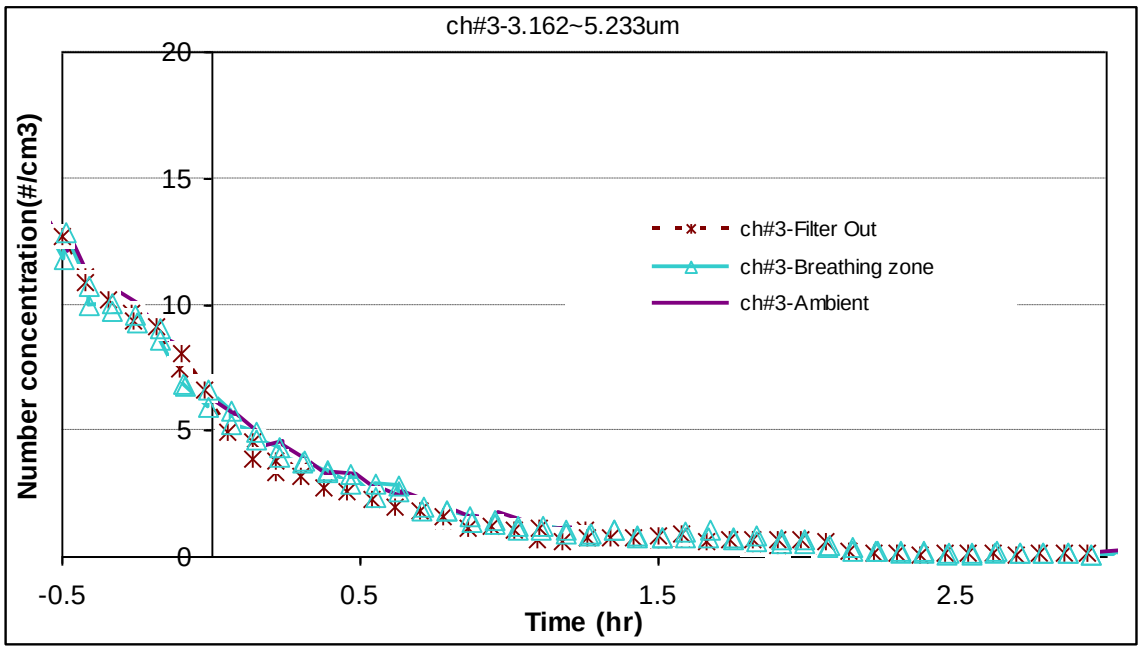

Fig. 4-15 Particle concentration decay in performance test 3.

Table 4-12 CADR of PAV for particles with prototype filter #5 in performance test 3

	0.523-1.075um			1.075-3.162um			3.162-5.233um		
	Filter Out	Breathing Zone	Ambient	Filter Out	Breathing Zone	Ambient	Filter Out	Breathing Zone	Ambient
Decay rate calculated before turning on AC ke (ACH)		**0.06**			**0.21**			**1.27**	
Decay rate calculated after turning on AC ke (ACH)	**0.18**	**0.17**	**0.17**	**0.36**	**0.36**	**0.35**	**1.65**	**1.57**	**1.53**
Regression R^2	0.9652	0.9702	0.972	0.9835	0.9817	0.9878	0.9708	0.976	0.9752
CADR=V(ke -kn)/60 (CFM)	**3.58**	**3.48**	**3.32**	**4.76**	**4.85**	**4.57**	**11.99**	**9.69**	**8.13**
Single pass efficiency		**10.5%**			**14.8%**			**-**	

The single pass efficiency for particles in the range of 0.523~1.075μm and 1.075~3.162μm is calculated and plotted in Fig. 4-16. The efficiency for particles of 3.162~5.233μm was unsteady and is not plotted here.

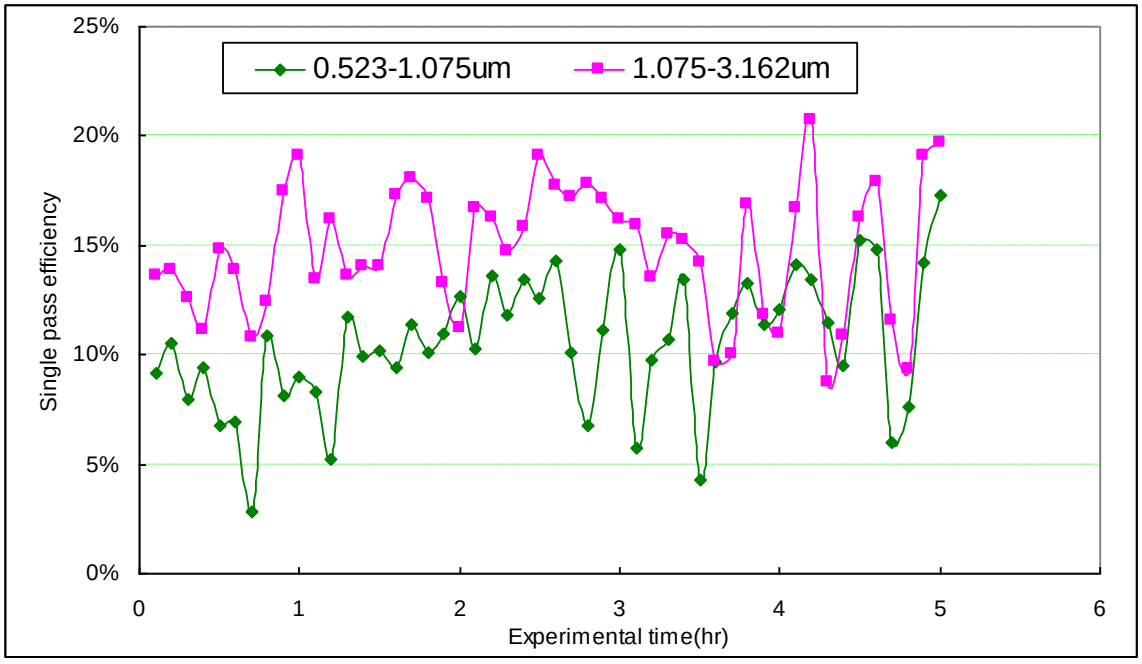

Fig. 4-16 Single pass efficiency for particles with Filter #5.

4.5 Performance Test 4 – Results Given in Summary Table

4.6 Performance Test 5

This test was conducted with prototype filter #8 installed. The packed media was activated carbon BPL 6x16 and 8% KMnO4 impregnated activated alumina with 50:50 by weight, with packing density about 1980g/m^2. The DC power supply was set to 15.5V in this test, which resulted in an airflow rate of 1.5 cfm.

Table 4-13 Air flow rate through the PAV in test 5

Voltage:	15.5V
Velocity along the filter outlet vent (ft/min)	115
Dimensions of the filter outlet vent (ft^2)	0.013
Air flow rate through the PAV device (cfm)	**1.5**

Fig. 4-17 shows the gas phase pollutant decay during the test. The concentration of both toluene and formaldehyde was reduced after going through the PAV device. The CADR and single pass efficiency was calculated. The fluctuation of formaldehyde was again due to the relative humidity change in the test chamber (Fig. 4-18), but generally it exponentially decayed. The CADR calculation is listed in Table 4-14.

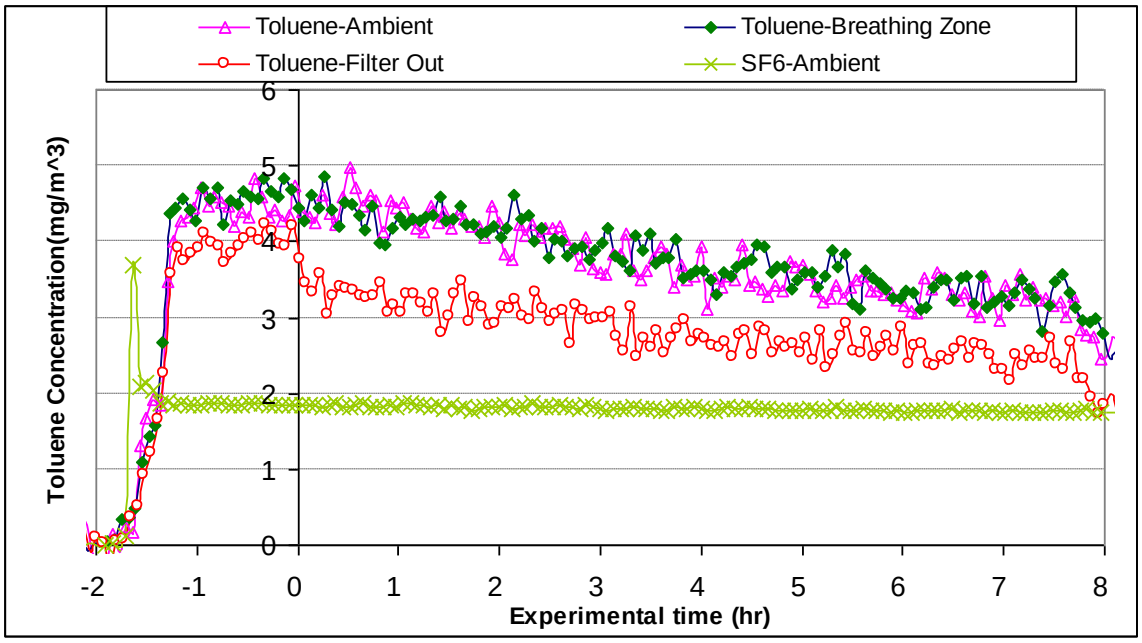

(a) toluene

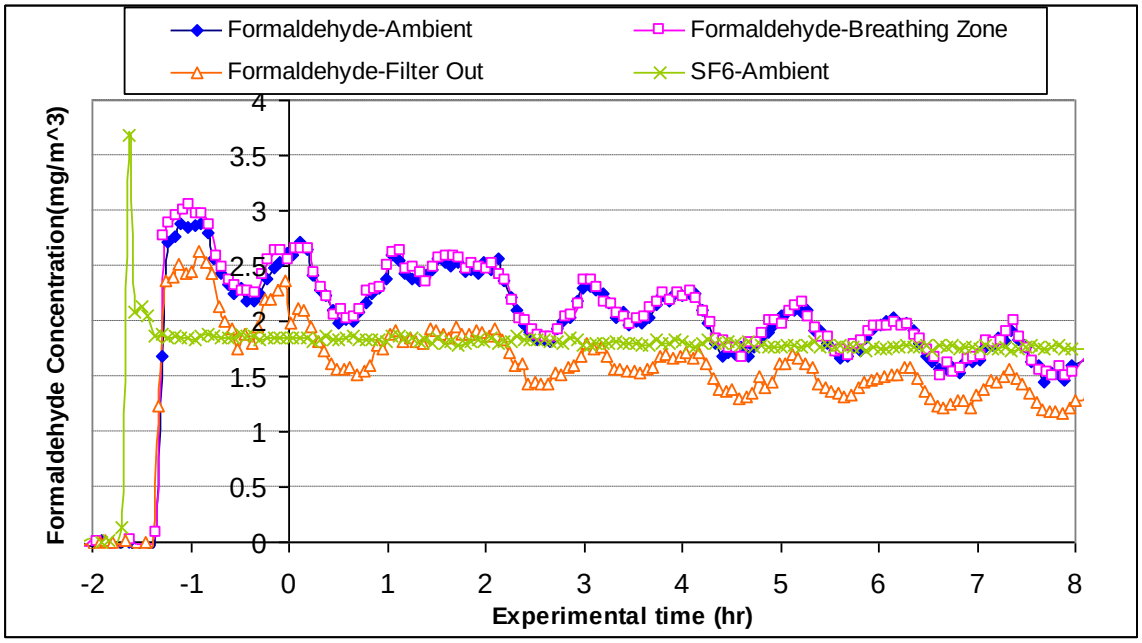

(b) formaldehyde

Fig. 4-17 Pollutant concentrations in performance test 5.

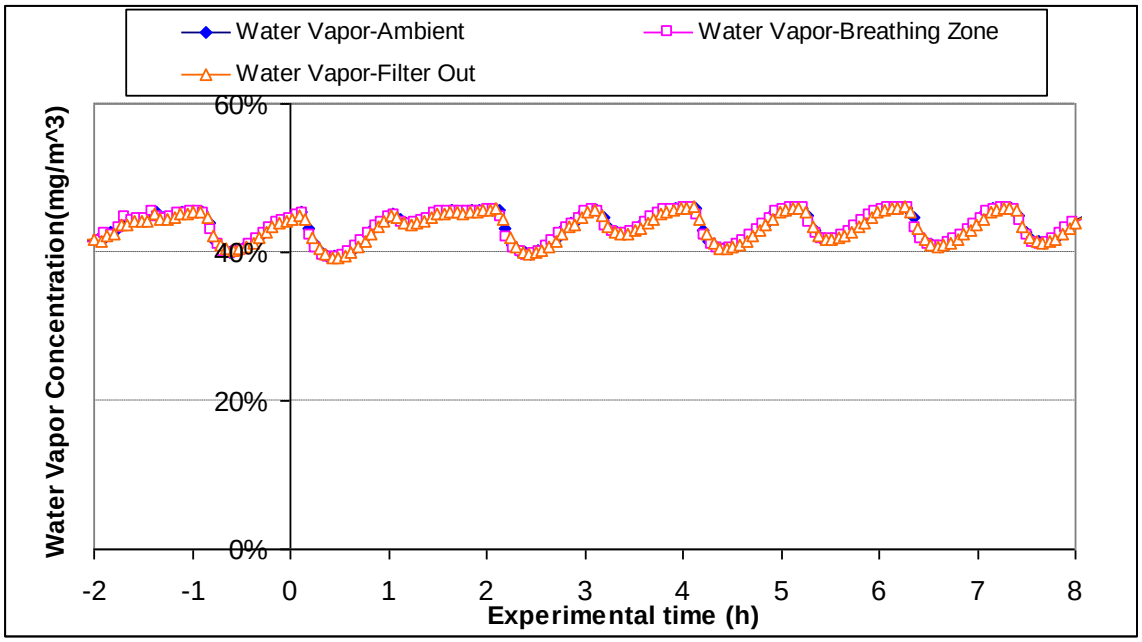

Fig. 4-18 Relative humidity in performance test 5.

Table 4-14 CADR for toluene and formaldehyde with prototype filter #8 in performance test 5

	Toluene			Formaldehyde		
	Filter Out	Breathing Zone	Ambient	Filter Out	Breathing Zone	Ambient
Air leakage rate calculated by SF6(ACH)	**0.0064**	**0.0064**	**0.0063**	**0.0064**	**0.0064**	**0.0063**
Regression R^2	0.8631	0.8538	0.8625	0.8631	0.8538	0.8625
Decay rate calculated after turning on AC k_e (ACH)	**0.0733**	**0.0693**	**0.0666**	**0.041**	**0.048**	**0.0486**
Regression R^2	0.8488	0.9154	0.9137	0.7799	0.8373	0.831
CADR=V(k_e -k_n)/60 (CFM)	**2.14**	**2.01**	**1.93**	**1.11**	**1.33**	**1.35**
Single pass efficiency	**24.74%**			**22.32%**		

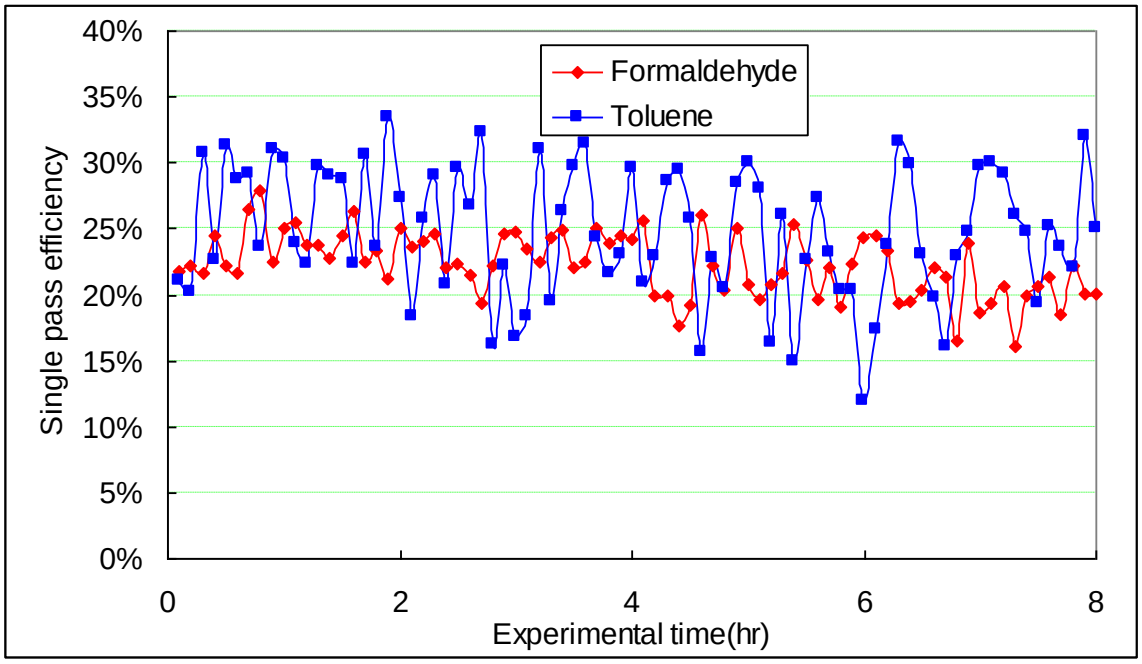

Fig. 4-19 Single pass efficiency for toluene and formaldehyde in performance test 5.

For particle concentration measurements, an optical particle concentration measurement instrument (Lasair 1003) was used instead of APS 3321. The sampling flow rate of the Lasair 1003 is 0.0283L/min (0.001cfm), which is much smaller than the airflow rate from the PAV device. However, the measurement of particle concentration was not very successful in this test since: 1) Due to the small sampling flow rate and the multi-point sampling valve system, particles could only be measured up to 0.5um -- very few particles larger than 0.5um were detected; 2) The measured concentration at all three sampling points was not very steady -- there were unexpected peaks; and 3) The ambient concentration was generally larger than “Filter Out” and “Breathing Zone” for particles in the range of 0.1~0.3um, but still not significantly. Results are shown in Fig. 4-20.

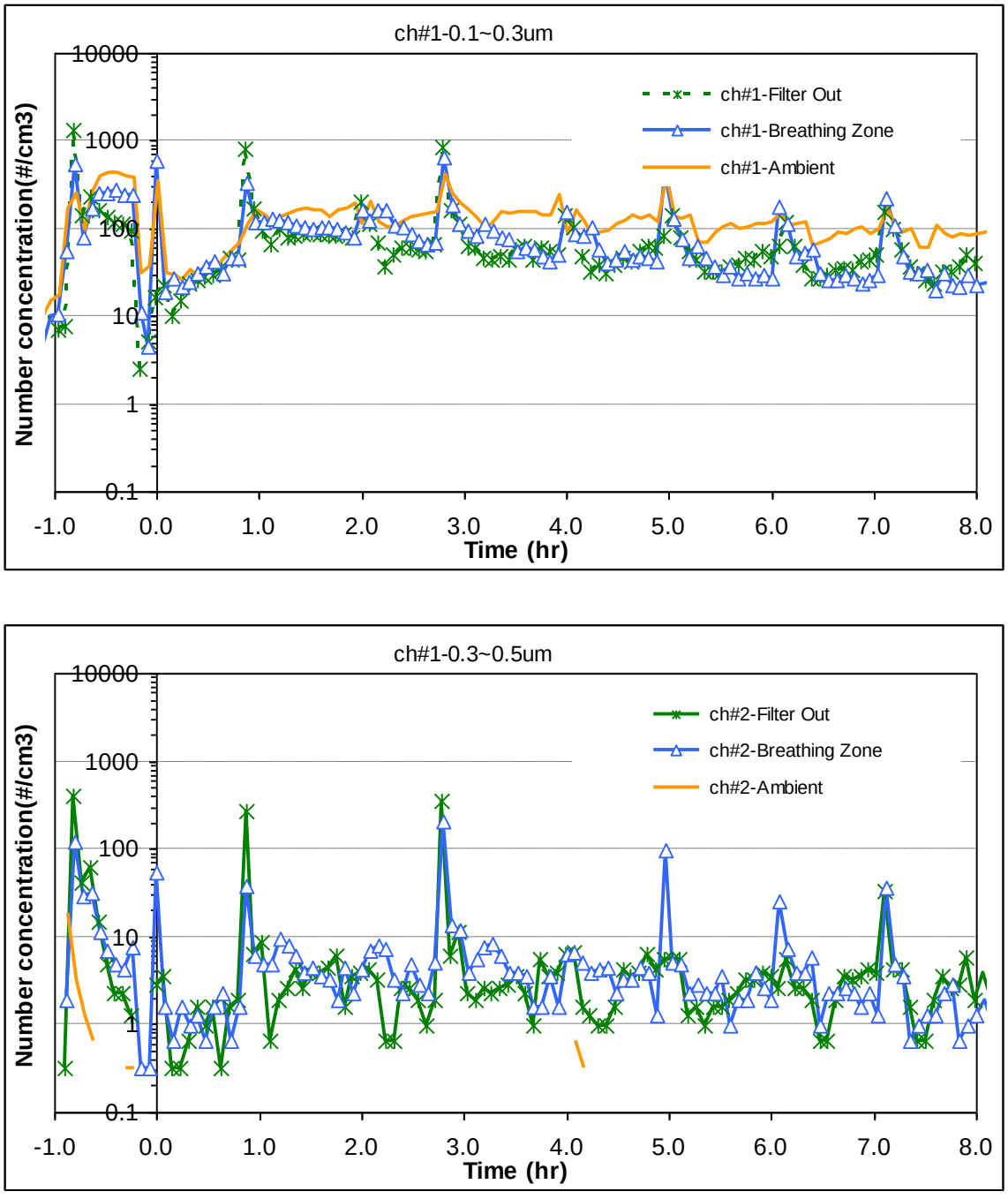

Fig. 4-20 Particle concentrations in test 5.

Table 4-15 Summary of prototype filters

No.	Particle filtration media	Layer number	VOC filtration media	Filter size	Weight of AC (g)	Density (g/m2)
#1	MERV7	Double	BPL4x6	6.125" x 3.75"	18.9	1278
#2	MERV7	Double	BPL6x16+CHS 1/16" (5:5)	6" x 4.25"	16.7	1017
#3	MERV11+cloth mesh	Single	BPL 4x10 +PSP 1/8" (5:5)	6.5" x 4.5"	22.6	1372
#4	MERV8	Double	BPL 6x16	6.5" x 4.5"	19.5	1033
#5	MERV7	Double	BPL 6x16	7" x 5"	43.8	1940
#6	MERV7	Double	BPL6x16+CHS 1/16" (5:5)	7.5" x 4.75"	45.6	1982
#7	MERV8	Double	BPL 4x10 +PSP 1/8" (5:5)	7.25" x 5"	41.9	1793
#8	MERV11	Double	BPL6x16+CHS 1/16" (5:5)	7" x 5"	44.7	1981

Table 4-16 Summary of tests

Test ID	Filter	Media	Power (V)	Air flow rate of PAV (cfm)	Chamber recirculation flow rate (cfm)	Note	Date
R #1	N/A	N/A	N/A	N/A	800	Get the natural decay rate for particles with 800cfm	July-09-2008
R #2	N/A	N/A	N/A	N/A	800	Get the natural decay rate for toluene with 800cfm	July-23-2008
R #3	N/A	N/A	N/A	N/A	160	Get the natural decay rate for particles with 160cfm	Aug-06-2008
T #1	#4	MERV8 + BPL 6x16	12	1.88	800	CADR calculated for toluene, formaldehyde failed; no difference between "filter out" and "ambient" observed for particles,but CADR calculated for particles	July-18-2008
T #2	#2	MERV7 + BPL6x16+ CHS 1/16" (5:5)	12	1.17	160	Formaldehyde good, CADR and single pass efficiency calculated; toluene bad; no difference between "filter out" and "ambient" observed for particles, but CADR calculated	July-30-2008
T #3	#5	MERV7 + BPL 6x16	12	1.11	160	both toluene and formaldehyde good! Single pass efficiency calculated for both, CADR calculated for toluene; sampling ports for particles are modified, difference observed for different sampling point, CADR and single pass efficiency calculated for particles	Aug-01-2008
T #4	#6	MERV7 + BPL6x16+ CHS 1/16" (5:5)	12	0.97	160	The efficiency decay quickly for toluene and formaldehyde. CADR can not be calculated. Only single pass efficiency obtained for VOCs and particles	Aug-04-2008
T #5	#8	MERV11 + BPL6x16+ CHS 1/16" (5:5)	15.5	1.5	160	both toluene and formaldehyde good! CADR and single pass efficiency calculated for both; Lasair 1003 was used for particle sampling, but results bad	Aug-11-2008

4.7 Performance Test 6

After several trials, another particle-only test was conducted without the generation of gaseous pollutants. The filter used was the same as in test 5: filter #8. The particle filtration media was double layer MERV11. Figure 4-21 shows the particle concentration at the sampling points for “Filter Out”, “Breathing Zone”, and “Ambient”. Particles are shown in four groups: 0.1~0.3μm, 0.3~0.4μm, 0.4~0.5μm, and 0.5~2.0μm.

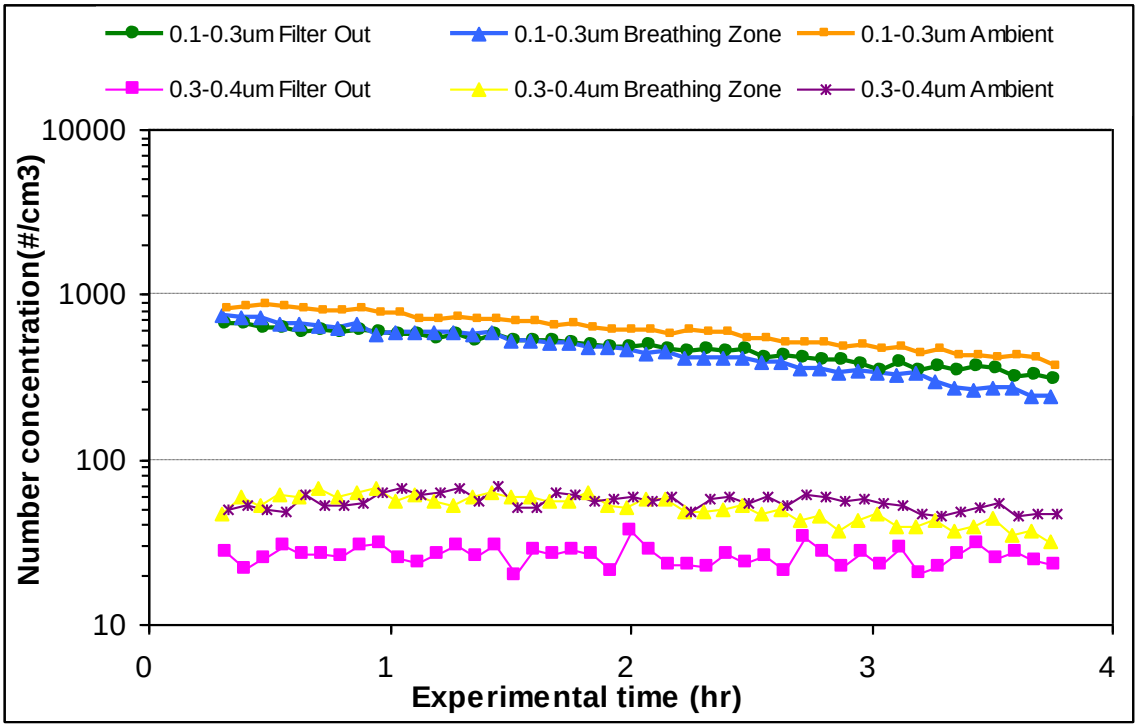

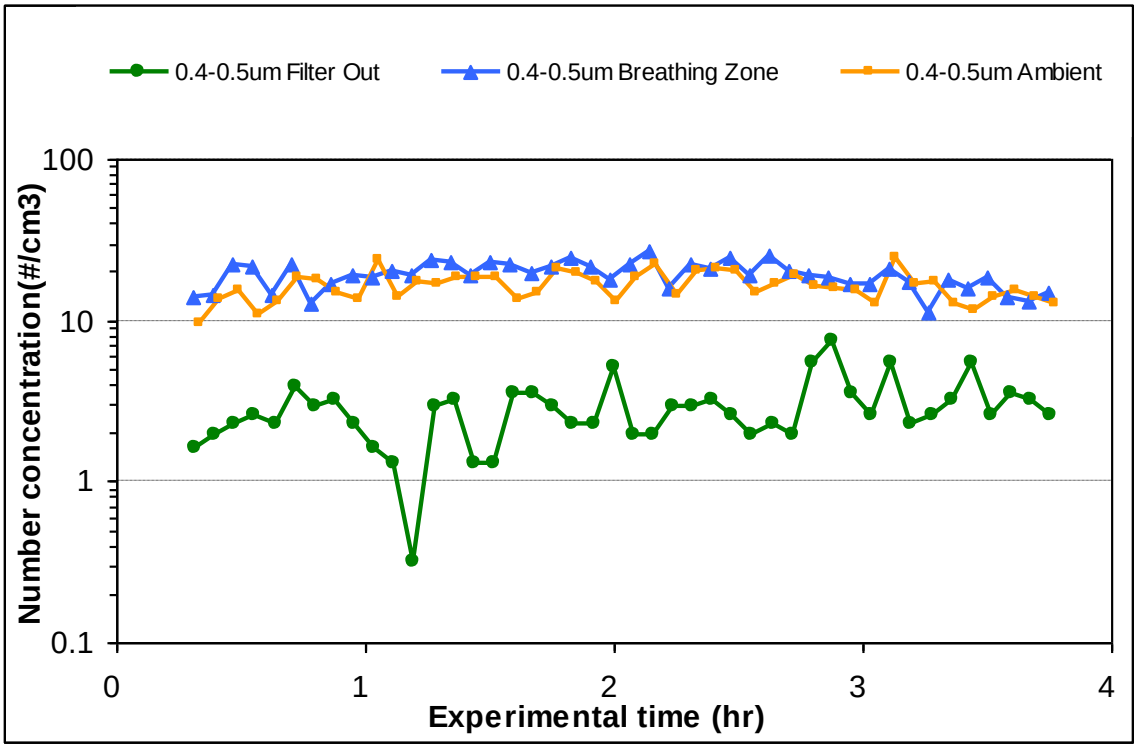

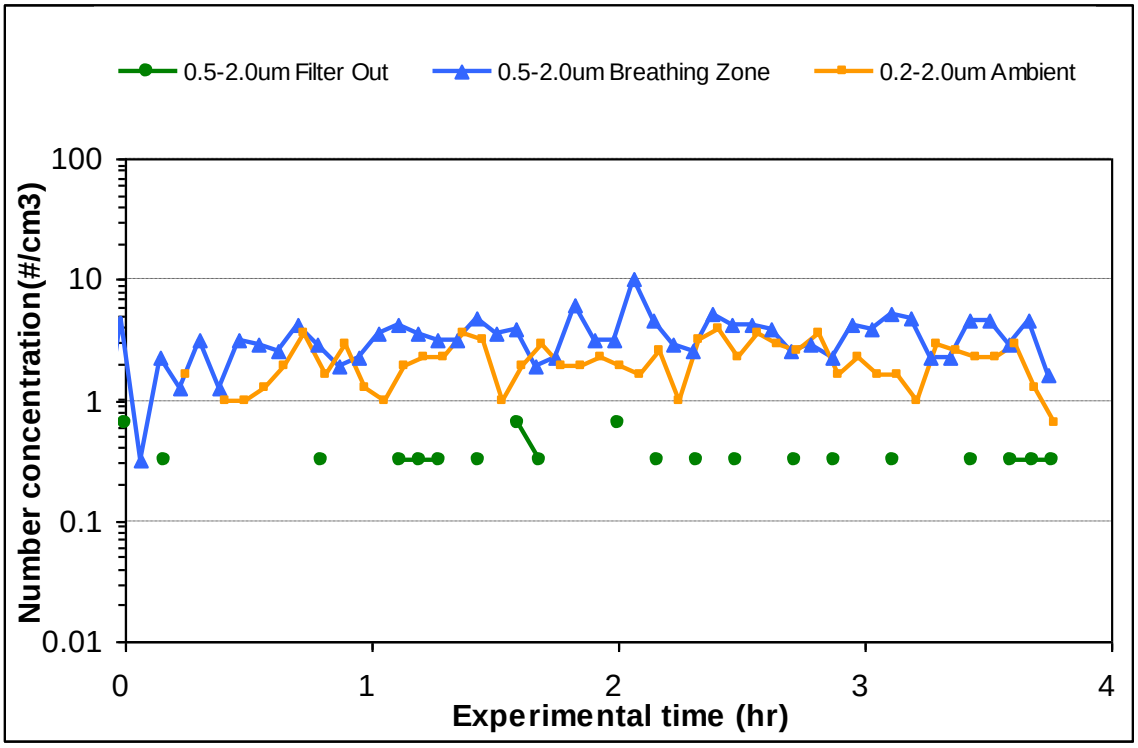

Fig. 4-21 Particle concentrations in test 6.

It was clearly observed that the “Filter Out” concentration was lower than that of “Breathing Zone” and “Ambient”, which were almost at the same level. The single pass efficiency of each group of particles was calculated relative to the ambient concentration, and is shown in Fig. 4-22. A summary of the results is given in Table 4-17.

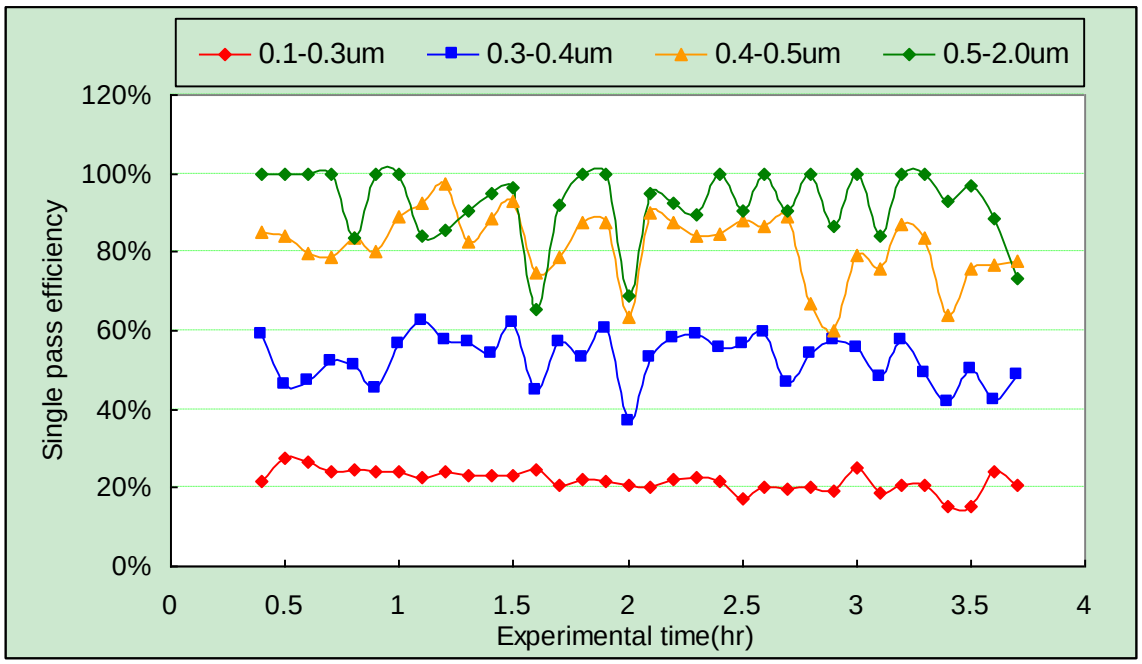

Fig. 4-22 Single pass efficiency of particles in test 6.

Table 4-17 Single pass efficiency for particles with prototype filter #8 in performance test 6

	0.1~0.3μm	0.3~0.4μm	0.4~0.5μm	0.5~2.0μm
Single pass efficiency	21.8%	52.8%	81.8%	92.4%

4.8 Performance Test with Thermal Manikin

Testing was performed with the PAV device mounted to a desk in front of a thermal manikin. The focus here was on particle removal. The configuration is shown in Fig. 4-23. Data was collected with the PAV device turned on both directly at the outlet of the device, as well as with a sampling port located near the mouth. The direct (at PAV outlet) and exposure (at mouth) efficiencies were calculated by comparing the particle density values at these locations with the ambient. The data is plotted in Fig. 4-24. As expected, the efficiency dropped as the air traveled from the PAV outlet up to the breathing zone due to mixing. However, for particles greater than 0.3 μm, the data showed that the exposure rate was consistently reduced by 40-50%. Although not quantified in this experiment, from the earlier results, it is expected that the exposure rate would be even lower for larger particles (since the filter removal efficiency was much higher as the particle size increased). In addition, if one were to use a slightly better filter, the exposure rate should also improve, particularly at the smaller sizes shown here.

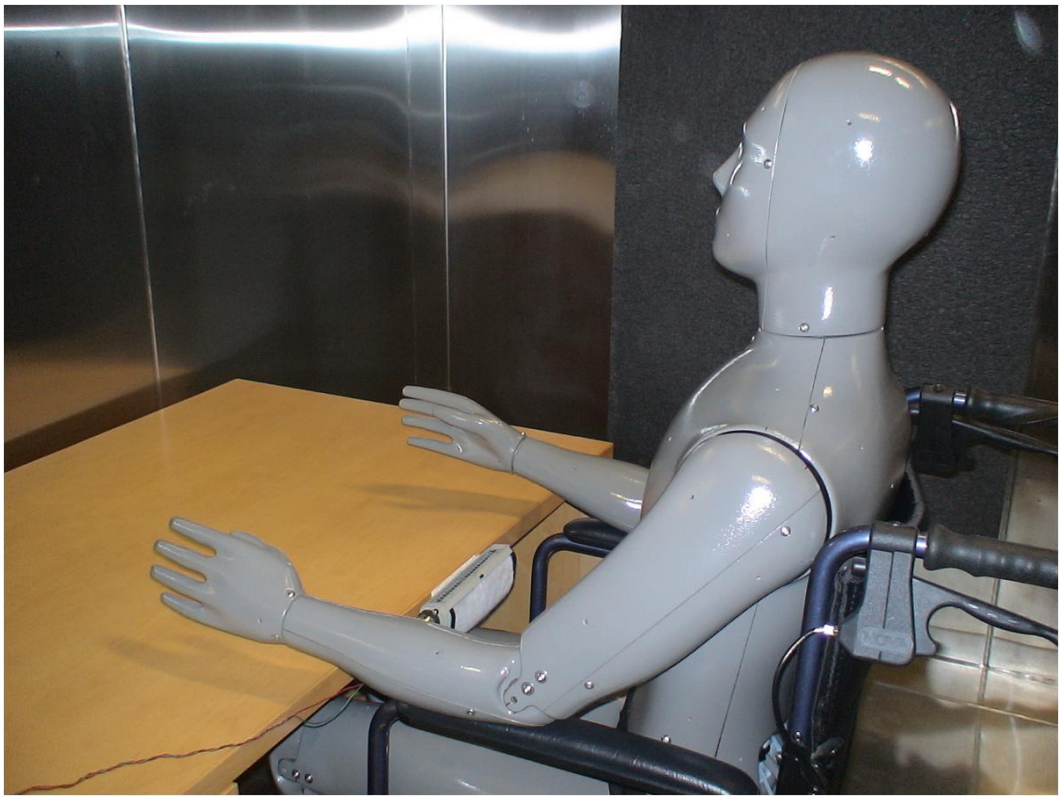

Fig. 4-23 PAV unit mounted on desk in front of thermal manikin.

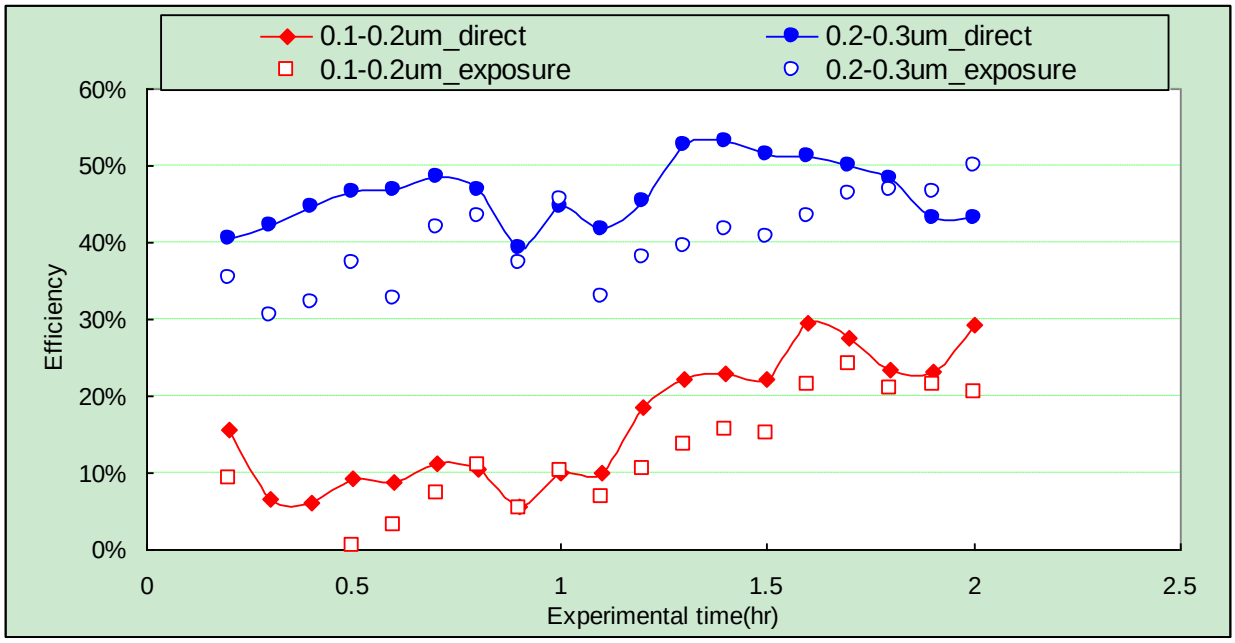

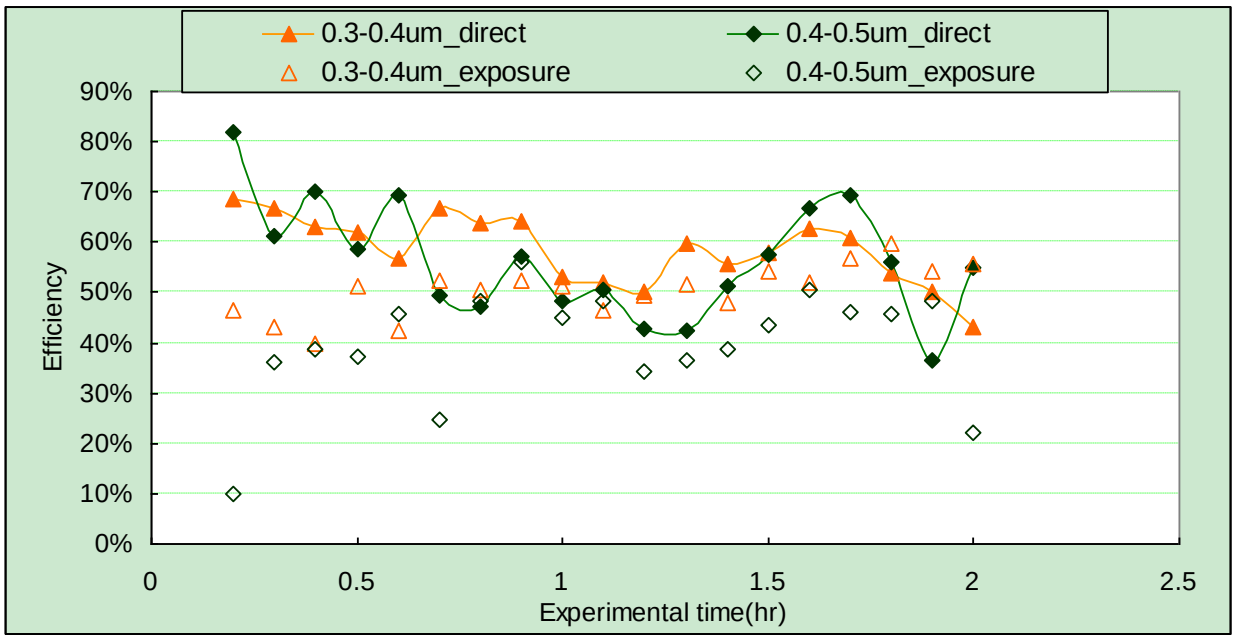

Fig. 4-24 Particle removal efficiency at PAV outlet (direct) and at breathing zone (exposure).

SECTION 5

Prototype Refinement

In tandem with the prototype refinement, additional CFD simulations were completed on the PAV prototype design itself, as well as its interaction with the human thermal plume. These new simulations were not only to provide valuable data to help with design, but also invaluable marketing tools in the form of visual representation of the air purifier system for websites, fliers, conference presentations, etc. For this, a commercial license for an accurate human CAD model was purchased from Bodyworks. The new CAD model of the simulated geometry is shown in Fig. 5-1, and includes the new human model sitting at a desk, working on a laptop computer. Figure 5-2 shows the CFD surface mesh, as well as the streamlines entering the breathing zone. As was shown previously, the breathed air originates from below the torso of the individual, and the majority of this air comes from the floor.

Figure 5-3 shows a CAD model of the PAV-4 prototype. Some of the key features are the wrap-around filter geometry held in an easily removable filter frame, the inclusion of buttons and LEDs for control and response from the unit, and connections for both USB and wall power adapters. Figure 5-4 depicts the unit mounted on the front of a desk, ready for use. Figure 5-5 shows a closeup of this installation, and Fig. 5-6 shows the entire CAD model of the individual working at a desk with the PAV device installed.

Fig. 5-1 CAD model for CFD simulations.

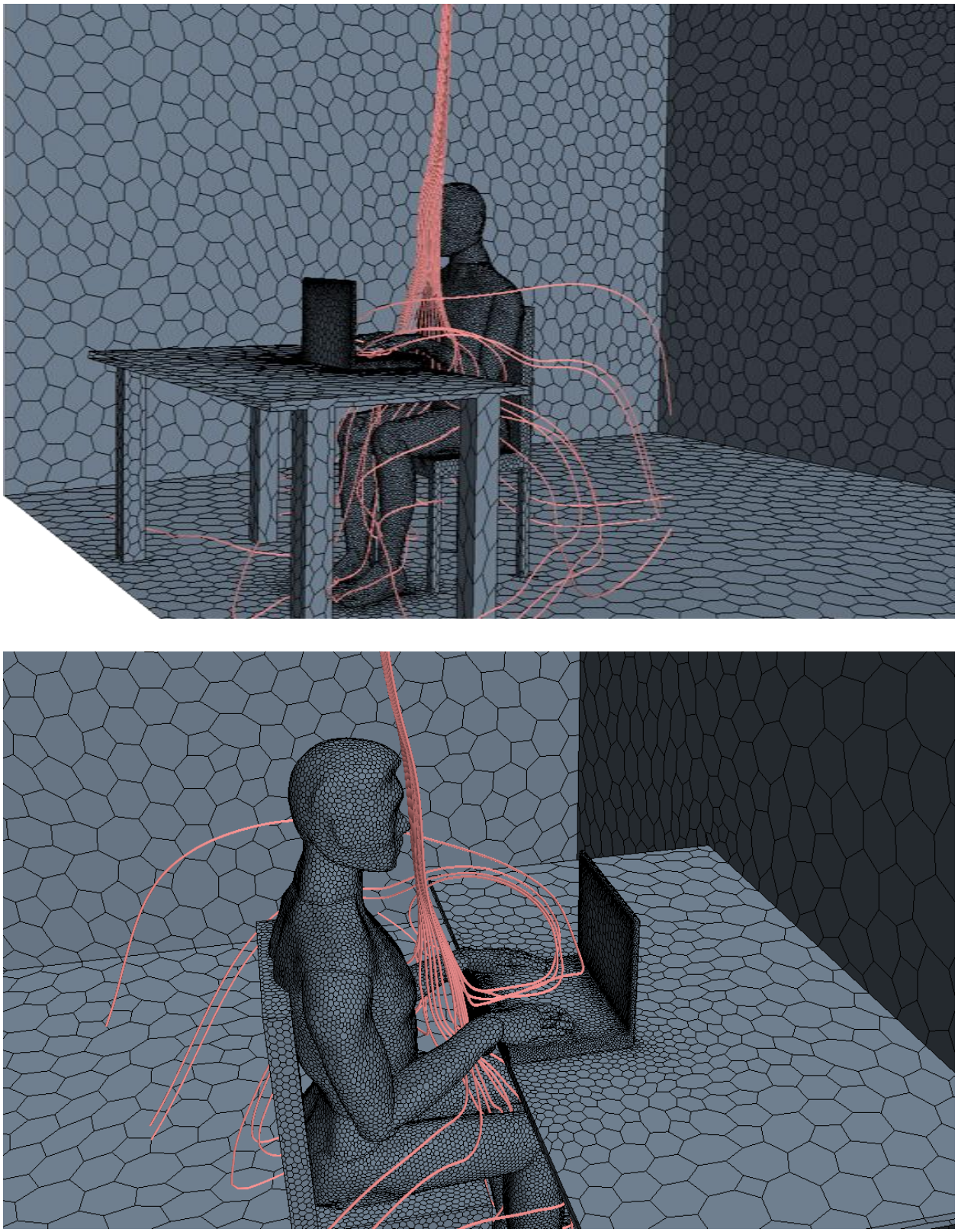

Fig. 5-2 Surface mesh and streamlines entering breathing zone.

Fig. 5-3 CAD model of PAV-4 prototype.

Fig. 5-4 CAD model of PAV-4 prototype mounted on the front of a desk.

Fig. 5-5 Closeup of prototype mounted on the front of a desk.

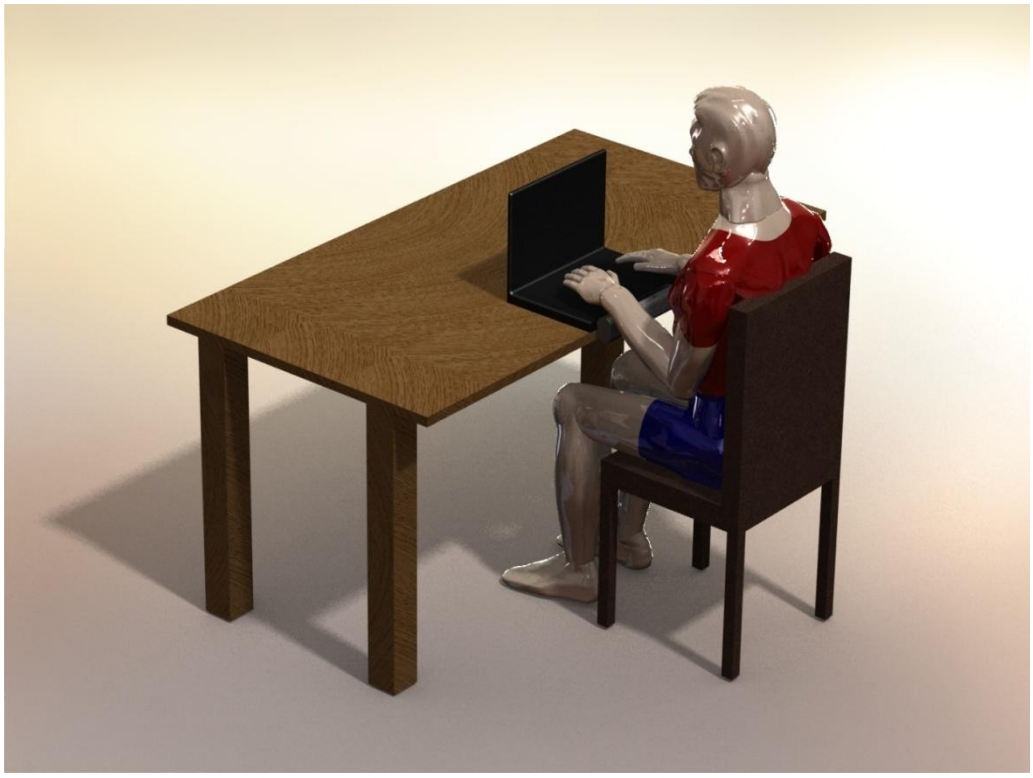

Fig. 5-6 CAD geometry of individual working at desk with PAV device.

As with earlier cases, the CFD simulations were run with the PAV device turned on. In this case the outlet velocity was set to 0.75 m/s. The model still retains the “black-box” type of PAV inlet and outlet boundary conditions, which allow for a steady simulation to be run. Figure 5-7 shows the results for this case. Here, the red streamlines show the path taken by the air entering the PAV device, and the blue streamlines represent the air leaving. For this particular setup, a large portion of the air breathed by the individual comes directly from the PAV unit, and hence is filtered.

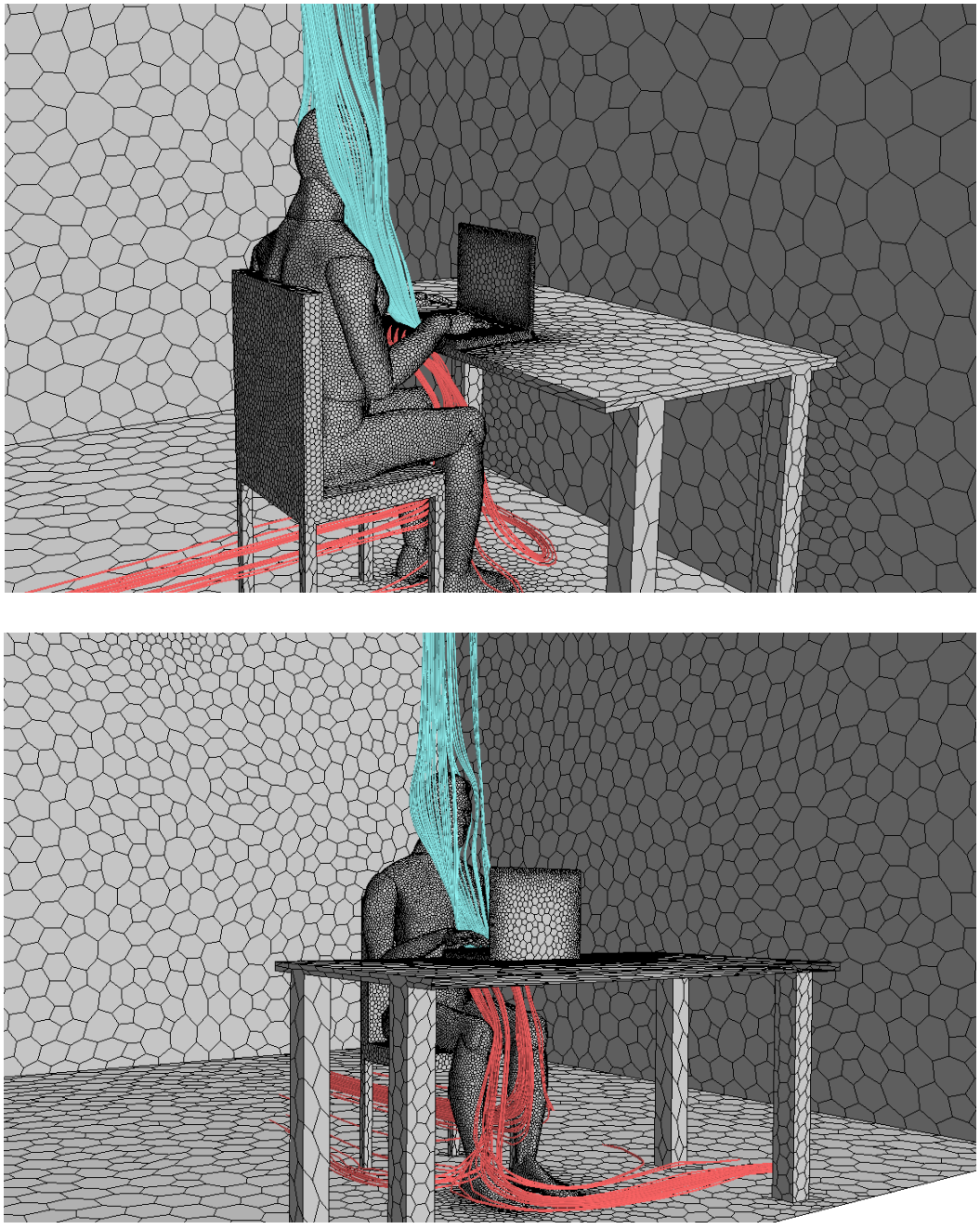

Fig. 5-7 Streamlines entering and leaving PAV device (PAV outlet velocity = 0.75 m/s).

Figure 5-8 shows the completed PAV-4 prototype. The components were fabricated using an ABS-like rapid prototyping resin by DPT-FAST. They were then painted to give a “production-quality” look. The filter was custom made by Propulsive Wing from two layers of MERV particle filter material, with activated carbon pellets, purchased from Calgon Carbon Corp., sandwiched in between. The unique aspect of this filter is that a Nomex honeycomb core was used to create small “wells” in order to support the activated carbon. Fabrication was not only easy, but relatively quick as well, demonstrating that the possibility exists for creating such filters on a production scale. A closeup of the filter and filter frame alone is shown in Fig. 5-9.

Fig. 5-8 PAV-4 prototype.

Fig. 5-9 Filter and filter frame for PAV-4 prototype.

The complete PAV-4 system is shown in Fig. 5-10. Here, the circuit board and battery were kept outside the PAV unit for demonstration purposes.

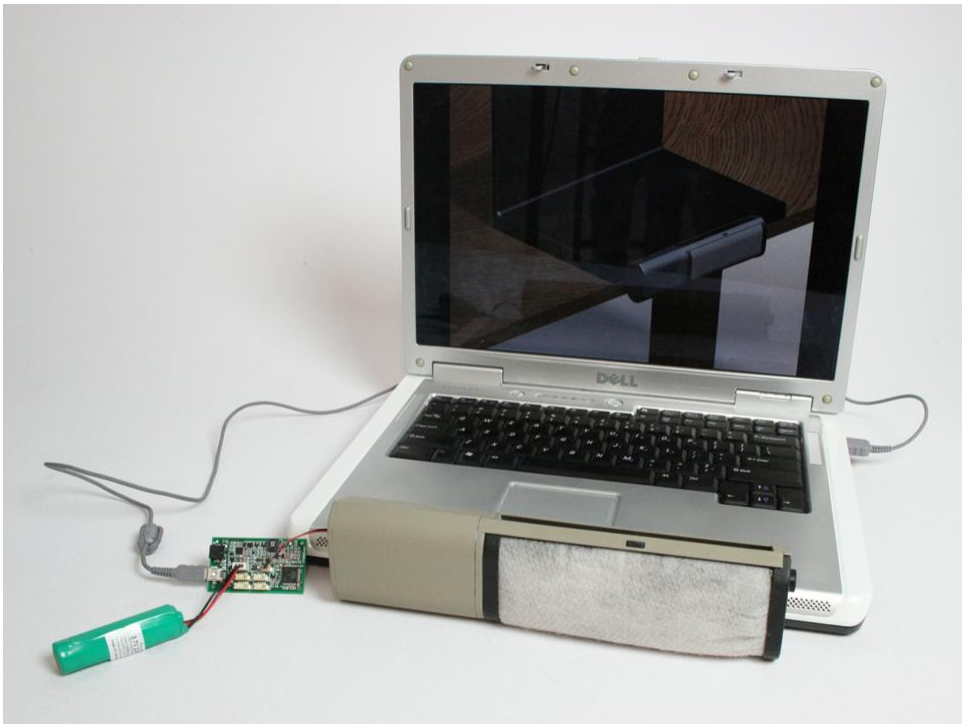

Fig. 5-10 Complete PAV-4 system.

Two additional revisions were completed (PAV-5 and PAV-6). These prototypes finalized several smaller details. The final PAV-6 prototypes are shown in Fig. 5-11. An installed PAV unit attached to an office desk and plugged into a laptop computer is shown in Fig. 5-12.

Fig. 5-11 PAV-6 prototype units.

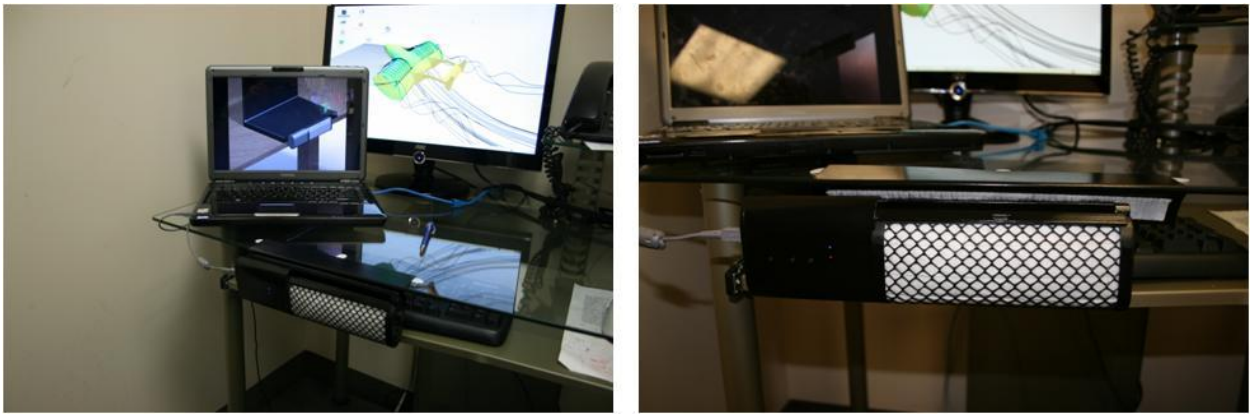

Fig. 5-12 PAV-6 prototype installed on an office desk.

SECTION 6

Design and Fabrication of Custom PC Control Board and Software

Through a collaboration with Allred Embedded Systems, a custom PC Board was designed and fabricated for the PAV device. Figs. 6-1 and 6-2 give a systems-level overview of the control logic for this program. The main features include:

1) Rechargeable lithium-ion battery that operates the system for approximately 4 hours
2) Both USB and AC power connections for main power and battery recharging
3) Pulse-width modulation (PWM) motor speed controller
4) Board-mounted buttons for control of unit On/Off and fan speed
5) Real-time VOC detection
6) “Breeze” mode that simulates the natural random fluctuations found in wind
7) Control of the PAV unit on a Windows-based computer via the USB port

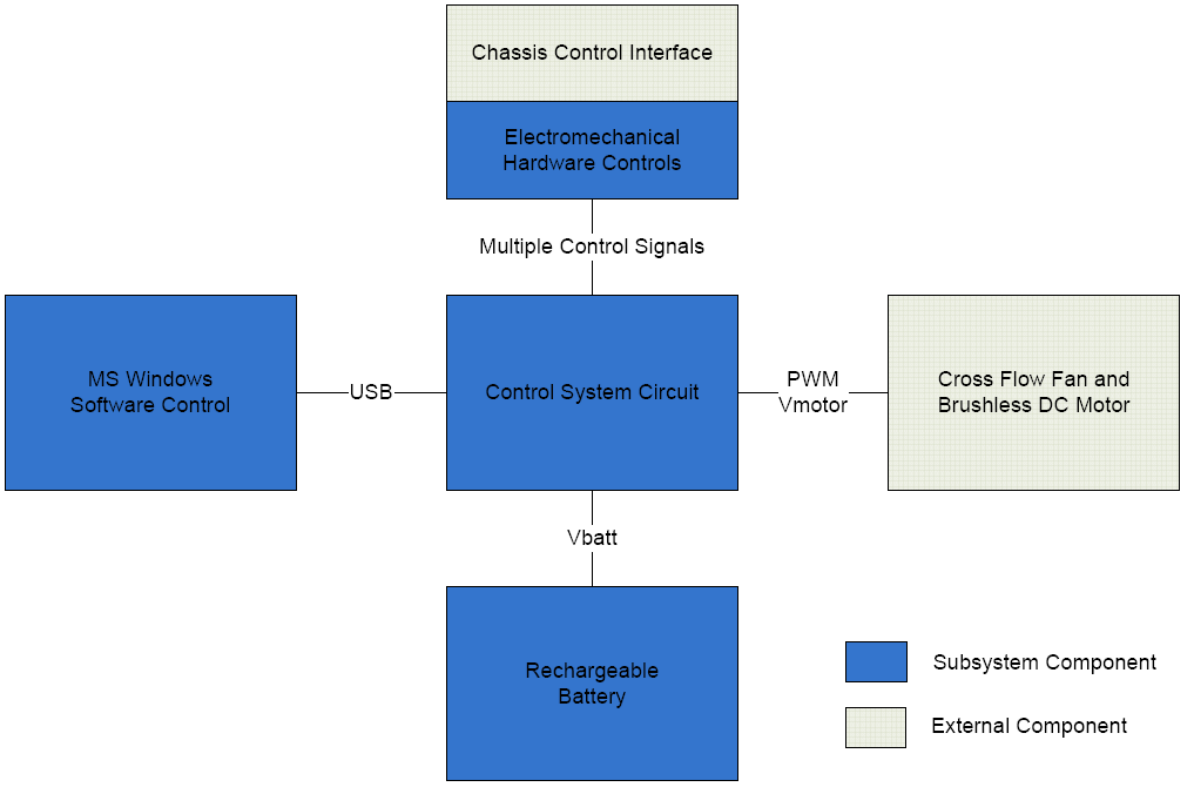

Fig. 6-1 Top-level components.

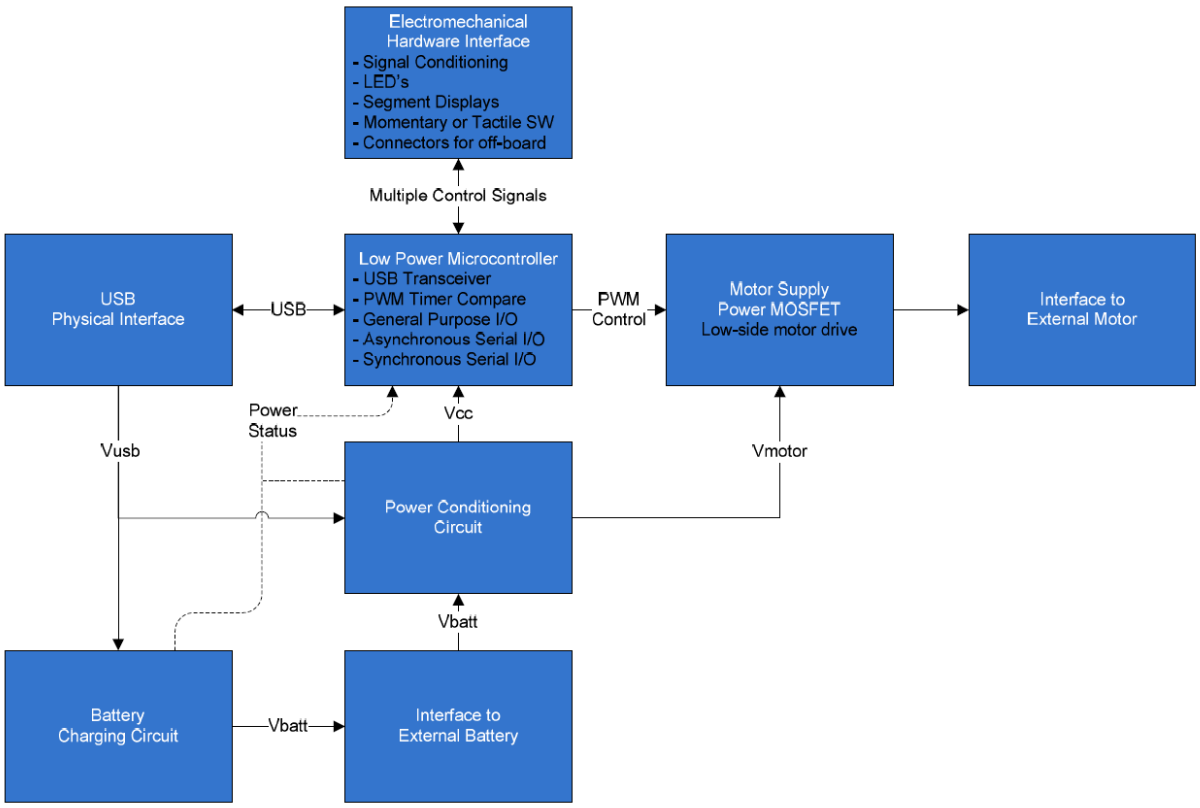

Fig. 6-2 Control circuit components.

The first-generation PC board is shown in Figs. 6-3 and 6-4.

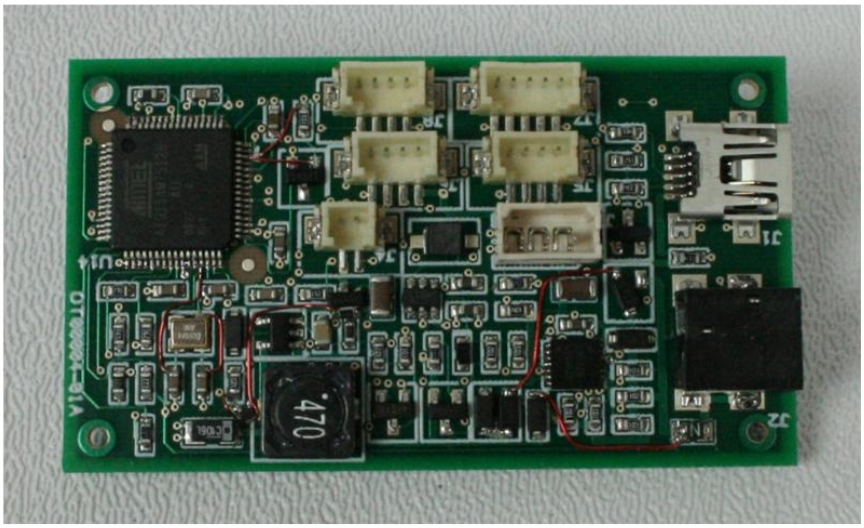

Fig. 6-3 View of front side of first-generation control board.

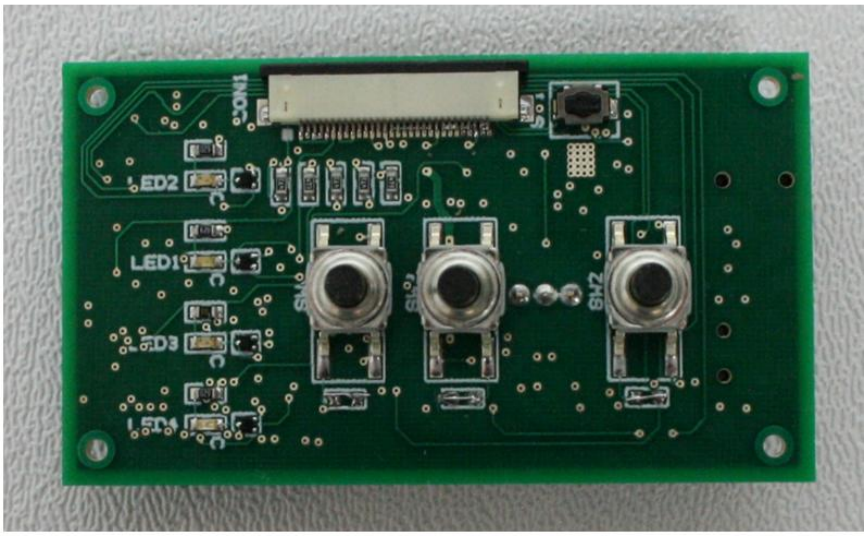

Fig. 6-4 View of back side of first-generation control board

In order to facilitate mounting in the PAV-6 prototype, a second-generation PC board was designed and fabricated. This board is shown in Figs. 6-5 and 6-6.

Fig. 6-5 View of front side of second-generation control board.

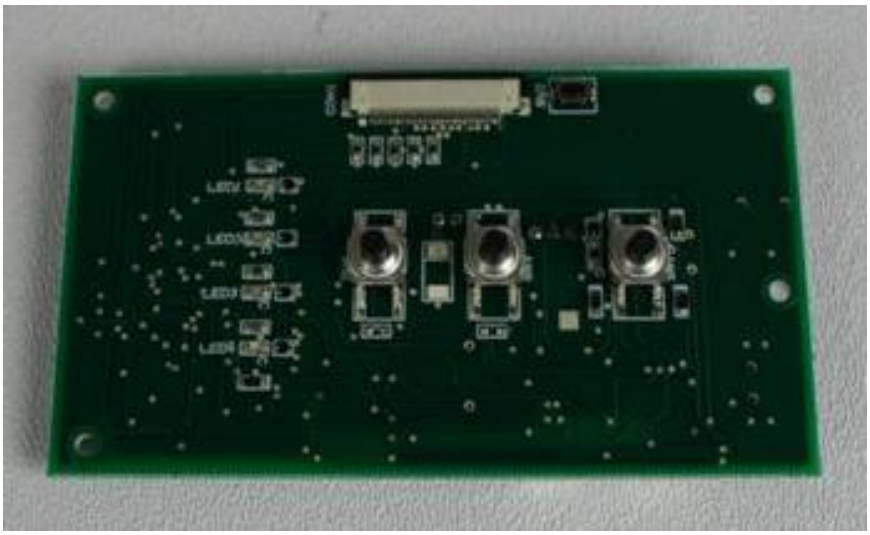

Fig. 6-6 View of back side of second-generation control board

The Windows graphical user interface is shown in Fig. 6-7. When the unit is plugged into a computer, the operating system automatically recognizes this and registers the device. The user can then operate the PAV unit from the computer.

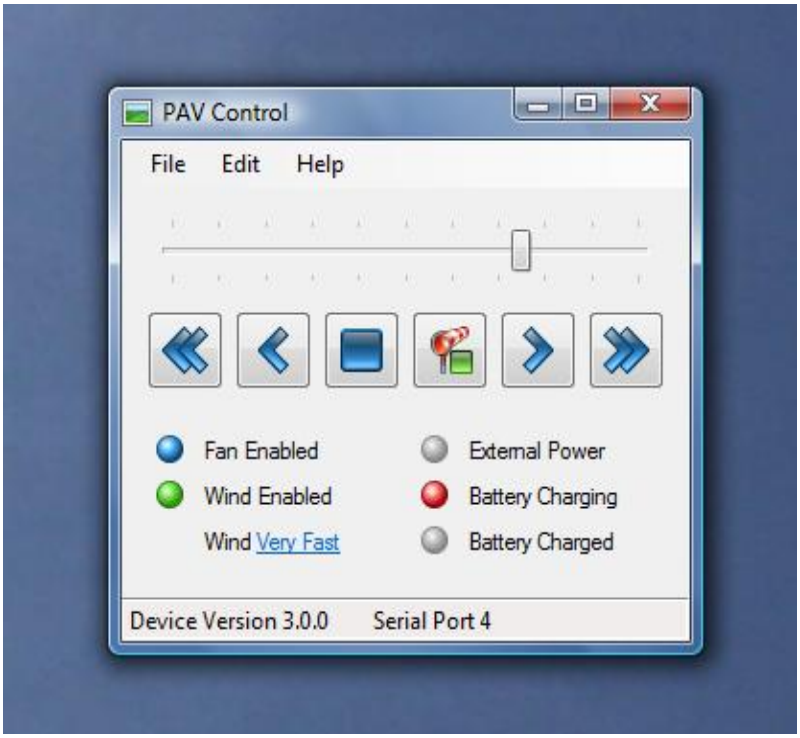

Fig. 6-7 PAV control software graphical user interface.

References

ANSI/AHAM Standard AC-1-2005, 2005, Method for Measuring Performance of Portable Household Electric Cord-connected Room Air Cleaners, Association of Home Appliance Manufacturers.

Chen W., Gao Z., Zhang J., 2006, "Reduced Energy Use through Reduced Indoor Contamination in Residential Buildings," Final Report NCEMBT 061101.

Deevy, M., Sinai, Y., Everitt, P., Voigt, L., and Gobeau, N., "Modelling the Effect of an Occupant on Displacement Ventilation with Computational Fluid Dynamics," Energy and Buildings, Vol. 40, 2008, pp. 255-264.

Melikov, A., Cermak, R., and Majer, M., "Personalized Ventilation: Evaluation of Different Air Terminal Devices," Energy and Buildings, Vol. 34, 2002, pp. 829-836.

Nielsen, P.V., Murakami, S., Kato, S., Topp, C., and Yang, J.H., "Benchmark Tests for a Computer Simulated Person," Aalborg University, Nov. 2003.

Salvador, P., CAD model of human, used with permission from www.zxys.com.

Sideroff, C., and Dang, T., "Computation of Transport in PME: Flow and Pollutant Transport," SAC Review Presentation, Aug. 2007.

Appendix: PAV Control Architecture

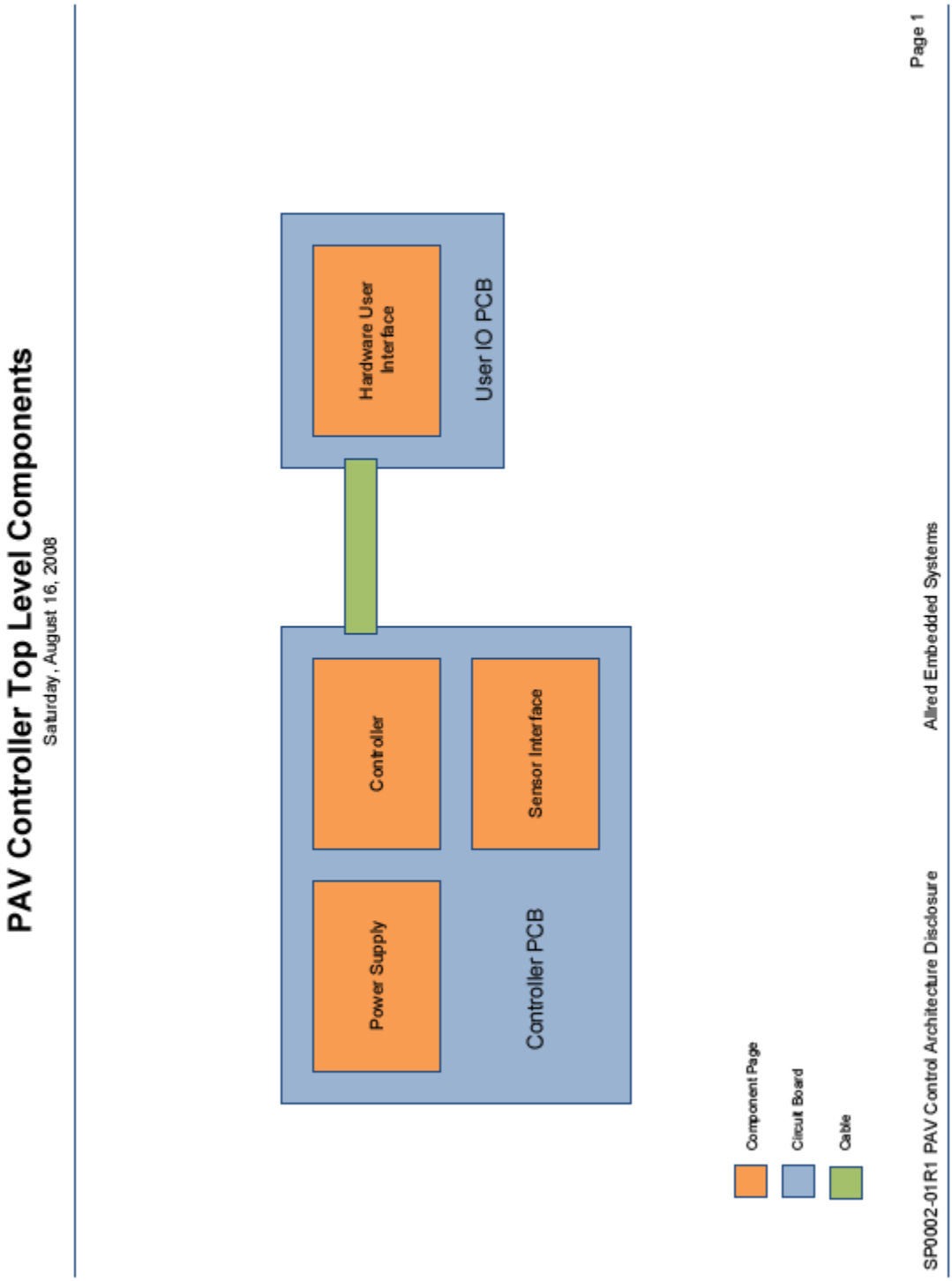

PAV Controller Power Supply Diagram

Saturday, August 16, 2008

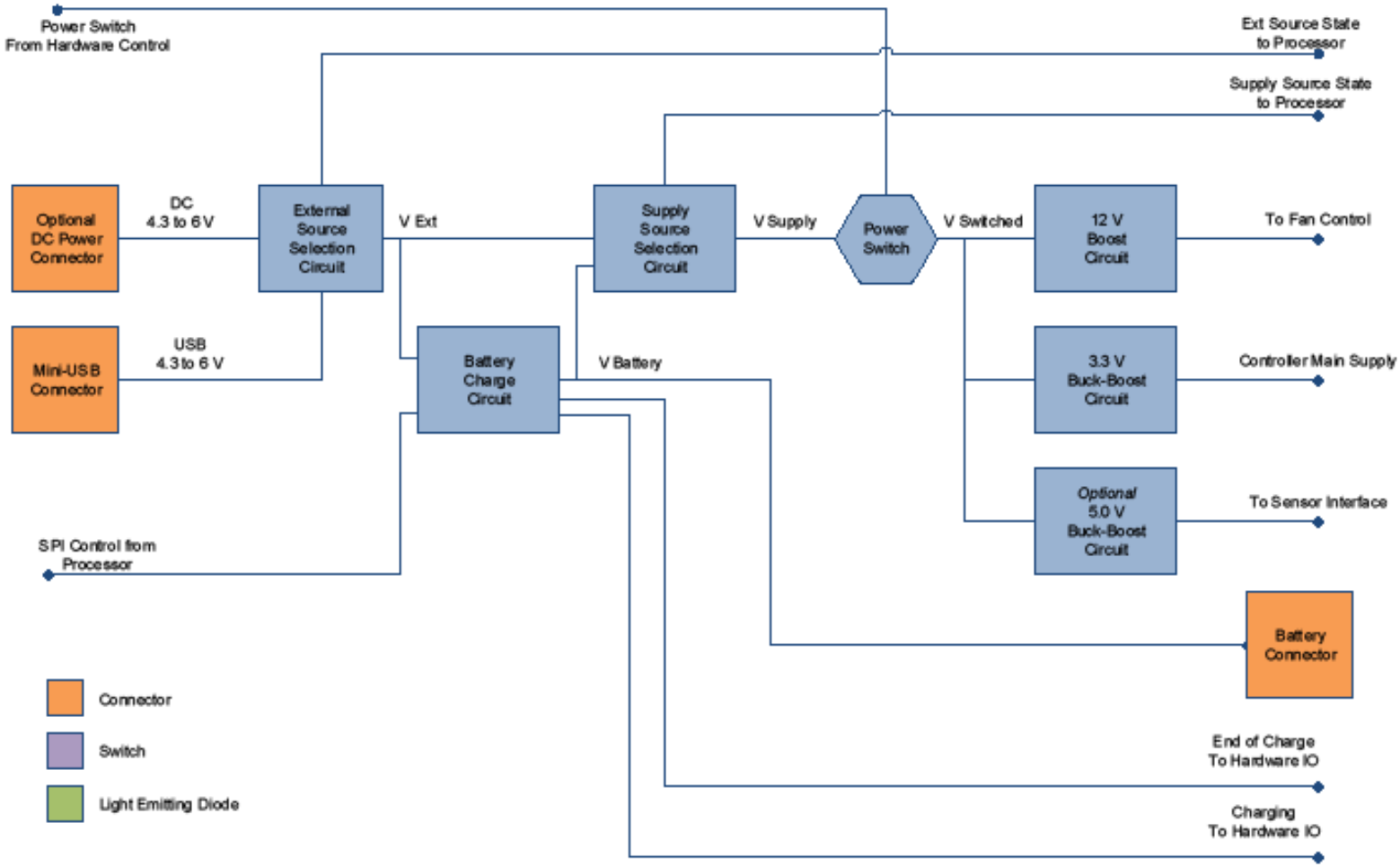

PAV Controller Microcontroller

Saturday, August 16, 2008

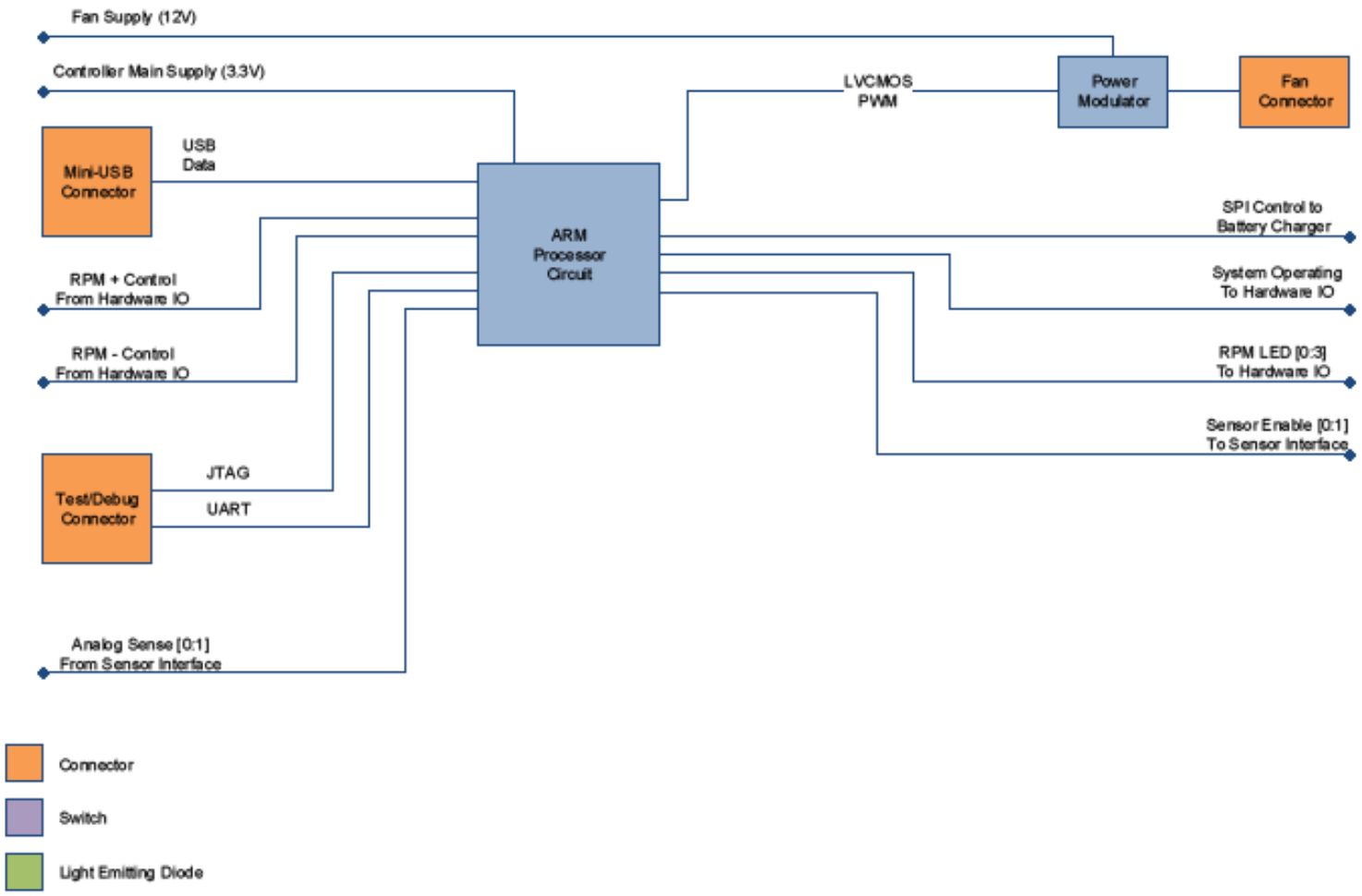

PAV Controller Hardware User Interface

Saturday, August 16, 2008

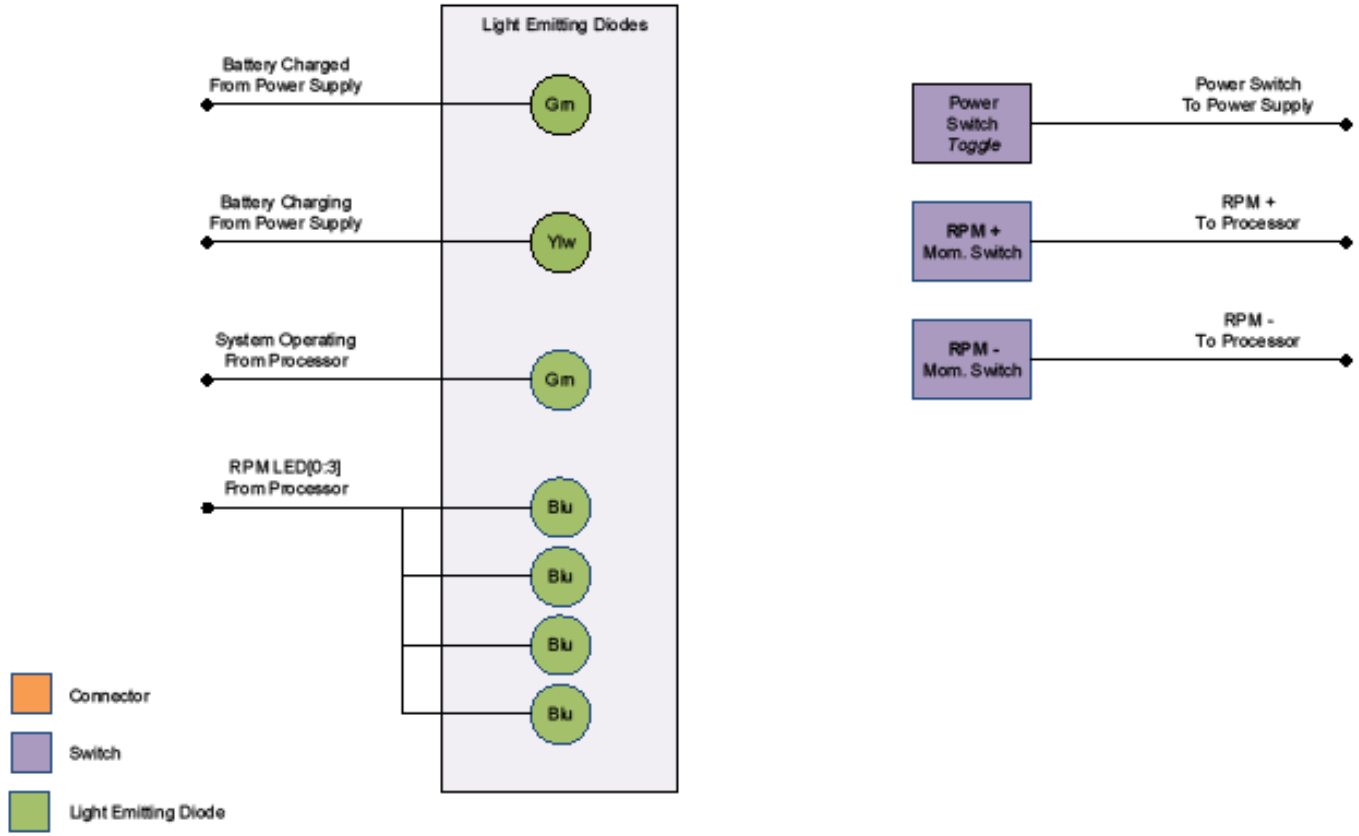

PAV Controller Sensor Interface

Saturday, August 16, 2008

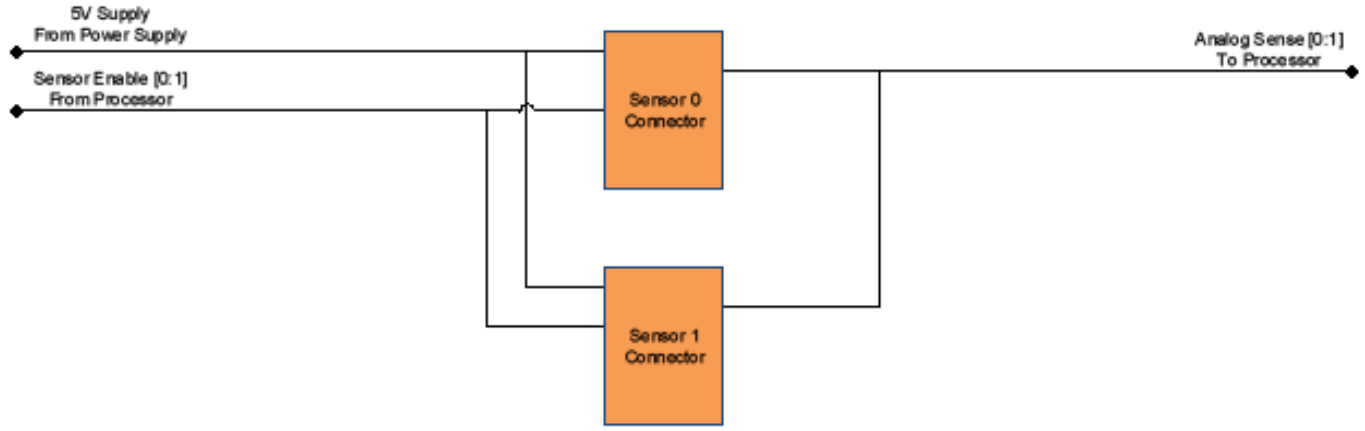

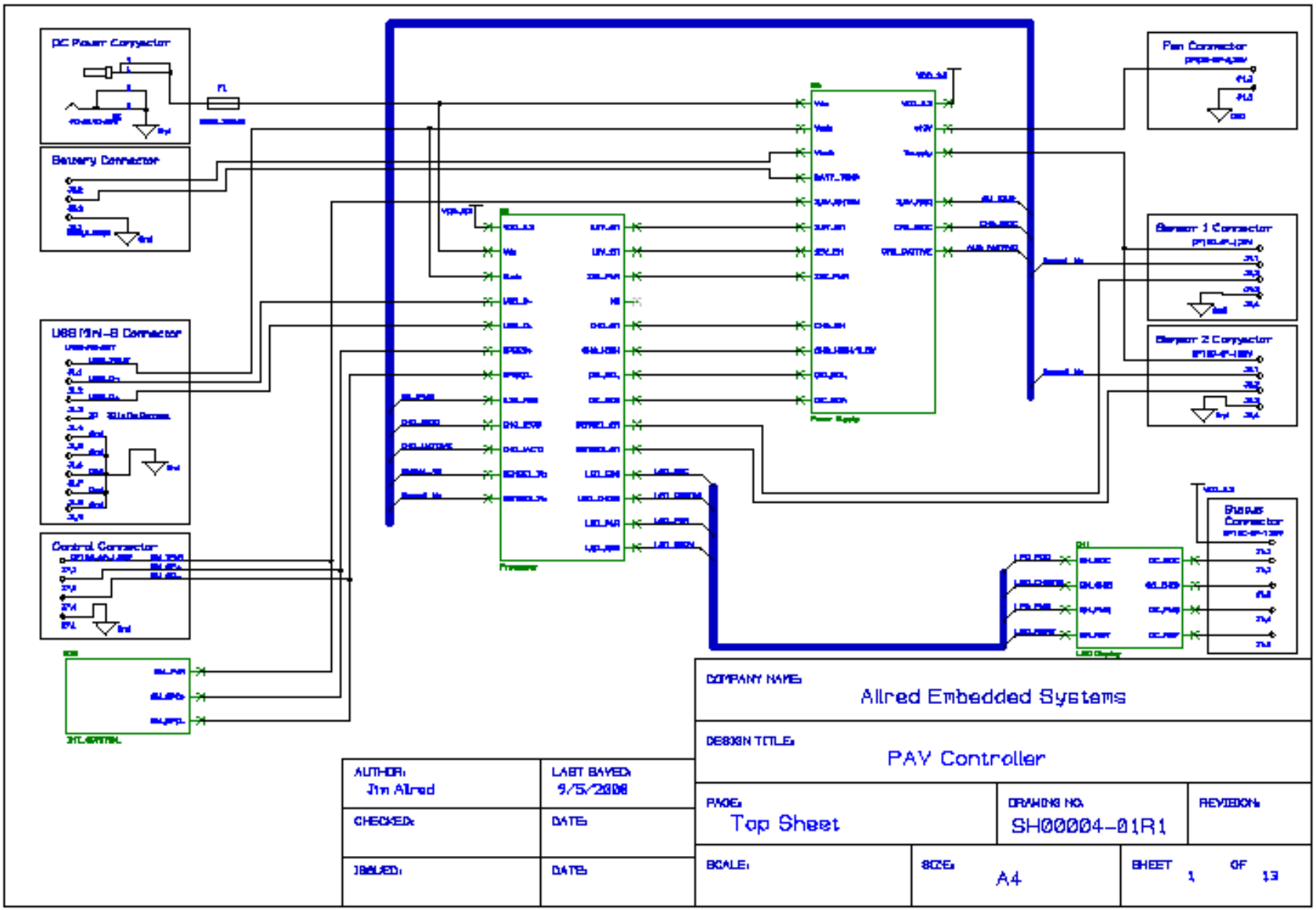
DC Power Connector
F1
Battery Connector
USB Mini-B Connector
Control Connector
Fan Connector
Sensor 1 Connector
Sensor 2 Connector
Buzzer Connector
COMPANY NAME:
Allred Embedded Systems
DESIGN TITLE:
PAV Controller
AUTHOR:
Jim Allred
LAST SAVED:
9/5/2008
CHECKED:
DATE:
ISSUED:
DATE:
PAGE:
Top Sheet
DRAWING NO.
SH00004-01R1
REVISION:
SCALE:
SIZE:
A4
SHEET 1 OF 13

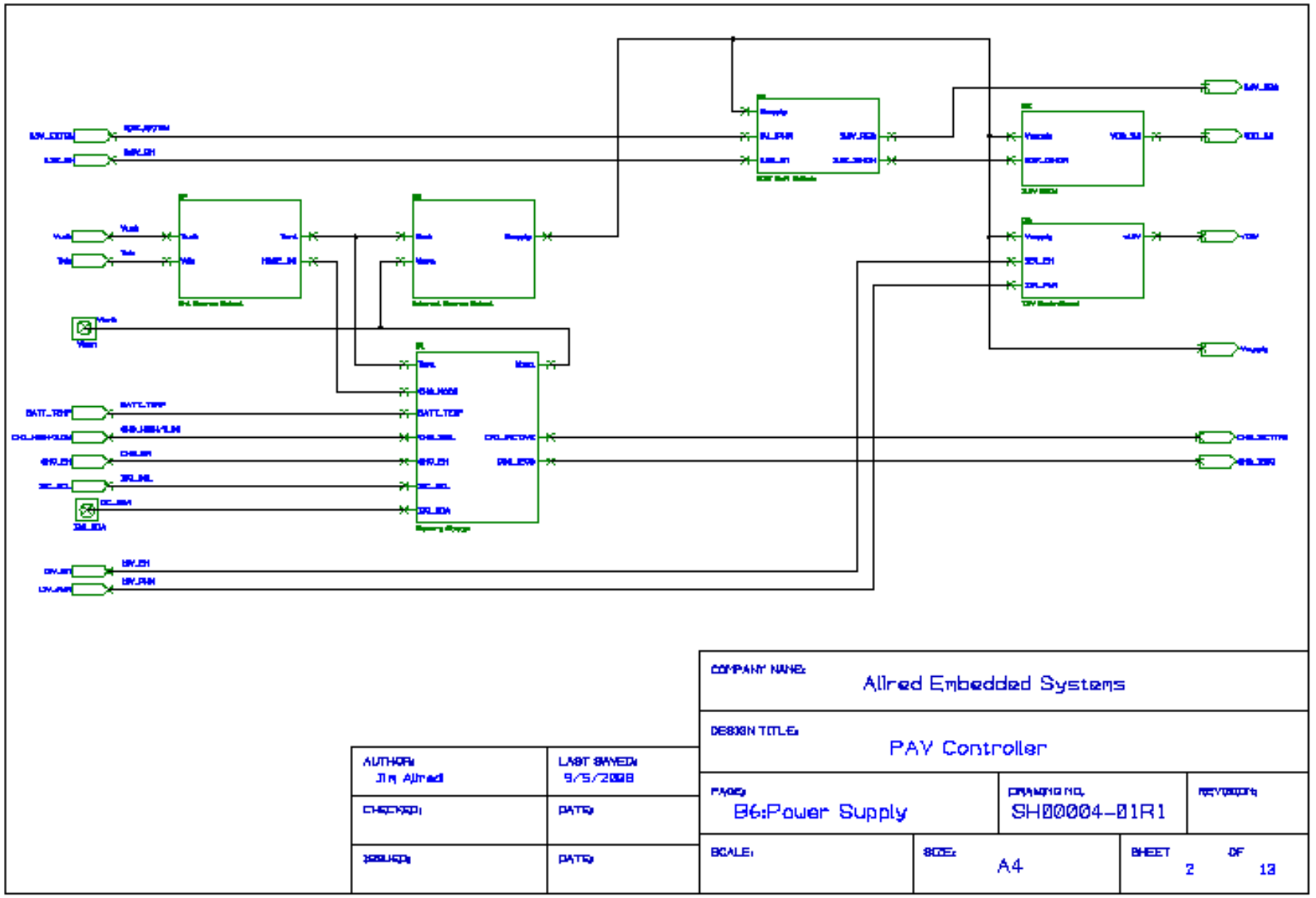
COMPANY NAME:
Allred Embedded Systems
DESIGN TITLE:
PAV Controller
AUTHOR:
Jim Allred
LAST SAVED:
9/5/2008
CHECKED:
DATE:
ISSUED:
DATE:
PAGE:
B6:Power Supply
DRAWING NO.
SH00004-01R1
REVISION:
SCALE:
SIZE:
A4
SHEET
2
OF
13

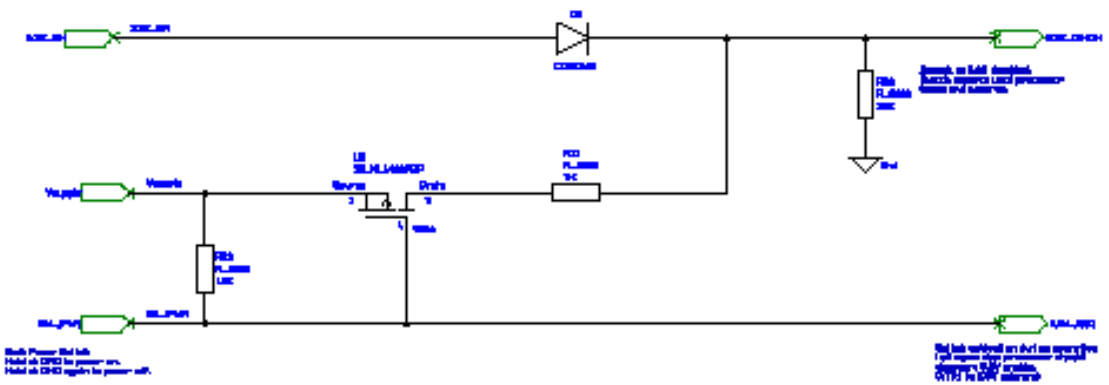

COMPANY NAME:	Allred Embedded Systems
DESIGN TITLE:	PAV Controller
AUTHOR: Jim Allred	LAST SAVED: 9/5/2008
CHECKED:	DATE:
ISSUED:	DATE:
PAGE: B4:3.3V Soft Switch	DRAWING NO.: SH00004-01R1
REVISIONS:	
SCALE:	SIZE: A4
SHEET 3 OF 13	

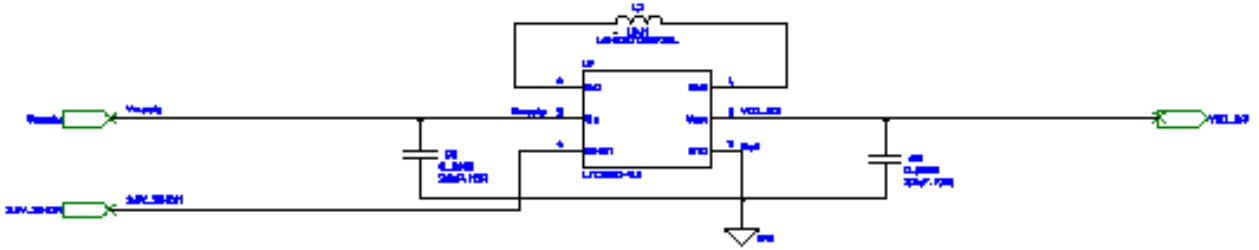

COMPANY NAME:	Allred Embedded Systems
DESIGN TITLE:	PAV Controller
PAGE: B2:3.3V Buck	DRAWING NO.: SH00004-01R1
SCALE:	SIZE: A4
SHEET 4 OF 13	

AUTHOR: Jim Allred	LAST SAVED: 9/5/2008
CHECKED:	DATE:
ISSUED:	DATE:

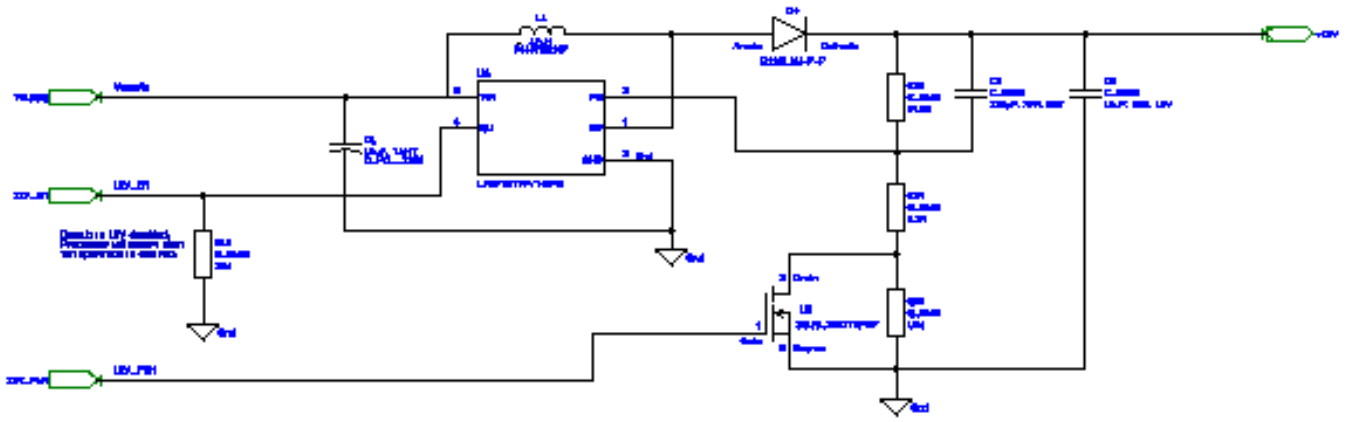

COMPANY NAME:	Allred Embedded Systems
DESIGN TITLE:	PAV Controller
AUTHOR: Jim Allred	LAST SAVED: 9/5/2008
CHECKED:	DATE:
ISSUED:	DATE:
PAGE: B3:12V Buck-Boost	DRAWING NO.: SH00004-01R1
REVISION:	
SCALE:	SIZE: A4
SHEET 5 OF 13	

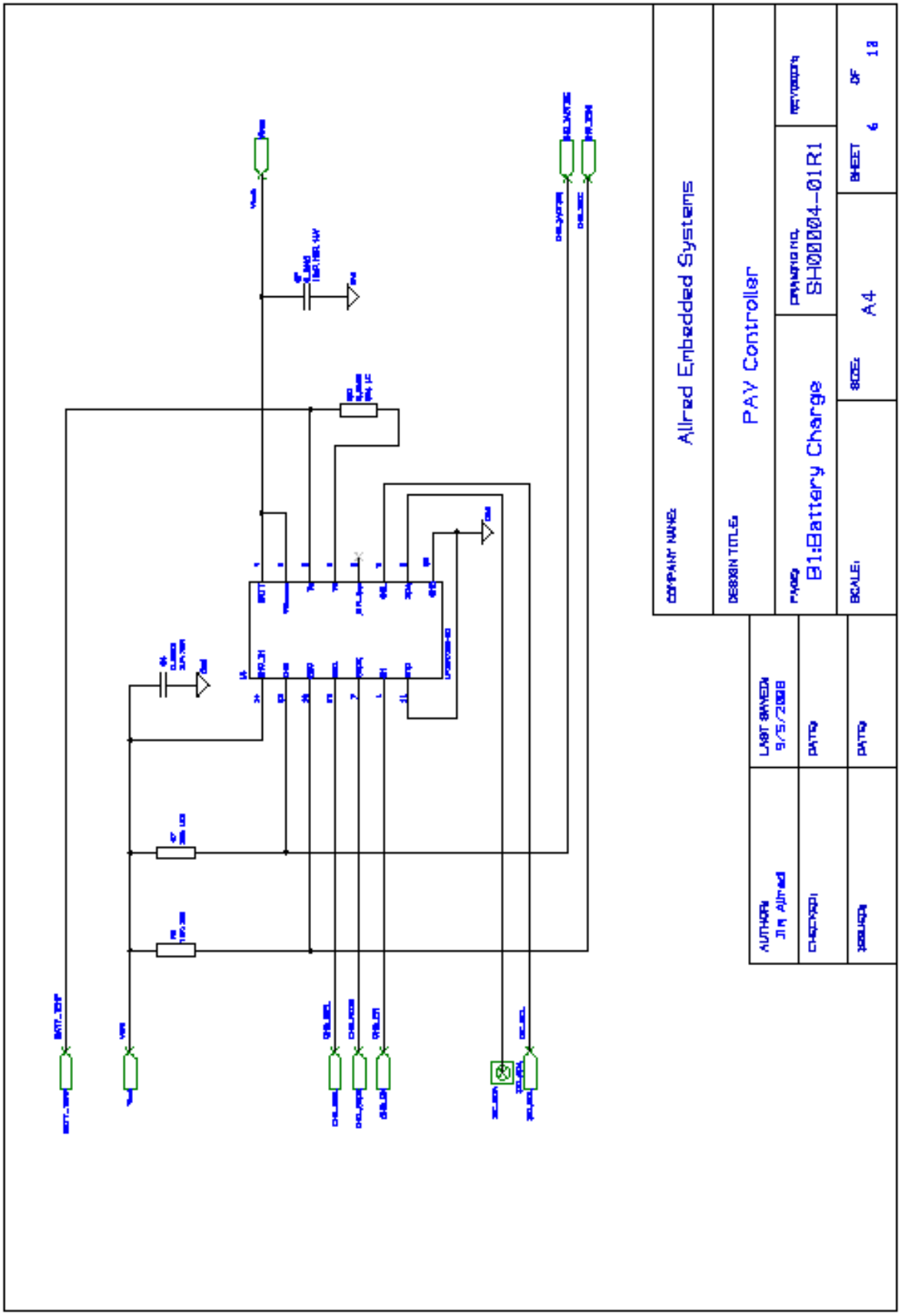
COMPANY NAME: Allred Embedded Systems
DESIGN TITLE: PAY Controller
PAGE: B1:Battery Charge
DRAWING NO.: SH000004-01R1
SIZE: A4
SHEET 6 OF 18
AUTHOR: Jim Allred
LAST SAVED: 9/5/2008
CHECKED:
APPROVED:
DATE
DATE
DATE

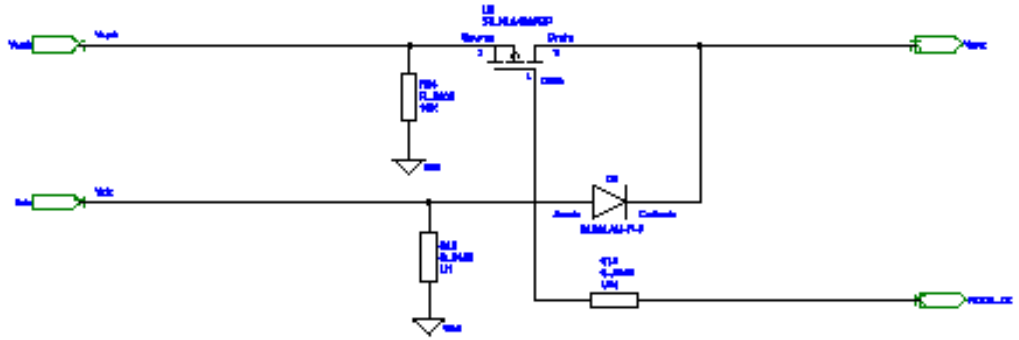

COMPANY NAME:	Allred Embedded Systems
DESIGN TITLE:	PAV Controller
PAGE: B7:Ext Source Select	DRAWING NO.: SH00004-01R1
SCALE:	SIZE: A4
SHEET 7 OF 18	

AUTHOR: Jim Allred	LAST SAVED: 9/5/2008
CHECKED:	DATE:
ISSUED:	DATE:

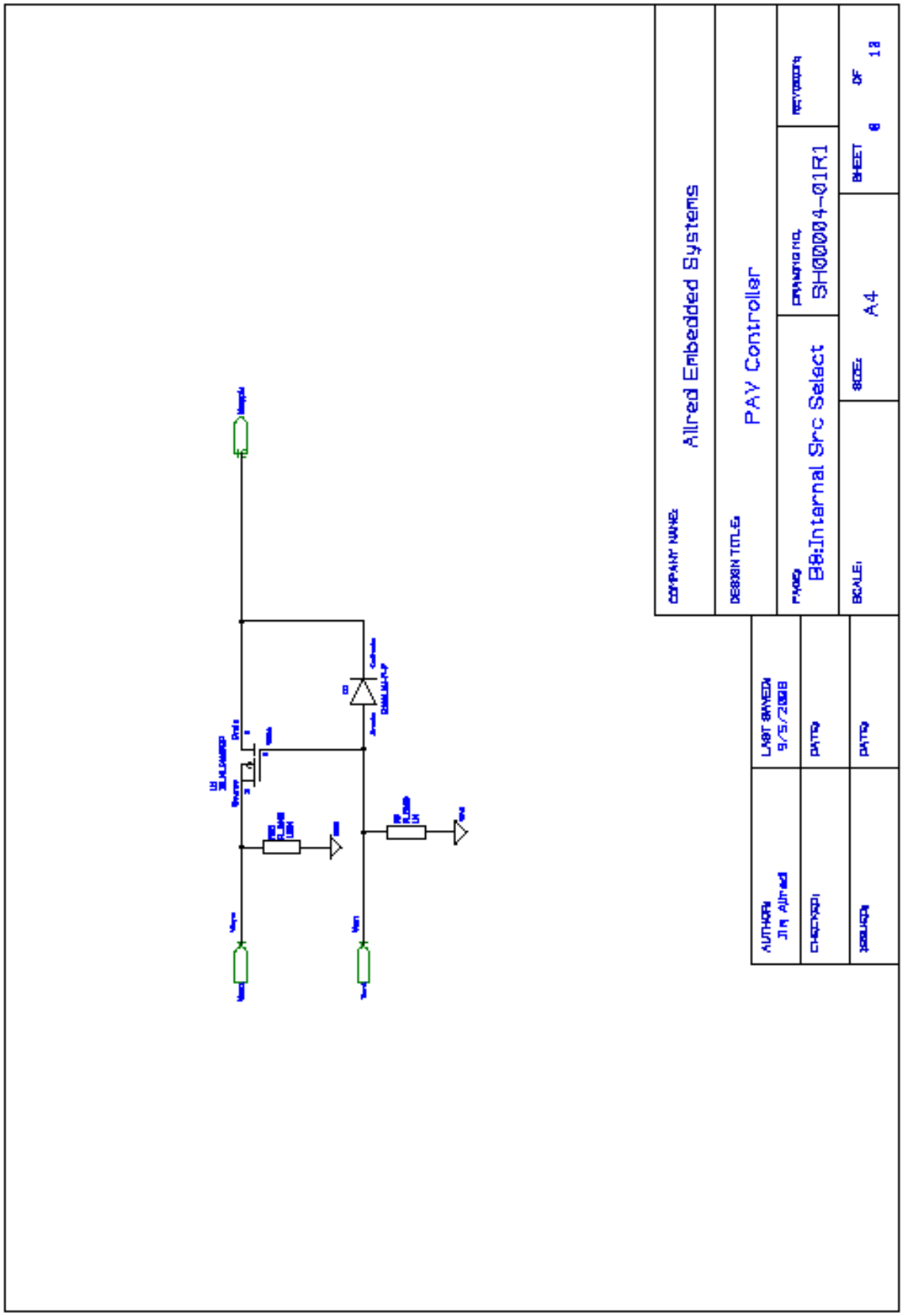
COMPANY NAME:
Allred Embedded Systems
DESIGN TITLE:
PAY Controller
PAGE:
B8:Internal Src Select
DRAWING NO.
SH00004-01R1
REVISION:
SIZE:
A4
SHEET
8
OF
18
SCALE:
AUTHOR:
Jim Allred
LAST SAVED:
9/5/2008
CHECKED:
DATE:
DRAWN:
DATE:

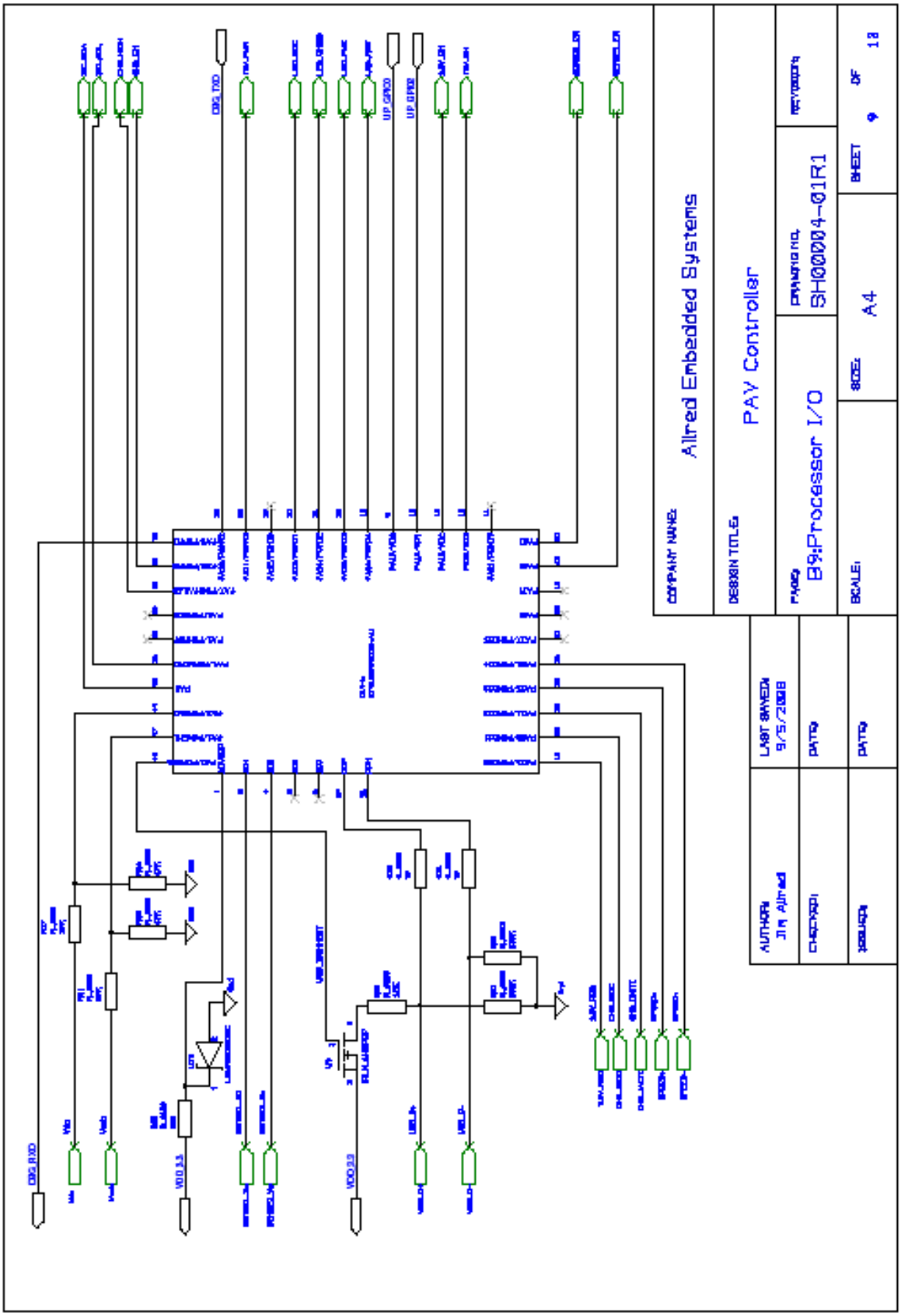
COMPANY NAME:
Allred Embedded Systems
DESIGN TITLE:
PAY Controller
PAGE:
B9:Processor I/O
DRAWING NO.
SH00004-01R1
SIZE:
A4
SHEET
9
OF
18
SCALE:
AUTHOR:
Jim Allred
LAST SAVED:
9/5/2008
CHECKED:
DATE:
APPROVED:
DATE:
REVISIONS

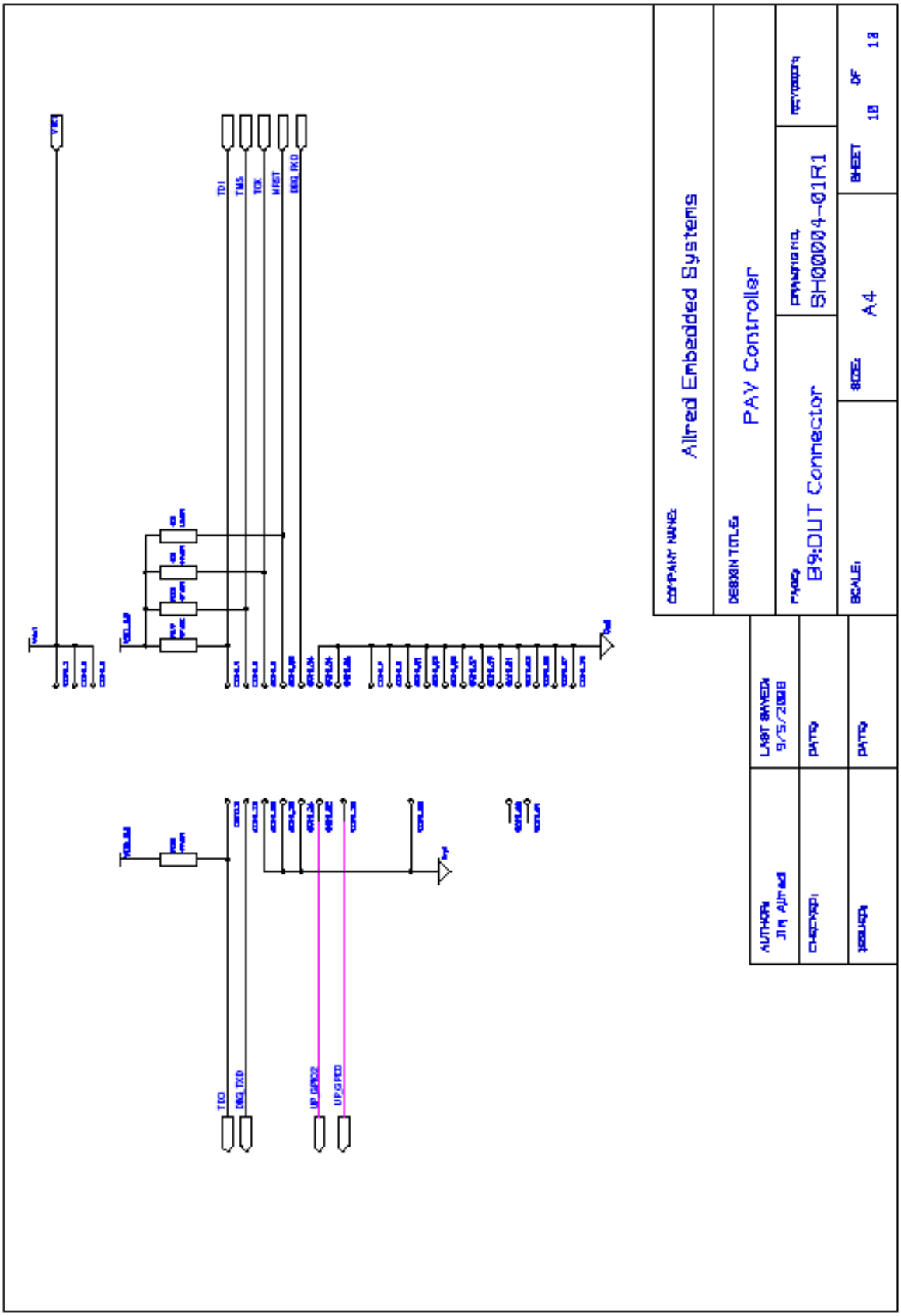
COMPANY NAME:
Allred Embedded Systems
DESIGN TITLE:
PAY Controller
PAGE:
B9:DUT Connector
DRAWING NO.
SH00004-01R1
REVISION:
SCALE:
A4
SHEET
18
OF
18
AUTHOR:
Jim Allred
LAST SAVED:
9/5/2008
CHECKED:
DATE:
APPROVED:
DATE:
TDI
TMS
TDO
NRST
DBG_RXD
TDO
DBG_TXD
UP_GPIO2
UP_GPIO3

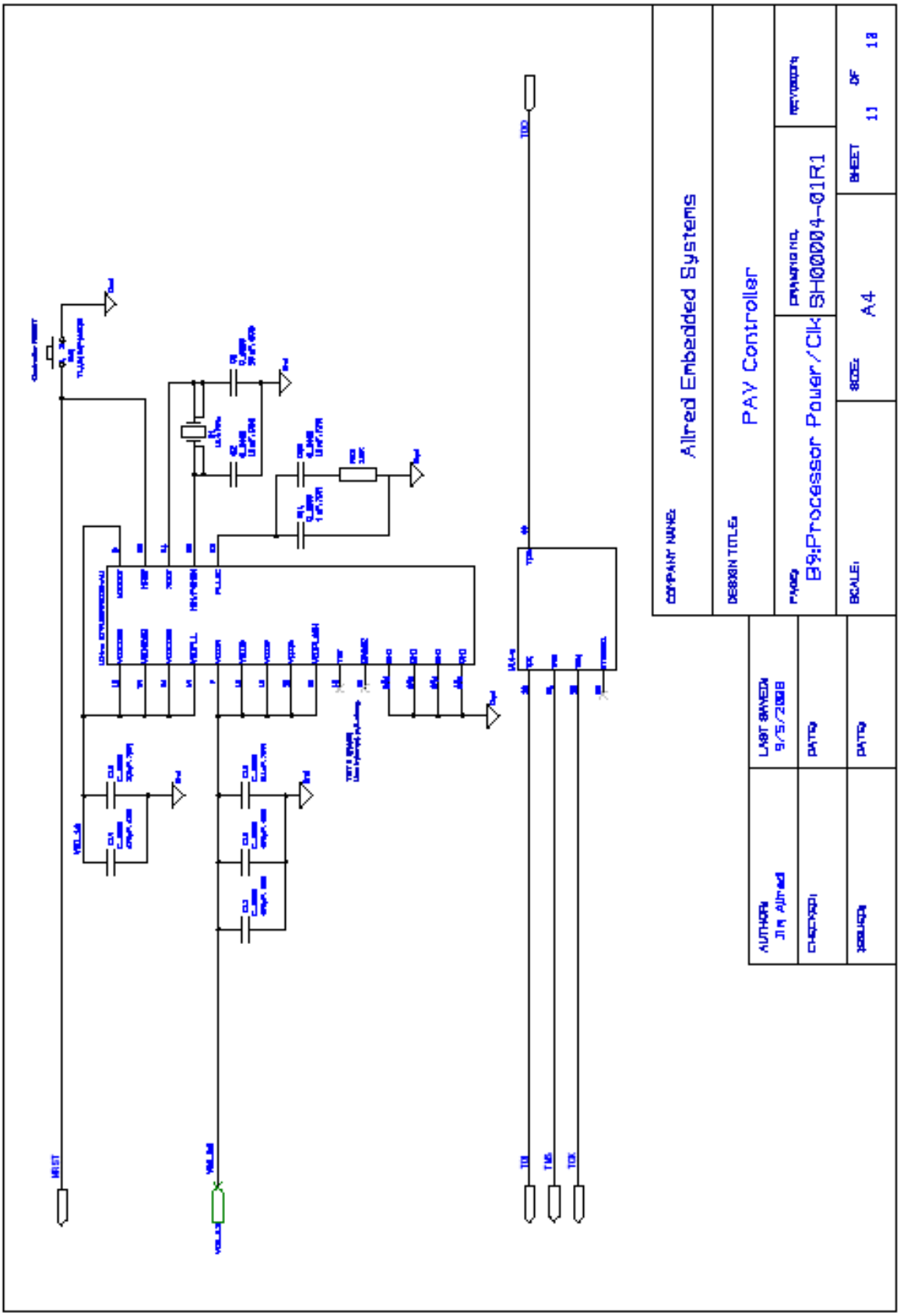
Alfred Embedded Systems
PAY Controller
B9:Processor Power/Clk
SH000004-01R1
A4

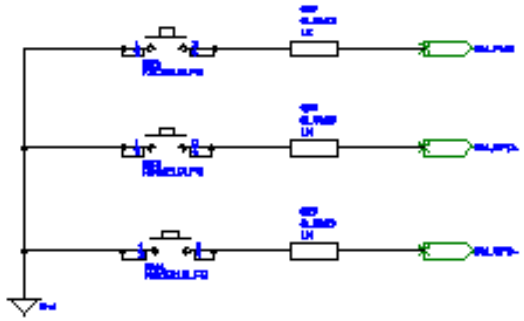

AUTHOR: Jim Allred	LAST SAVED: 9/5/2008	COMPANY NAME: Allred Embedded Systems		
CHECKED:	DATE:	DESIGN TITLE: PAV Controller		
ISSUED:	DATE:	PAGE: B10:Int_Control	DRAWING NO: SH00004-01R1	REVISION:
		SCALE:	SIZE: A4	SHEET 12 OF 13

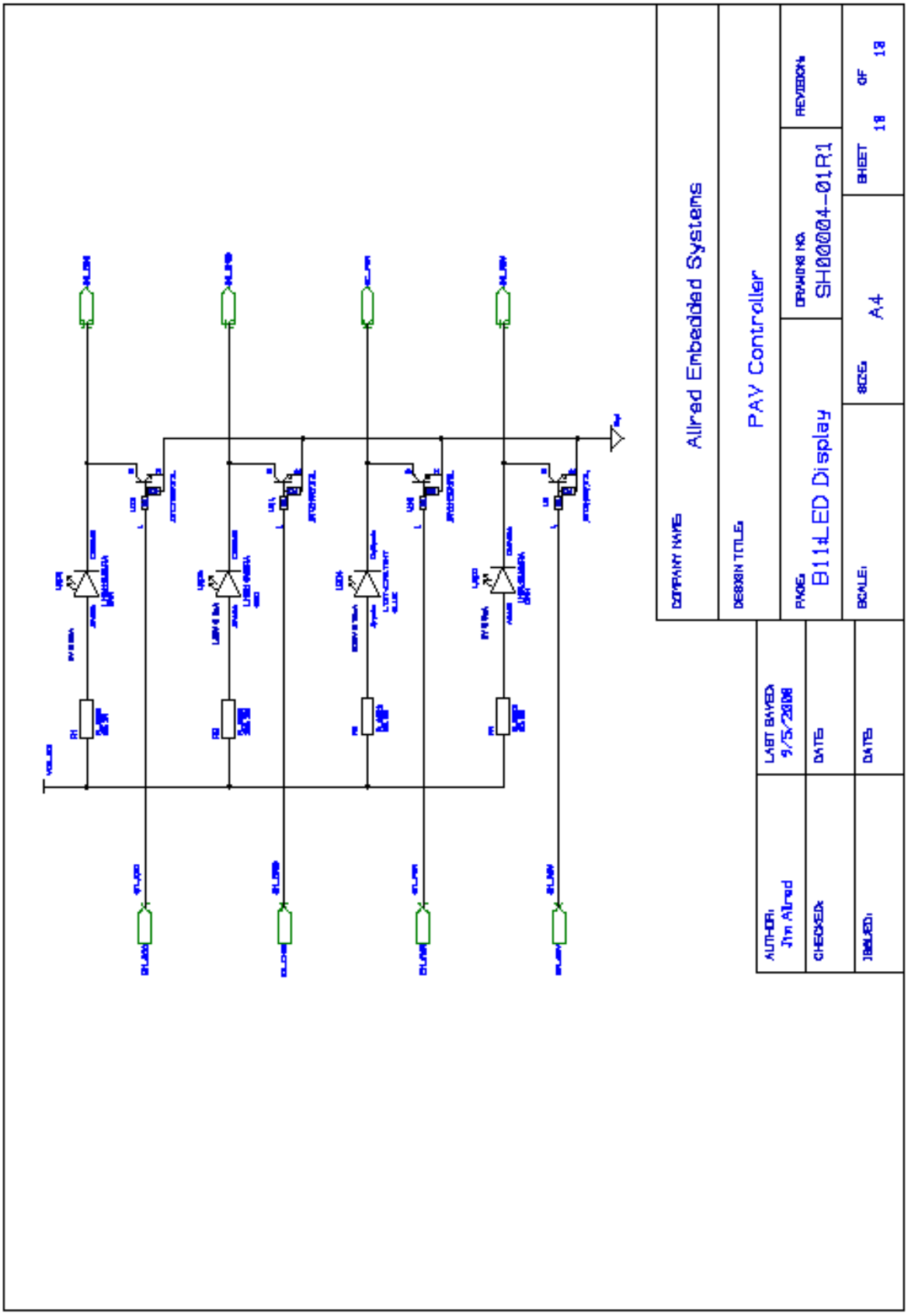
COMPANY NAME:
Allred Embedded Systems
DESIGN TITLE:
PAY Controller
PAGE:
B11LED Display
DRAWING NO.
SH00004-01R1
REVISION
SIZE:
A4
SHEET
18
OF
18
SCALE:
AUTHOR:
Jim Allred
LAST SAVED:
9/5/2008
CHECKED:
DATE
APPROVED:
DATE